The Dynamics and Control of Large Space Structures with Distributed Actuation

University of Glasgow

Bonar Robb

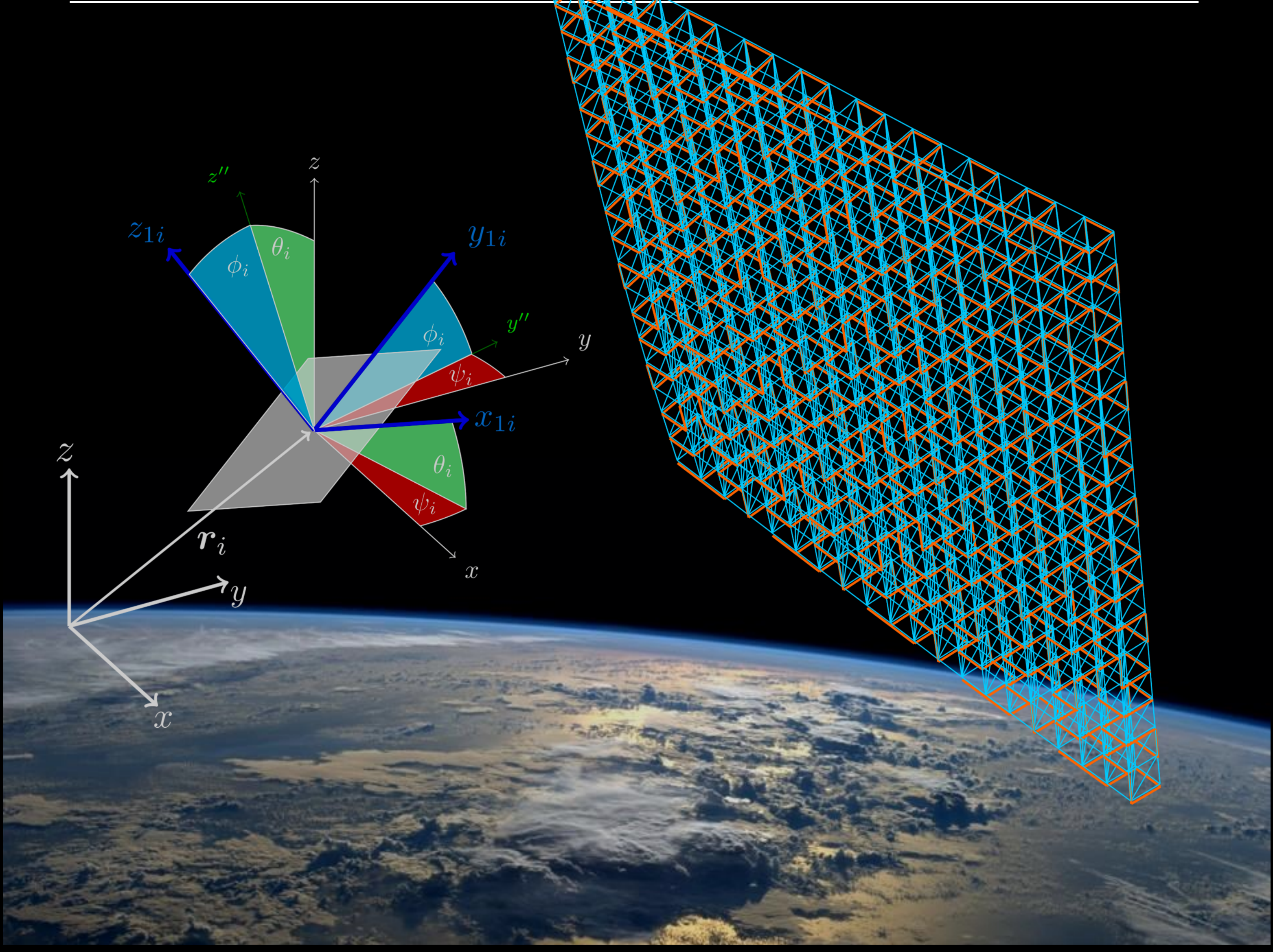

The Dynamics and Control of Large Space Structures with Distributed Actuation

Bonar Robb

Submitted in fulfilment of the requirements for the
Degree of Doctor of Philosophy

James Watt School of Engineering
College of Science and Engineering
University of Glasgow

November 2022

Abstract

Future large space structures are likely to be constructed at much greater length-scales, and lower areal mass densities than has been achieved to-date. This could be enabled by ongoing developments in on-orbit manufacturing, whereby large structures are 3D-printed in space from raw feedstock materials. This thesis proposes and analyses a number of attitude control strategies which could be adopted for this next generation of ultra-lightweight, large space structures. Each of the strategies proposed makes use of distributed actuation, which is demonstrated early in the thesis to reduce structural deformations during attitude manoeuvres. All of the proposed strategies are considered to be particularly suitable for structures which are 3d-printed on-orbit, due to the relative simplicity of the actuators and ease with which the actuator placement or construction could be integrated with the on-orbit fabrication of the structure itself.

The first strategy proposed is the use of distributed arrays of magnetorquer rods. First, distributed torques are shown to effectively rotate highly flexible structures. This is compared with torques applied to the centre-of-mass of the structure, which cause large surface deformations and can fail to enact a rotation. This is demonstrated using a spring-mass model of a planar structure with embedded actuators. A torque distribution algorithm is then developed to control an individually addressable array of actuators. Attitude control simulations are performed, using the array to control a large space structure, again modelled as a spring-mass system. The attitude control system is demonstrated to effectively detumble a representative 75×75 m flexible structure, and perform slew manoeuvres, in the presence of both gravity-gradient torques and a realistic magnetic field model.

The development of a Distributed Magnetorquer Demonstration Platform is then presented, a laboratory-scale implementation of the distributed magnetorquer array concept. The platform consists of 48 addressable magnetorquers, arranged with two perpendicular torquers at the nodes of a 5×5 grid. The control algorithms proposed previously in the thesis are implemented and tested on this hardware, demonstrating the practical feasibility of the concept. Results of experiments using a spherical air bearing and Helmholtz cage are presented, demonstrating rest-to-rest slew manoeuvres and detumbling around a single axis using the developed algorithms.

The next attitude control strategy presented is the use of embedded current loops, conductive pathways which can be integrated with a spacecraft support structure and used to generate control torques through interaction with the Earth's magnetic field. Length-scaling laws are derived by determining what fraction of a planar spacecraft's mass would need to be allocated to the conductive current loops in order to produce a torque at least as large as the gravity gradient torque. Simulations are then performed of a flexible truss structure, modelled as a spring-mass system, for a range of structural flexibilities and a variety of current loop geometries. Simulations demonstrate rotation of the structure via the electromagnetic force on the current carrying elements, and are also used to characterise the structural deformations caused by the various current loop geometries. An attitude control simulation is then performed, demonstrating a 90° slew manoeuvre of a 250×250 m flexible structure through the use of three orthogonal sets of current loops embedded within the spacecraft.

The final concept investigated in this thesis is a self-reconfiguring OrigamiSat, where reconfiguration of the proposed OrigamiSat is triggered by changes in the local surface optical properties of an origami structure to harness the solar radiation pressure induced acceleration. OrigamiSats are origami spacecraft with reflective panels which, when flat, operate as a conventional solar sail. Shape reconfiguration, i.e. "folding" of the origami design, allows the OrigamiSat to change operational modes, performing different functions as per mission requirements. For example, a flat OrigamiSat could be reconfigured into the shape of a parabolic reflector, before returning to the flat configuration when required to again operate as a solar sail, providing propellant-free propulsion. Shape reconfiguration or folding of OrigamiSats through the use of surface reflectivity modulation is investigated in this thesis. First, a simplified, folding facet model is used to perform a length-scaling analysis, and then a 2d multibody dynamics simulation is used to demonstrate the principle of solar radiation presure induced folding. A 3d multibody dynamics simulation is then developed and used to demonstrate shape reconfiguration for different origami folding patterns. Here, the attitude dynamics and shape reconfiguration of OrigamiSats are found to be highly coupled, and thus present a challenge from a control perspective. The problem of integrating attitude and shape control of a Miura-fold pattern OrigamiSat through the use of variable reflectivity is then investigated, and a control algorithm developed which uses surface reflectivity modulation of the OrigamiSat facets to enact shape reconfiguration and attitude manoeuvres simultaneously.

Contents

List of Tables

List of Figures

Acknowledgements

First, I'd like to thank my supervisor, Colin McInnes, for his guidance, support, and invaluable contributions throughout the preparation of this thesis. I'm truly grateful to have had the opportunity to work on such an interesting topic, and to have had the freedom to follow so many of the different questions and varied directions that the research has taken during the project.

I'd also like to thank the macro-scale theme leads. First Malcolm McRobb, for those early discussions and insights that lead to so much of the work forming this thesis, and then Gilles Bailet, for his support and guidance throughout. Special thanks to Gilles for sharing his expertise in the lab and the comments and suggestions which helped the experimental work come together. Similarly, thanks to Zhongxu and Jim for the electronics advice and help with the hardware design.

Thanks also to everyone I shared the corner of room 734 with at various points, Federico, Liviu, Merel and Tom, for all the brainstorming sessions, lunch breaks and occasional games of mario-kart. Further thanks to all the other pals made along the way, and everyone in the wider SET group for all the discussions, presentations and Paesano visits that helped create such a welcoming and positive research environment.

Finally, thanks to all my friends and family for the innumerable other ways I've been supported during my studies. Thanks to my parents for always supporting me in all of my choices, and to my sisters for all of their encouragement. Lastly, thanks to Rebecca for her support, friendship, and patience, particularly during the final months of writing up.

Nomenclature

α	Temperature coefficient
ϵ	Emmissivity
Γ	Temperature
γ	Damping coefficient
κ	Curvature
κ_τ	Magnetorquer dipole moment to mass ratio
λ_f	Magnetorquer/conductor mass fraction
$\mathbf{A}$	Adjacency matrix
$\mathbf{I}$	Inertia tensor
$\mathbf{J}$	Jacobian matrix
$\mathbf{M}$	Mass matrix
μ	Standard gravitational parameter
$\overline{q}$	Quaternion
ψ, θ, ϕ	Euler angles
ρ	Reflectivity
ρ_r	Resistivity
σ	Stefan-Boltzman constant
σ_A	Areal mass density
$\boldsymbol{\lambda}$	Lagrange multipliers
$\boldsymbol{\omega}$	Angular velocity

$\boldsymbol{\rho}$	Panel reflectivity vector
$\boldsymbol{B}$	Magnetic field
$\boldsymbol{C}$	Constraint vector
$\boldsymbol{F}$	Force
$\boldsymbol{m}_d$	Magnetorquer magnetic dipole moment
$\boldsymbol{Q}_a$	Applied forces
$\boldsymbol{Q}_c$	Constraint forces
$\boldsymbol{Q}_v$	Inertial forces
$\boldsymbol{r}$	General position vector
$\boldsymbol{T}, \boldsymbol{\tau}$	Torque
ξ_n	Damping ratio
A_e	Current loop enclosed area
d	Structure side-length
EI	Flexural rigidity
I	Current
k	Spring constant
L_b	Beam length
l_b	Beam element length
m, M	Mass
n	Number of elements
N_x, N_y	Number of activated magnetorquers
P	Power
P_ω	Derivative gain
P_j	Joule heating
P_q	Proportional gain
P_r	Thermal radiation

R	Resistance
R_E	Radius of the Earth
R_o	Orbital radius
t	Time
V	Potential
$x_E y_E z_E$	Earth-centered inertial frame
$x_o y_o z_o$	Orbital frame
xyz	Spacecraft body frame

Declaration

I hereby declare that except where specific reference is made to the work of others, the contents of this doctoral thesis are original and have not been submitted in whole or in part for consideration for any other degree or qualification.

Permission to copy without fee all or part of this doctoral thesis is granted, provided that copies are not made or distributed for commercial purposes and that the name of the author, the title of the thesis and date of submission are clearly visible on the copy.

Bonar Robb

Glasgow, Scotland
25$^{\text{th}}$ November, 2022

Chapter 1

Introduction

Large space structures will likely underpin a significant portion of humanity's future activities in space. In recent years, the trend in spacecraft technology has been towards increasingly smaller satellites, driven by the miniaturisation of various technologies and the use of standardised form factors. For many applications in space however, there is a need for large surface areas and large supporting structures. Often this need is driven fundamentally by the underlying physics of the application, and thus such systems cannot be miniaturised or scaled down through engineering ingenuity alone. Capturing solar energy in space necessitates solar panels covering a large surface area; communications antennas benefit from large aperture reflectors; and looking further into the future, crewed interplanetary spaceflight or human space-habitats will need to be much larger than present space stations and vehicles if they are to comfortably accommodate large numbers of people on an extended basis. The design, construction and operation of such structures will require significant efforts, both in terms of the technical, engineering challenges involved, and the investment of resources required. And yet the potential scientific, economic and societal benefits of realising ever-larger structures in space suggest that such efforts will surely be worthwhile. This fact is clearly evidenced by the steadily increasing interest in large space structures and applications observed in recent decades; an interest which spans academia, national agencies and private enterprise.

This thesis is concerned with a specific engineering challenge in the design of large space structures: their dynamics and control. Furthermore this challenge is considered specifically in the context of large space structures which may be manufactured on-orbit, through the use of 3D-printing or additive manufacturing technologies. In this introductory chapter a review of published research on large space structures is presented. First a general overview of the potential applications for which large space structures are required is given, covering both past missions and those which have been proposed for the future. After discussing the potential applications, attention is then given to research regarding the more specific concerns of this thesis; on-orbit manufacturing and the attitude dynamics and control of large space structures.

1.1 Large Space Structures: Past, Present and Future

The design space of what could be considered a Large Space Structure (LSS) is vast, as is the range of applications and mission proposals to be found in the literature. In this section, three broad categories of LSS are identified: space stations and in-space platforms; telescopes and antennas; and gossamer spacecraft. These categories are by no means definitive (Ref. [18] considers planetary entry vehicles as a further category for example) nor exclusive (i.e. a gossamer structure could serve as the collector of a large telescope [19]). However, taken together they cover the majority of LSS designs which have been proposed and those which are relevant to this thesis. Additionally, categorising LSS by these general applications further serves to group LSS by physical properties (mass, length-scale, structural flexibility) according to the design requirements of each category. This is illustrated in Fig. 1.1, in which examples of existing and future LSS are placed according to mass and length. The figure shows that LSS of each category are generally grouped according to these properties (in similar bands of areal mass density), though there is a clear overlap and outliers belonging to each group, examples of which will be examined in the following discussion.

Existing spacecraft belonging to each category are depicted in Fig. 1.2. Figure 1.2a shows the International Space Station (ISS), the largest and most complex structure constructed in space to date. The ISS has been an immense engineering project, and has served as a symbol of international cooperation for over 20 years. Yet the convoluted and challenging history of its development also demonstrates the difficulty in realising such large structures in space. Figure 1.2b shows the James Webb Space Telescope (JWST), developed by NASA, ESA and CSA. One of the next generation of "great observatories", the JWST's 6.5 m diameter primary mirror will allow astronomical observations at a greater range and level of sensitivity than ever before. And yet again the project has presented a massive undertaking, with well documented engineering challenges and organisational setbacks throughout, including a complete redesign of the spacecraft at one point [7]. Finally Fig. 1.2c shows the Interplanetary Kite-craft Accelerated by Radiation Of the Sun (IKAROS) solar sail demonstration, launched by JAXA in 2010. IKAROS, an example of a gossamer spacecraft, was the first spacecraft to successfully deploy a solar sail, using solar radiation pressure (SRP) as a form of propellant-free propulsion in interplanetary space while travelling to Venus [5]. In addition to a number of valuable scientific objectives, IKAROS succesfully demonstrated several key technologies which will be crucial in the development of future, even larger gossamer spacecraft. Together these projects all demonstrate the great value that LSS can offer humanity, yet they also demonstrate significant engineering complexity and the need for technological innovations involved in such endeavours.

In this section examples belonging to each of the identified LSS categories are discussed, primarily to give the historical background of LSS, and also to provide a general overview of the design requirements and features of each class. At this stage it is thought important to make a distinction between the actually existing "LSS" of today (crewed spacecraft and space

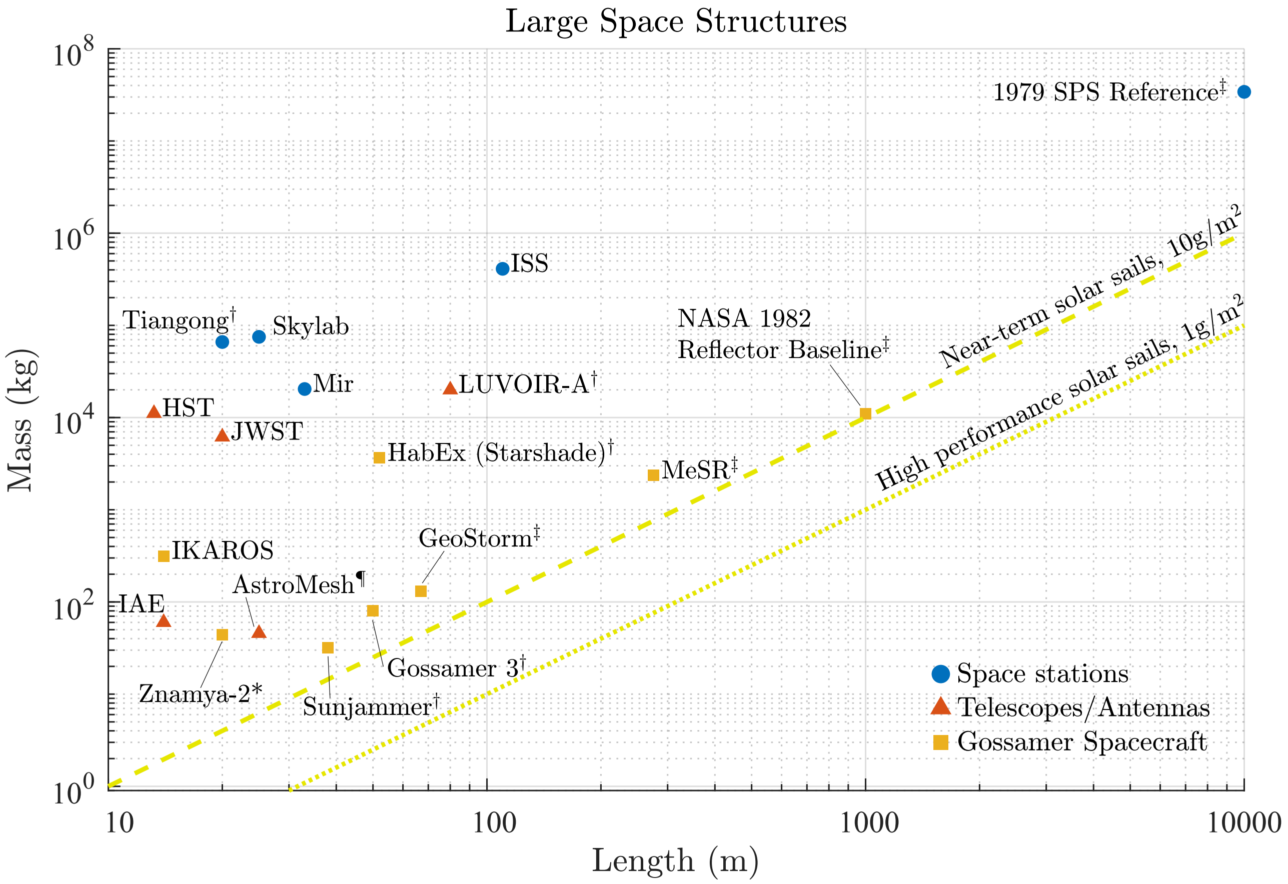

Figure 1.1: Catalogue of LSS by weight and length of largest dimension [1–15]. ISS - International Space station, HST - Hubble Space Telescope, JWST - James Webb Space Telescope, IAE - Inflatable Antenna Experiment, MeSR - Mercury Sample Return Solar Sail.
*estimated mass, †stage of development reached with a detailed architecture proposal, ‡conceptual study/baseline mission requirements only, ¶largest standard design offered.

stations with length on the order of 10 to 100 m), and what is likely to be considered a LSS in the future (solar power satellites, reflectors or solar sails with lengths on the order of 1 to 10 km or more). While this thesis is primarily concerned with the latter type of structure, during this introductory discussion “LSS” is taken to refer to the broader range of spacecraft belonging to the three categories identified previously. This approach is taken primarily so that later discussion of potential future LSS can be grounded by reference to existing spacecraft and technologies, avoiding unfounded speculation. Overall, this section aims to provide an overview of the (existing and future) LSS design space, providing context and motivating applications for the research objectives of the thesis, and a basis for many of the assumptions made in the technical chapters which follow.

1.1.1 Space Stations and In-Space Platforms

The largest structures in space to date have all been space stations, in terms of both their mass, and length scale, as shown by the data in Fig. 1.1. Space stations are facilities designed to provide a habitable environment and maintain a long-term human presence in space. The

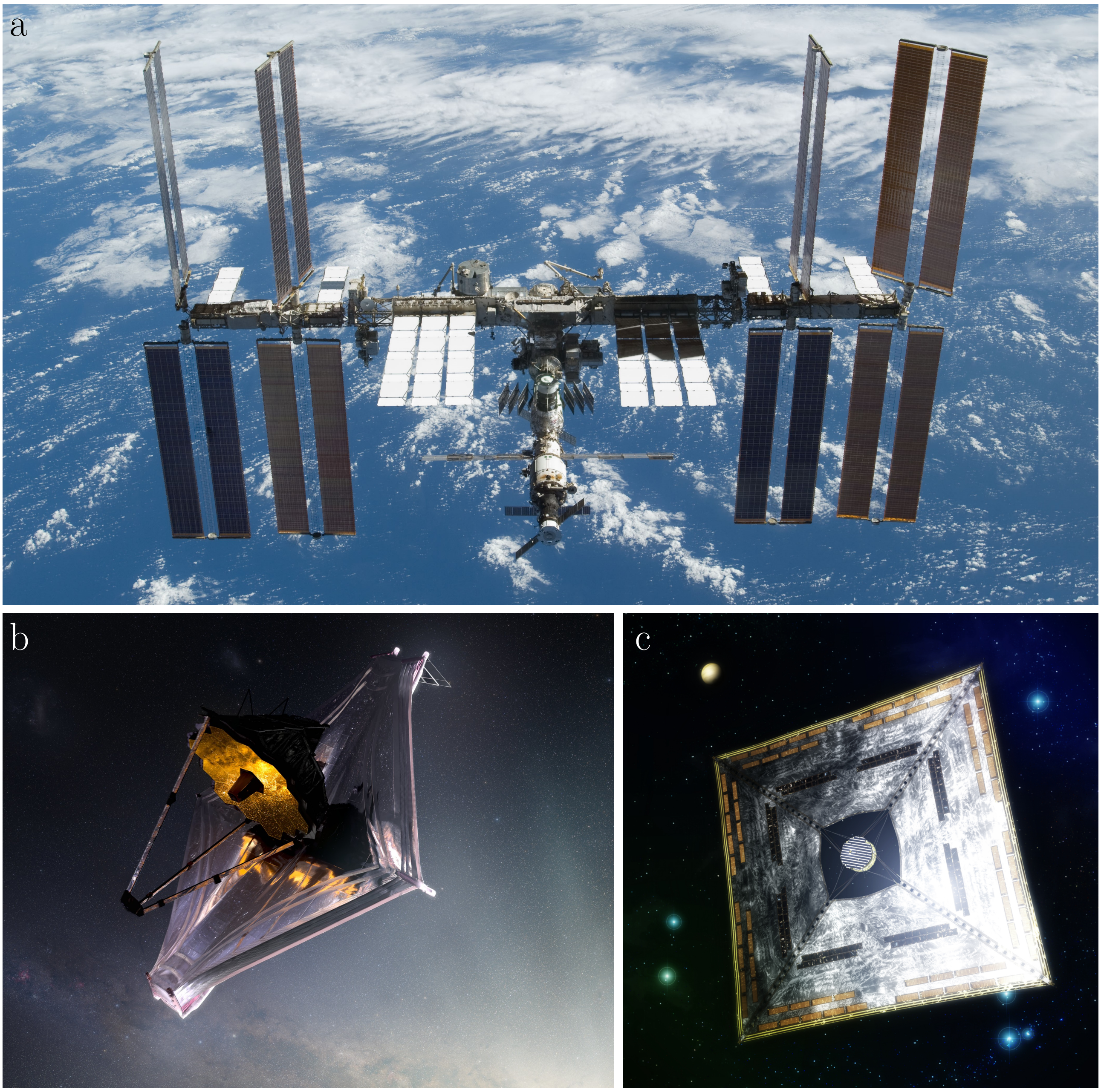

Figure 1.2: Existing large space structures of different categories, the ISS (a), the JWST (b) and IKAROS (c). (*Images courtesy: NASA, NASA, JAXA*)

largest of these, at 100 m in length [3], is the ISS, which was preceded as the largest structure by the Soviet and then Russian operated Mir station, at 33 m [2]. Although space stations as a category are not the type of LSS with which this thesis is primarily concerned, as the largest actually existing structures in space an understanding of their design and operation serves as a reference for understanding the feasibility of realising even larger LSS in the future.

The first operational space station was Salyut-1, launched by the Soviet union in 1971 [2]. The station was 15 m in length and comprised of three pressurised modules, four solar arrays and a Soyuz service module which provided attitude control and station-keeping. The station was occupied by a crew of three for 24 days, during which time they made astronomical measurements using the Orion-1 telescope, and attempted to grow plants in a hydroponics unit [2]. Salyut-1 was followed by the US launched Skylab in 1973 [1], Salyut 2-7 (individual launches between 1974-1982) and Mir (multiple launches between 1986-1996). Mir was the first modular spacecraft, assembled in orbit from individual modules, each with separate launches. This on-orbit assembly was a key development for future LSS, in that structures were no longer constrained by the mass and fairing volume of a single launch vehicle. This approach was also followed for the ISS, the assembly of which has taken place over 40 separate missions so far [20]. Tiangong-1 and 2, launched by CNSA as prototype stations for the planned Tiangong station [9], complete the list of operational space stations to have existed to date. A planned future space station is NASA's Gateway project, which is to be placed in a Halo orbit at the Earth-Moon L_1 Lagrange point, and serve as a staging platform for missions to the lunar surface and future deep space missions [21]. Additionally, at least two commercial space stations have been announced as being under development [22, 23]. These stations are set to offer individuals or organisations the opportunity to lease space on-board for research or other purposes, and even operate as space-tourism facilities, signifying a significant step forward for this burgeoning industry.

Future space-tourism notwithstanding, the purpose of space stations has primarily been to serve as orbital laboratories, in which a diverse range of experiments can be carried out by crewmembers. The effects of spaceflight on the human body, Earth observation, astronomy, and many other sciences have been the subject of research carried out in these unique environments [20]. In addition to the science carried out on board, space stations themselves have often served as demonstration platforms for new spaceflight technologies. For example, during the development of Skylab, engineers were actively encouraged to consider using new technologies that did not yet have flight heritage, including the use of large Control Moment Gyros (CMGs) for attitude control and molecular sieves for CO_2 removal [24]. In terms of their general design, space stations comprise of cylindrical pressurised modules connected via docking ports, onto which large solar arrays and radiators are mounted (visible on the ISS in Fig. 1.2a). Compared to the other types of LSS to be discussed, space stations have a much greater mass and rigidity, required to provide a safe and habitable environment for crewmembers. In terms of their dynamics and control, they can be mathematically modelled as rigid central buses onto which flexible appendages are attached [25], as opposed to other types of LSS in which the entire spacecraft is essentially a flexible body.

Complementary to their function as technology demonstration platforms, space stations are often viewed as an enabling step towards larger structures and in-space platforms. Indeed, much of the seminal research on LSS suggested that these large structures could be constructed manually by astronauts [26], with space stations effectively serving as on-site accommodation for the construction efforts [27]. More recently, a stated aim of the Chinese space station program is "mastering the construction and operation technology of large space facilities" [9]. One potential large space facility being referenced here, which has been a topic of great interest globally, is space-based solar power (SSP) platforms. SSP is a concept which has been

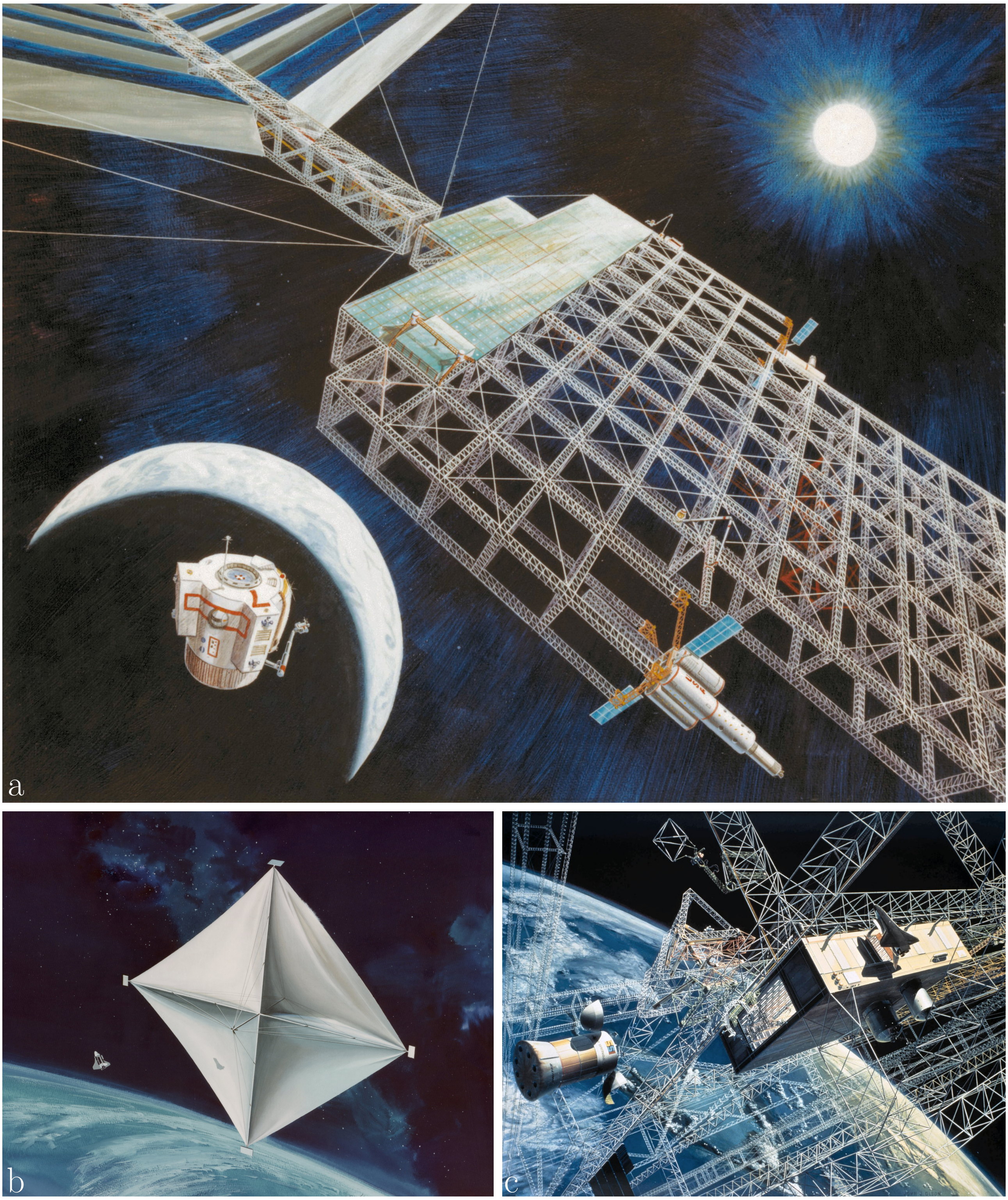

Figure 1.3: Artist renditions of future LSS concepts: a) the NASA 1976 reference SSP architecture, b) an 850×850 m solar sail, proposed by JPL for a Halley's comet rendezvous mission, c) a generic large space truss structure being constructed on-orbit (*Images courtesy: NASA, NASA/JPL-Caltech, NASA*)

the subject of numerous studies, dating back to the first engineering treatment of the topic by Peter Glaser in 1968, though the general idea of harvesting energy from space was first mentioned by Tsiolkovsky in 1912 [28]. In the 1970s NASA performed a large scale study of the concept, the result of which was the 1979 SPS Reference Architecture [15]. The design comprised of a 10 km solar panel array placed in a geostationary orbit, from which 5 GW of power would be transmitted back to Earth through a 1 km diameter microwave antenna array. An artist's rendition of the concept is shown in Fig. 1.3a. Though the study determined that the concept was not economically feasible at the time, in the years since the trends of falling launch costs and rising energy demand has led to numerous reassessments of SSP, with a variety of potential architectures proposed [29–31]. While implementing SSP at scale will be an ambitious engineering project it is generally accepted that it could be realised with technologies which are readily available today, and that the greater barrier is the large initial investment required. If the economic viability of SSP continues to improve in the coming decades it seems inevitable that these types of LSS will become a reality.

1.1.2 Telescopes and Antennas

Telescopes and antennas are another application which require the use of LSS. For telescopes, larger mirrors are capable of collecting more radiation, providing observations at a higher resolution and greater distance than is otherwise possible. Similarly, large aperture antennas allow higher data throughput and improved signal quality [32]. A challenge in both cases is that a high degree of precision in the shape of the reflector or antenna is generally required, which adds to the difficulty of realising these types of structures at greater length scales. This requirement has led to the development of complex deployable systems, and also driven research into how such structures could be assembled or manufactured on-orbit in the future. Space telescopes, as flagship scientific missions for space agencies, and large aperture antennas, due to their significant economic value in telecommunications, have been a driving application in the development of LSS technology and likely will remain so in the coming years.

A significant number of space telescopes have been launched to date, capable of making astronomical observations in various parts of the electromagnetic spectrum. Space telescopes have the advantage of being outwith the Earth's atmosphere, and can therefore make observations in parts of the spectrum which are either blocked or distorted by atmospheric gases, which accounts for the majority of the spectrum other than radio frequency (RF) waves [33]. The first operational space telescope was the OAO-2 (Orbiting Astronomical Observatory), launched in 1968, followed by the aforementioned Orion-1 telescope onboard the Salyut-1 station in 1971. Both observatories collected data in the ultraviolet range, imaging a variety of objects and demonstrating the feasibility and advantages of space-based astronomy [34]. Prior to the launch of the JWST, the largest space telescope was the Hubble Space Telescope (HST), which has been operating since 1990. The HST, 14 m in length and featuring a 2.5 m primary mirror [33], operates in the ultraviolet to near-infrared regions of the electromagnetic spectrum.

Hubble has provided data investigating a number of long-standing questions in astronomy, and been the source of iconic astronomical images, such as the "Pillars of Creation" image of the Eagle Nebula, and the "Deep Field" images which show some of the youngest and most distance galaxies to have ever been observed [33].

The recently commissioned JWST, Hubble's successor, is now the largest operational space telescope. In addition to a 6.5 m diameter primary mirror, the telescope also features a large (20×14 m) reflective membrane sunshield, which cools the instrument to below 50 K and allows faint objects in the infrared frequency range to be imaged. The architecture of the JWST is visually quite different to that of the HST, which comprises of a single cylindrical structure containing the telescope and spacecraft bus, with deployable solar panels. Designing the JWST to fit within the 5 m fairing volume of the Ariane-5 launch vehicle required the primary mirror itself to be deployable, with the mirror being constructed of three segments that unfolded once in space. Along with the sunshield, the JWST deployment process involved 40 deployable structures and 178 release mechanisms [7]. The difference between the architecture of the HST and JWST can be seen as a first step in a paradigm shift similar to the progression seen towards modular space stations, where space telescopes are no longer conceived of as single, monolithic entities. Instead, the JWST and future telescope designs (such as the proposed 15 m diameter primary mirror LUVOIR-A concept [11]), can be thought of as an assembly of multiple structures, each serving a different purpose (mirrors, sunshields, starshades etc.). The development of lightweight, rigid structures capable of serving these diverse needs is therefore a key technology for future ultra-large space telescopes [35]. While the deployable strategy adopted for the JWST has been successful, it is also likely that even larger future space telescopes will require on-orbit assembly or manufacturing [36].

Like telescope mirrors, reflector antennas are another application in which greater sizes are inherently advantageous due to the underlying physics of their operation. The area of the antenna reflector and thus the aperture are directly related to the gain of the antenna [32], and so large reflectors have been a necessary development for satellite communications. Unlike the space telescopes discussed previously, in which the entire spacecraft is considered the telescope, an antenna is just one appendage of a typical spacecraft, (reflected in the lower mass shown for the two examples of IAE and Astromesh shown in Fig. 1.1). Generally, the design requirements for an antenna reflector are that the structure is rigid enough to maintain the correct reflecting shape (typically parabolic) to the required precision, while remaining as lightweight as possible to reduce launch costs. As with other LSS discussed this is currently achieved through the use of complex deployable systems.

The largest of these existing deployable antennas are typically in the 10 - 20 m diameter range [37]. While this aperture size is sufficient for geostationary (GEO) communications satellites, there is also a need for even larger reflector antennas. For example, analysis has suggested that accurate monitoring of rainfall on Earth would require a 40 m aperture reflector antenna in GEO [38]. The study also suggested that a rigid reflector of this length scale would require an areal mass density on the order of 2 kg/m^2, whereas if membrane reflectors could be used at this scale the mass density would be greatly reduced (0.4-0.5 kg/m^2). This requirement prompted the development of the Inflatable Antenna Experiment (IAE) in 1996. The IAE was launched and successfully demonstrated the deployment of a 14 m diameter antenna supported by an inflatable rigidising structure, though the surface precision of the reflector attained was not as high as was hoped [39]. The AstroMesh antenna system is another example of a large deployable mesh reflector with flight heritage, with up to 12 m diameter examples flown [40], though the design is claimed to be scalable up to 22 m aperture sizes [10]. The JAXA ETS V-III satellite featured two 19 m diameter reflector antennas, some of the largest reflectors flown, and was designed to test geostationary communications for mobile devices [41]. Many other deployable antenna designs exist, including elastic rib designs, cable tensioned systems, among others [37], and the development of these systems is an active field of research currently.

1.1.3 Gossamer Spacecraft

These current deployable reflector designs can also be thought of as "gossamer structures", where gossamer refers to the lightweight mesh or membrane which forms the reflecting surface. This classification leads to the final category of LSS identified, gossamer spacecraft. This category refers to a class of spacecraft which is ultra-lightweight and largely comprised of a thin, likely reflective membrane, i.e. the spacecraft itself can be thought of as a membrane structure, as opposed to a rigid spacecraft onto which a flexible appendage is mounted. The archetypal spacecraft of this category is the solar sail, a means of achieving propellant-less propulsion through solar radiation pressure. Although gossamer spacecraft are the category with perhaps the least flight heritage, they are also a category with great future potential. As has already been seen, gossamer structures can serve as sunshields (JWST) and antenna reflectors (the IAE) among other applications. Gossamer spacecraft, i.e. free-flying membrane structures, could also be designed to serve a number of applications, including the aforementioned solar sailing, orbital reflectors for solar energy delivery and starshades for exoplanet astronomy. Here a brief discussion of the various proposed applications for gossamer spacecraft are given, along with a discussion of the few existing examples of gossamer spacecraft and the more numerous examples of proposed architectures and missions.

As noted, solar sails are perhaps the first application which could be considered to be gossamer spacecraft. A solar sail is a reflective surface designed to reflect sunlight and in doing so gain momentum, thus providing propellant-free propulsion. With the addition of attitude control, the direction of the radiation pressure induced force can be controlled, allowing orbit control of the spacecraft and opening up new trajectories [4]. Despite the potential benefits of solar sailing, there are numerous challenges associated with their construction and deployment in space. As noted, the solar sail must be extremely lightweight, and yet rigid enough to not deform and allow the sail membrane to be tensioned. This sail tensioning can either be achieved by structural booms, or by spinning the solar sail, or a combination of both. For the first strategy, sail designs typically consist of a large square membrane with four booms across the diagonals. These booms support the membrane and allow tensioning of the material. Spinning sail designs can be disc shaped, or the heliogryo design, in which long reflective blades extend from a central hub [4].

Although the concept of solar sailing has been actively researched for some decades now, relatively few solar sail missions have been flown to date. The aforementioned IKAROS spacecraft, launched in 2010, is the only spacecraft to date to have used a solar sail as a means of propulsion in interplanetary space, and was the first successfully deployed solar sail [5]. While not specifically a solar sail, the Znamya-2 reflector was a 20 m wide reflective membrane, deployed in 1993 by Roscosmos [12]. The reflector was designed with the proposed application of reflecting sunlight to polar latitudes, but the mission itself was intended to demonstrate centrifugal deployment of a reflective membrane spacecraft [12]. Other solar sail missions flown since have similarly had the primary objective of demonstrating sail deployment (in Earth orbit). These technology demonstrations include Nanosail-D2 (2011), which successfully deployed a 10 m^2 sail from a 3U Cubesat and became the first solar sail to orbit the Earth [42]. Lightsail-1 (2015)[43] and Lightsail-2 (2019) [44] were developed and launched by the Planetary Society, after being funded by the donations of over 50,000 individuals around the world [44]. The two missions demonstrated deployment and SRP propulsion, and attitude control in the case of Lightsail-2 [44], which became the first controlled solar sail in Earth orbit.

Solar sail missions in development include NASA's Near Earth Asteroid (NEA) scout, planned to launch in 2022. The mission aims to deploy an 86 m^2 solar sail from a 6U Cubesat form factor and use the solar sail to perform a NEA flyby [45]. The much larger Solar Cruiser sailcraft is planned for launch in 2025. The Solar Cruiser is to feature a 1653 m^2 sail, used to maintain a halo orbit sunward of the Sun-Earth L_1 Lagrange point [46]. Other significant programs include the gossamer roadmap initiative by DLR, which was established to explore the near term possibilities of solar sailing, and included the ground based deployment of a 20 $\times$ 20 m sail [47]. The program envisioned three Gossamer 1/2/3 missions, involving sails of 5, 20 and 50 m sidelength respectively, where each mission would successively build upon the lessons of the previous, accelerating the development future solar sail missions [48]. Figure 1.3b depicts an artist rendition of an 850 $\times$ 850 m solar sail, proposed by an early NASA study as a candidate rendezvous mission to Halley's comet. While the construction of such large solar sails remains a significant technical challenge, sails at this length scale could provide an efficient way of exploring the solar system and a wide variety of missions have been proposed that could make use of this form of propellant-free propulsion [49].

A closely related concept to the solar sail is orbiting solar reflectors. Such orbital mirrors may be used to reflect sunlight to the Earth to illuminate densely populated areas (as was proposed for the Znamya reflector missions) or terrestrial solar PV-farms. This concept was studied by NASA in the 1970s, with further analysis concluding that the idea was not economically feasible at the time [14, 50]. More recent work examined the use of aluminised-Kapton films as solar mirrors and performed analysis of the film's mechanical and optical properties, with promising results [51, 52]. Lior [51] also performed an economic analysis, which agreed with the earlier NASA studies that the concept would not be economically viable unless transportation costs could be reduced to several hundred \$/kg. It is possible that falling launch costs and the development of in-orbit fabrication technologies may lead to growing interest in the orbital mirror concept in the future. More recently the concept has been revisited by the SOLSPACE project at the University of Glasgow, with investigations made of potential mirror architectures, orbital dynamics and economic considerations [53]. Economic analysis has determined that, depending on market conditions, economic breakeven of the orbital solar reflector concept is comparable with terrestrial energy storage systems, which have also been proposed as complementary systems for terrestrial solar power farms [54]. Detailed modelling of reflector orbits and energy delivery has been carried out, and further extended to consider energy delivery by solar reflectors for other planetary bodies [55]. Another use of orbiting solar reflectors is climate engineering [56, 57]. Reference [58] provides an in-depth discussion of a number of ways in which orbiting reflectors could be used to engineer the Earth's climate. These include the use of occulting disks at the Earth-Sun L_1 Lagrange point to partly block incoming solar radiation to offset the impact of human-driven climate change. While such macro-engineering projects may not be realised in the near-future, this remains an interesting area of research and adds to the range of applications for which gossamer spacecraft may be used.

1.2 On-Orbit Manufacturing

A common theme found across the various LSS applications discussed in the previous section was the inherent difficulty of realising large structures in space. This arises due to the need for any space structure to first fit within a launch vehicle's fairing volume. As was discussed, one way this has been overcome is through on-orbit assembly (modular space stations), but the most common solution is the use of deployable systems, complex mechanisms which expand from a compact stowed volume after launch. While deployable systems have been successfully used for many missions, the mechanisms required add a significant level of engineering complexity to designs which could otherwise be relatively simple structures, and the strategy does not scale well to length scales greater than tens of meters. As was noted, the JWST had 178 individual release mechanisms for deployment of the observatory, and many of these mechanisms were a single point failure for the mission [7]. A further redundancy in the current designs of deployable LSS is that the structures must be designed to withstand the extreme forces and vibrations of launch, whereas while in their operational environment on-orbit, the forces acting upon the structure are much smaller. This leads to structures often having a greater mass or different design than would otherwise be required for the majority of the structure's lifetime. One solution to these problems is to manufacture structures on-orbit from raw materials which can then be launched as an efficient package, filling the available launch fairing volume. The potential benefits of on-orbit manufacturing were identified in the early years of LSS research, though due to the low technology readiness of the required technologies the concept only saw limited interest at the time. The concept has seen a marked increase in interest in recent years, primarily due to advances in terrestrial additive manufacturing and robotic technologies which may be adapted for use in space.

From the 1960s onwards many mission applications were proposed for which LSS were required, examples of which have been given in the previous section. These proposals, in particular the studies on SSP, resulted in research on how best to construct arbitrarily large structures in space [59]. The strategies proposed at this time, many as part of the NASA Large Space Structures program (1970s-1980s), can be divided into three categories: deployables, erectable structures, and in-space fabrication [26]. As noted, deployable systems have been used extensively for linear booms and masts, extending solar arrays or instruments from a primary spacecraft bus. They have also been used for antennas and reflectors, such as the IAE and ETS V-III satellite reflectors mentioned previously. Realising large planar structures however, such as would be required for SSP systems for example, would be difficult to achieve with deployable systems. This is particularly true if the structure is desired to be scalable. Due to this, proposed construction strategies for such structures largely focussed on erectable structures, i.e. structures assembled from components either by astronauts engaged in EVAs or by robotic units. Erectable structures have some flight heritage, with examples being construction operations on the ISS, or service missions to HST. The absence of their use in other cases is primarily due to the high costs of human spaceflight, high risks of EVA missions and low technology readiness (at the time of these studies) of robotic manipulators for assembly. Despite these difficulties, erectable structures have clear advantages to deployables: the components can be packed with greater efficiency in the launch vehicle fairing volume; the structures can be modified, repaired or scaled with greater ease; and finally the structures can be relatively simpler in design, and have greater structural performance [26]. Figures 1.3 a and c show envisioned erectable structures (an SSP platform and a generic/non-specified structure respectively) being assembled in orbit by robotic free flying units.

On-orbit fabrication, where structural elements are manufactured in-space from raw materials, carries the same advantages as erectable structures. Additionally, such a strategy can have the advantage of forming structures from continuous elements rather than mechanically connected separate components, which can result in greater strength and simplicity of the structures. Two in-orbit fabrication systems were developed in the 1970s under NASA contracts. General Dynamics' Convair Division designed a composite "beam builder", which formed triangular beams from graphite, glass, or thermoplastic through an automated roll forming process [16]. Grumman Aerospace developed a similar system, which formed triangular beams out of roll-formed aluminium flatstock [60]. The two beam builder systems are illustrated in Fig 1.4 a and b respectively, showing the general features of the roll-forming systems, and the large scale of the apparatus required to produce the 1 m diameter beams. While full scale demonstrations a

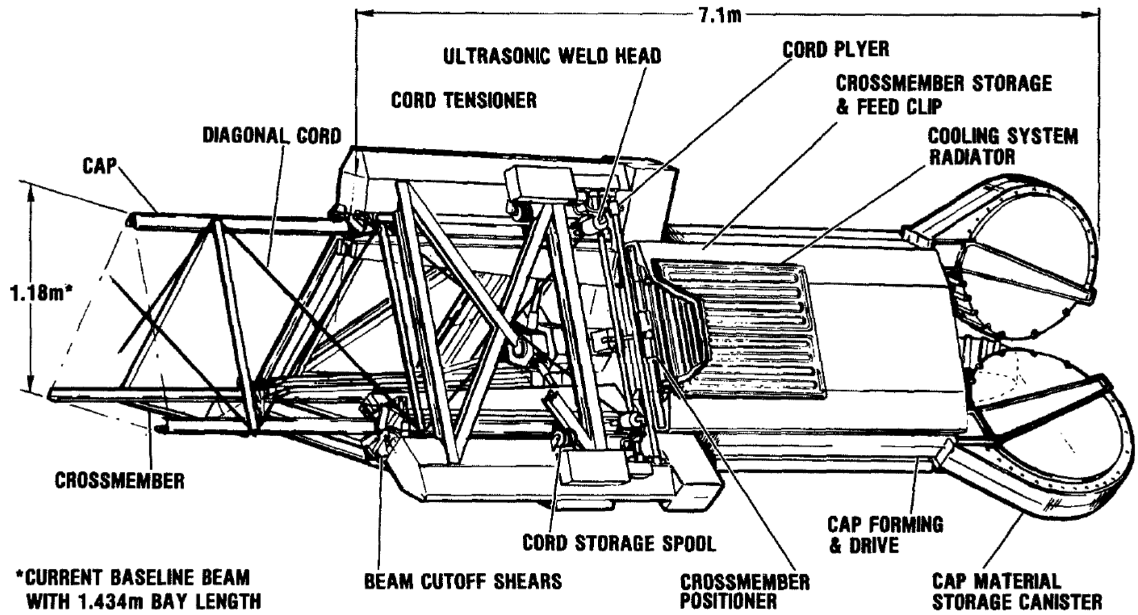

b

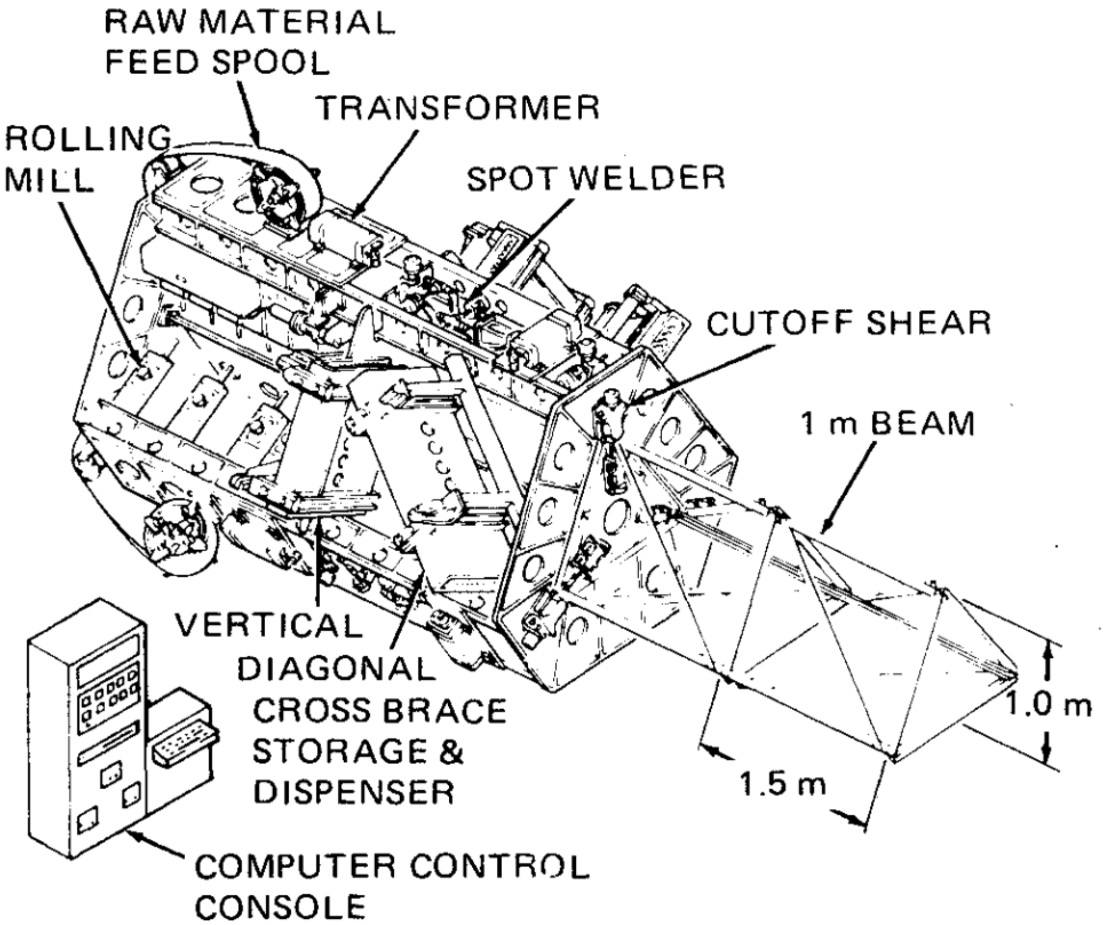

Figure 1.4: Two automated “beam builders” built under NASA contracts in the 1970s, the General Dynamics composite beam builder (a, [16]), and Grumman Aerospace’s roll-formed aluminium system (b, [17]) (Images courtesy: NASA, NASA)

were constructed of both systems, the concept was not developed further and research efforts at this time were instead redirected towards erectable systems.

Following these early efforts, in-orbit fabrication in general received little attention in the following decades, primarily due to the complexity and cost of the autonomous systems required, and relative immaturity of the related technologies. This lack of activity was likely also due to the contemporary interest in SSP waning, as this was the main application driving these early studies. Recently the NASA In-Space Manufacturing Program, beginning in 2014, has seen a renewed interest in on-orbit manufacturing, awarding multiple contracts for the development of on-orbit additive manufacturing systems [61]. Advancements in the two following areas mean that the technological landscape today is much more amenable to the concept of on-orbit manufacturing than it was when the “beam-builders” were developed in the 1970s. The first of these favourable advances is that there is now a proven history of on-orbit robotic manipulation, a key technology for the assembly of on-orbit manufactured structures. Examples such as the Canadarm and European Robotic Arm have extensively demonstrated on-orbit servicing via robotic arms [62], and it is thought that similar robotic manipulators can be used for on-orbit manufacturing [61]. The second area that has seen major development and is perhaps the primary enabling technology is additive manufacturing; where autonomous systems capable of converting raw feedstock material into 3D geometries are now freely available as off-the-shelf systems in the form of desktop 3D-printers.

Made in Space, Inc.[1] is one company which has developed 3D-printing technologies for use in space. With NASA funding, the company launched its Zero-G Printer to the ISS in 2014, demonstrating 3D-printing in orbit for the first time [63]. The Zero-G Printer uses fused filament fabrication, where filaments of polymer feedstock material loaded on spools are melted and then extruded in layers, and produced a variety of objects including small tools and designs which were uploaded to the ISS from Earth [64]. The Zero-G Printer demonstration was followed by the launch of the Additive Manufacturing Facility to the ISS in 2016, an improvement on the original printer, incorporating lessons of the first demonstration and offering a wider range of print materials [65]. The printer was installed on-board the pressurised environment of the ISS and thus demonstrated 3D-printing in microgravity conditions, but not in vacuum.

The mission was funded under NASA’s aforementioned In-Space Manufacturing (ISM) program, which has the broad goals of developing manufacturing capabilities for supporting future deep-space exploration [66]. One application of in-space additive manufacturing targeted by the ISM is to 3D-print Moon and Mars habitats [65], while a more near-term goal is the “on-demand” production of equipment and tools, where parts are produced as needed in-orbit rather than having spare equipment take up valuable launch space [63]. Additionally there has been a focus on recycling 3D printed materials for reuse, further easing the supply logistics for extended missions [66]. Recycling of 3D-printed parts has been demonstrated by the “Refab-

[1] Recently acquired by Redwire Space. At the time of writing it is unclear if Made in Space is to continue operating under the same name.

ricator", designed by Tethers Unlimited, Inc. Launched to the ISS in 2018, the system is a hybrid 3D-printer recycling unit capable of reusing printed materials [61]. Outwith the ISM, research has taken place more widely on the adaptation of 3D-printing technologies for use in space. This includes ongoing work at the University of Glasgow investigating the adaptation of 3D printing to microgravity and vacuum conditions, as would be required for a free flying 3D-printer [67]. Similarly, Ref. [68] presents the development of a vacuum rated 3D printer, where the main challenges encountered are that all components must meet certain outgassing requirements; and thermal management of the hot-end (heated extruding head), which are typically air-cooled in normal 3D-printing cases. The use of a free flying additive manufacturing unit equipped with robotic manipulators is investigated in Ref. [69], with tests conducted using a 3D printing unit freely moving in 2 dimensions atop an air table.

In addition to the on-demand supply of tools, components, and future habitats, the use of in-space 3D-printing technologies is also being considered for the construction of LSS. Multiple systems are currently being developed for this purpose. Tethers Unlimited are developing the "Spiderfab", or self fabricating satellite concept [70, 71]. The concept consists of an additive manufacturing facility with multiple robotic arms, capable of producing structural elements and assembling them into large structures. The robotic arms are proposed so that the system is versatile and capable of joining various types of structural elements, and will also be used to manoeuvre around the structure during the fabrication process. Proposed applications include the fabrication of large occulting disks (starshades) for exoplanet imaging, which are required to be on the order of 100 m diameter with 0.1 m shape accuracy [70], along with large aperture antennas, solar sails, and many of the other applications previously discussed. Development of the Spiderfab is ongoing with orbital mission demonstrations proposed for the mid 2020s [71]. In addition to the overarching Spiderfab proposal, Tethers Unlimited have also developed the "Trusselator" concept, an additive manufacturing system which is capable of producing arbitrarily long truss-like beams from raw feedstock material [72–74]. The system is markedly similar in function to the early beam builders developed during the 1970s (Fig. 1.4), though much smaller in scale, producing 75 mm diameter beams [74]. A proof of concept system has been built and ongoing research aims to conduct further testing, including thermal vaccuum tests. A roadmap for orbital demonstration has been laid out, proposing that the technology could be implemented on a 6U Cubesat platform and used to deploy a 10 m long boom [72]. While the trusses produced are relatively small in diameter, it has then been proposed that trusses could be joined to form second order truss structures (i.e. a truss of trusses), through the use of robotic manipulators such as the proposed Spiderfab system [70].

A similar system has also been proposed by Made in Space, named the "Archinaut" [75, 76]. While technical details are somewhat sparse, artist renderings have depicted a similar concept to the Spiderfab, in which a central 3D-printing facility is equipped with robotic manipulators for structural assembly of printed parts. The company has also demonstrated similar capabilities to Tethers Unlimited, releasing images of extruded/additively manufactured booms supporting solar panels in ground tests [75]. Archinaut One, later renamed OSAM-2 (On-Orbit Servicing, Manufacturing and Assembly), is a mission intended to demonstrate these capabilities on-orbit, by manufacturing and extending two opposing 10 m booms which will support a deployable solar array in space [61]. While development is ongoing for both the Spiderfab/Archinaut concepts, the idea seems to hold much promise, especially when compared to the beam builder concepts discussed previously. For one, the ability to deploy the Trusselator on a Cubesat sized platform means that orbital demonstration is much easier and less costly to achieve (as opposed to the space shuttle mission proposed to demonstrate the Grumman beam builder [17]). Secondly, it is only through the combination of the beam extrusion system with robotic manipulators that more complex, 3D geometries will be capable of being produced. While still technically challenging, the prospect of developing such a system appears much more feasible today given advancements in robotics. Given the potential advantages over deployable systems (potentially 2-5 times reduction in structural mass [71]), if the development of these systems continues at the current pace it will soon be possible to envision large, customised structures being produced in space at a greater length scale, and lower mass, than has been possible before.

1.3 Dynamics and Control of LSS

The specific concern of this thesis is the dynamics and control of LSS, and specifically of LSS which may be manufactured on-orbit. As has been seen, there are a vast range of mission applications and architectures for LSS, and thus there is great variation in the proposed attitude control strategies for the different spacecraft which have been discussed in the previous sections. The attitude control of LSS poses some specific challenges; such structures are likely to be more lightweight and flexible than traditional spacecraft for one, and thus difficult to manoeuvre without excessive structural deformation or vibration. LSS also experience disturbances which may not be significant perturbations for smaller spacecraft, such as the effects of gravity-gradient torques, SRP, thermal gradients, or aerodynamic torques [25]. In this section an overview of the challenges of LSS attitude control and the various control strategies which have been proposed in the literature are discussed.

1.3.1 Attitude Dynamics of LSS

Gravity gradient torques arise on spacecraft due to the variation in the gravitational field strength across the length of the spacecraft body. This effect is magnified for structures with greater mass moment of inertia, and so can be a significant disturbance for LSS. It is a well known result that gravity gradient torques result in some stable configurations (attitudes), depending on the inertia tensor of the spacecraft [77], and these stable configurations can potentially be exploited for LSS. For example Refs. [78] and [79] discuss the use of magnetic damping for a gravity gradient stabilised satellite (not specifically a LSS), demonstrating that gravity gradient torques can be exploited to provide coarse pointing requirements. For many

LSS however, the specific pointing requirements may mean that gravity gradient torques must be counteracted by active attitude control [80].

In addition to gravity gradient torques being a more significant disturbance for LSS than for conventional spacecraft, the force of gravity can lead to dynamic coupling of orbital and attitude motion, which has been a subject of great research interest in LSS dynamics. Reference [81] investigates the effect of gravitational orbit-attitude coupling for very large spacecraft, and demonstrates that higher moments of inertia may need to be included to accurately model the attitude dynamics of such structures. This adds a level of complexity to mathematical models which may often be overlooked, and shows that accurate modelling of large structures requires careful consideration if results from more traditional spacecraft attitude dynamics research are applied. This may also limit the insights that can be gained into the attitude dynamics of LSS by simulation alone, as it is well known that the inclusion of gravity gradient torques and orbit-attitude coupling can result in chaotic dynamic systems [82]. Reference [83] investigates the effect of orbital motion on attitude motion, demonstrating dynamic coupling between orbital motion, pitch motion, and axial vibration of a large tethered SSP satellite model. For a similar system, Ref. [84] shows that for some ranges of fundamental frequencies of a flexible LSS gravity-gradient forces can lead to buckling of the structure. Further examples of research on orbit-attitude coupling includes Refs. [85–87], which discuss the coupling of gravity gradient, SRP, and thermal gradient effects on flexible structures in a variety of scenarios.

Reference [88] investigates the dynamics of a large flexible structure at the Earth-Moon L_1 point (e.g. the proposed lunar gateway), finding that the flexibility of the structure is not strongly coupled with the orbital motion, but suggests that further work will be required to investigate the orbit-attitude coupling of large structures in non-Keplerian orbits such as the halo orbit considered here. Reference [89] also considers coupled dynamics of a LSS at Lagrange points, an important topic given the variety of LSS applications proposed for this class of orbits.

Mathematical modelling of LSS is also an important topic of research, with a wide variety of approaches to be found. Structure-control interaction emerged as an important topic of research in the 1980s. References [25] and [90] discuss contemporary trends in control theory for LSS, dividing modelling strategies into continuum models and distributed parameter systems, discussing the mathematical considerations of controller design in both cases. Reference [91] discusses continuum modelling and computational problems in LSS control design, while [92] presents a finite element formulation unifying gravitational and structural modelling, such that orbit-structure interactions are captured by a single general model. Membrane structures (i.e. gossamer spacecraft) have some unique characteristics which must be considered in modelling efforts, as described in Ref. [93] and [19]. In some cases, a LSS can be modelled with a multibody dynamics formulation, where the system is modelled as a series of interconnected flexible bodies [94]. Reference [95] considers the control of such a structure, composed of multiple systems with separate controllers, and investigates stability conditions when some of these controllers fail. As noted, mathematical models of LSS vary greatly depending on the specific application or research purpose. The few examples of modelling efforts given here are intended to demonstrate the variety of approaches to be found, rather than provide a comprehensive overview of computational methods for LSS.

1.3.2 Attitude Control Strategies

A variety of attitude control systems and actuators have been considered for LSS. Potential actuators include thrusters, reaction wheels, control moment gyros, reflectivity control devices (RCD) and magnetic torquers [25]. The early NASA SOLARES reflector study considered the use of flywheels affixed to the reflector's large supporting structure for attitude control. One concept discussed was to attach three flywheels to orthogonal axes, and use SRP to accelerate them before the reflector became operational [80]. Once the wheels were sufficiently accelerated control torques could then be enacted by braking. The direct use of SRP is also often proposed as a means of attitude control, most commonly for solar sail applications. SRP can be used to induce control torques in a number of ways. Proposed methods include controllable vanes [96, 97], gimbal systems to shift the centre of pressure on the sail [98, 99], and more recently the use of surface reflectivity modulation [85, 100, 101]. The IKAROS sailcraft used RCD devices for attitude control purposes, with RCDs mounted on the sail membrane used to generate control torques [5]. Reference [102] describes the use of an RCD based on a polymer dispersed liquid crystal (PDLC), which enables propellant-less attitude control in this manner through reflectivity modulation via an applied voltage. Reference [100] proposes the use of a discrete grid of electro-chromic cells for the control a gossamer spacecraft. In the model of Ref. [100], a voltage can be applied to each cell which modifies the reflectivity. Attitude control is then achieved by finding combinations of activated cells which give desired torques on the spacecraft.

In this thesis, distributed actuation for attitude control is one of the topics investigated, as it was identified that the 3D-printing of a LSS allows actuators to easily be placed at any point of the structure during fabrication. Distributed actuation has been studied primarily in relation to vibration control of LSS rather than attitude control. References [103–106] consider spacecraft with distributed gyricity, such as an array of control moment gyros. These works are primarily concerned with shape control and vibration suppression, rather than attitude control, for which distributed actuation has not been widely studied. A notable exception is the recent work of Ref. [107], which integrates attitude control with vibration suppression for an array of reaction wheels. Reference [108] investigates vibration damping through direct velocity feedback. Reference [109] proposes an active structure composed of octahedral units, where selected structural units can be controlled and thus vibrations reduced in a decentralised fashion. Reference [110] discusses the problem of vibration control during slew manoeuvres, developing a nonlinear controller which addresses this problem and implementing command-shaping, whereby the actuator torques are delayed in order to suppress induced vibrations. Overall, vibration control of flexible LSS is an important consideration, and the coupling of attitude motion with structural vibrations is seen to be a technically challenging problem in

LSS design.

Chapters 4-6 of this thesis consider the use of magnetorquer rods or large current loops for the attitude control of LSS, as this was identified as an attitude control strategy for LSS which has not received significant attention in the literature. Magnetic torquers are a proven technology for spacecraft attitude control, but are often not considered for large space structures due to the large disturbance torques this class of spacecraft may experience. Reference [111] discusses this issue, and shows that with judicious orbit selection, control of a solar sail in low Earth orbit may be possible with reaction wheels and magnetorquers. An issue with the sole use of magnetic control for any spacecraft is that it cannot provide full 3-axis attitude control, as torques cannot be generated in the direction of the external magnetic field. However, this issue can be overcome in practice by performing sequences of manoeuvres or by considering that the external field direction changes over the course of an orbit, providing "average" controllability [112]. This is demonstrated by in Ref. [113] and [114], which investigate the stability conditions of magnetic actuation. Reference [115] demonstrates the design of a fully magnetic attitude control system for picosat platforms, while further examples of magnetic attitude control system design are found in the survey of Ref. [112].

An early example of a current loop being used for attitude control of a LSS is found in Ref. [116], in which a conceptual design for a 1500 m diameter radiotelescope is presented. Reference [116] proposes the use of a large current loop around the perimeter of the disk-like telescope structure. When a current is applied to this loop a torque is produced which is used to precess the spin-axis of the rotating telescope, enabling the telescope to scan the celestial sphere. Reference [117] investigates the use of four current loops for the attitude control of a 15×15 m spinning membrane spacecraft, performing numerical simulations with the membrane modelled as a multi-particle system. These simulations demonstrate precession of the spin-axis by $20°$ to a target orientation for a variety of cases (different orbits and spin-rates). Similar to Ref. [116], Ref. [117] uses the current loop torque to precess the spin axis of a spin-stabilised spacecraft, though Ref. [117] is based on an earlier concept study which demonstrated slew manoeuvres of a non-spinning membrane spacecraft with a perimetric current loop [118]. Also notable is that in these examples the current loops lie in the plane of the spacecraft, and so a torque can only be produced around one axis.

A related but distinct concept is the use of current loops for the deployment or tensioning of membrane spacecraft [119–121]. Reference [119] investigates the use of superconducting current loops to deploy and tension solar sails with radii in the range of 5 to 150 m. A key principle of this strategy is that the forces acting on the superconducting loop in Ref. [119] are due to self-interaction of the wire with its own generated magnetic field, rather than current loops interacting with the external geomagnetic field. Generation of these self-forces requires much larger loop currents (on the order of 10^4 A for a 10 m solar sail in Ref. [119]) than are found to be necessary for attitude control purposes, hence the need for superconducting materials in Refs. [119–121].

1.3.3 Origami LSS

Chapter 6 of this thesis presents analysis of the shape and attitude control of "OrigamiSats", a new concept in solar sailing where the solar sail is formed by an origami structure that is capable of shape reconfiguration to serve different mission requirements. The active shape control of solar sails has previously been considered for some specific applications, though the degree of shape reconfiguration required by a multi-functional OrigamiSat would be more extensive than any of the following proposed concepts. Reconfiguring the shape of a solar sail modifies the area-to-mass ratio of the spacecraft, allowing orbit control and enabling new missions. For example, Ref. [122] shows that instantaneous changes of the area-to-mass ratio of a spacecraft can be used to perform fuel-free transfers between Lissajous orbits in the Sun-Earth system, suggesting this could be achieved through the use of foldable "flaps" being deployed or stowed as required. Reference [123] introduces a quasi-rhombic pyramidal solar sail design in which the sail geometry is actively controlled via extendable booms, enabling orbit control. Reference [124] investigates the active-shape control of spinning solar sails, demonstrating effective shape control can be achieved using either tethers or RCD devices. Reference [100] demonstrates that a parabolic shape can be produced in a slack reflective membrane by varying the surface reflectivity across the membrane surface. This concept is similar to suggestion that the shape-reconfiguration of an OrigamiSat could be triggered by SRP and differences in local surface reflectivity, though the mechanics of an origami pattern folding are quite different to the membrane dynamics considered in this example.

Origami in general has been considered for a number of applications in spaceflight engineering. The use of origami-based designs for deployable structures is discussed in Ref. [125], where benefits include a reduction in stowed volume, and an ability to deploy the structure with minimal actuation and few moving parts [126]. Reference [127] gives an overview of the advantages of origami designs specifically for aerospace applications, and demonstrates the wide range of potential uses, including: protective bellows for Martian rovers, expandable habitats for the ISS, and deployable antennas. The most well-known example of origami used in spaceflight engineering is the Miura fold [128], which allows a structure composed of rigid panels to be folded compactly and then unfolded in one motion, and has been used for deployable solar panel arrays. As origami-based design is so frequently found in the area of spaceflight engineering, there is a need to accurately model the behaviour of these origami structures in orbit. Reference [129] gives a review of research on the dynamics and performance estimation of origami space structures, highlighting the importance of accurate dynamic models, particularly during the deployment phase. Examples given by Ref. [129] includes the work of Ref. [130], where a spring mass model is used to model the membrane dynamics of a six panel solar sail. Reference [131] presents a simplified model of a spinning solar sail during deployment, and performs an ABAQUS simulation of the origami fold pattern deploying. Although there is some literature on modelling the deployment dynamics of solar sails, the deployment of these sails is most often enacted by centrifugal means as the central hub spins and the sail unfolds [124], and the sail itself is considered to be a flexible membrane, rather than a rigid origami structure.

The attitude control and shape reconfiguration of multibody spacecraft more generally (i.e. not specifically Origami structures) has been well studied in the literature for a variety of scenarios/spacecraft architectures, and using a range of modelling approaches. Trovarelli et. al demonstrate the attitude control of planar [132] and 3D [133] multibody systems using momentum preserving internal torques, demonstrating reorientation manoeuvres of linked bars/panels using hinge torques, finding optimal control solutions for these manoevures and investigating the effect of collision or impingement constraints on the optimal control solutions. Similar work includes that of Gong et. al, who also demonstrate attitude control through the use of shape reconfiguration for microsatellites [134], and femtosatellites [135], with the latter work including the design and testing of a foldable PCBsat. Ashrafiuon and Erwin [136] present an approach for the design of sliding mode control for underactuated, nonlinear multibody systems, proving the stability of the closed-loop control system through Lyapunov stability analysis for certain conditions, and demonstrating simulation results for the control of an inverted pendulum, and a multibody communication satellite. Though the method proposed here by Ashrafiuon and Erwin is clearly extendable to many different multibody spacecraft architectures, the same approach cannot be adopted for OrigamiSat's because the system is non-conservative, as the force due to SRP introduces momentum to the system. While the OrigamiSat concept is quite new, there are some examples of similar multi-body membrane spacecraft to be found. Gong et. al [137] propose the relatively similar concept of a multibody solar sail, comprised of four pivoting triangular sail "wings" mounted on a central bus, and demonstrate attitude manoeuvres through controlled pitching of each wing. Sinn and Vasile [138] investigate the multibody dynamics of a membrane structure consisting of inflatable cells which is capable of shape reconfiguration. While similar in purpose to an OrigamiSat the method of actuation and modelling is quite different to the approach taken in Chapter 6.

1.4 Thesis Objectives and Contributions

This introductory chapter has sought to provide an overview of the potential applications for LSS in general, including discussion of existing and past missions and proposed concepts. As has been shown, on-orbit manufacturing of LSS has received much attention in recent years and it is increasingly likely that these emerging technologies will be used to construct the next generation of LSS. The dynamics and control of LSS is a field of research that has been active for many years now, with a broad range of technical challenges and control strategies to be found in the research literature. However, given the emerging field of on-orbit manufacturing, new research is required regarding how 3D-printed structures will behave in space, and how they can be most effectively controlled. This fresh look is required for two reasons; firstly this new class of on-orbit manufactured LSS will be much more lightweight than previous LSS designs based around deployable or erectable systems, and may be quite different in design. Such LSS may therefore have quite different dynamic behaviour and control requirements to previously studied systems, given they occupy this new area of the LSS design space. Secondly, this new method of construction could enable new spacecraft architectures, and new control strategies that would not previously have been possible or viable for traditional LSS constructions. The main objective of this thesis is therefore to identify and analyse novel concepts in LSS dynamics and control, within the specific context of LSS which may be manufactured on-orbit with emerging additive manufacturing technologies.

1.4.1 Thesis Outline

This thesis is divided into 8 chapters. Chapter 2 contains a technical introduction, in which some key mathematical and technical concepts relevant to the later work are presented. Chapters 3-6 contain the original work of the thesis, the contents of which are detailed below. Chapter 7 then concludes the thesis, and discusses potential future work. The technical chapters contain the following original work and contributions:

- Chapter 3 investigates the utility of distributed magnetic torque rods for the attitude control of a large space structure. First, distributed torques are shown to effectively rotate highly flexible structures. This is compared with torques applied to the centre-of-mass of the structure, which cause large surface deformations and can fail to enact a rotation. This is demonstrated using a spring-mass model of a planar structure with embedded actuators. A distributed torque algorithm is then developed to control an individually addressable array of actuators. Attitude control simulations are performed, using the array to control a large space structure, again modelled as a spring-mass system.

- Chapter 4 presents the development and experimental results of laboratory work relating to the magnetic control strategy of Chapter 3. The development of a Distributed Magnetorquer Demonstration Platform (DMDP), a PCB mounted magnetorquer array and control circuit, is presented, followed by the results of attitude control experiments performed on a spherical air bearing within a magnetic field.

- Chapter 5 then investigates a different potential magnetic control strategy, which uses large current loops embedded within a LSS. Length-scaling laws are derived by determining what fraction of a planar spacecraft's mass would need to be allocated to the conductive current loops in order to produce a torque at least as large as the gravity gradient torque. Simulations are then performed of a flexible truss structure, modelled as a spring-mass system, for a range of structural flexibilities and a variety of current loop geometries. Simulations demonstrate rotation of the structure via the electromagnetic force on the current carrying elements, and are also used to characterise the structural deformations caused by the various current loop geometries. Finally, an attitude control simulation is performed, demonstrating a 90° slew manoeuvre of a 250×250 m flexible structure through the use of three orthogonal sets of current loops embedded within the spacecraft.

- Chapter 6 discusses the attitude and shape control of OrigamiSats, large, origami solar sail type structures which could potentially be manufactured on orbit. This work was part of a collaborative research project with the University of Liverpool covering simulation and laboratory-based work, however the simulation work reported here is my own contribution to the collaboration. Analysis is made of the principles of shape reconfiguration through the use of SRP and local surface reflectivity modulation. First, a length-scaling analyis is undertaken of panel folding times under the effect of SRP, considering hinge resistance. A planar multibody dynamics model of linked reflective panels is then presented, and used to demonstrate the principle of SRP induced shape reconfiguration. Finally, a 3D multibody dynamics formulation for arbitrary origami patterns is presented, and numerical simulations are performed of different OrigamiSat designs, investigating the topics of shape and attitude control of these structures.

1.4.2 List of Publications

The following journal articles have been published based on the contents of this thesis:

- A. Russo, B. Robb, S. Soldini, P. Paoletti, C. R. McInnes, J. Reveles, A. K. Sugihara, S. Bonardi, and O. Mori. Mechanical Design of Self-reconfiguring 4D-printed OrigamiSat: a New Concept for Solar Sailing. *Frontiers in Space Technologies*, 3, 2022

- B. Robb, M. McRobb, G. Bailet, J. Beeley, and C. R. McInnes. Distributed Magnetic Attitude Control for Large Space Structures. *Acta Astronautica*, 198(September):587–605, 2022

- B. Robb, M. McRobb, G. Bailet, and C. R. McInnes. 3D-printed, electrically conductive structures for magnetic attitude control. *Acta Astronautica*, 200(July):448–461, 2022

- M. McRobb, B. Robb, S. Ridley, and C. R. McInnes. Emerging Space Technologies: Macro-scale On-orbit Manufacturing. *Journal of the British Interplanetary Society*, 72 (12), 2019

Additionally the following conference papers have been presented:

- B. Robb, M. Mcrobb, and C. R. McInnes. Magnetic Attitude Control of Gossamer Spacecraft using a 3D-printed , Electrically Conducting Support Structure. In *AIAA Scitech 2020 Forum*, 2020

- B. Robb, G. Bailet, J. Beeley, and C. R. McInnes. Laboratory-Scale Demonstration of a Distributed Magnetorquer Array for the Attitude Control of Large Space Structures. *73rd International Astronautical Congress*, (IAC-22,C1,2,3,x69274), 2022

- B. Robb, A. Russo, S. Soldini, P. Paoletti, J. Reveles, G. Bailet, and C. R. McInnes. Integrated Attitude and Shape Control for OrigamiSats with Variable Surface Reflectivity. *73rd International Astronautical Congress*, (IAC-22,C2,9,2,x69275), 2022

Chapter 2

Technical Introduction

The attitude of a spacecraft refers to its orientation in space. Attitude dynamics then refers to how a spacecraft's attitude evolves over time, and how the attitude is influenced by the torques which the spacecraft may experience. Spacecraft may experience disturbance torques, caused by external forces such as gravity, or interaction with a planet's atmosphere or magnetic field. Solar radiation pressure is another potential cause of a disturbing torque, as momentum is imparted to the spacecraft by incident and reflected photons. Attitude control refers to the process by which the attitude and angular velocity of a spacecraft is affected to reach a desired state. Generally attitude control is provided by actuators, devices mounted on the spacecraft which generate desired torques on command. Some forms of attitude control actuation were discussed in the introduction, with common choices including thrusters, reaction wheels, control moment gyroscopes, or magnetic torquers. Attitude control can also be achieved by exploiting environmental torques. For example variation in the force due to gravity across a spacecraft's body can lead to gravity gradient torques. These torques can be used to provide gravity gradient stabilisation, whereby the spacecraft's attitude remains in the region near a stable equilibrium configuration relative to the gravity vector as it orbits the Earth or another body. Attitude control of course requires some knowledge of the spacecraft's attitude at a given moment in time, the attainment or estimation of which is known as attitude determination. This is provided by sensors such as accelerometers, gyroscopes, magnetometers, Sun sensors or star trackers. Such devices are used to obtain information regarding the spacecraft's dynamics and it's attitude in relation to some external references. This information is used to generate an estimate of the spacecraft's attitude, which may be represented mathematically in a number of ways.

Before beginning the technical chapters, in which the original research of this thesis is presented, a brief introduction is given in this chapter to some of the mathematical concepts which are referred to later. In each of the technical chapters which follow, the models and nomenclature used are defined as they appear. This technical introduction aims to include only those concepts which are most frequently referred to in the following chapters, and those which are a prerequisite for the study of attitude dynamics and control. In this chapter, the different rotation representations which are used in the thesis are discussed, followed by a discussion of the foremost governing equations of rigid-body rotational dynamics, Euler's equations. Finally, a derivation of the gravity gradient torque is given, as this is a disturbance torque of particular importance for large spacecraft and is referred to at numerous points of the later chapters. As noted, the content of this chapter is provided only to serve as an introduction to the mathematical discussion of the later chapters and as such no original content is provided here. All of the concepts discussed here may be found in any introductory text on spacecraft dynamics and control, for example Refs. [77, 145, 146], amongst others.

2.1 Reference Frames and Rotations

In order to mathematically describe the attitude of a spacecraft, the first requirement is a reference frame, generally defined by a set of three, mutually perpendicular axes which is fixed within the body of the spacecraft. A further reference frame is then needed, generally one which is defined relative to the Earth, Sun, or other celestial body, with which the spacecraft body frame is compared, in order to consistently describe the spacecraft attitude. Figure 2.1 shows two example reference frames, the $x_E y_E z_E$ frame, an Earth-centred inertial frame, and the $x_1 y_1 z_1$ body frame, centered on the centre-of-mass of the spacecraft and oriented some 3D rotation away from the $x_E y_E z_E$ frame. Note that in the later chapters, the notation and labelling for the various body or inertial reference frames varies between the models, but as noted all frames are defined as they appear in the text.

Another commonly used reference frame in attitude dynamics and control is a rotating orbital frame, shown in Fig. 2.2. This frame is defined such that the z_o axis is always aligned with the gravity vector, pointing towards the central body (also known as nadir), the x_o points in the direction of the orbital velocity. Then y_o completes the right-handed coordinate system, and is thus antiparallel to the direction of the orbital angular momentum. The Euler angles (to be defined in Sec. 2.1.2) ψ, θ and ϕ which parametrise a spacecraft's rotation in relation to the orbital frame are then referred to as roll, pitch and yaw respectively, in-keeping with the conventional method of describing the attitude of aircraft.

2.1.1 Rotation Matrices and Euler Angles

A rotation matrix is a transformation matrix which acts to rotate coordinates around the origin of a given reference frame. The rotation matrix which rotates the basis vectors of a given reference frame to align with the axes of the spacecraft body frame then encodes the current attitude of the spacecraft in a mathematically convenient way, which can be used for computations as needed. Of particular use are three principal rotation matrices, which perform rotations of $\theta_{x,y,z}$ around the x, y and z axes of the given reference frame, given by:

$$R_x(\theta_x) \begin{bmatrix} 1 & 0 & 0 \\ 0 & \cos\theta_x & \sin\theta_x \\ 0 & -\sin\theta_x & \cos\theta_x \end{bmatrix} \tag{2.1}$$

$$R_y(\theta_y) = \begin{bmatrix} \cos\theta_y & 0 & \sin\theta_y \\ 0 & 1 & 0 \\ -\sin\theta_y & 0 & \cos\theta_y \end{bmatrix} \tag{2.2}$$

$$R_z(\theta_z) = \begin{bmatrix} \cos\theta_z & \sin\theta_z & 0 \\ -\sin\theta_z & \cos\theta_z & 0 \\ 0 & 0 & 1 \end{bmatrix} \tag{2.3}$$

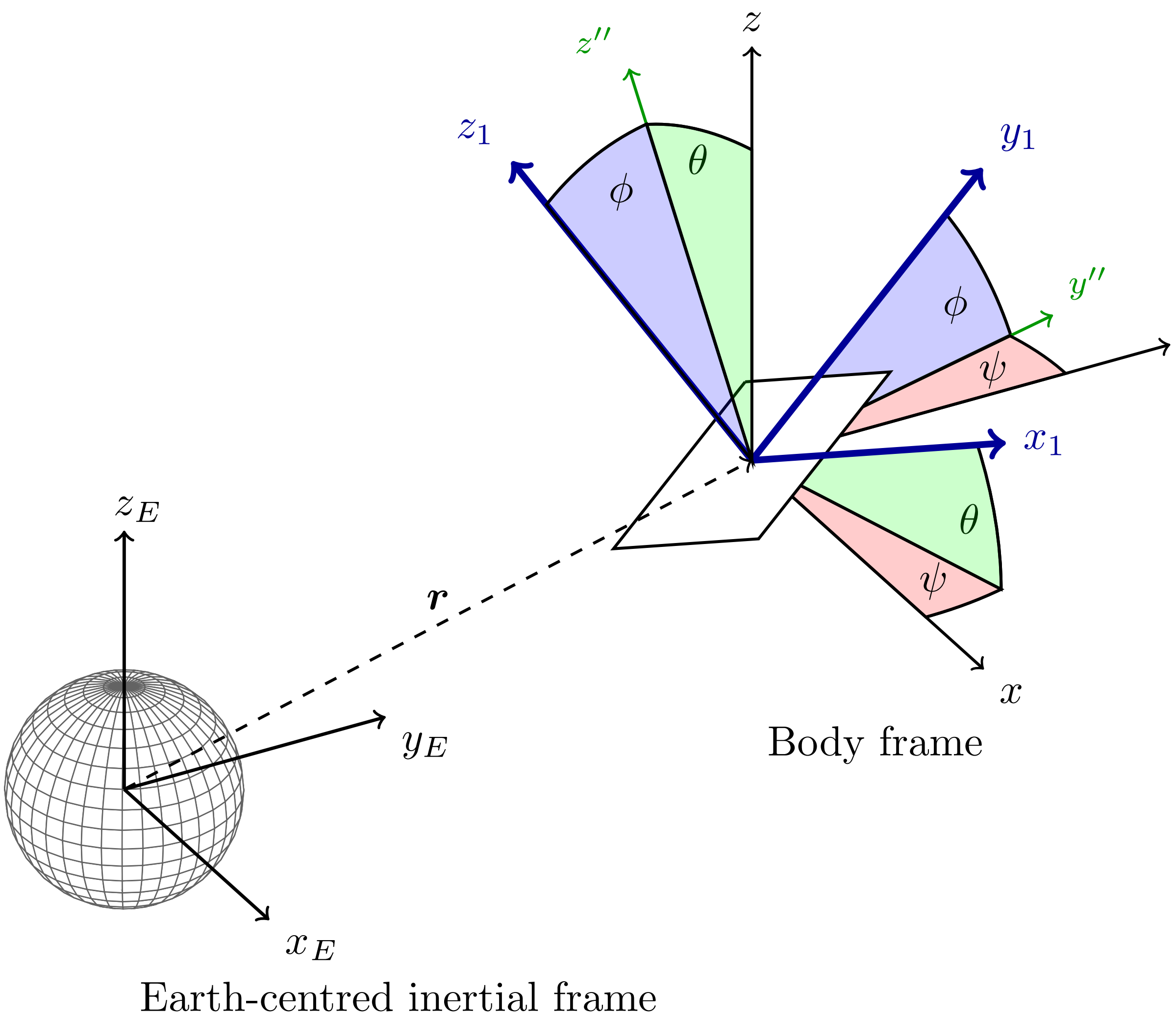

Figure 2.1: Earth-centred inertial frame, $x_E y_E z_E$, and sequence of rotations to the $x_1 y_1 z_1$ body frame.

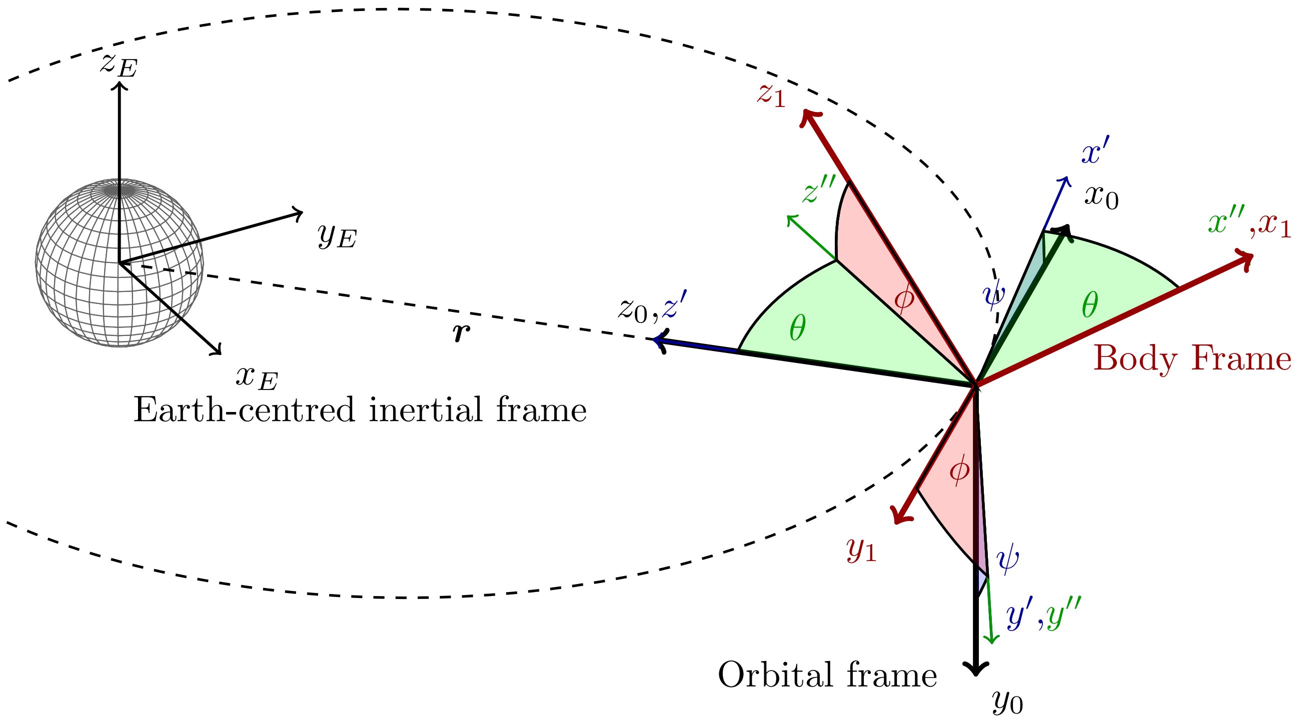

Figure 2.2: Earth-centred inertial frame, $x_E y_E z_E$, orbital frame $x_o y_o z$, and sequence of rotations to the $x_1 y_1 z_1$ body frame.

2.1.2 Euler Angles

The rotation matrix which provides the rotation to the spacecraft body frame can be parametrised in a variety of ways. One of the most common, and one which appears in the later chapters, is the use of Euler angles. These are three angles which describe successive rotations around specified axes, allowing any orientation to be described with just three parameters, and in an intuitive manner. For example, Fig. 2.1 shows the Euler angles ψ, θ and ϕ, which correspond to successive rotations around the inertial frame x-axis, the intermediate y'-axis (the rotated y-axis, also y''), and the body-frame x_1 axis. These angles are thus referred to as the intrinsic ZYX Euler angles. They are termed intrinsic because the second and third rotations are performed around the intermediate, rotated axes, as opposed to all rotations performed around the axes of the initial frame. Here ZYX specifies the order of rotations, and any combination of three rotations around at least two axes may be used. A rotation matrix which provides the rotation between the inertial frame and body frame can then be constructed by combining the principal rotation matrices given above (Eqs. 2.1-2.3), resulting in:

$$R = R_x(\phi) R_y(\theta) R_z(\psi) \tag{2.4}$$

Such matrices and their transposes can then be used to perform coordinate transformations between any desired frames of reference and other computations as required, following the standard rules of linear algebra.

2.1.3 Quaternions

One disadvantage of the use of Euler angles to parametrise rotations is that for some attitudes a singularity occurs. That is to say that there exists some orientations for which the three Euler angles are not uniquely determined, which is in fact true of all three value parametrisations of 3D rotations. Quaternions are an alternative method of describing rotations which avoid this singularity, as a quaternion is composed of four components, and which have further useful properties which make them computationally efficient for the study of attitude dynamics. A general quaternion is given by:

$$\overline{q} = [a, \boldsymbol{b}] \tag{2.5}$$

where a is a scalar and $\boldsymbol{b}$ a vector, $[b_1, b_2, b_3]$. In terms of an axis and angle, a rotation of θ around $\boldsymbol{r}$ may be described by the quaternion given by:

$$\overline{q} = \left(\cos\frac{\theta}{2}, \sin\frac{\theta}{2}\boldsymbol{r}\right) \tag{2.6}$$

For a general quaternion, $\overline{q} = (a, \boldsymbol{b})$ the properties which are used at various points in the later chapters are as follows.
Addition:

$$\overline{q}_1 + \overline{q}_2 = (a_1 + a_2, \boldsymbol{b}_1 + \boldsymbol{b}_2) \tag{2.7}$$

Quaternion product (in general quaternions are non-commutative):

$$\overline{q}_1\overline{q}_2 = (a_1a_2 - \boldsymbol{b}_1 \cdot \boldsymbol{b}_2, a_1\boldsymbol{b}_2 + a_2\boldsymbol{b}_1 + \boldsymbol{b}_1 \times \boldsymbol{b}_2) \tag{2.8}$$

Conjugate:

$$\overline{q}^* = (a, -\boldsymbol{b}) \tag{2.9}$$

Norm:

$$|\overline{q}| = \sqrt{\overline{q}\overline{q}^*} = \sqrt{\overline{q}^*\overline{q}} = \sqrt{a^2 + b_1^2 + b_2^2 + b_3^2} \tag{2.10}$$

The 3D rotation matrix equivalent to a quaternion is also given by:

$$R_q = \begin{bmatrix} 1 - 2b_2^2 - 2b_3^2 & 2b_1b_2 - 2ab_3 & 2b_1b_3 + 2ab_2 \\ 2b_1b_2 + 2ab_3 & 1 - 2b_1^2 - 2b_3^2 & 2b_2b_3 - 2ab_1 \\ 2b_1b_3 - 2ab_2 & 2b_2b_3 + 2ab_1 & 1 - 2b_1^2 - 2b_2^2 \end{bmatrix} \tag{2.11}$$

For a rigid-body rotating around it's centre of mass with angular velocity $\boldsymbol{\omega}$, the quaternion describing the body's orientation is governed by the equation

$$\dot{\bar{q}} = \frac{1}{2}\bar{q}[0, \boldsymbol{\omega}] \tag{2.12}$$

Th quaternion product (Eq. 2.8) can also be written using a skew-symmetric matrix, and so Eq. 2.12 can be written as:

$$\dot{\bar{q}} = \frac{1}{2}\begin{pmatrix} 0 & -\omega_1 & -\omega_2 & -\omega_3 \\ \omega_1 & 0 & \omega_3 & -\omega_2 \\ \omega_2 & -\omega_3 & 0 & \omega_1 \\ \omega_3 & \omega_2 & -\omega_1 & 0 \end{pmatrix}\begin{pmatrix} a \\ b_1 \\ b_2 \\ b_3 \end{pmatrix} \tag{2.13}$$

2.2 Euler's Equations

The most fundamental equations of attitude dynamics are the Euler equations, which relate the angular velocity $\boldsymbol{\omega}$, accelerations $\dot{\boldsymbol{\omega}}$ and applied torques $\boldsymbol{T}$ acting upon a rigid body with inertia tensor $\boldsymbol{I}$. They are thus the equivalent, for rotational motion, of Newton's second law and are thus essentially an expression of the rate of change of angular momentum. The Euler equations are given by:

$$\boldsymbol{I}\dot{\boldsymbol{\omega}} + \boldsymbol{\omega} + (\boldsymbol{I}\boldsymbol{\omega}) = \boldsymbol{T} \tag{2.14}$$

or, explicitly:

$$\begin{aligned} I_1\dot{\omega}_1 - (I_2 - I_3)\omega_2\omega_3 &= T_1 \\ I_2\dot{\omega}_2 - (I_3 - I_1)\omega_3\omega_1 &= T_2 \\ I_3\dot{\omega}_3 - (I_1 - I_2)\omega_1\omega_2 &= T_3 \end{aligned} \tag{2.15}$$

Where $I_{1,2,3}$ are the principal moments of inertia of the body. Thus the Euler equations are a set of three coupled equations which describe the time evolution of a rigid-body's rotational motion, under the application of external torques. As the equations are coupled, there are non-trivial solutions even in the case when the components of the torque are equal to zero, known as torque-free precession. Physically this means that the rotational axis of a rigid body can appear to change relative to a fixed inertial frame despite no external torques being applied, despite (though in-fact a consequence of) angular momentum being conserved. Precession of the body may also also occur when torques are applied, known as gyroscopic precession, and this behaviour can often also be unintuitive. The best known example would be a spinning top, where the torque on the spinning body due to gravity acts to rotate the top around the vertical axis, even though the direction of the torque is perpendicular to the vertical (i.e. gravity acts to precess the top around the vertical rather than topple it over).

An understanding of the Euler equations and the dynamics of rotating bodies is thus the core of spacecraft attitude dynamics, and they can be used to predict the behaviour of many scenarios, when the applied torques and spacecraft properties are known. Analysing the dynamics of flexible spacecraft requires more detailed modelling than is offered by the Euler equations alone, and so in the later chapters of the thesis more complex formulations are used. Nevertheless, the equations are used later in the thesis when it is appropriate to approximate the spacecraft as a rigid body, and to provide a starting point for more detailed analysis.

2.3 Gravity Gradient Torques and Stabilisation

Throughout the later chapters of this thesis, the effects of gravity gradient torques on large space structures are considered and included in the numerical simulations. This is a disturbance torque which arises due to the variation in the magnitude and direction of the gravitational force across the span of a spacecraft's body. For small spacecraft, the torque is generally negligible, as there is not a significant variation in the strength of the gravitational field across their length-scale. For large spacecraft, such as those considered in this thesis, this effect can become a significant disturbance and thus receives significant attention in the later analysis. The derivation of the commonly used expression for the gravity gradient torque is given here, to provide an understanding of how this important disturbance torque arises and its implications for large space structures.

The Newtonian gravitational force acting on an infinitesimal mass element located at $\boldsymbol{r} + \boldsymbol{\rho}$ is given by:

$$\mathrm{d}\boldsymbol{F}_g = -\frac{\mu(\boldsymbol{r} + \boldsymbol{\rho})}{|\boldsymbol{r} + \boldsymbol{\rho}|^3}\,\mathrm{d}m \tag{2.16}$$

where $\boldsymbol{\rho}$ is the distance from the body's centre-of-mass to an infinitesimal mass element $\mathrm{d}m$, $\boldsymbol{r}$ is the distance to the centre-of-mass from the central body, and μ is the standard gravitational parameter. The components of $\boldsymbol{T}_g$, the gravity gradient torque, are found by integrating this gravitational force over the body of the spacecraft:

$$\begin{aligned} \boldsymbol{T}_g &= \int_B \boldsymbol{\rho} \times \mathrm{d}\boldsymbol{F}_g \\ &= \mu\boldsymbol{r} \times \int_B \frac{\boldsymbol{\rho}}{(r^2 + 2\boldsymbol{r}\cdot\boldsymbol{\rho} + \rho^2)^{3/2}}\,\mathrm{d}m \end{aligned} \tag{2.17}$$

where a Taylor expansion is then performed, assuming ($r \gg \rho$):

$$\boldsymbol{T}_g \approx \mu\boldsymbol{r} \times \int_B \boldsymbol{\rho}\frac{1}{r^3}\left(1 - 3\frac{\boldsymbol{r}\cdot\boldsymbol{\rho}}{r^2}\right)\mathrm{d}m \tag{2.18}$$

The definition of the centre-of-mass implies that the integral of $\rho\,\mathrm{d}m$ vanishes. Using the double cross product identity $\boldsymbol{\rho} \times (\boldsymbol{\rho} \times \boldsymbol{r}) = (\boldsymbol{r}\cdot\boldsymbol{\rho})\boldsymbol{\rho} - (\boldsymbol{\rho}\cdot\boldsymbol{\rho})\boldsymbol{r}$ results in:

$$\boldsymbol{T}_g = -\frac{3\mu}{r^5}\boldsymbol{r} \times \int_B \boldsymbol{\rho} \times (\boldsymbol{\rho} \times \boldsymbol{r}) + (\boldsymbol{\rho}\cdot\boldsymbol{\rho})\boldsymbol{r}\,\mathrm{d}m \tag{2.19}$$

Here, the second cross product in the expression also vanishes, while the first integral can be re-written using a skew-symmetric multiplication matrix:

$$\boldsymbol{T}_g = -\frac{3\mu}{r^5}\boldsymbol{r} \times \int_B [\boldsymbol{\rho}]_\times [\boldsymbol{\rho}]_\times \boldsymbol{r} \, \mathrm{d}m \tag{2.20}$$

It can then be shown that the final term of the equation is by definition the inertia tensor, and so the final expression for the gravity gradient torque is given by:

$$\boldsymbol{T}_g = 3\frac{\mu}{r^5}(\boldsymbol{r} \times \mathbf{I}\boldsymbol{r}) \tag{2.21}$$

Another important result in attitude dynamics, and one referred to throughout this thesis, is gravity gradient stabilisation. By substituting T_g into the Euler equations as the applied torque, and linearising the resulting equations for small angular deviations of the spacecraft body frame from the orbital frame (Fig. 2.2), it can be shown that there are certain configurations (configurations meaning spacecraft of a certain inertia and orientation relative to the orbital

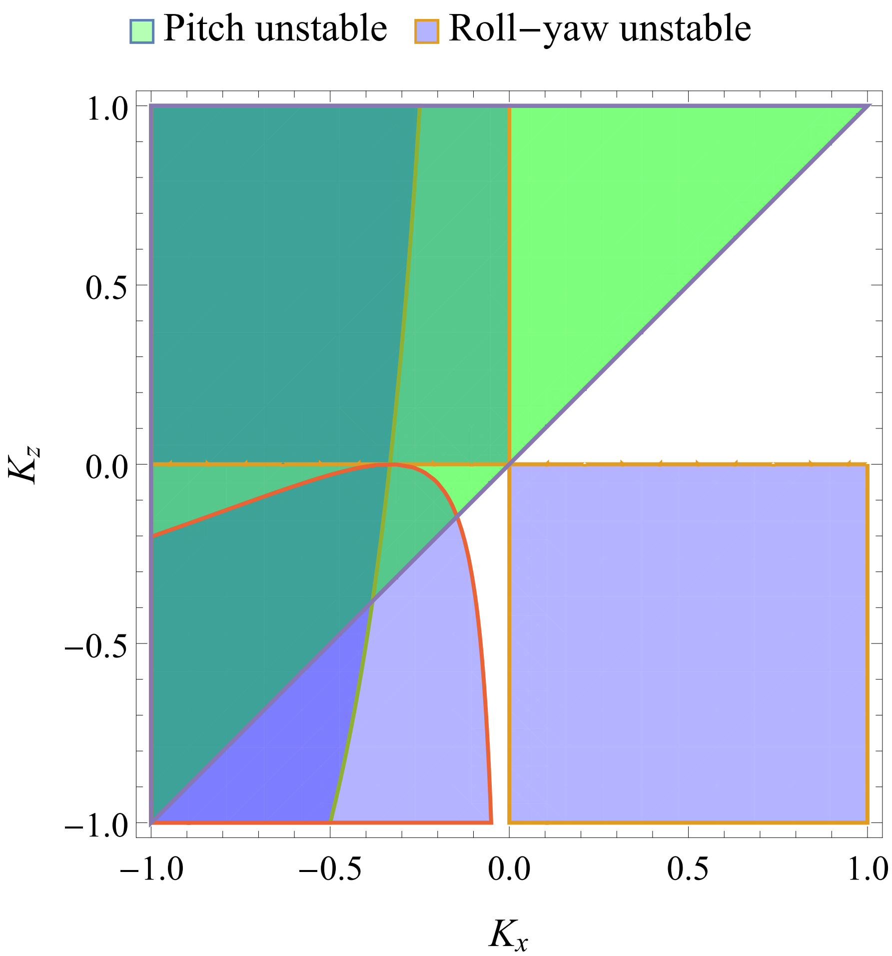

Figure 2.3: Gravity gradient stability map, showing the overlapping pitch (green) and roll-yaw (blue) unstable regions.

frame) at which the spacecraft attitude is stable. There are both stable equilibria, where the spacecraft attitude will oscillate around the gravity vector, and unstable equilibria, where the gravity gradient torque is zero yet small deviations in the attitude will result in the attitude moving away from this configuration. The result of this process gives the well known stability map shown in Fig. 2.3. The two parameters relate to the mass distribution of the body around the orbital frame, and are given by:

$$K_x = \frac{I_y - I_z}{I_x} \qquad K_y = \frac{I_y - I_z}{I_x} \tag{2.22}$$

where $I_{x,y,z}$ are the principal moments of inertia for the orbital frame xyz axes respectively.

2.4 Magnetorquers

A rigid current loop in a uniform external magnetic field experiences no net force, but will experience a torque which is proportional to the area enclosed by the loop, and the current flowing. The torque arises due to the Lorentz force on the moving charges within the conductive loop, and is given by:

$$\boldsymbol{T} = I\boldsymbol{A}_e \times \boldsymbol{B} \tag{2.23}$$

where I is the current in the loop, $\boldsymbol{A}_e$ a vector with magnitude equal to the area enclosed by the loop and normal to that surface, and $\boldsymbol{B}$ the magnetic field vector. The product $I\boldsymbol{A}_e$ is often referred to as the magnetic dipole moment, $\boldsymbol{m}_d$, which characterises the strength the coil. For magnetorquer rods, the coil is wound around a core material of high relative magnetic permeability, which acts to concentrate the magnetic field lines around the central axis of the rod and increase the magnitude of torque generated. In this case the magnetic dipole moment is given by

$$\boldsymbol{m}_d = \mu_c N I \boldsymbol{A}_e \tag{2.24}$$

Where μ_c is the relative magnetic permeability of the core material, N is the number of turns of the coil, I the current and $\boldsymbol{A}_e$ the area enclosed by a single turn or equally the cross sectional area of the core material.

Chapter 3

Distributed Magnetorquer Arrays

Magnetorquers are a common form of attitude control actuation for small satellites. A magnetorquer is an electromagnet, a coil of conductive wire which generates a magnetic field when a current is passed through it. Often a material with high magnetic permeability is used as a core material within the coil, which concentrates the magnetic field lines in the core and increases the field strength. Through interaction with the Earth's (or another body's) magnetic field, a torque is generated by the magnetorquer which can then be used for attitude control purposes, either to directly point the spacecraft or for angular momentum dumping. Magnetorquers have a number of advantages over other forms of attitude control actuators. Firstly, they don't use propellant, only requiring electrical power to operate. They are also relatively simple in design with no moving parts, meaning they are more robust than mechanical devices such as reaction wheels or CMGs. One disadvantage however is that there is a geometrical constraint on the direction of the torque that a magnetorquer can produce, determined by the external magnetic field direction. This constraint is discussed in greater detail later in this chapter. Furthermore, a major disadvantage is that the torque produced by a magnetorquer is often smaller than what can be produced by other actuators of similar mass. This is because producing large torques with magnetorquers requires large currents, which can then generate excessive heat or require significant power. Due to this, magnetorquers are not often considered for the attitude control of LSS, as the greater mass and moment of inertia of these structures means that larger torques are required for their attitude control.

As presented in Chapter 1, an objective of this thesis is to consider new attitude control strategies for LSS which may be 3D-printed on-orbit. As such structures may have a much lower mass (i.e. "sparse" or gossamer structures) than conventional erectable or deployable designs, magnetorquers may be a feasible form of attitude control. A further motivating assumption here is that magnetorquers are relatively simple in design, and so it was proposed that actuator placement could be easily integrated with the on-orbit fabrication process. For example, it was envisaged that while 3D-printing a long boom, magnetorquers could be placed within the boom at regular intervals as it is printed, or wire could even be coiled around the boom itself to form a magnetorquer. So long as the torquer is then connected to a power source with switching capabilities, attitude control torques can be generated. This would then allow customised architectures to be considered, with attitude control provided by magnetorquers placed anywhere within the structure.

In this chapter, the concept of using distributed magnetorquer arrays for the attitude control of lightweight, flexible LSS is investigated. The analysis addresses the three following research questions:

1. Is there any benefit to having a distributed array of magnetorquers as opposed to a single, larger torquer at the spacecraft centre-of-mass?
2. Up to what length-scale and mass density could magnetorquers provide large enough torques for attitude control of a LSS?
3. Can a magnetorquer array demonstrate attitude control in orbital simulations, where the external field direction is constantly changing and there are disturbing gravity gradient torques?

Research question 1 pertains to the motivating assumption that it would be desirable to distribute magnetorquers throughout a LSS as it is being printed, as opposed to producing control torques at a central spacecraft-bus only. Intuition led to the hypothesis that a distributed array of torquers would lead to more uniform slew manoeuvres, and reduced structural deformation. Distribution of the torquers will have an associated increase in the structure's moment of inertia however, and so analysis was undertaken to first evaluate the motivating assumption and then to quantify any benefits of distributed torquing. This analysis is presented in Sec. 3.1, first through the use of a 2D flexible beam model with centralised or distributed torquing elements in Sec. 3.1.1, and then with a 3D spring-mass model of a planar truss-like structure in Sec. 3.1.2. Numerical simulations are used to compare the torquing strategies for both models, across a range of physical properties which are selected with reference to the properties of existing lightweight space structures. Two geometric configurations for magnetorquer arrays are then proposed and investigated in Sec. 3.2. The first of these is a radial array, where magnetorquers are aligned radially around the centre of the structure; and the second is an orthogonal array, where two perpendicular magnetorquers are placed at each point of a square grid. Control strategies are proposed for both array types and assessed through rigid-body dynamics simulations of attitude control manoeuvres. In Sec. 3.3, a length scaling analysis is performed to address research question 2, considering the impact of magnetorquer performance on the maximum length-scale at which magnetorquers could provide useful attitude control. Orbital simulations are then performed, addressing research question 3 by demonstrating detumbling and slew manoeuvres of a flexible planar spacecraft in the presence of a time-varying magnetic field and gravity gradient torques. Chapter conclusions are then given in Sec. 3.4.

3.1 Distributed Control Torques for Large Space Structures

The motivation for distributed magnetorquer arrays is that it is assumed desirable to distribute actuator torques across the body of a large flexible space structure, in order to reduce structural deformation during manoeuvres. For a rigid body, a torque applied at a distance from the centre-of-mass is equivalent to one applied at the centre-of-mass. For a flexible body however, the location of torquing actuators and the induced flexible response is an important consideration when designing the attitude control system. In this section distributed and central torquing strategies are compared using two different models. First, a 2D model of a flexible beam is used, comprised of rigid bars linked by torsional springs. Then, a 3D spring-mass model representing a large, truss-like planar space structure is presented, and used to compare the flexible dynamics of a planar structure with central or distributed torquing. Spring-mass or multi-particle models allow continuous structures to be modelled accurately with relatively low computational effort. They have been used extensively by JAXA for modelling the membrane dynamics of the IKAROS solar sail [147], and found to accurately predict the membrane dynamics when compared with flight-data. Here, the 2D beam model, and the spring-mass model of a truss-structure are used as generic models of a flexible support boom and a flexible planar structure respectively. The aim of this section is to demonstrate that for structures of the length-scale and flexibilities considered, distributed attitude control torques will reduce structural deformation when compared to centralised torquing strategies. Later simulations are then used to demonstrate that an array of magnetorquers could serve this purpose, given the constraints and scaling laws unique to these actuators specifically.

3.1.1 Motivation for Distributed Torques: 2D Beam Model

The beam is modelled as n rigid bars of length l_b and mass m_b, connected by torsional springs with spring constant k_b. The beam's shape is parametrised by the angles, θ_i, between each bar element and the x-axis, shown in Fig. 3.1. The coordinates of the centre-of-mass of the i^{th} bar element, located at (x_i, y_i), can be found using the angles θ_i, and is given by:

$$\begin{aligned} x_i &= x_1 + \frac{1}{2} l_b \cos(\theta_1) + \sum_{j=2}^{i-1} l_b \cos(\theta_j) + \frac{1}{2} l_b \cos(\theta_i) \\ y_i &= y_1 + \frac{1}{2} l_b \sin(\theta_1) + \sum_{j=2}^{i-1} l_b \sin(\theta_j) + \frac{1}{2} l_b \sin(\theta_i) \end{aligned} \tag{3.1}$$

for all $i > 1$. The first element's centre-of-mass coordinates, x_1 and y_1, are additional degrees of freedom in the system and appear in Eq. 3.1 as the reference point from which all other element positions are taken. The kinetic energy of the entire system can then be defined by considering, for each element, the translation of the centre-of-mass and rotation around that centre-of-mass, and performing a summation over all elements:

$$T = \sum_i \left[\frac{1}{2} m_b (\dot{x}_i^2 + \dot{y}_i^2) + \frac{1}{2} I_b \dot{\theta}_i^2 \right] \tag{3.2}$$

where I_b is the moment of inertia of each bar around its centre, given by $I_b = \frac{1}{12} m_b {l_b}^2$. The expressions for $\dot{x}_i$ and $\dot{y}_i$ are found by taking the derivatives of Eq. 3.1 with respect to time, meaning that T is given in terms of the generalised coordinates and velocities, θ and $\dot{\theta}$ only. The potential energy, V, of the system comes from the relative angle, ϕ, between successive elements. Each connection contributes $\frac{1}{2} k_b \phi^2$ to the potential, with ϕ given by the difference in angle θ of the specified elements. Thus, for a beam of n elements, the Lagrangian is given by:

$$\begin{aligned} L &= T - V \\ &= \sum_{i=1}^{n} \left[\frac{1}{2} m_b (\dot{x}_i^2 + \dot{y}_i^2) + \frac{1}{2} I_b \dot{\theta}_i^2 \right] - \frac{1}{2} k_b \sum_{i=1}^{n-1} (\theta_{i+1} - \theta_i)^2 \end{aligned} \tag{3.3}$$

This expression is in terms of the generalised coordinates and velocities θ_i and $\dot{\theta}_i$ only and can be substituted into the Euler-Lagrange equations to solve for the motion of the beam, such that:

$$\frac{\mathrm{d}}{\mathrm{d}t} \left(\frac{\partial L}{\partial \dot{\theta}_i} \right) - \frac{\partial L}{\partial \theta_i} = \tau_i \tag{3.4}$$

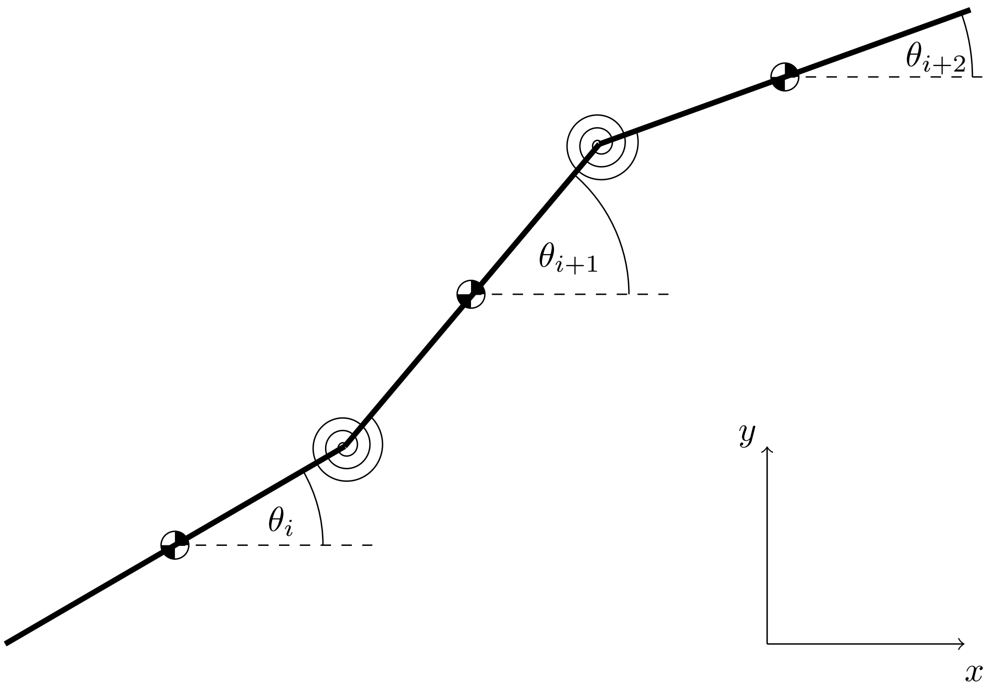

Figure 3.1: A section of the flexible beam model showing three elements, with the shape parametrised by angles θ_i

where τ_i are the torques associated with beam element i, which act upon each individual beam element around its centre-of-mass. A comparison can then be made between applying a large torque to the central element and applying smaller distributed torques to each beam element. This comparison is analogous to having a single large magnetorquer at the centre of a flexible spacecraft boom compared to a set of magnetorquers distributed along its length.

3.1.1.1 Validation of the Flexible Beam Model

The flexible beam model adopted here has the advantage of allowing large rotational displacements to be simulated, due to the generalised coordinates being the beam element angles rather than considering displacements of the beam elements only. The choice of these coordinates also means that the generalised forces are identified as torques acting on each beam element. Therefore, the subject of our investigation, distributed magnetorquers, may be introduced quite naturally to the equations of motion. However, the set of Euler-Lagrange equations given by Eq. 3.4 results in a set of nonlinear, coupled differential equations. The validity of the model is now demonstrated by showing that in the limit of small displacements and large n, the dynamic behaviour approaches that of an Euler-Bernoulli beam.

The Lagrangian for a continuous Euler-Bernoulli beam [148], not subjected to external loads, is:

$$L = \int_0^{L_b} \left(\frac{1}{2}\mu \left(\frac{\partial w}{\partial t} \right)^2 - \frac{1}{2} EI \left(\frac{\partial^2 w}{\partial x^2} \right)^2 \right) \mathrm{d}x \tag{3.5}$$

where L_b is the total beam length, μ the mass per unit length, and $w(x)$ represents the vertical deflection at x. The x-axis coincides with the undeflected beam, which extends from the origin to $x = L_b$. The quantity EI, also known as the bending stiffness, is the product of Young's modulus and the second moment of area. This is taken to be constant across the length of the beam. Comparing Eq. 3.4 with Eq. 3.5, the kinetic energy terms are first examined. For small displacements, the horizontal velocity of each element is negligible, as $\sin\theta_i \approx 0$ after taking the time derivative of the first of Eqs. 3.1. The same reasoning gives:

$$\dot{y}_i \approx \left. \frac{\partial w}{\partial t} \right|_{x_i} \tag{3.6}$$

which allows the first term in the integral of Eq. 3.5 to be rewritten as:

$$\begin{aligned} \frac{1}{2}\mu \int_0^{L_b} \left(\frac{\partial w}{\partial t} \right)^2 \mathrm{d}x &= \frac{1}{2} \frac{n \cdot m_b}{L_b} \lim_{\Delta x \to 0} \sum_{i=1}^{n} \dot{y}_i^2 \Delta x \\ &\approx \frac{1}{2} m_b \sum_{i=1}^{n} \dot{y}_i^2 \end{aligned} \tag{3.7}$$

where the beam mass density is expressed as the total mass divided by the total length, $n{\cdot}m_b/L_b$, and for small displacements $\Delta x \approx l_b$. Equation 3.7 is therefore equivalent to the kinetic energy term of the discretised model, as both $\dot{x}_i$ and I_b tend to zero in the limit of small displacements and large n. With this result, the discretised model is equivalent to an Euler-Bernoulli beam for sufficiently large n if the potential terms are also equal. For small deflections, the first derivative of $w(x)$ can be approximated as the angle between the x-axis and the slope at that point:

$$\frac{\partial w}{\partial x} \approx \theta(x) \tag{3.8}$$

Taking the potential from Eq. 3.5, the integral is replaced with a Riemann sum and the definition of the derivative is used to obtain an expression in terms of θ such that:

$$\frac{1}{2}EI\int_0^{L_b}\left(\frac{\partial^2 w}{\partial x^2}\right)^2 \mathrm{d}x = \frac{1}{2}EI\lim_{\Delta x\to 0}\sum_{i=1}^{n-1}\left(\frac{\theta_{i+1}-\theta_i}{\Delta x}\right)^2\Delta x \tag{3.9}$$

again substituting $\Delta x \approx l_b$. Equation 3.9 will equal the potential term in Eq. 3.3 so long as the spring constant is chosen such that:

$$k_b = \frac{EI}{l_b} = \frac{EIn}{L_b} \tag{3.10}$$

a result corroborated by Ref. [149], where the internal moments of a cantilevered beam are considered. Thus, the flexible beam model developed here is accepted as a sufficient approximation of the linear Euler-Bernoulli beam theory, in the limit of small deflections and large n. This gives a suitable model for the purposes of this thesis, as the aim is to analyse long, thin beams or trusses in which shear effects are negligible. The nonlinear equations given by Eq. 3.4 may be numerically integrated with low computational effort to simulate large rotations of the beams under the application of distributed torques. They are assumed to accurately represent the dynamics of a long, thin beam so long as local deformation, or the difference in angle between consecutive elements, remains small.

The number of elements needed to sufficiently approximate the beam is chosen by evaluating the potential term in Eq. 3.3, while varying n. The calculation is performed for a beam with constant curvature, i.e. $n(\theta_{i+1} - \theta_i)/L_b = \kappa$, a constant. An Euler-Bernoulli beam with equivalent, constant curvature would have a potential given by $\frac{1}{2}EIL_b\kappa^2$, by evaluation of Eq. 3.5. The potential of the discrete model is non-dimensionalised by dividing by the equivalent Euler-Bernoulli potential. Results of this calculation are shown for increasing n in Fig. 3.2, showing that the non-dimensional potential approaches 1 for large n, as expected. For the subsequent numerical simulations, a value of $n = 31$ is chosen as a compromise between computational effort and a modest error of 3.2% of the Euler-Bernoulli beam potential. The value $n = 31$ is chosen over an even number to ensure that a beam element lies at the mid-point of the beam.

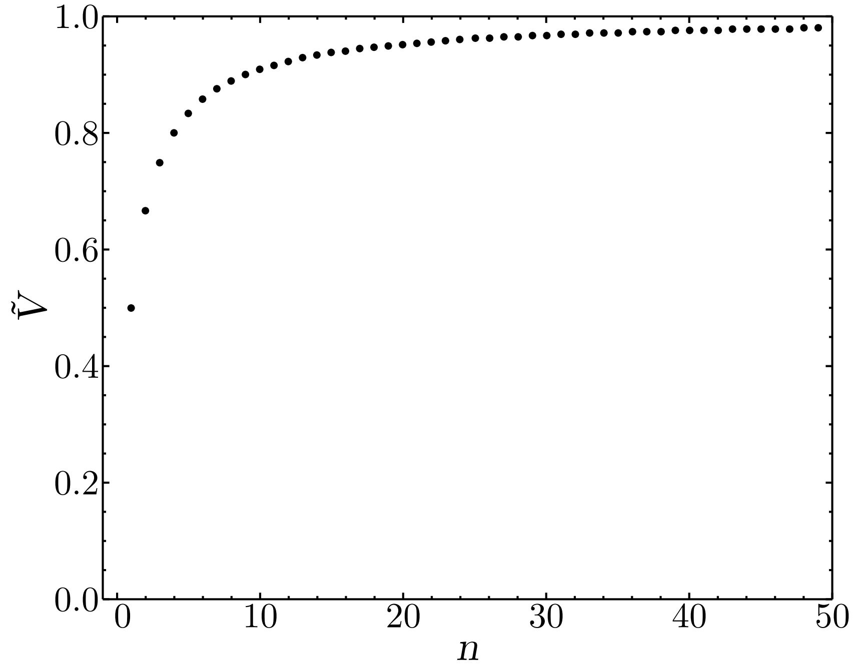

Figure 3.2: Non-dimensional potential, $\tilde{V}$, against number of beam elements, n.

3.1.1.2 Dynamics of Flexible Beams with Distributed Magnetorquers

The equations of motion for a long, slender beam with distributed magnetorquers are now numerically integrated to compare the potential advantages of distributed torques against a large torque applied at the centre. Physical data for the beams is taken from Table. 3.1, which contains a selection of three deployable booms developed for use in large space structures, and which cover a range of bending stiffnesses and linear mass densities. For all examples, the beam length is set to $L_b = 100$ m, which is then discretised into $n = 31$ elements.

A total torque of 1 N m is applied to each beam, with the full 1 N m applied to the central element for the centralised case, and 1/15 N m applied to the 15 torqued elements in the distributed case. The actual torque achievable by real magnetorquers depends on the orbital altitude, external field direction and of course the specific magnetorquer design. The relatively large torque value used here is chosen to avoid extremely long simulation times, while both an overall rotation of the beam and flexible dynamics are observed. The value of the torque does not significantly affect the results of this analysis, as the purpose of these simulations is to compare the difference between centralised and distributed torques and so the same total torque is applied in each case. Realistic magnetorquer sizing is considered in later analysis.

For each beam, two cases are examined. In the first case, the mass of the torquing actuators is assumed negligible compared to the beam mass. This represents the ideal case, showing the greatest possible benefit of distributing actuators to be investigated. In the second case, the total mass of the torquing elements is taken to be comparable to that of the beam itself. In this case, when actuators are distributed across the beam the overall inertia is increased, which may reduce manoeuvrability and offset the potential benefits of distributed torques. Additionally, the mass distribution of the beam is then not constant across it's length, which will affect the flexible response of the system.

The potential, V, defined in Eq. 3.3, is now used to compare the centralised and distributed torque cases, as it provides a scalar measure of the total deflection of the beam at each point in time. For each beam given in Table 3.1, simulations are performed over a time range of 500 s for both distributed and centralised magnetorquers. For the first quarter of the simulation, a positive torque is applied to each torqued element, for the next quarter a negative torque is applied, and the torque is then set to 0. This simulation represents a simple slew manoeuvre with on/off control of the magnetorquers, allowing comparison of beam deflection during, and after, a manoeuvre. The deflection ratio V_c/V_d is then calculated by finding the maximum of the potential during each simulation, with V_c the maximum potential observed in the centralised case and V_d the maximum for the distributed torques. The results of the simulations are shown in Table 3.1. These results show that for all beams, distributing the magnetorquers results in a significant reduction in beam deflection. The results also show that when the distributed mass of the magnetorquers is included in the analysis, this reduction of beam deflection is only slightly lower than when they are considered to have neglible mass, as for each beam the effect of distribution still gives approximately an order of magnitude reduction in beam deflection. The effect is illustrated in Fig. 3.3, which shows the shape of the deflected beam at the point of maximum deflection (of Beam 3 in Table 3.1) for both centralised (a) and distributed (b) magnetorquers. When a large centralised torque is applied, we see there are points of high curvature in the beam shape near to the torquing element, while for the distributed beam the overall deflection is much lower and also the curvature is more constant across the beam. This would be desirable behaviour for a lightweight truss or beam as it would prevent concentrated

	Beam	Bending Stiffness EI, N m^2	Mass Density kg/m	Deflection Ratio V_c/V_d: *Negligible Torquer Mass*	Deflection Ratio V_c/V_d: *Comparable Torquer Mass*	Reference
1	*L'Garde* SSP Rigidizable Truss	15.4×10^5	0.7	15.10	9.217	Guidanean (2006)[150] (EI calculated by Ref. [151])
2	*ATK Space Systems*, Coilable Boom	0.8×10^5	0.07	11.96	8.925	Murphy (2005) [152] (EI calculated by Ref. [151])
3	*DLR*, Deployable CFRP boom	0.0521×10^5	0.1	17.45	15.34	Herbeck (2001) [153]

Table 3.1: Beam data and results of simulation.

stresses and possible buckling at points with large curvature.

Figure 3.4 shows the plot of the potential for Beam 2, for the centralised (Fig. 3.4a) and distributed (Fig. 3.4b) torque cases. The figure shows that distributing the magnetorquers leads to an order of magnitude reduction in the deflection, and also shows that the frequency of beam vibrations, seen as oscillations in the potential, are significantly reduced by distributing the magnetorquers. The natural frequencies for both mass distributions are found by linearising Eqs. 3.3 around equilibrium. For the beam with a central mass, the fundamental frequency is 0.05 Hz, while for the beam with distributed magnetorquers, it is 0.023 Hz. While these

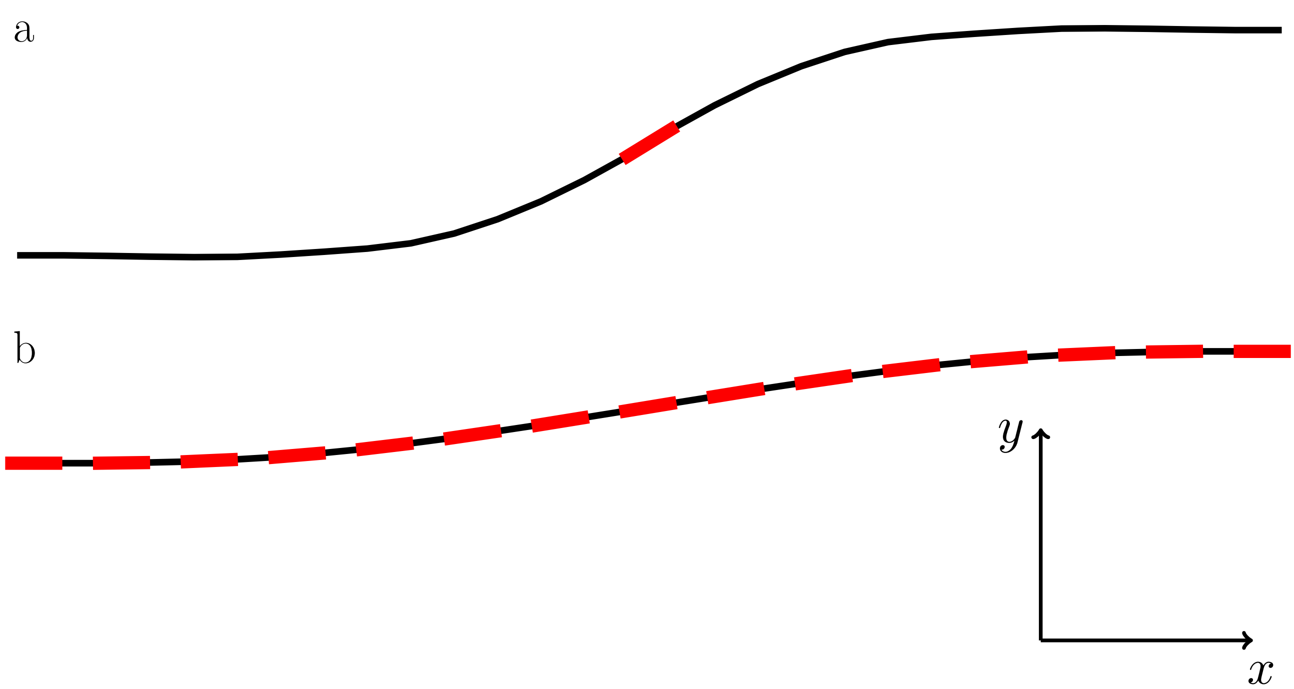

Figure 3.3: Exaggerated shape of the 100 m beam at the point of maximum deflection for a central torque (a) and distributed torques (b). Y-axis is scaled by a factor of 50 for illustration.

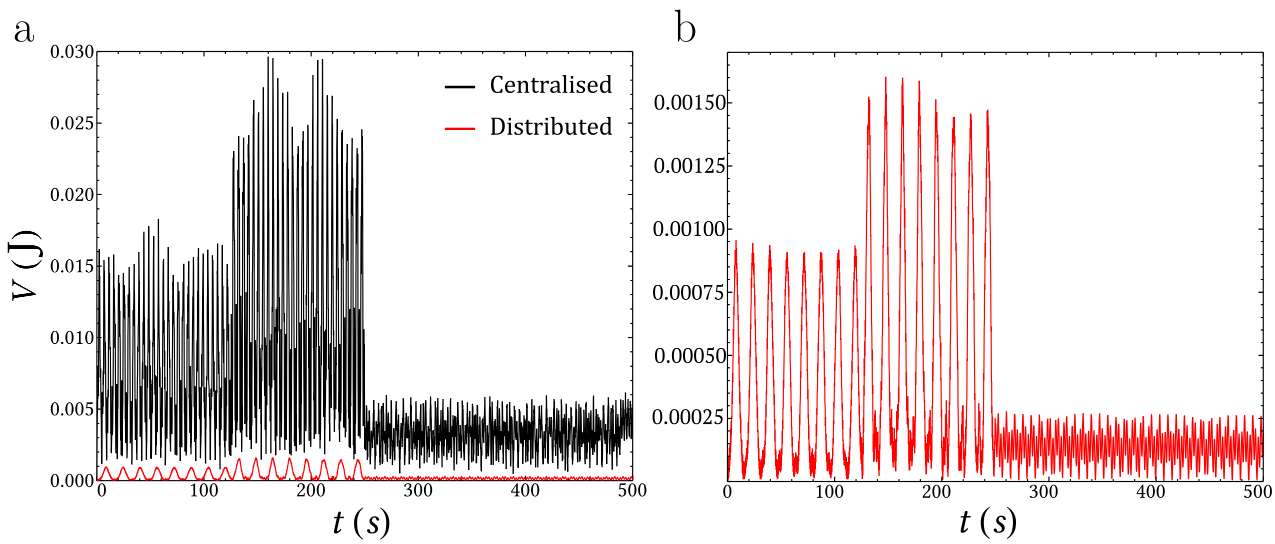

Figure 3.4: Potential against time for beam 3, comparing centralised and distributed torquing on the y-axis (a), and with the y-axis scaled to show distributed torquing only (b).

differences in natural frequencies are evident from Fig. 3.4, it is also clear from the figure that in the centralised case higher frequency vibration modes are being excited. This is most evident in the last half of the simulation, when the magnetorquers are switched off and only residual vibrations remain. In Fig. 3.4b, regular oscillations are observed in the potential, suggesting the beam is vibrating at some superposition of the lower frequency modes. In Fig. 3.4a however, the oscillations are much less regular, suggesting the manoeuvre has excited a number of higher frequency modes, which are not modelled as well by the nonlinear equations of the model studied here.

While it may also be desirable to reduce the natural frequencies by distributing magnetorquers, it is important to note that this effect is due to the redistribution of mass rather than the distributed torques, and thus comes with an associated increase in inertia which may not be desirable. However, the excitation of the normal modes is shown to be reduced by distributed torques, and is apparent when the magnetorquer mass is considered. The motivation for distributing magnetorquers is to reduce deflection of a spacecraft support structure, and distributing actuators across the beam length has proved to successfully achieve this goal. Due to the increase in moment of inertia caused by distributing the magnetorquers, the usefulness of the proposed concept for specific applications would require a trade-off between pointing rate requirements, and the required flatness or buckling moments of a gossamer spacecraft. Applications such as solar power arrays or reflectors may meet the criteria for distribution of magnetorquers to be worth the increased inertia, as it may be more important for this type of spacecraft to remain flat during operation than to be particularly agile.

3.1.2 Motivation for Distributed Torques: 3D Spring-Mass Model

Having demonstrated that distributed torquing results in reduced deformation for a 2D beam, a 3D model of a flexible planar structure is now presented and used to further investigate torque distribution. The structure is modelled as a cubic lattice of nodes, connected by struts to give an octahedral-tetrahedral truss configuration, illustrated in Fig 3.5. This configuration is a common type of truss-structure used architecturally for wide-spanning roofs, due to its rigidity and high strength-to-weight ratio [154]. The mass of the structure is taken to be concentrated at these nodes, and the struts are approximated as linear, damped springs. The mechanical model is illustrated in Fig. 3.6. The spring force between connected particles is given by:

$$\boldsymbol{F}_s = k(r - l_0)\frac{\boldsymbol{r}}{r} + \gamma\left(\dot{\boldsymbol{r}} \cdot \frac{\boldsymbol{r}}{r}\right)\frac{\boldsymbol{r}}{r} \tag{3.11}$$

where k, γ and l_0 are the spring constant, damping coefficient, and natural length of the strut between the particles, and $\boldsymbol{r}$ and $\dot{\boldsymbol{r}}$ the relative position and velocity of neighbouring particles. The particle position vectors and force directions are illustrated in Fig. 3.7. The total force on particle i due to the spring and dashpot is then found by summation over all connected

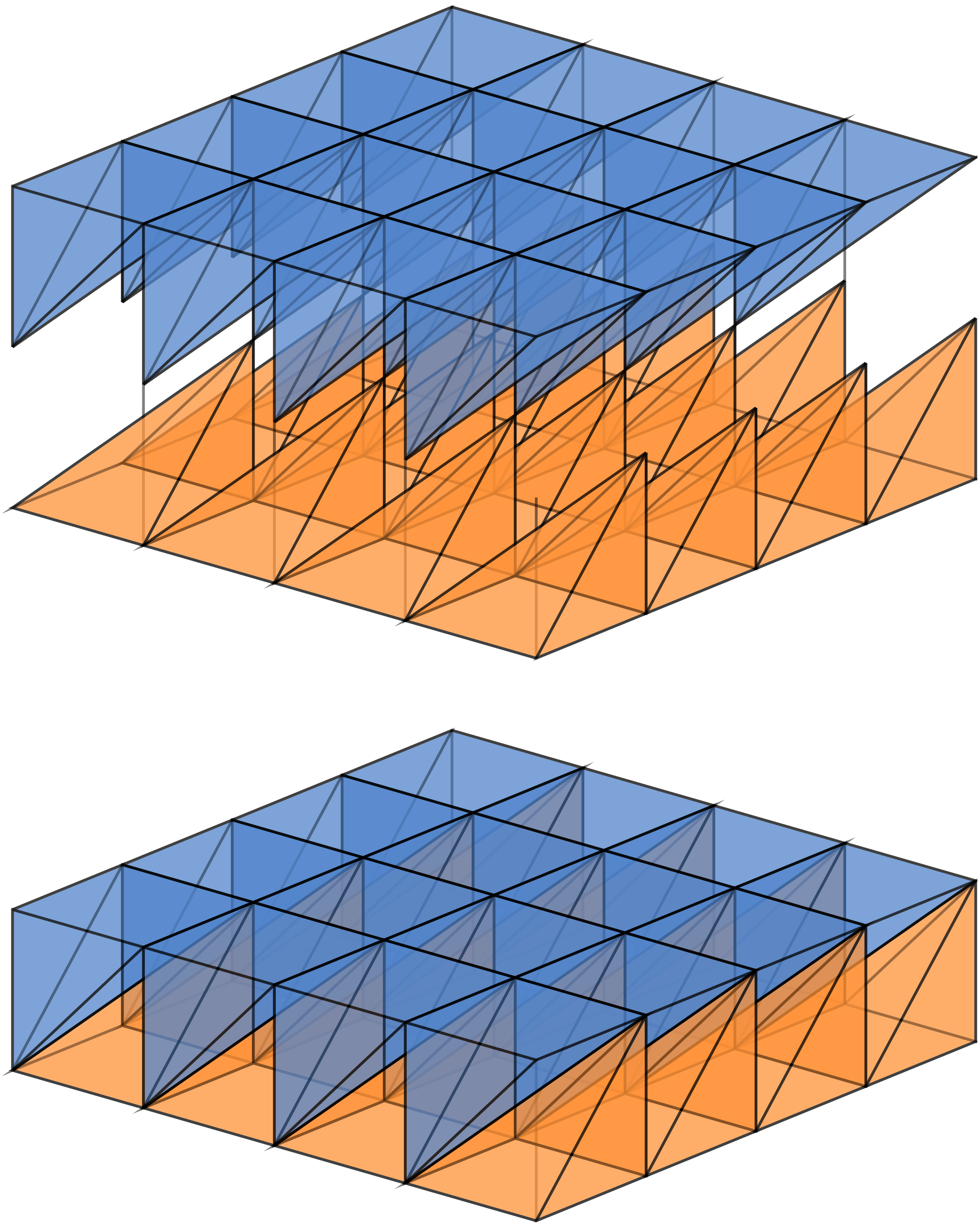

Figure 3.5: The octahedral-tetrahedral truss structure, the half octahedrons are highlighted in blue and orange with tetrahedrons filling the space in between.

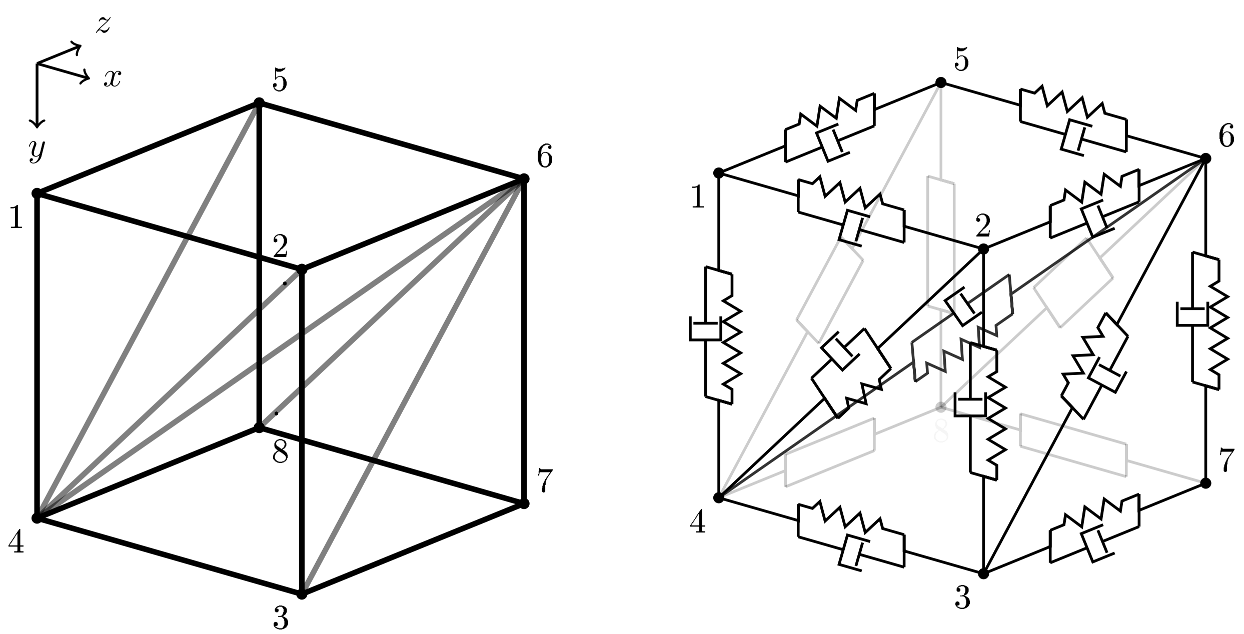

Figure 3.6: A cubic unit of the truss structure, showing the spring and dashpot connections between point masses at the numbered nodes.

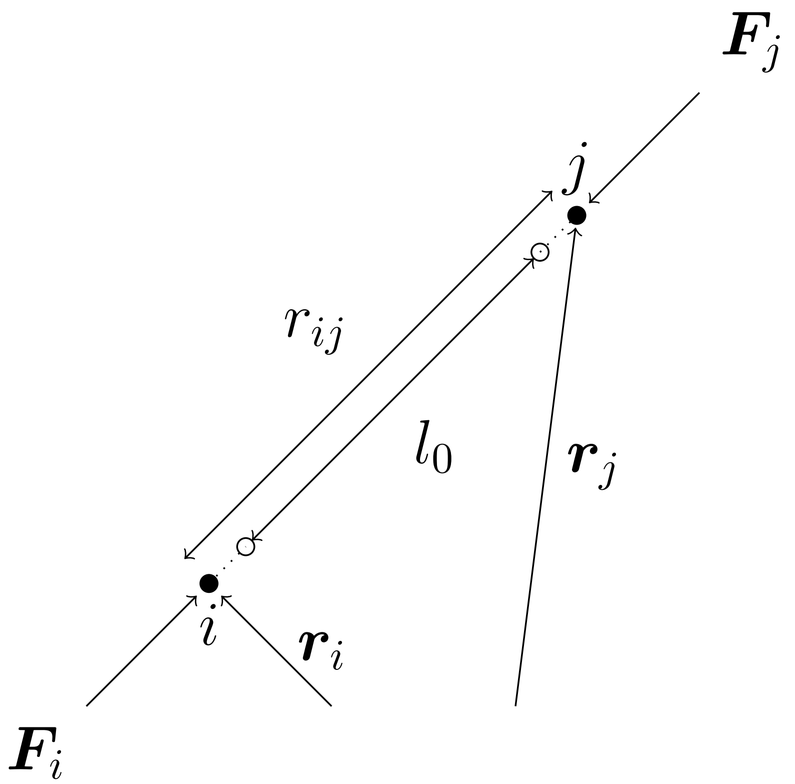

Figure 3.7: The spring force directions for two displaced particles i and j.

particles:

$$\boldsymbol{F}_i^{\text{spring}} = \sum_{j \in C} \left[k(r_{ij} - l_0)\frac{\boldsymbol{r}_{ij}}{r_{ij}} + \gamma \left(\dot{\boldsymbol{r}}_{ij} \cdot \frac{\boldsymbol{r}_{ij}}{r_{ij}} \right) \frac{\boldsymbol{r}_{ij}}{r_{ij}} \right] \tag{3.12}$$

where the relative position of the particles is denoted by $\boldsymbol{r}_{ij} = \boldsymbol{r}_j - \boldsymbol{r}_i$, and C is the set of connected particles.

Actuator torques are included in the model by the appropriate application of forces to the individual particles. This chapter is concerned with magnetorquers, which as discussed in the technical introduction produce a torque given by:

$$\boldsymbol{\tau} = \boldsymbol{m_d} \times \boldsymbol{B} \tag{3.13}$$

In the spring mass model, the mass is concentrated at the structure nodes as point masses, and so a torque cannot be applied to the nodes directly. To include these actuators, magnetorquers are placed between connected nodes, i.e. the magnetorquers are taken to be embedded within the connecting struts. If there is a magnetorquer rod embedded within the strut connecting particles i and j, its dipole moment is aligned with the strut and given by $\boldsymbol{m}_d = m_d\hat{\boldsymbol{r}}_{ij}$. The torque within the connecting element is experienced by the particles as a transverse force, given by:

$$\boldsymbol{F}_i^{\text{mag}} = -\boldsymbol{F}_j^{\text{mag}} = \frac{1}{r_{ji}} \left(m_d\boldsymbol{B} - \left(\frac{1}{2} m_d \boldsymbol{B} \cdot \hat{\boldsymbol{r}}_{ji} \right) \hat{\boldsymbol{r}}_{ji} \right) \tag{3.14}$$

This expression gives forces which are perpendicular to the connecting strut, and result in a torque around the centre of the strut which satisfies Eq. 3.13, i.e. $\frac{1}{2}\boldsymbol{r}_{ji} \times \boldsymbol{F}_i^{\text{mag}} + \frac{1}{2}\boldsymbol{r}_{ij} \times \boldsymbol{F}_j^{\text{mag}} = \boldsymbol{m}_d \times \boldsymbol{B}$.

The final force included in the model is gravity. The gravitational force on particle i is:

$$\boldsymbol{F}_i^{\text{grav}} = -\frac{\mu m_p}{R_i^2}\hat{\boldsymbol{R}}_i \tag{3.15}$$

where μ is the standard gravitational parameter of the primary body, m_p the particle mass, and $\boldsymbol{R}_i$ the absolute position vector expressed in a frame with origin at the centre of the primary body. The total force on particle i is given by summation of Eqs. 3.12, 3.14 and 3.15:

$$\boldsymbol{F}_i = \boldsymbol{F}_i^{\text{spring}} + \boldsymbol{F}_i^{\text{mag}} + \boldsymbol{F}_i^{\text{grav}} \tag{3.16}$$

Equation 3.16 is evaluated for all particles in the model, and the dynamics simulated by numerically integrating the position and velocity of all particles simultaneously. In the simulations, Runge-Kutta 4th order integration is used.

3.1.2.1 Comparison of Distributed and Centralised Torques

The spring-mass model is now used to compare distributed and centralised torques by constructing a model of a planar structure with an embedded distributed array of torquing actuators, and one in which all torques are applied at the centre of the structure only. The two cases are illustrated in Fig. 3.8, which shows 40×40 m structures with actuators embedded in the blue and red highlighted elements. Figure 3.8a, shows actuators embedded within the struts between all nodes on the top layer of the structure, giving torques aligned with the x_1 and y_1 body axes. Figure 3.8b shows the same structure with actuators placed at the central cube unit only. Two highlighted elements are shown for each direction in the central case to maintain symmetry around the centre-of-mass. A 40×40 m structure is shown here to clearly illustrate the actuator location and directions, but in the following simulations a 100×100 m structure is also considered.

In this section, general torquing actuators are considered, rather than magnetorquers specifically, because the torque produced by a magnetorquer depends on its orientation relative to the magnetic field, according to Eq. 3.13. Furthermore, the magnetic field direction will be constantly changing while on-orbit. In this section, the aim is to investigate torque distribution across a flexible structure, and so assuming a constant torque for now allows direct comparison to be made between the distributed and centralised cases. The simulations are performed by integrating the particle positions, with the forces given by Eq. 3.16, and a Runge-Kutta 4th order integration method.

A number of simulations are performed to compare distributed and centralised torques. Three structures are considered, with the spring constants adjusted to represent a range of structural flexibility. For each structure a simulation is performed with a single large torque applied to the centre of the structure, as illustrated in Fig. 3.8b, and then that same total torque is distributed across the grid of elements, as shown in Fig. 3.8a. The specific geometry used in the simulations is that of a 100 m side-length square structure, made up of a 19×19 grid of the unit cubes illustrated in Fig. 3.6, resulting in a side length for each cube of 5.26 m. The grid dimension of 19 is an odd number to ensure that a single cube lies at the centre of the structure, and so the centre-of-mass of the stucture lies in the centre of a unit cube rather than at a node. This means that, for centralised torquing, a torque can be applied to a single unit cube with the resulting torque symmetrical around the centre-of-mass of the structure, as illustrated in 3.8b. The torque applied is around the body frame x_1-axis. The $x_1y_1z_1$ body frame is initially aligned with the inertial xyz frame, shown in Fig. 3.8. Although the structure is actually a collection of particles, a body frame is defined by least-squares fitting a rotation between the initial particle positions and the displaced positions. The least-squares problem to minimise is:

$$\min_{\mathcal{R},\boldsymbol{d}_t} \sum_{i=1}^{n} ||\mathcal{R}\boldsymbol{p}_i + \boldsymbol{d}_t - \boldsymbol{q}_i|| \tag{3.17}$$

where $\boldsymbol{p}_i$ and $\boldsymbol{q}_i$ are the initial and final set of points in the structure respectively, and $\mathcal{R}$ and $\boldsymbol{d}_t$ the rotation matrix and translation vector describing the mapping from $\boldsymbol{q}_i$ to $\boldsymbol{p}_i$. This problem can be solved using singular value decomposition, as described in Ref. [155]. The angular velocity body-rates of this rotating frame are then estimated using a backward difference

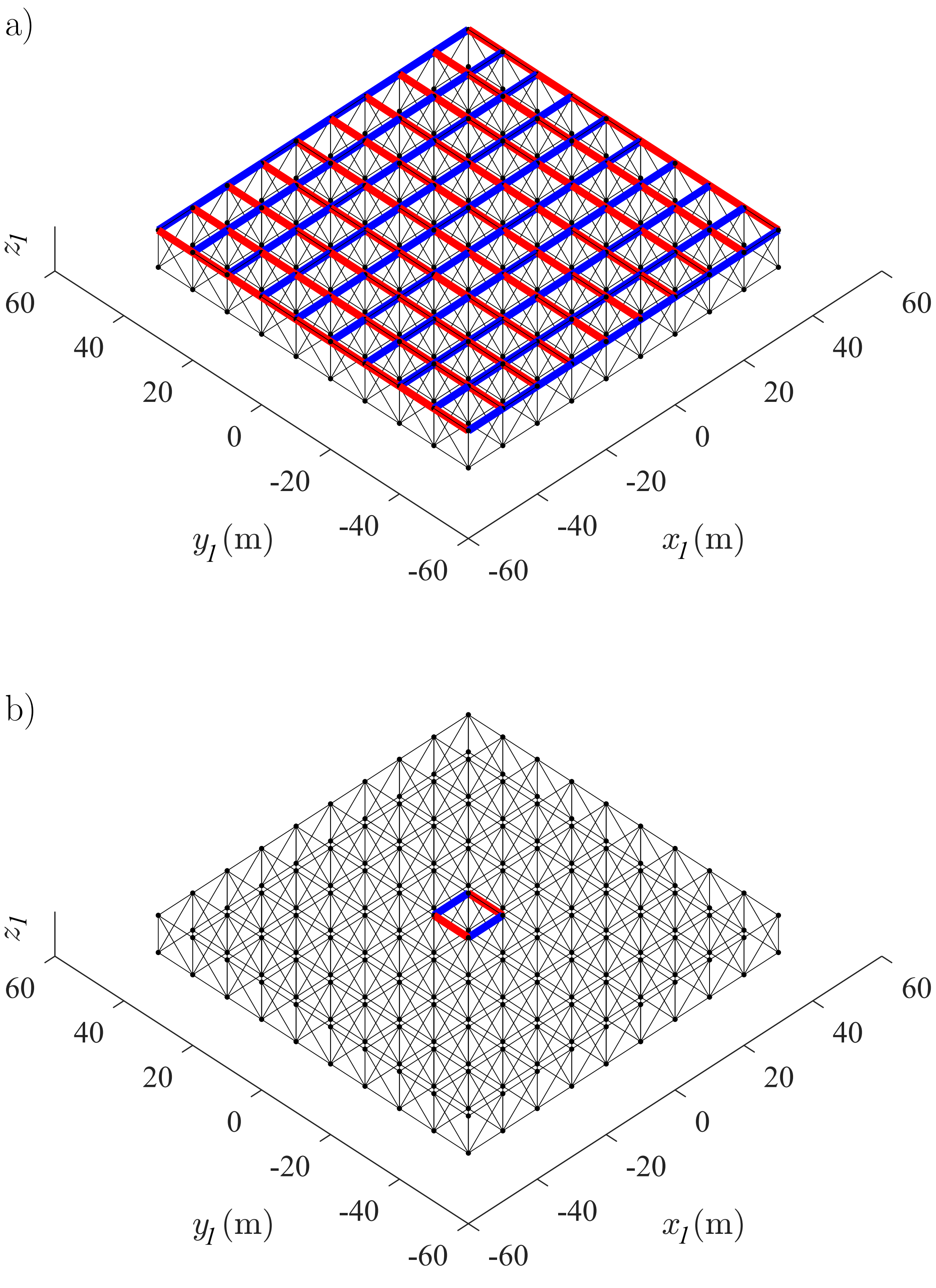

Figure 3.8: Example of the spring-mass model of the truss-structure with distributed (a) and centralised (b) torquing actuators. The x_1 and y_1 body axis actuators are highlighted in red and blue respectively.

formula, applied to the current best-fitting rotation matrix and that of the previous simulation timestep. Throughout the simulation, the standard ZYX intrinsic Euler angles ψ, θ, ϕ are used to represent the orientation of this body-frame, as described in the technical introduction of Chapter 2.

The structural mass, stiffness and magnitude of the actuator torques are selected by considering large solar sails, which may have areal densities of on the order of 10 g/m^2 [156]. This value is adopted for all three simulations, such that only the structural flexibility varies between the cases. For a 100×100 m structure, this results in a total mass of 100 kg. Commercial magnetorquers are available with a dipole moment to mass ratio of 100 A m^2/kg [157], and it is assumed that the maximum dipole moment of a magnetorquer scales linearly with its mass. If one third of the structural mass is allocated for magnetorquers, the maximum dipole moment is then taken to be 3333 A m^2. If the external magnetic field has a magnitude of 30 μT, such as may be found in low Earth orbit (LEO), the maximum achievable torque is found by applying Eq. 3.13, resulting in a representative torque of 0.1 N m.

The model spring constant is determined by selecting a value for the overall bending stiffness of the structure. The bending stiffness of a four longeron truss with diagonal battens on each face is given by:

$$EI = 2EAR_c^2 \tag{3.18}$$

where E is the Young's modulus, A is the longeron cross sectional area and R_c is the radius of a circle enclosing the truss cross-section [152]. The structure considered here is comprised of 10 such trusses arranged in parallel, and so the total bending stiffness of the structure is found by multiplying Eq. 3.18 by 10, where any contribution of the connecting elements between layers is assumed to be negligible. The spring constants are related to EA by the formula

Side length	100 m
Structural units	20
Maximum torque, $\tau_{\max}$	0.1 N m
Simulation runtime, t_{end}	30 minutes
Simulation timestep, δt	0.1s
Areal Density, σ	10 g/m^2
Total mass	100 kg
Particle mass, m_p	0.1250 kg (distributed) 0.0833 kg (centralised)
Bending stiffness, EI	
Case A:	10^3 N m^2
Case B:	10^2 N m^2
Case C:	10^1 N m^2
Torque Applied	$\tau_{\max}$ if $t \leq \frac{1}{3}t_{\text{end}}$ $-\tau_{\max}$ if $\frac{1}{3}t_{\text{end}} < t \leq \frac{2}{3}t_{\text{end}}$ 0 if $t > \frac{2}{3}t_{\text{end}}$

Table 3.2: Parameters used for structural simulations.

$k = EA/l_0$, where l_0 is the natural length of the spring. Equation 3.18 treats the truss as an Euler beam, and so while the bending stiffness may be equivalent, other behaviour may not be well modelled by this approach. However, it is assumed to be a suitable approximation for the generic flexible structure modelled here. This process was verified by performing a cantilever test on the numerical model, where one side of the structure was held fixed and a load applied to the free end. The resulting deflection matched the expected value for a beam or plate with the specified bending stiffness. The most common solar sail design comprises diagonal booms supporting a tensioned membrane. The bending stiffness of these booms varies depending on the sail length-scale, but is generally on the order of 10^3 N m^2. This bending stiffness is taken as the most rigid case to be examined. Cases two orders of magnitude lower are also investigated, to determine whether distributed torquing allows effective attitude control for even more flexible structures. As noted previously, the structural mass and the applied torque are held fixed across the three cases considered to allow direct comparison of the results, but in practice a reduced bending stiffness would also be associated with a reduced structural mass.

Table 3.2 summarises the data which is common to all simulations. Simulations are performed over 30 minutes, denoted t_{end}, which is sufficient time for the structure to perform a significant rotation of at least 0.4 radians. A timestep, δt, of 0.1 s is selected for the Runge-Kutta integration, a value which was found to provide stable solutions with reasonable computation times. The torque profile described in Table 3.2 corresponds to a bang-bang-off signal, with the torque magnitude set to the maximum, τ_{max}, and the direction either positive or negative along the x_1 axis. Table 3.2 shows the three structural cases which are considered. The difference across each case is the spring constant used in the model, which is chosen such that the beam-like bending stiffness of the square structure, for bending around the x_1 or y_1 directions, is equal to 10^3, 10^2 and 10 N m^2 for cases A, B and C respectively. These values correspond to the order of magnitude of bending stiffness of current solar sail designs (Case A), and two orders of magnitude lower. For the distributed torque case, the total mass of 100 kg is distributed between all particles, while for the central torque case one third of this mass, the fraction allocated for the actuators, is concentrated at the centre of the structure only.

If the structures were rigid bodies, the torque profile in Table 3.2 would result in a rest-to-rest manoeuvre. For the flexible structures considered here this excitation signal allows the response of the structure to be investigated when the torque is first applied and when it switches direction. Finally, when the torque is switched off the resulting residual vibrations in the structure can be observed as a measure of how much energy has been absorbed by the flexibility of the structure. For example, if the structure is found to have large amplitude residual vibrations it suggests that a significant portion of the control effort has been absorbed by the flexing structure as strain energy rather than working to rotate the structure. The surface standard deviation (SD), σ, is used as a measure of flatness in the following results, and is found by taking the average plane formed by the top layer of points in the structure, and then calculating the standard deviation of the normal distance of each particle to this plane.

This measure of the surface flatness is of interest because if this parameter remains low then the structure is relatively un-deformed and is not likely to fail due to buckling. It is also important to consider this measure of surface flatness since many applications for space structures of this scale, such as reflectors, antennas, or solar power arrays would require a high degree of flatness during operation.

3.1.2.2 Results of Simulation

Results of the simulations for Cases A, B and C with central and distributed torquing are shown in Figs. 3.9, 3.10 and 3.11 respectively. In all cases, distributed torquing results in a rigid-body like rotation of the structure. With central torquing however, a rigid-body like response is seen for Case A, but for more flexible structures much smaller rotations occur and the behaviour is less uniform, with rotations seen around axes other than the x_1 body axis. For Cases A and B, distributed torquing leads to an order of magnitude reduction in the surface SD, showing that distributed actuation has had the desired effect of reducing the surface deformation considerably.

For Case C the magnitude of the surface SD throughout simulation is comparable for both distributed and central torquing. Figure 3.12 shows the shape of the structure plotted at 500 s intervals. This shows that although the surface is deformed a comparable amount, with distributed torquing the deformation is much more uniform, creating a wave-like shape along the x_1 body axis. With central torquing the structure has points of high local deformation, particularly at the centre-of-mass where the torque is applied, and would therefore be more

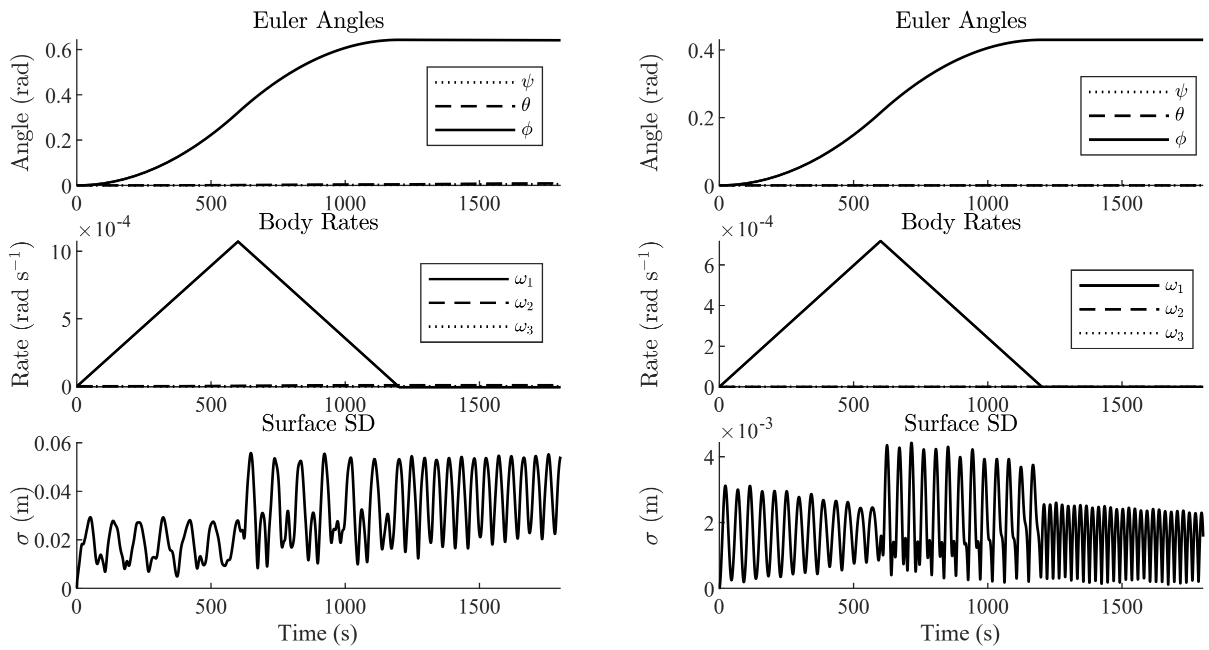

(a) Centralised torques. **(b)** Distributed torques.

Figure 3.9: Results of simulation for Case A

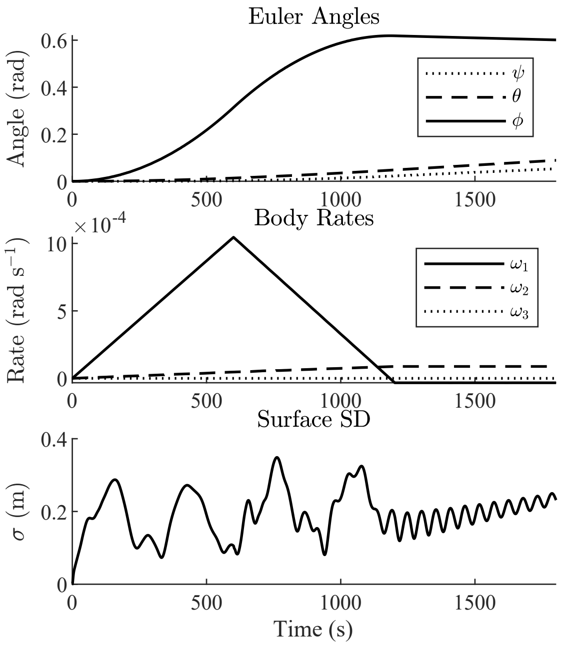

(a) Centralised torques.

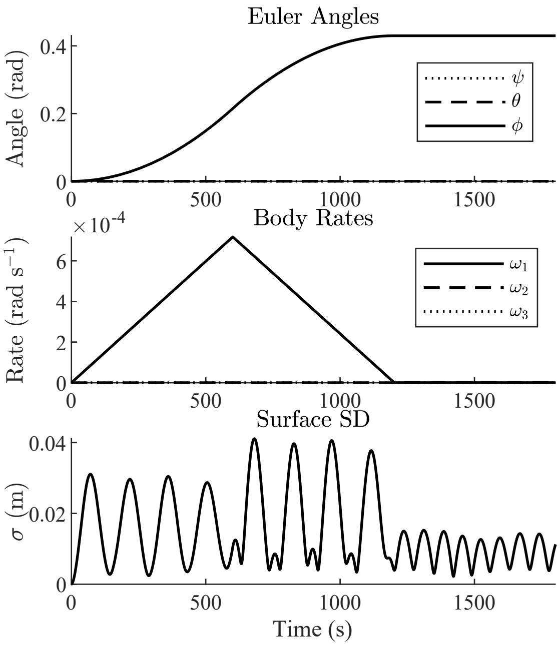

(b) Distributed torques.

Figure 3.10: Results of simulation for Case B

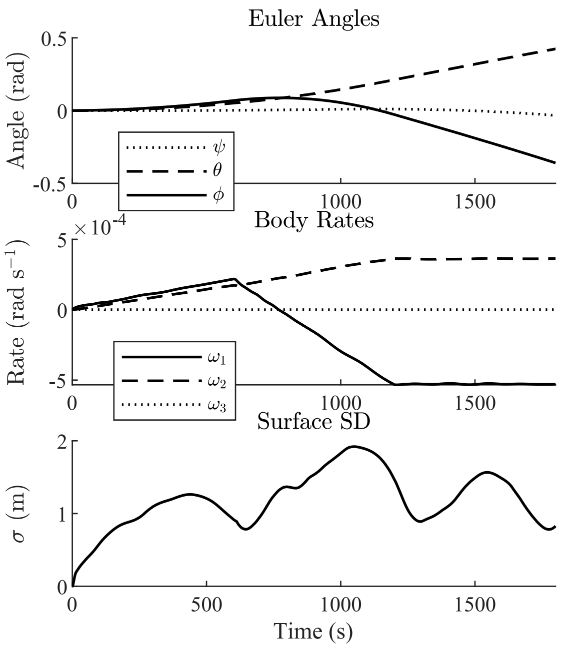

(a) Centralised torques.

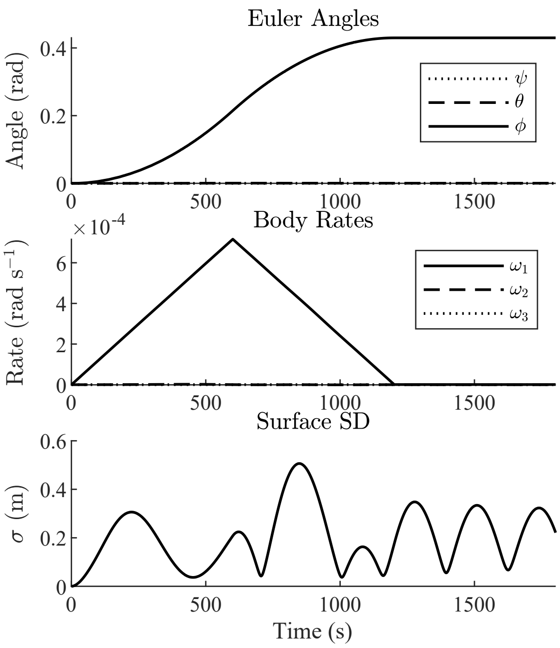

(b) Distributed torques.

Figure 3.11: Results of simulation for Case C.

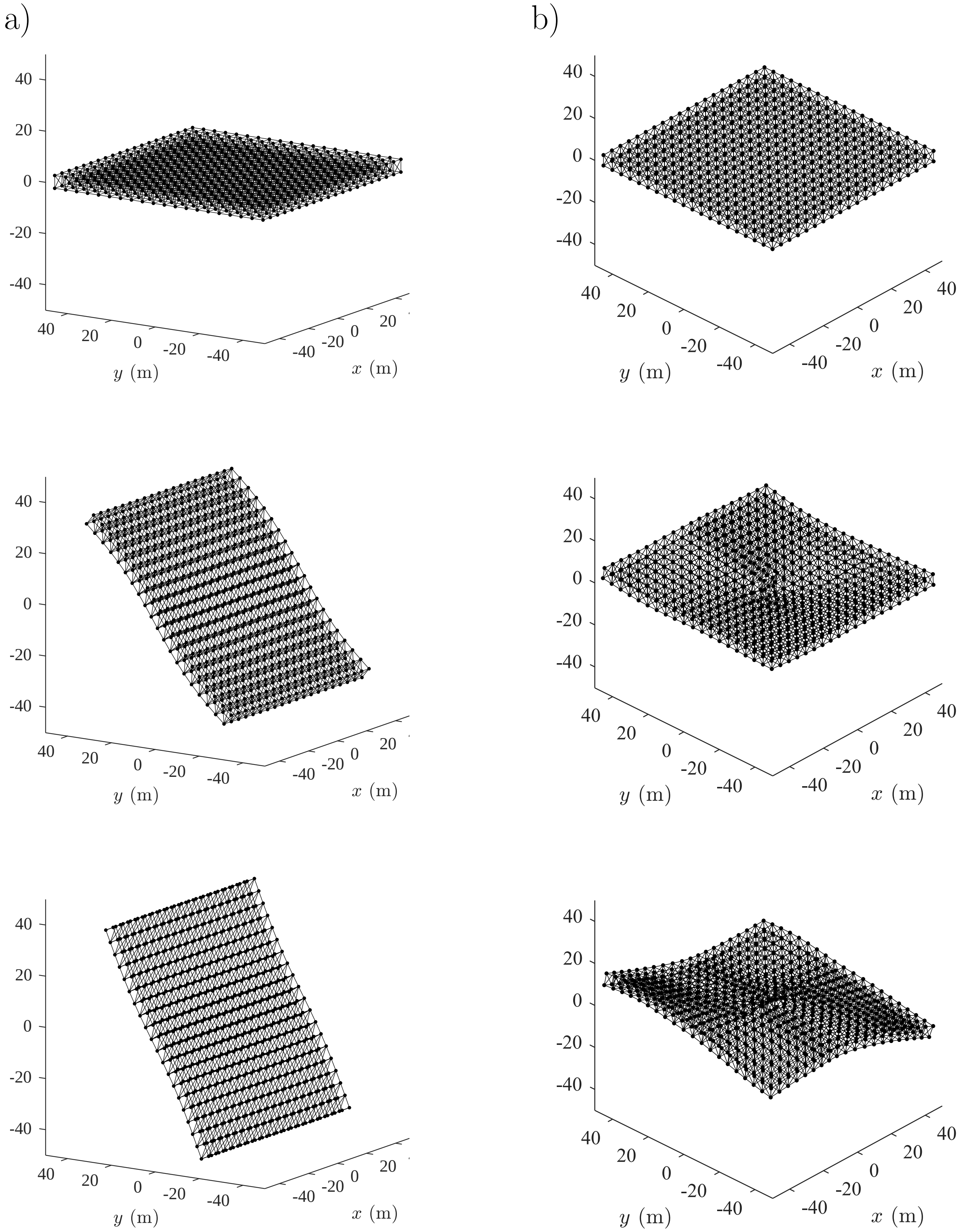

Figure 3.12: Structure shown in the inertial frame at 500 s intervals for Case C, after application of distributed (a) and central (b) torques.

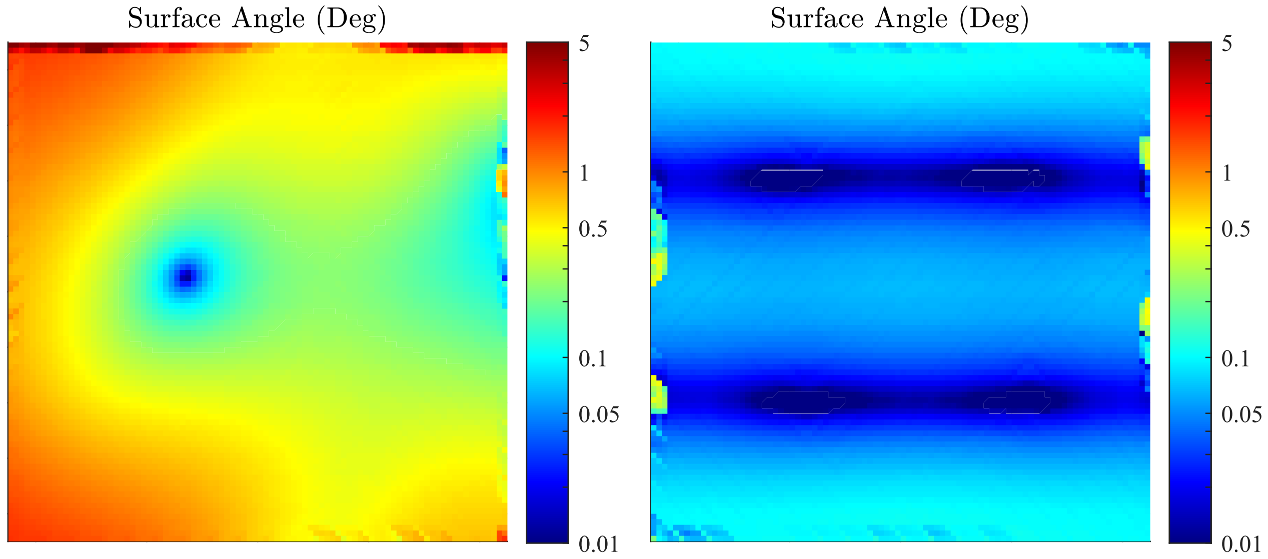

(a) Centralised torques.

(b) Distributed Torques.

Figure 3.13: Local surface angle at the point of maximum surface SD for Case A.

likely to fail due to buckling. Additionally, centralised torquing is unable to enact the desired rotation for Case C. This is because as the structure deforms, the orientation of the central points and thus the direction of the torque being applied is significantly altered, resulting in angular displacements around both the x_1 and y_1 body axes. This behaviour is often described as follower forces (e.g. [158]), as the applied forces "follow" the geometry of the structure as it deforms.

For distributed torquing, in the final third of the simulation the surface SD oscillates steadily with a small amplitude, which suggests that little energy has been absorbed as strain energy during torquing. With central torquing, the surface SD is found to continue rising at this point. This is because the structure settles into a more uniform shape after the torque is switched off, which is a lower energy configuration despite having higher surface SD. Therefore the surface SD is not a direct measure of the potential energy in the spring-mass system because areas of high local deformation, such as the where the central torque is applied, can contribute significantly to the potential energy but not result in a large surface SD.

The "surface flatness" can also be measured by considering the angle the surface makes to the average plane at each point, which would be important if the surface were to be used as a reflector or solar sail as this would alter the local angle of incidence for incoming solar radiation. The local surface angle across the structure is determined by first fitting a continuous surface to the particle positions using a cubic interpolation, taking the gradient of this surface, and finally taking the inverse tangent to determine the angle between a plane tangent to the surface and the x_1y_1 plane, at each point of the interpolated surface. For the most rigid structure, Case A, there was little difference between rotations performed by central and distributed torquing, but there was a large difference in the surface SD for both cases. Further insight into this difference is gained by considering the local surface angle at the point of maximum surface SD, shown in Fig. 3.13. The figure shows that the order of magnitude reduction in surface SD achieved by distributed torquing corresponds to an order of magnitude reduction in the typical local surface angle as well. The figure also demonstrates that, for distributed torquing, the deformation is uniform along the x_1 axis, and the structure has settled into a wave-like shape, similar to Fig. 3.12a) but with a much smaller amplitude. For central torquing (a), the deformation is much less uniform, and the structure's edges make an angle of over 5° to the average plane. Of note is that the triangular artefacts visible in Fig. 3.13 are simply the effect of fitting a surface to the square units of the structure, and the large values at the structure's edges are a result of overfitting between the node positions. It is thought that the asymmetry in Fig. 3.13 is a result of compounding errors in the numerical integration, and the nonlinearity of the system dynamics and follower forces discussed previously.

3.1.2.3 Torque-Shaping

Another approach adopted for the control of large, flexible structures is torque-shaping. Simulations are now performed to investigate the response of the structure after applying a smooth torque profile, rather than the discontinuous on-off control profile considered previously. The aim of these simulations is to determine whether a smooth torque profile improves the performance of central torquing and could be an alternative to distributed actuation. Simulations of Cases A, B and C are repeated, but now with torque-shaping implemented to smooth the excitation signal in an attempt to reduce the magnitude of the flexible response and improve performance. Torque-shaping is well-studied for the control of spacecraft with flexible appendages, and is known to reduce the impact of the flexible response of the structure on control

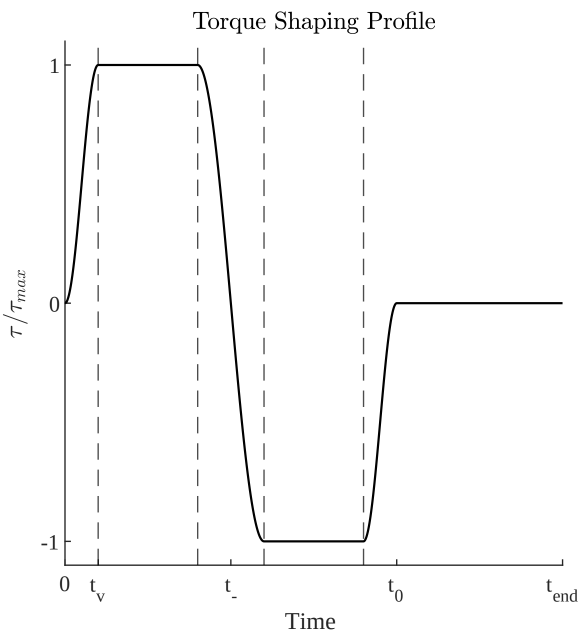

Figure 3.14: Versine-smoothed torque profile

efficacy [159]. One torque-shaping strategy is to use the versine function (versine(θ)=1-cos(θ)) to remove discontinuities in the excitation signal and provide a smooth function, which has been shown to reduce jerk in attitude manoeuvres of a flexible spacecraft [160]. Simulations are repeated with the same parameters, but with a torque profile now given by:

$$
\begin{aligned}
\tau(t) &= \frac{1}{2}\left[1-\cos\left(\pi\frac{t}{t_v}\right)\right]\tau_{\max} && \text{if} \quad t \leq t_v \\
\tau(t) &= \tau_{\max} && \text{if} \quad t_v < t \leq t_- - t_v \\
\tau(t) &= \cos\left(\frac{\pi}{2}\cdot\frac{t_- - t_v - t}{t}\right)\tau_{\max} && \text{if} \quad t_- - t_v < t \leq t_- + t_v \\
\tau(t) &= -\tau_{\max} && \text{if} \quad t_- + t_v < t \leq t_0 - t_v \\
\tau(t) &= -\frac{1}{2}\left[1+\cos\left(\pi\frac{t_0 - t_v - t}{t_v}\right)\right]\tau_{\max} && \text{if} \quad t_0 - t_v < t \leq t_0 \\
\tau(t) &= 0 && \text{if} \quad t > t_0
\end{aligned}
\tag{3.19}
$$

where $t_- = \frac{1}{3}t_{\text{end}}$ is the point at which the torque is reversed, $t_0 = \frac{2}{3}t_{\text{end}}$ is the point where the torque is switched off and t_v is the ramp-up time of the versine smoothing function, chosen as $\frac{1}{10}t_{\text{end}}$ here. The torque profile is shown in Fig. 3.14, which is a versine-smoothed version of the previous bang-bang-off excitation signal.

Results of the simulations for Cases A, B and C with central and disributed torquing, and torque shaping implemented, are shown in Figs. 3.15, 3.16 and 3.17 respectively. In

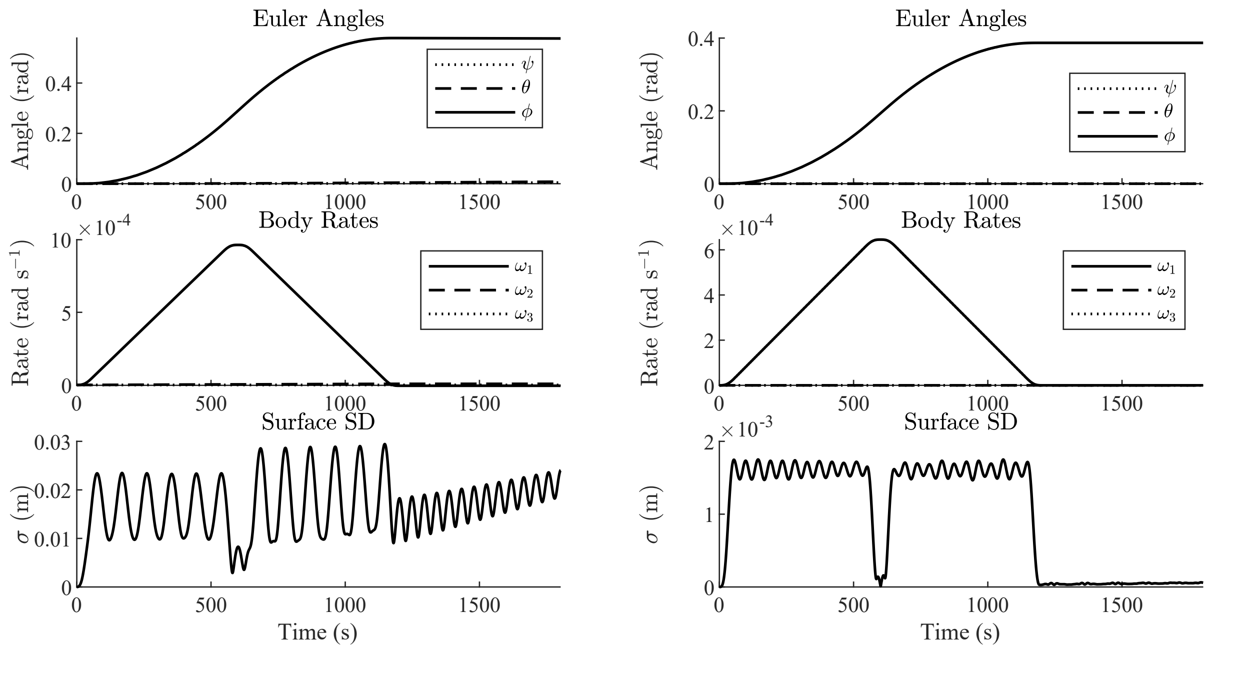

(a) Centralised torques with torque shaping. **(b)** Distributed torques with torque shaping.

Figure 3.15: Results of simulation for Case A with torque shaping implemented.

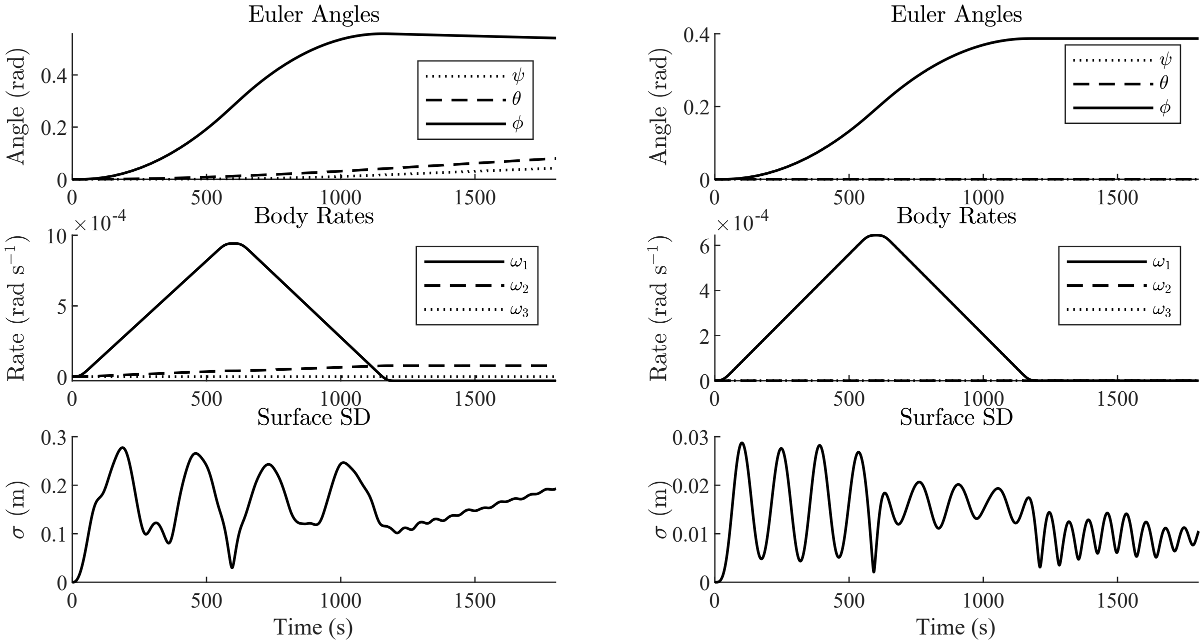

(a) Centralised torques with torque shaping. **(b)** Distributed torques with torque shaping.

Figure 3.16: Results of simulation for Case B with torque shaping implemented.

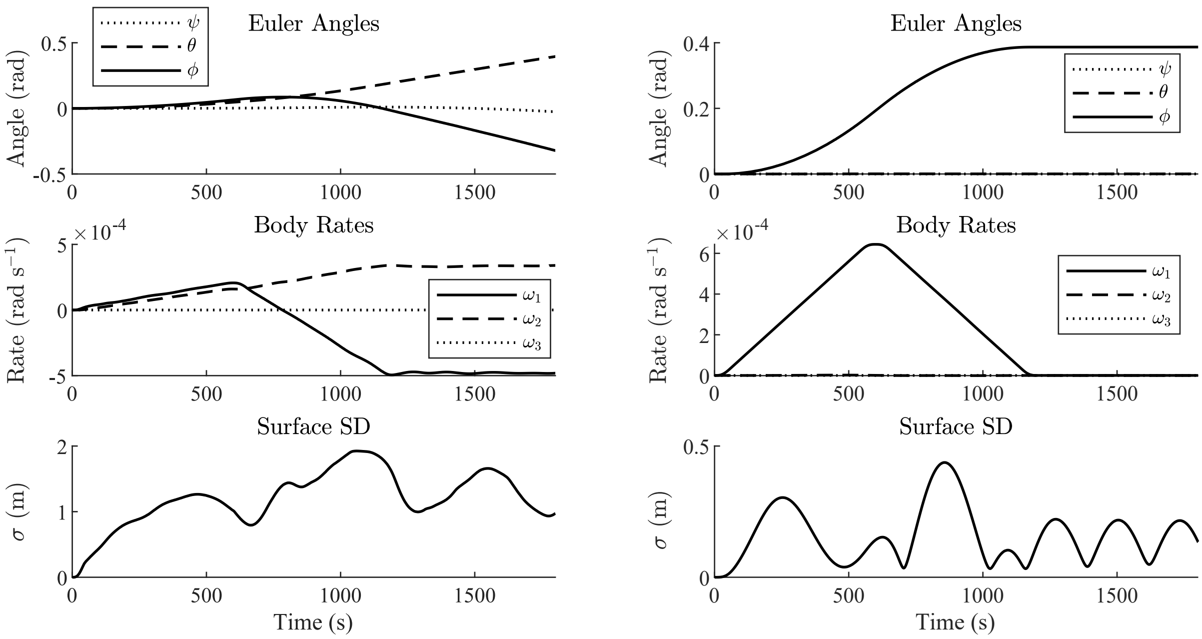

(a) Centralised torques with torque shaping. **(b)** Distributed torques with torque shaping.

Figure 3.17: Results of simulation for Case C with torque shaping implemented.

all cases, the overall rotational motion of the structure is very similar to the on-off control simulations, with the exception of the angular velocity profile which has now been smoothed by the torque shaping, as is to be expected. The main result here is that, even with torque shaping implemented, the centralised torquing cases still exhibit unwanted rotations around axes other than the x_1 direction. This is most evident for Case C, the most flexible structure, which fails to perform a significant rotation at all. Comparing the surface SD in all cases, there is again an order of magnitude reduction in deformation when distributed torquing is used. For Case A, torque shaping is found to greatly reduce the amplitude of oscillations of surface SD, and with distributed torquing the structure appears to deform into an equilibrium position at each stage of the simulation. This suggests that a combination of distributed torquing and torque shaping could be used for the attitude control of relatively rigid structures, where it is desired to reduce oscillations of the surface deformation. The results also show that distributed torquing could be particularly suitable for the attitude control of extremely flexible structures, represented by Case C, as although there is a large surface deformation the structure is successfully rotated around the desired axis. There is again a notable rise in SD in the last third of the simulations total runtime, when central torquing is implemented, seen in Figs. 3.15 and 3.16. As noted for the previous simulations, this arises due to the initially large local deformation settling into a more uniform deformation across the structure, which has a larger surface SD despite being a lower energy configuration of the spring-mass system. The simulation shown in Fig. 3.15 was performed for an extended duration and the SD was seen to continue rising to a maximum value of 0.085 at 7800 s, before returning to zero due to the structural damping.

3.2 Magnetorquer Array Configurations and Rigid Body Dynamics

Simulations have demonstrated that distributed torquing results in reduced structural deformation when compared with centralised torquing strategies, for both a 2D flexible beam model and for a 3D, planar truss-like structure. Two configurations of planar magnetorquer arrays are now presented, and control strategies are developed for each. Then, numerical simulations are presented, where a planar spacecraft is modelled as a rigid body. Rigid body dynamics are used here to quickly analyse the proposed control strategies, as this section is primarily focused on algorithmic concerns and the magnetorquer array geometries rather than structural considerations. In general, the output of a magnetorquer is scaled by using pulse-width modulation (PWM), or bang-bang excitation signals are used. The algorithms developed here present an alternative to applying PWM to the full array of magnetorquers, where magnetorquers are assumed to be either off, or on (with positive or negative polarity). If a torque with a value lower than the maximum torque achievable by the full array is desired, then a fewer number of magnetorquers are activated. This strategy reduces the losses associated with the rapid switching of the magnetorquers required by PWM, losses primarily due to the ripple currents induced in such devices, as discussed in Ref. [161]. Later simulations in Sec. 3.3 again consider flexible structures, using the 3D spring-mass model of the previous section.

3.2.1 Radial Dipole Array

The first magnetorquer array configuration takes the dipole directions to be arranged radially on a square grid or disc. This configuration was chosen due to the fact that many structures may be fabricated with radial booms extending from a central hub [27, 70]. For a conducting coil with magnetic dipole moment $\boldsymbol{m}$, in a magnetic field $\boldsymbol{B}$, the torque produced is given by the cross product (as in Eq. 3.13, repeated here for clarity of discussion):

$$\boldsymbol{T} = \boldsymbol{m} \times \boldsymbol{B} \tag{3.20}$$

The spacecraft is assumed to be a rigid body in this analysis, and so a torque applied at a distance from the centre-of-mass is equivalent to a torque of the same magnitude and direction applied at the centre-of-mass. The spacecraft is modelled as a large, thin square structure, appropriate for the modelling of a large planar reflector for example. The $x_1y_1z_1$ body frame (as defined in Chapter 2) is affixed to the spacecraft, with the x_1 and y_1 axes lying in the square plane of the array, shown in Fig. 3.18. The inertial frame in which the spacecraft is situated is again xyz. Magnetorquers are placed at equally spaced points on the structure. A 3×3 lattice is shown in Fig. 3.18, but the analysis is provided for a general, $n \times n$ array. With a lattice dimension a, the position of the cenral point of a magnetorquer labelled i, j is given by:

$$\boldsymbol{r}_{ij} = a\left(i - \frac{n+1}{2}\right)\hat{\boldsymbol{x}}_1 + a\left(j - \frac{n+1}{2}\right)\hat{\boldsymbol{y}}_1 \tag{3.21}$$

The term $(n+1)/2$ in Eq. 3.21 is included so that the central point of the array lies at the

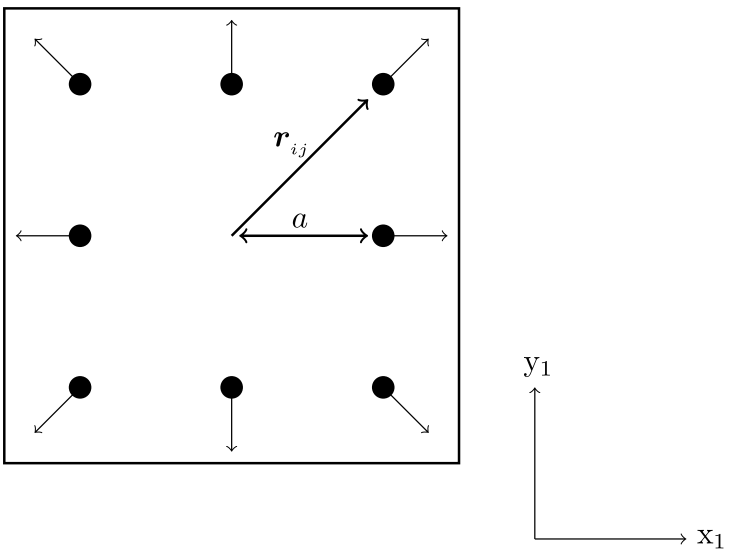

Figure 3.18: Square array of magnetorquers with radial dipole directions

origin, and the values of i and j are positive integers. The magnetic dipole moments of the torquers are taken to lie within the plane. This assumption is used in order to demonstrate 2-axis control with an array of magnetorquers. The magnetic dipole moments are therefore taken to lie in the direction of $\boldsymbol{r}_{ij}$, resulting in the dipole moments being arranged radially around the centre of the structure. This configuration gives an even distribution of dipole moment components in the x_1 and y_1 directions, and so for a large enough array, torques may be generated in any direction in the plane normal to the magnetic field. It is also assumed that each magnetorquer may be individually addressed, and in one of three possible states; on, with current flowing in either direction, or off. The magnetic dipole moment of magnetorquer i, j is then given by:

$$\boldsymbol{m}_{ij} = m\mathcal{C}_{ij}\hat{\boldsymbol{r}}_{ij} \tag{3.22}$$

The scalar magnetic dipole moment value, m, is a constant determined by the magnetorquer geometry and current applied. $\mathcal{C}$ is an $n \times n$ control matrix with each element $\mathcal{C}_{ij} \in \{1, 0, -1\}$ denoting the state of magnetorquer i, j. From Eq. 3.22 it can be seen that $\mathcal{C}_{ij} = 1$ or -1 results in the dipole vector pointing radially outward or inward respectively, while $\mathcal{C}_{ij} = 0$ denotes an inactive magnetorquer. With this model the total torque, $\boldsymbol{T}$, produced by an $n \times n$ array is found by combining Eqs. 3.20-3.22 and performing a double summation over i and j such that:

$$\boldsymbol{T} = ma\sum_{i=1}^{n}\sum_{j=1}^{n}\frac{\mathcal{C}_{ij}}{|\boldsymbol{r}_{ij}|}\left[\left(i - \frac{n+1}{2}\right)\hat{\boldsymbol{x}}_1 + \left(j - \frac{n+1}{2}\right)\hat{\boldsymbol{y}}_1\right] \times \boldsymbol{B} \tag{3.23}$$

As each magnetorquer can be in one of 3 states and there are n^2 magnetorquers, the total number of possible combinations of individual magnetorquer states, and equivalent number of possible control matrices, is 3^{n^2}. If n is odd, there is a magnetorquer which lies at the origin. As there is no radial direction defined for this magnetorquer's dipole moment, it is not included so as to not break the symmetry of the system. The number of possible matrices is then 3^{n^2-1}, ignoring the central point. Although this results in a large number of possible control torques, many configurations result in identical torques due to symmetrical arrangements of torque rods. For example, with $n = 3$, there are 19,683 possible $\mathcal{C}$ matrices, but these can result in as few as 84 unique torques, depending on the orientation of the array relative to the magnetic field.

Figure 3.19 shows an example of the possible torques generated by a 3×3 array when the array plane (blue plane in Fig. 3.19a) lies in the plane normal to the magnetic field direction (the z-direction, which is perpendicular to the yellow plane). Torques are shown as grey lines in Fig. 3.19a. The cross product in Eq. 3.20 results in any torque created also lying in this plane. With the field taken to be in the z-direction, all torques then lie in the xy-plane. Non-dimensional torques are shown in Fig. 3.19b, which are found by dividing by the maximum possible torque which is achieved by activating all magnetorquers, T_{max}. The possible torque vectors are evenly distributed within the unit circle in Fig. 3.19b, so it can be seen that in this orientation the distributed magnetorquers may generate a torque vector close to any desired reference torque. Figure 3.20 shows the same information after an arbitrary rotation of the

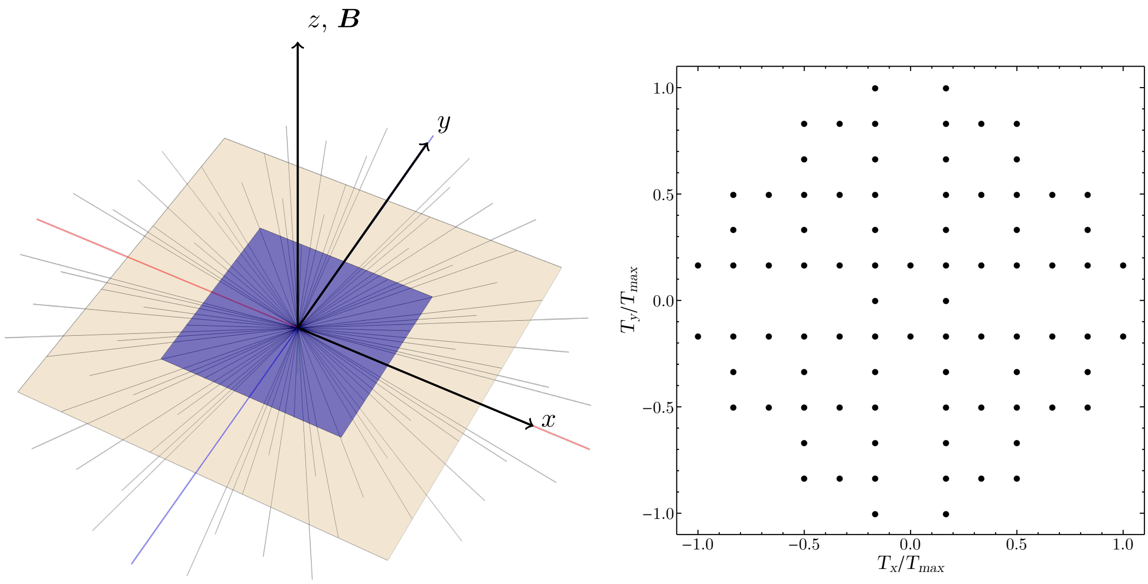

(a) **(b)**

Figure 3.19: a) Visual representation of magnetorquer array plane and torque vectors. b) Non-dimensional torques when the magnetorquer array plane is normal to the magnetic field direction

array relative to the field direction. Figure 3.20b shows that the pattern of achievable torques in the xy-plane has now been somewhat skewed and rotated compared to Fig. 3.19b. This demonstrates that the achievable torque directions and performance of the array are highly dependent upon the field direction.

3.2.1.1 Free-Space Simulation of a Radial Dipole Array

The performance of the radial model described can be investigated by performing a simulation of the system's attitude dynamics, in the absence of any environmental disturbances. Slew manoeuvres will be considered using torques generated by the array to perform rotations between target orientations, with a constant field direction. Rigid-body dynamics will be used along with the quaternion kinematic equations to model the array's orientation. As presented in the technical introduction, for a rigid body rotating around its centre-of-mass, the time derivative of a quaternion describing its current orientation is given by:

$$\dot{q} = \frac{1}{2}\overline{q}[0, \boldsymbol{\omega}] \tag{3.24}$$

Along with the three Newton-Euler equations, the equations of motion are solved numerically, with a control torque, $\boldsymbol{T}$ generated using the radial array model defined by Eq. 3.20. In vector form, the Newton-Euler equations are:

$$\mathbf{I}\dot{\boldsymbol{\omega}} + \boldsymbol{\omega} \times (\mathbf{I}\boldsymbol{\omega}) = \boldsymbol{T} \tag{3.25}$$

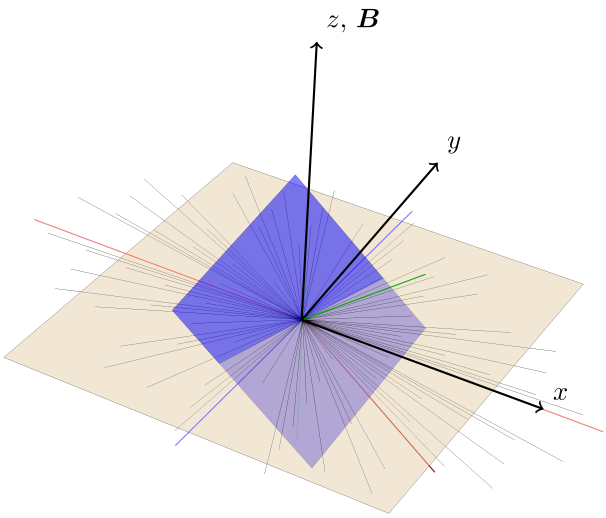

(a)

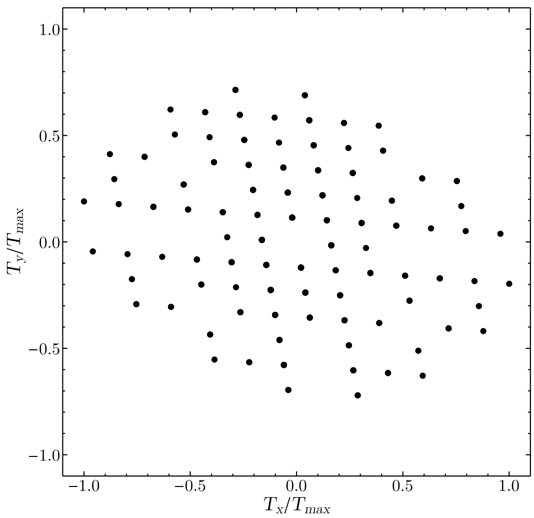

(b)

Figure 3.20: a) Visual representation of magnetorquer array and torque vectors. b) Non-dimensional torques when the magnetorquer array plane has rotated by Euler angles of 10, 45 and 20° (zyx extrinsic convention)

A quaternion error feedback scheme is now used to control the magnetorquer array. An error quaternion $\overline{q}_{err}$ is defined using the quaternion product of the desired orientation quaternion, $\overline{q}_{ref}$, with the current orientation conjugate, $\overline{q}_t^*$ [146], such that:

$$\overline{q}_{err} = \overline{q}_{ref}\overline{q}_t^* \tag{3.26}$$

The vector part of this (pure) quaternion then gives the direction of the torque required to achieve the desired orientation. A reference torque can be built from this vector along with a damping term proportional to the current angular velocity vector, such that:

$$\boldsymbol{T}_{ref} = -P_q\boldsymbol{q}_{\text{err}} - P_\omega\boldsymbol{\omega} \tag{3.27}$$

where $\boldsymbol{q}_{err}$ is the vector part of the $\overline{q}_{err}$ quaternion. The ratio of the proportional and derivative gains, P_q and P_ω, can be adjusted to change the characteristics of the controller, while both are scaled to generate reference torques with a magnitude achievable by the dipole array. Once a reference torque is calculated, a look-up table is created of all current possible torques which may be generated by different combinations of dipole directions on the array, following [101] where a similar approach was taken for an array of reflectivity control devices. The best achievable torque is then selected based on the Euclidean distance between the two torque vectors. The look-up table of possible torques is generated by finding every possible control matrix and applying Eq. 3.20. For a 3×3 array these control matrices are defined by all possible combinations of $1, 0$ and -1. A sample of the 19,683 possible control matrices are shown in Eq. 3.28, where the matrices were generated by cycling every matrix element through each of the possible values.

$$
\begin{pmatrix} 1 & 1 & 1 \\ 1 & 1 & 1 \\ 1 & 1 & 1 \end{pmatrix}, \begin{pmatrix} 1 & 1 & 1 \\ 1 & 1 & 1 \\ 1 & 1 & 0 \end{pmatrix}, \begin{pmatrix} 1 & 1 & 1 \\ 1 & 1 & 1 \\ 1 & 1 & -1 \end{pmatrix}, \begin{pmatrix} 1 & 1 & 1 \\ 1 & 1 & 1 \\ 1 & 0 & 1 \end{pmatrix},
$$
$$
\begin{pmatrix} 1 & 1 & 1 \\ 1 & 1 & 1 \\ 1 & 0 & 0 \end{pmatrix}, \begin{pmatrix} 1 & 1 & 1 \\ 1 & 1 & 1 \\ 1 & 0 & -1 \end{pmatrix}, \begin{pmatrix} 1 & 1 & 1 \\ 1 & 1 & 1 \\ 1 & -1 & 1 \end{pmatrix}, \begin{pmatrix} 1 & 1 & 1 \\ 1 & 1 & 1 \\ 1 & -1 & 0 \end{pmatrix} \dots \tag{3.28}
$$

3.2.1.2 Results of Free-Space Simulation

Simulations are now performed in *MATLAB* in order to test the dipole array model and define the actuator characteristics. The goal of this analysis is to determine what attitude manoeuvres a dipole array may achieve, and how closely the torques generated by the dipole array track the reference controller torque given by Eq. 3.27. The equations of motion were integrated with *ode45*. The controller gains were determined manually by adjusting P_q such that the magnitude of the reference torque remained within a range achievable by the actuators and then adjusting the ratio P_q/P_ω to give sufficient damping to the response. The controller was tested by setting the desired orientation to a 90° rotation around the y-axis, which corresponds to a reference quaternion $\overline{q}_{ref} = -0.7071 + 0\hat{\boldsymbol{i}} - 0.7071\hat{\boldsymbol{j}} + 0\hat{\boldsymbol{k}}$. Controller gains were set at $P_q = 1000$ N m, $P_\omega = 20000$ N m s rad^{-1}. The resulting reference torques lie in the range of 0 to 200 N m, which covers the range of torques the simulated array produces. Actuator torques are determined by an implementation of Eq. 3.20 in *MATLAB* with the magnetic dipole moment of the magnetorquers set to $m = 100$ A m^2, moments of inertia of (15,15,30)$\times 10^4$ kg m^2, and magnetic field strength $|\boldsymbol{B}| = 1$ T for illustration. These parameters are chosen to yield torques on the order of 100 N m, but this scaling is arbitrary and does not affect the behaviour of the controller or torque tracking, so long as the reference torques and actuator torques are compatible. Essentially, the simulation performed here is to demonstrate that the actuator torque *direction* can approximate $\boldsymbol{T_{ref}}$ accurately rather than a realistic simulation of the orbital environment, which is explored later in Sec. 3.3.

Results of the simulation are shown in Fig. 3.21, where the quaternion components move smoothly to the desired orientation with no oscillation. The reference torque y component, T_y, produced by Eq. 3.27 is shown in Fig. 3.22, along with the actual torque produced by the array. The actual torque tracks the reference reasonably well, notably oscillating around the reference value at $t = 150$ s when the array cannot reproduce the reference torque, and so switches between the nearest values. As this is a rotation around the y-axis only the other torque components are zero.

For general 3D attitude motion, the controller is not capable of tracking the reference torque

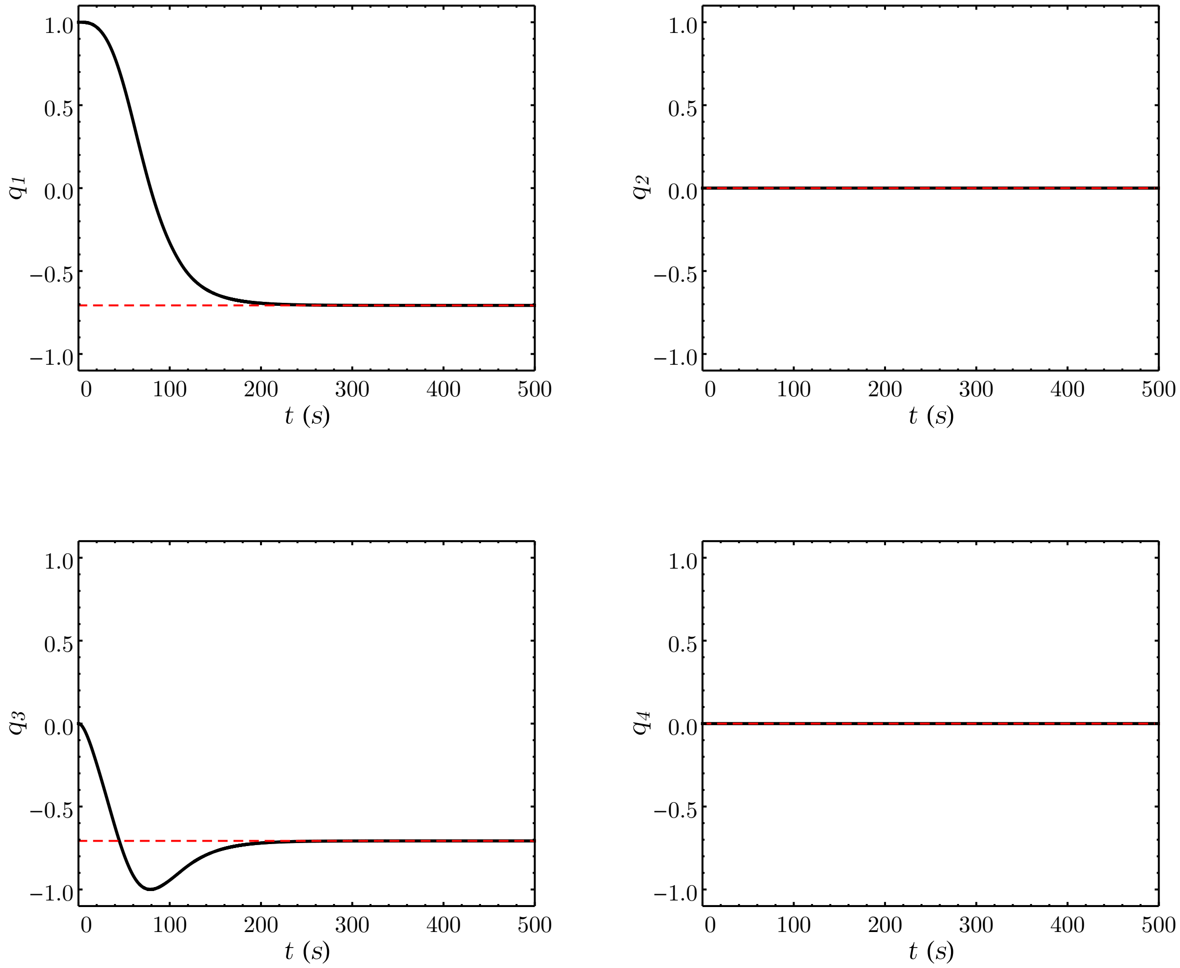

Figure 3.21: Quaternion components against time for a rotation around the y-axis of $\pi/2$ radians. Current quaternion component shown in black while the desired reference quaternion is dashed red.

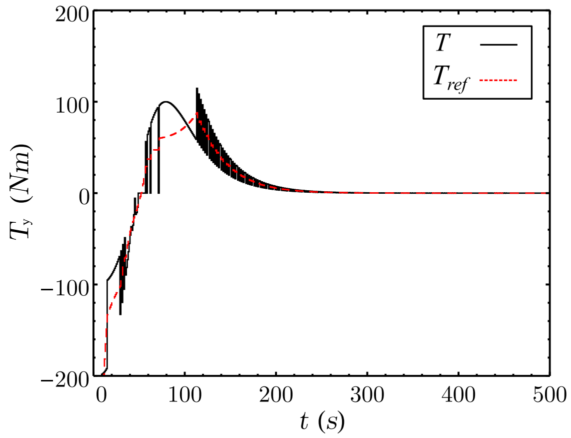

Figure 3.22: Reference torque T_{ref} and actuator torque T produced by the controller for the y-axis rotation.

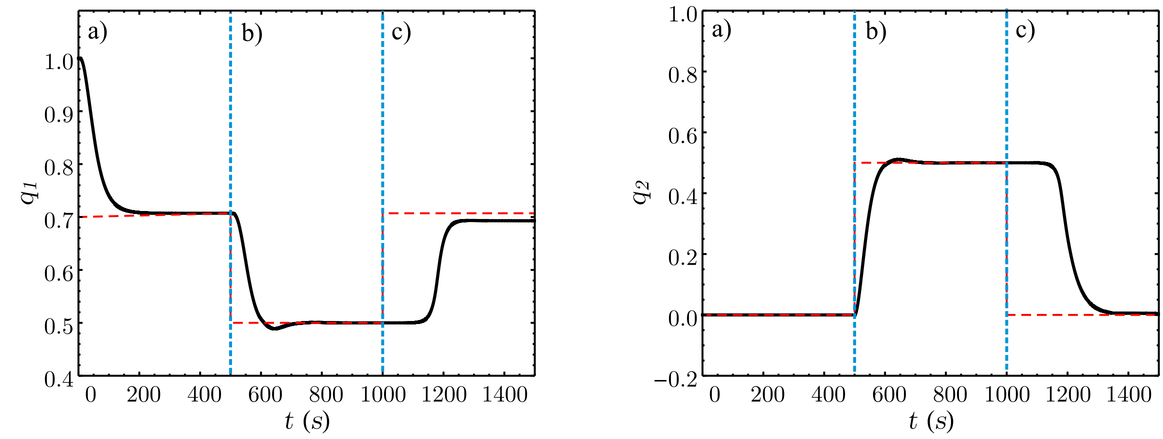

Figure 3.23: Quaternion components against time for a composite manoeuvre. Current quaternion component shown in black while the desired reference quaternion is dashed red.

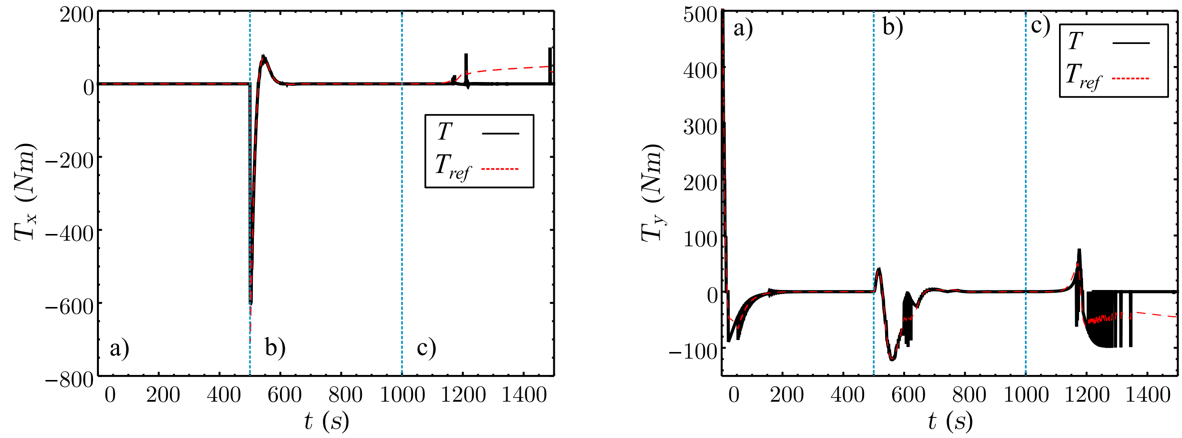

Figure 3.24: Torque components in inertial frame during simulation, T_x is tracked accurately while some oscillation occurs around T_y due to discrepancies between required torques and T_{ref}. T_z is zero as this is the field direction.

as the magnetorquers are not capable of producing a torque in the magnetic field direction (here, the z-direction). However, with a sequence of rotations it is still possible to achieve an overall rotation around the z-axis, despite not being able to create a torque outwith the xy plane [162]. Figure 3.23 shows the simulation results of performing such a manoeuvre, where the sequence of rotations is; (a) $\frac{\pi}{2}$ radians around y-axis, (b) $\frac{\pi}{2}$ radians around x-axis and (c) $-\frac{\pi}{2}$ radians around the y-axis. The resulting final attitude corresponds to a rotation of $\frac{\pi}{2}$ around the z-axis, which would not be possible directly. The reference and control torques are shown in Fig. 3.24. Notable is the oscillation in T_y, since during the second rotation the array lies on the yz plane and so the choice of torques in the y direction is much more limited, making it harder to find a possible torque which matches $\boldsymbol{T}_{ref}$. Also notable is that after the third rotation $\boldsymbol{T}_{ref}$ does not reach zero since when the array returns to the xy plane, it is slightly offset from the desired orientation around the z-axis. The calculation producing $\boldsymbol{T}_{ref}$ would generate a torque mostly in the z direction to correct the attitude, but this is not possible to create with the array so the "nearest" possible torque is zero. This behaviour can be corrected by taking smaller timesteps in the simulation and allowing longer for the body to settle between rotations. This is also evidenced by the steady state errors after the final rotation in Fig. 3.24. Also note that there is a slight delay during the final manoeuvre and time where $\boldsymbol{T}_{ref}$ is small in magnitude, this is because at this point the dipole direction of the array is almost aligned with the external field, and so the largest torque which can be produced by the array (which $\boldsymbol{T}_{ref}$ is scaled by) is very small.

3.2.2 Orthogonal Dipole Array

The second proposed magnetorquer array configuration consists of an $n \times n$ square grid, which has two perpendicular magnetorquers placed at each point. The magnetic dipole moments of these magnetorquers are coplanar with the structure's surface, and aligned with the body-frame x_1 and y_1 axes. Figure 3.25 illustrates the dipole moment directions, which are labelled $\boldsymbol{m}_{x1}$ and $\boldsymbol{m}_{y1}$, for the dipole moments in the x_1 and y_1 directions respectively. The torque produced by each dipole is found by taking the cross product with the external field $\boldsymbol{B}$, and are denoted by $\boldsymbol{\tau}_1$ and $\boldsymbol{\tau}_2$. The subscripts 1 and 2 are used to denote this and avoid implying that $\boldsymbol{\tau}_1$ and $\boldsymbol{\tau}_2$ are aligned with the x_1 and y_1 axes, as these vectors lie in the plane normal to the magnetic field. Although $\boldsymbol{m}_{x1}$ and $\boldsymbol{m}_{y1}$ are perpendicular, for an arbitrary orientation of the plane with respect to the magnetic field, $\boldsymbol{\tau}_1$ and $\boldsymbol{\tau}_2$ will not be perpendicular in general. This can be shown by taking the scalar product of the two torque vectors:

$$\begin{aligned}\boldsymbol{\tau}_1 \cdot \boldsymbol{\tau}_2 &= (\boldsymbol{m}_{x1} \times \boldsymbol{B}) \cdot (\boldsymbol{m}_{y1} \times \boldsymbol{B}) \\ &= (\boldsymbol{m}_{x1} \cdot \boldsymbol{m}_{y1})(\boldsymbol{B} \cdot \boldsymbol{B}) - (\boldsymbol{B} \cdot \boldsymbol{m}_{y1})(\boldsymbol{m}_{y1} \cdot \boldsymbol{B}) \\ &= -(\boldsymbol{m}_{x1} \cdot \boldsymbol{B})(\boldsymbol{m}_{y1} \cdot \boldsymbol{B})\end{aligned} \tag{3.29}$$

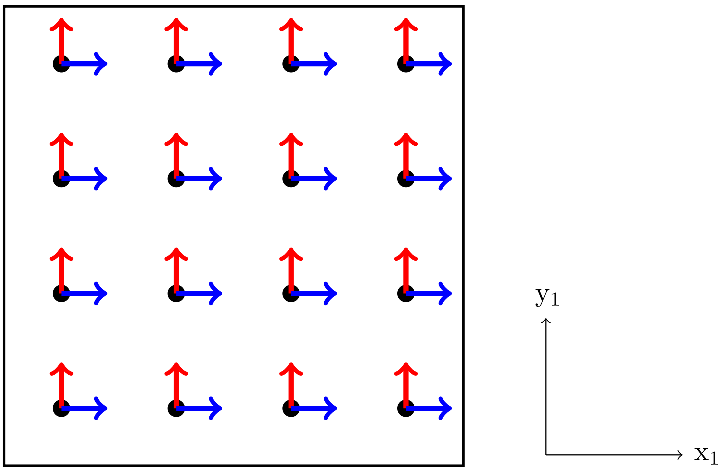

Figure 3.25: Square array of magnetorquers with two orthogonal dipoles at each grid point

Equation 3.29 vanishes only in the case when the magnetic field is perpendicular to one of the dipole directions, which shows that $\boldsymbol{\tau}_1$ and $\boldsymbol{\tau}_2$ are not generally perpendicular. As the torque vectors provided by the magnetorquers of each direction are not perpendicular in general, an expression must be found for the number of dipoles in each direction to activate in order to compose a reference torque. Figure 3.26 shows an example of how a reference torque may be generated using this configuration. It can be seen that, in this example, $\boldsymbol{T}_{ref}$ is closely approximated by activating two x_1 direction magnetorquers, and two y_1 direction magnetorquers. In general, the number of magnetorquers in each direction to activate can be found by decomposing an arbitrary reference torque vector into components.

The total actuation torque, $\boldsymbol{T}$, must be constructed from some integer multiples of $\boldsymbol{\tau}_1$ and $\boldsymbol{\tau}_2$, since there can only be an integer number of activated dipoles. This requirement can be written as:

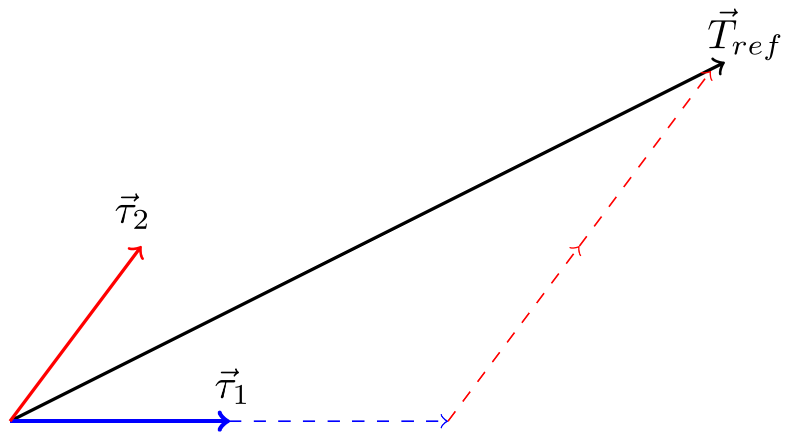

Figure 3.26: Example composition of torque $\boldsymbol{T}_{ref}$ from component vectors $\boldsymbol{\tau}_1$ and $\boldsymbol{\tau}_2$ for an arbitrary orientation of the array. Here $N_1 = N_2 = 1$ and the resulting vector is close to the reference torque T_{ref}

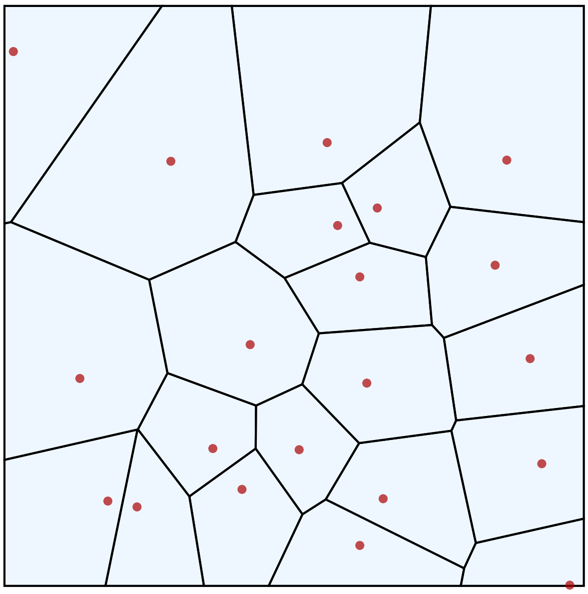

Figure 3.27: Voronoi diagram for 21 points placed at random in a square region

$$\boldsymbol{T} = N_1\boldsymbol{\tau}_1 + N_2\boldsymbol{\tau}_2 \tag{3.30}$$

Then N_1 is found using the scalar product of the reference torque and $\boldsymbol{\tau}_1$, and rounding to the nearest integer, unless the value is greater than n^2. In that case, all the magnetorquers are activated and the controller is saturated. Therefore:

$$N_1 = \left\lfloor \frac{\boldsymbol{T}_{ref} \cdot \boldsymbol{\tau}_1}{|\boldsymbol{\tau}_1|^2} \right\rceil \tag{3.31}$$

Similarly, N_2 is given by an equivalent expression, except that N_2 is reduced by taking into account the contribution to the $\boldsymbol{\tau}_2$ direction already given by $N_1\boldsymbol{\tau}_1$, so that:

$$N_2 = \left\lfloor \frac{\boldsymbol{T}_{ref} \cdot \boldsymbol{\tau}_2 - N_1\boldsymbol{\tau}_1 \cdot \boldsymbol{\tau}_2}{|\boldsymbol{\tau}_2|^2} \right\rceil \tag{3.32}$$

There is now the issue of deciding which magnetorquers are to be activated on the square array. It is assumed desirable to have the activated magnetorquers as evenly distributed as possible, to make full use of the array and distribute the loads throughout the structure. The issue of selecting which actuators to activate can be considered an analogue to placing N points evenly within a square region, which is in general not a trivial problem and has been studied extensively in the field of computer science [163, 164]. If N is a square number, it is easy to visualise an even distribution where the points are placed on the vertices of a square grid, and for certain numbers the solution is given by dividing the area into hexagonal cells, known as hexagonal packing. These geometries cannot be exploited to give a solution for all N however. A common numerical solution to this problem, which is adapted for the magnetorquer allocation problem, is the use of Voronoi diagrams and *Lloyd's Algorithm*, which evenly distributes a set of points in Euclidean space within uniform cells [165].

A Voronoi diagram is a partitioning of a plane based on the distance to the nearest point of a set of specified points. Figure 3.27 shows the Voronoi diagram for a set of 21 random points placed in a square region. Each cell bounds the region of space that is nearer to the contained red generator point than any other. Lloyd's algorithm generates a Voronoi diagram for a set of points, and then calculates the centroid of each cell in that diagram. The set of initial generating points is then replaced with the centroids, and a new diagram generated. This process is repeated until the change in centroid position falls below a set tolerance. This algorithm is known to converge onto a distribution known as a centroidal Voronoi tesselation, proven to be an optimal solution for a number of resource allocation problems, as the points approach an even distribution in space with cells of equal area [166].

In the context of the orthogonal dipole array described here, this approach can be used to select which magnetorquers to activate at a given time. For a given orientation, and desired torque, the number of dipoles in both possible directions that must be activated are given by Eqs. 3.31 and 3.32. For each dipole direction $i = 1, 2$, N_i random points are generated within a square region which represents the array. Lloyd's algorithm is then applied until a satisfactory distribution of points is found. As the array consists of dipoles placed at discrete points, the nearest dipole to each generated point of the final set is then selected and activated. As an example, consider a 10×10 array of orthogonal dipoles, and assume that Eq. 3.31 has been evaluated so that the controller must activate 72 of the 100 dipoles. The algorithm is run until the centroids do not change by more than a set tolerance, in this case resulting in 1000 iterations. The algorithm runtime was 0.25 s within MATLAB on a 2.3 GHz CPU, though it is noted that the magnetorquer activation patterns could be precomputed in practice and so the

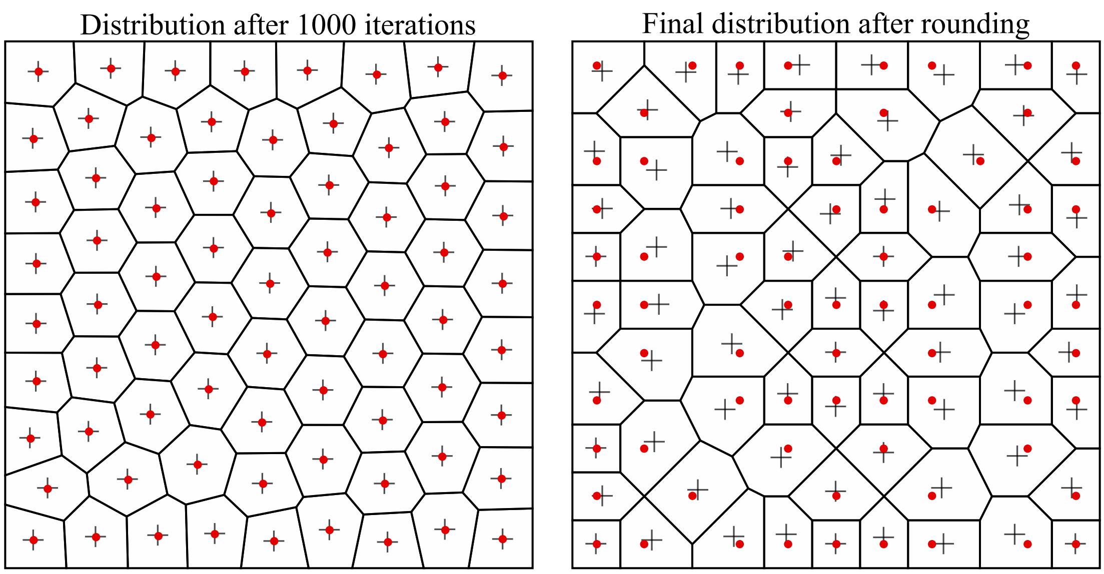

Figure 3.28: Placing 72 points evenly on a 10×10 grid with Lloyd's algorithm, The $\boldsymbol{e}_1$ direction magnetorquers located at the sites marked in red will be activated. The algorithm would then be repeated for the $\boldsymbol{e}_2$ direction magnetorquers.

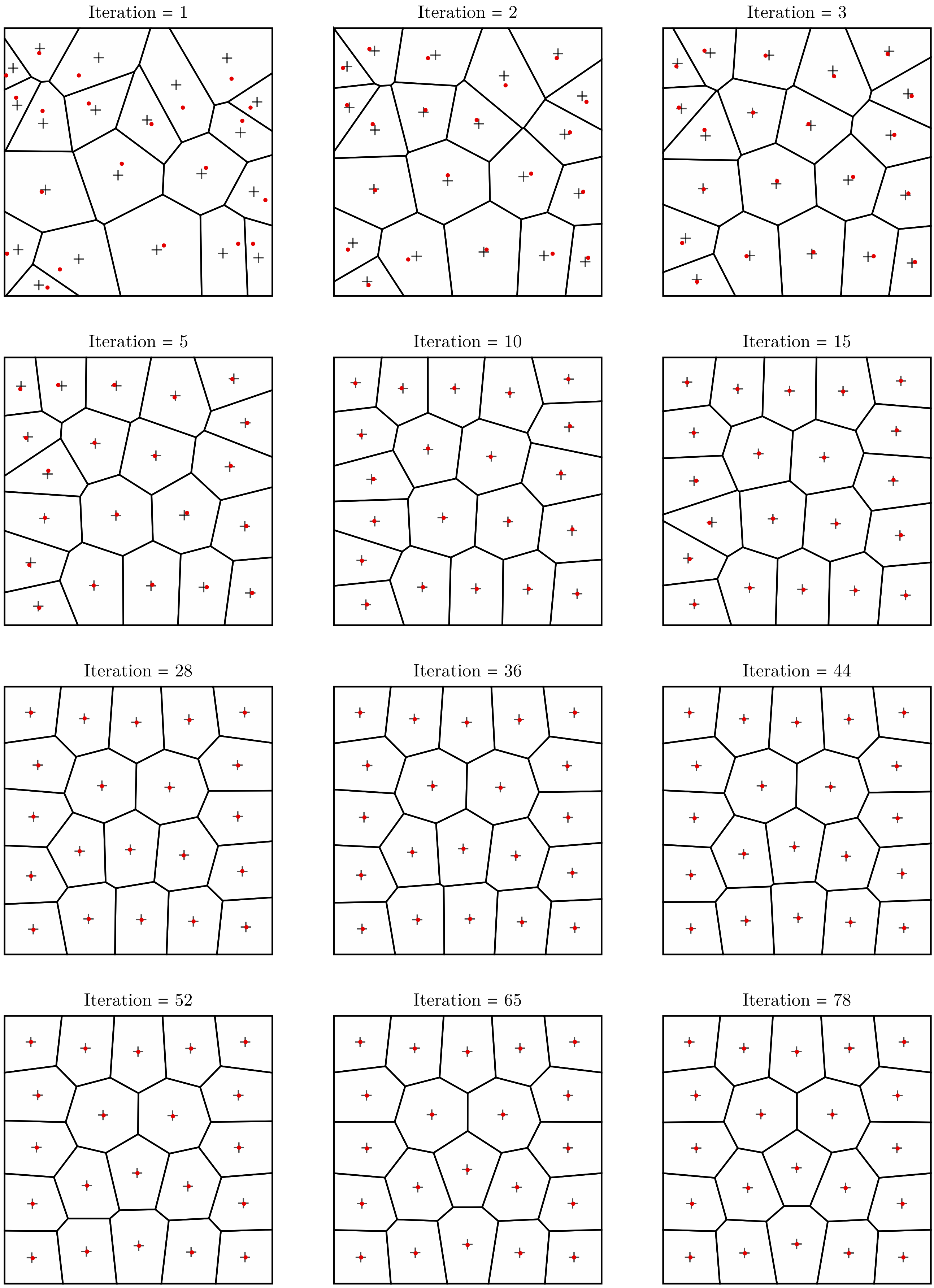

Figure 3.29: Voronoi diagrams at different steps of Lloyd's algorithm. Generator points (red points) are replaced with centroids (crosses) of the Voronoi cell polygon at each step. The points become evenly distributed as the diagram approaches a centroidal tesselation.

onboard runtime of the algorithm will not be an issue for future implementation. Figure 3.28 shows the point distribution and Voronoi diagram generated by the algorithm. The final step involves rounding the centroids to the nearest actuator point. The magnetorquers located at the sites marked in by the circular points on the right side of Fig. 3.28 will then be activated. Figure 3.29 shows the voronoi diagram at different steps of the algorithm, illustrating how the initially randomly placed points gradually approach the more evenly distributed centroidal tessellation pattern.

3.2.2.1 Free-Space Simulation of an Orthogonal Dipole Array

Simulations are now performed to test the orthogonal dipole model. Similar to the previous results for the radial array, these simulations assume no disturbances other than the control torques. The rigid body Euler equations are used again and solved numerically, where the reference torque $\boldsymbol{T}_{ref}$ is found using Eq. 3.27. The Voronoi/Lloyds algorithm method is then implemented to find the number and grid patterns of magnetorquers which must be activated.

Simulations were again performed in *MATLAB* in order to test the orthogonal array model, and to compare results with those of the radial dipole array. As the main constraint on the radial array was the look-up table method, which could not be used for an array larger than 3×3, the goal here is to demonstrate that the orthogonal dipole strategy is suitable for modelling much larger arrays. Therefore, a 20 × 20 grid of magnetorquers is implemented in *MATLAB*. The controller is tested by setting the desired orientation to a 90° rotation around the y-axis, as used for the first simulation performed in Sec. 3.2.1.1, which corresponds to a reference quaternion $q_{ref} = -0.7071 + 0\hat{\boldsymbol{i}} - 0.7071\hat{\boldsymbol{j}} + 0\hat{\boldsymbol{k}}$. The controller gains remain set at $P_q = 1000$, $P_\omega = 20000$. The resulting reference torques lie in the range of 0 to 200 N m as before, and now the magnetorquer dipole moments are selected such that the total torque produced by the array is in this range. This results in each magnetorquer having a magnetic dipole moment $m = 1$ A m^2. This value is much lower than for the radial model since there are now 400 magnetorquers in total. All other parameters are the same as for the radial array simulations.

The results of the simulation are shown in Fig. 3.30, demonstrating that the quaternion components smoothly approach the target orientation. The reference torque y_1 component produced by Eq. 3.27 is shown in Fig. 3.31, along with the actual torque produced by the array. The actual torque tracks the reference torque almost exactly. Comparing this with the radial dipole torque (Fig. 3.22) shows that the orthogonal array is much better at matching the reference torque. This is due to the larger number of dipoles in this array, which allow much smaller changes in actuator torque direction to be achieved and so direct comparison of this accuracy is not appropriate. These results demonstrate that the orthogonal model is capable of tracking the reference torque, and that the model can be scaled to larger arrays than was previously possible with the radial array.

A simulation is also performed in which the array performs a rotation around the field axis, through the sequence described in Sec. 3.2.1.1. Figure 3.32 shows the quaternion components

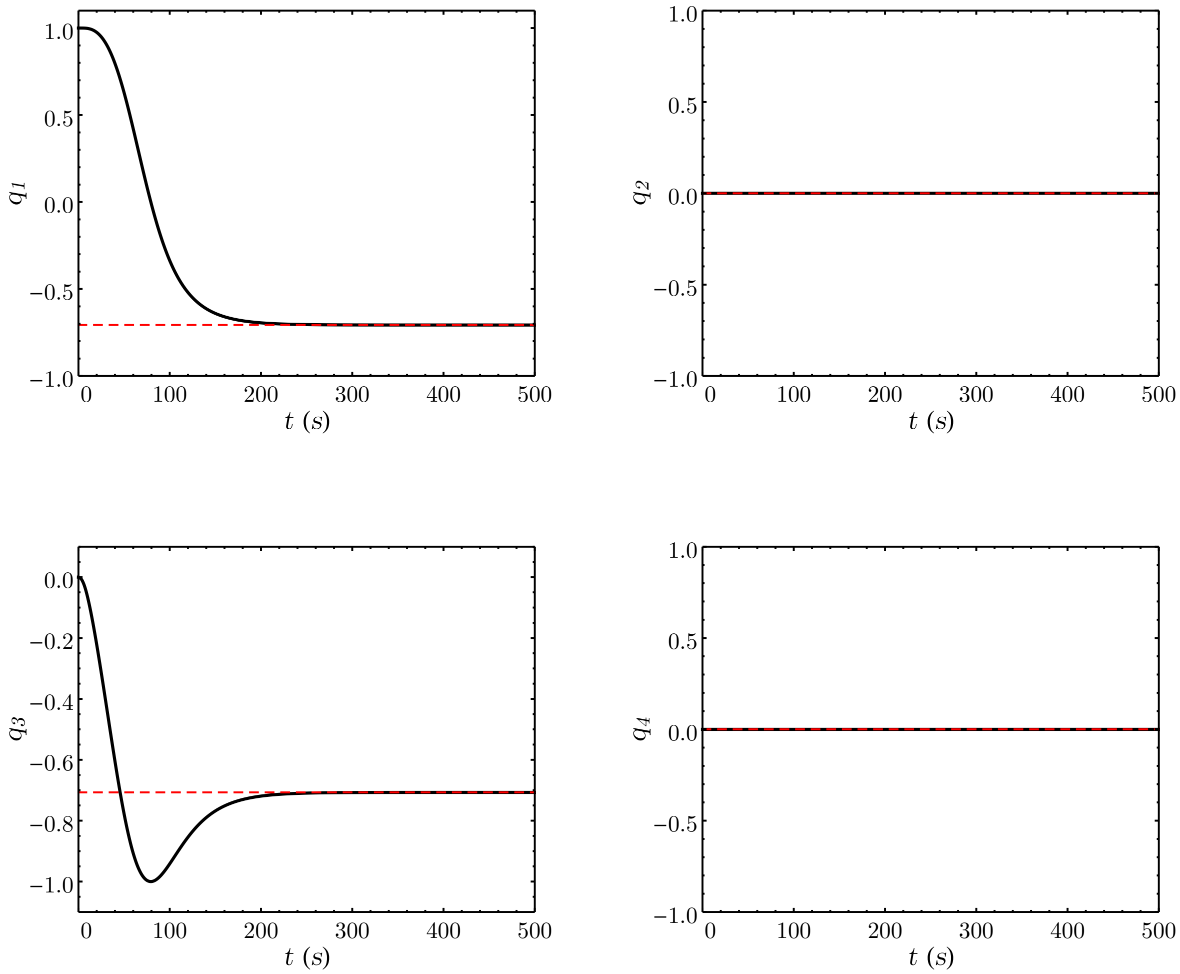

Figure 3.30: Quaternion components against time for a rotation around the y-axis of $\pi/2$ radians. Current quaternion component shown in black while the desired reference quaternion is dashed red.

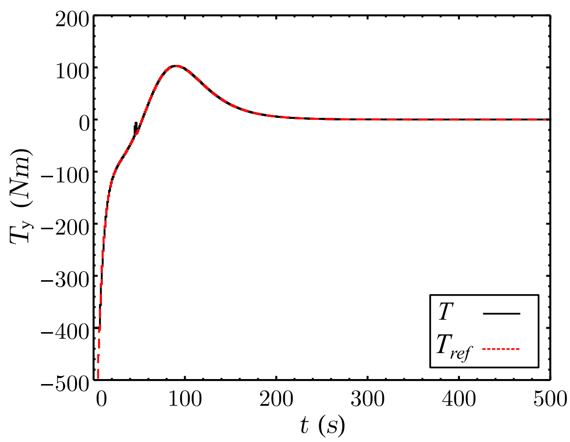

Figure 3.31: Reference torque T_{ref} and actuator torque T produced by the controller for the y-axis rotation.

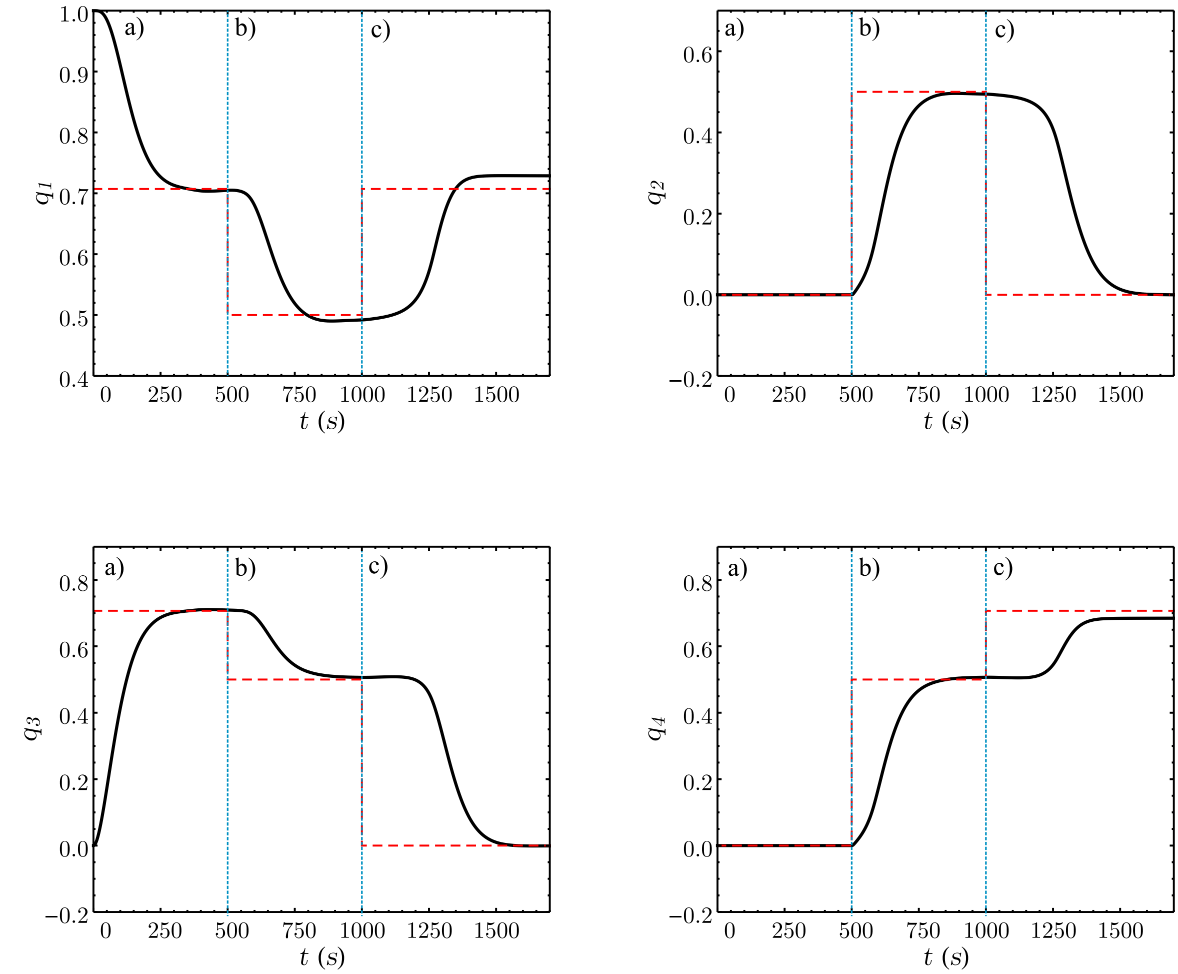

Figure 3.32: Quaternion components against time for a composite manoeuvre. Current quaternion component shown in black while the desired reference quaternion is dashed red.

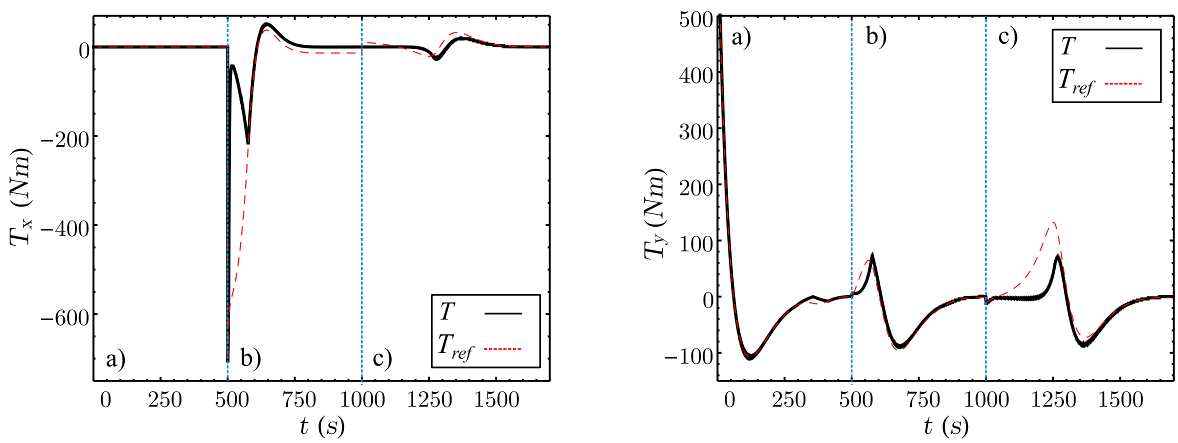

Figure 3.33: Torque components in inertial frame during simulation, T_x is tracked accurately while some oscillation occurs around T_y due to discrepancies between required torques and T_{ref}. T_z is zero as this is the field direction.

of the array during this simulation, which are markedly similar to the radial array results in that each manoeuvre is performed smoothly within 500 s, and the array achieves the final desired attitude with a slight steady-state error. A key difference with these results is that the second and third manoeuvres take slightly longer than for the radial array. This is because of the geometry of the orthogonal array. When the array plane attempts to perform the second manoeuvre around the x-axis, the radial array is more likely to have magnetorquers perpendicular to the field direction at all times, which gives the maximum possible torque as seen from Eq. 3.20. The orthogonal array only has two dipole directions however, so for a given orientation it is less likely that the dipoles will be perpendicular to the field direction. This effect is made clear by examining the torque output of the array during the sequence of manoeuvres, shown in Fig. 3.33. At $t = 500$ s, when performing a rotation around the x-axis the array quickly becomes unable to match the reference torque x-component in magnitude because neither of the two dipole directions are perpendicular to the field. This is in contrast with the radial array results (Fig. 3.23), where the array is capable of achieving the reference torque magnitude because as one dipole rotates out of the plane normal to the field direction, another will become perpendicular to it, as they are arranged like spokes on a wheel rotating around the x-axis. This limitation of the orthogonal array could be improved by placing magnetorquers in more directions at each point, but the combinatorial problem encountered with the radial array would then need to be solved, albeit in a reduced form. Despite this issue the array still manages to achieve the correct sequence of attitude manoeuvres, and it was chosen as a more suitable strategy for the attitude control of a large space structure as it would be very difficult to achieve the large magnetic dipole moments required by the radial array.

3.3 Orbital Simulations of a Large Space Structure with Distributed Magnetorquers

Simulations are now used to demonstrate the attitude control of a large, flexible structure using the orthogonal magnetorquer array described in Sec. 3.2.2, in the presence of gravity gradient torques and a changing magnetic field. First, a scaling law is developed to demonstrate how the magnetorquer array torque and gravity gradient torque scale with the structure's side length. These scaling laws lead to reasonable estimates of the structure's mass and required control torques, and are used to define the physical parameters used in the later orbital simulations. Simulations are performed to demonstrate detumbling, using the well-known Bdot control law, and two rest-to-rest manoeuvres which make use of a quaternion error feedback controller. The aims of these simulations are: 1) to show that magnetorquers can provide sufficient torques for the attitude control of a lightweight truss structure at this scale; 2) to demonstrate which axes these manoeuvres can be performed around given the geometric constraints of magnetic attitude control, and 3) to show that the distributed array and torque distribution algorithm allows flexible structures to be controlled successfully by the application of rigid-body control laws; since torque distribution reduces structural deformation and the response to the control torques more closely resembles that of a rigid body.

3.3.1 Scaling of Magnetorquer Arrays

To provide an adequate degree of attitude control, the magnetorquer array must be capable of producing a torque at least as large as the gravity gradient torque that a large structure will experience on orbit. Aerodynamic and radiation pressure torques are not considered for simplicity, and because these will generally be smaller disturbances than the gravity gradient unless, for aerodynamic torques, the structure is in a very low altitude orbit. The gravity gradient torque scales with the moment of inertia and thus the square of the structure's length. For a rigid body this is given by: [146]

$$\boldsymbol{T}_{\text{grav}} = 3\frac{\mu}{r^5}\boldsymbol{r}_b \times \mathbf{I}\boldsymbol{r}_b \tag{3.33}$$

where $\boldsymbol{r}_b$ is the position vector of the centre-of-mass, expressed in body frame coordinates, and $\mathbf{I}$ is the inertia tensor. Using the inertia tensor of a thin, square plate, $\mathrm{I}_1 = \mathrm{I}_2 = 1/12Md^2$, $\mathrm{I}_3 = 1/6Md^2$, and taking the maximum value which occurs when the structure is at a 45° angle to the local vertical, Eq. 3.33 leads to:

$$\boldsymbol{T}_{\text{grav}}^{\text{max}} = \frac{\mu M d^2}{8r^3} \tag{3.34}$$

where M is the total mass of the structure (assumed uniformly distributed), d the sidelength and r the orbital radius. As noted previously, it is assumed that the dipole moment and thus torque produced by a magnetorquer is proportional to its mass, i.e. the dipole moment produced by a given mass of magnetorquers is $M_{\text{dip}} = \kappa_\tau M_\tau$, where κ_τ is the constant of proportionality and M_τ the total mass of magnetorquers. This assumption is based on the fact that magnetic torque rods are solenoids, which produce a torque that is proportional to the number of turns in the coil. Increasing the number of turns in this solenoid then leads to a proportional increase in both mass and torque. It is also assumed that this relationship remains linear despite the magnetorquer mass being distributed between the array points. The maximum actuator torque is achieved when the dipole moment is perpendicular to the external field, and is found from Eq. 3.13:

$$T_{\text{ac}}^{\text{max}} = \kappa_\tau M_\tau B \tag{3.35}$$

For a given scale of structure, a certain mass of magnetorquers is required to have $T_{\text{ac}} \geq T_{\text{grav}}$. The fraction of structural mass which must be allocated to magnetorquers to meet this condition is found by equating Eqs. 3.34 and 3.35, and substituting $M_\tau = \lambda_f M$, where λ_f is the fraction of total mass allocated to magnetorquers. B is approximated as a dipole field for this analysis, given by $|B| = B_0 \left(\frac{R_E}{r}\right)^3$ where $R_E = 6370$ km is the radius of the Earth and B_0=3.12×10^{-5} T is the average field strength at the surface of the Earth. These substitutions lead to an

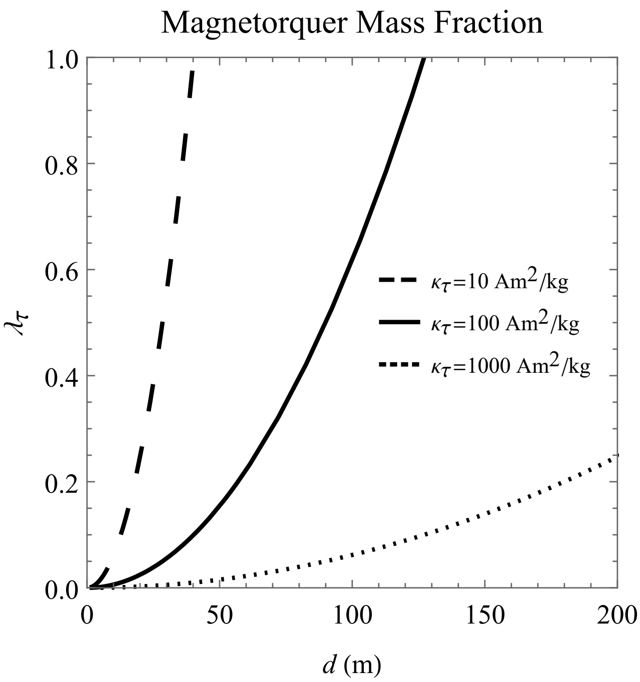

Figure 3.34: Required magnetorquer mass fraction as a function of structure sidelength for a range of dipole moment to mass ratios.

expression for λ_f, the fraction of total structural mass that must be allocated to magnetorquers in order to have an achievable actuator torque equal to the maximum gravity gradient torque:

$$\lambda_f = \frac{\mu d^2}{8 B_0 R_E^3 \kappa_\tau} \tag{3.36}$$

Equation 3.36 has no r dependence, since both the gravity gradient and dipole field strength scale as r^3. However, although the torques are equal, the magnetic torque magnitude available for active control falls with increasing orbit radius. Equation 3.36 shows that the required magnetorquer mass fraction scales with d^2, suggesting the scale of structures for which distributed magnetorquer arrays would be suitable is limited, and scales inversely to κ_τ, the dipole moment to mass ratio of the magnetorquers used. As noted previously, magnetorquers are available commercially with $\boldsymbol{m_d}$ =100 A m^2 [157], though this is a larger value than the majority of magnetorquers with flight heritage, which are found to have κ_τ on the order of 10 A m^2/kg, [167]. The range in values here is thought to be due to the fact that many of these torquers were flown in CubeSats, so their dipole moment is most likely limited by available power or thermal constraints. For the type of large structure considered here, a considerable quantity of solar radiation can be intercepted and so power will not likely be a limiting factor, and so the larger value of κ_τ =100 A m^2/kg is thought reasonable, though it is possible that even higher values of κ_τ could be achieved. Figure 3.34 shows λ_τ as a function of d for a range of κ_τ, demonstrating the maximum scale of structure for which distributed magnetorquer arrays with a given κ_τ would be suitable. For κ_τ = 100 A m^2/kg, the figure suggests a side length of 100 m could be controlled, assuming it were reasonable to allocate up to 60% of the total structural mass for the attitude control system. It is also notable that the total mass doesn't appear in Eq. 3.36, although more massive structures will experience smaller angular accelerations. In Sec. 3.1 it was found that distributed torquing allowed the control of more flexible structures than central torquing. More flexible structures will have a lower mass, and so although a 100 m structure would require a minimum of 60% of its mass to be magnetorquers, the structure itself can be much less massive than would be necessary to provide the required bending stiffness for centralised torquing. This analysis suggests that distributed magnetorquer arrays are particularly suitable for lightweight, flexible structures, at length scales up to approximately 100 m for currently available magnetorquers.

3.3.2 Detumbling with a *Bdot* Control Law

The Bdot control law is commonly used to allow angular momentum dumping through magnetorquers. This control law is considered here as it is so commonly used, and because angular momentum dumping is often the primary use of magnetic torque rods in conventional spacecraft. The algorithm provides an expression for the desired control torque, $\boldsymbol{T}_{Bdot}$, in terms of the body rates, $\boldsymbol{\omega}$, of the spacecraft and the magnetic field, $\boldsymbol{B}$, [168], such that:

$$\boldsymbol{T}_{Bdot} = k_{\mathrm{Bdot}}(\boldsymbol{\omega} \times \boldsymbol{B}) \times \boldsymbol{B} \tag{3.37}$$

where k_{Bdot} is the controller gain. Although we are considering a flexible body, we again use the best fitting rotation matrix of the nodal points to describe the structure's attitude, and estimate the angular rates at each time step using the backward difference formula. This treats the structure as a rigid-body for the controller, and so it is assumed to only be effective should the structure maintain its initial shape sufficiently. The structure is placed on a polar, circular orbit with altitude 800 km, and air drag is not considered in the simulation. Moreover, radiation pressure is also neglected in order to assess the use of magnetic attitude control. The magnetic field is calculated at each time step using the World Magnetic Model (WMM) for 2020 [169]. Although there will be slight variation in the magnetic field over the structure itself, this variation is negligible compared to the variation over the orbit, and so for computational efficiency the magnetic field is only calculated at the centre-of-mass of the structure and is assumed constant across its span.

Considering the scaling law Eq. 3.36, a 75×75 m square structure is selected for the following simulations. The magnetorquers are assumed to have κ_τ of 100 A m^2/kg, and so a side length of 75 m means that a magnetorquer mass fraction of 50% would provide an actuator torque greater than the gravity gradient torque, illustrated in Fig. 3.34. The structure's mass is set to 200 kg, 100 kg of which is allocated to magnetorquers while another 100 kg is the structural mass. This structural mass is assumed to provide a bending stiffness of 10^3 N m^2, the same as Case A in Sec. 3.1, based on the fact that areal densities on the order of 10 g/m^2 are capable of achieving this level of rigidity for solar sails. The spring constant used in the model is then determined as in Sec. 3.1. The 100 kg of magnetorquers are capable of producing a total dipole moment of 10000 A m^2, which is distributed between 380 magnetorquer sites along both the x_1 and y_1 body axis directions, as illustrated in Fig. 3.8, but here with 20×20 cube units. All other simulation parameters are the same as the previous simulations, given in Table 3.2. The initial angular velocity is set to $\boldsymbol{\omega}_0 = (0.01, 0.007, 0)$ rad s^{-1}. While this is a modest rate for a conventional satellite, it represents a significant angular velocity for a 75×75 m structure. Through simulation it was found that the structure failed through buckling at larger angular velocities due to centripetal forces. This was observed for angular velocities approximately an order of magnitude larger than ω_0, so the initial angular velocity selected is assumed to be a rate at which a structure of this scale could be considered tumbling but not at danger of structural failure. The magnitude of ω_0 is also approximately three times as large as the maximum angular velocity reached during the simulation in Fig. 3.9. It is also an order of magnitude larger than the orbital angular velocity. Structural parameters and other simulation data are summarised in Table 3.3

The results of the simulation are shown in Fig. 3.35. The structure is seen to detumble to a state with all rates below 1×10^{-3} rad s^{-1}, or 10% of the original rates, in 1 hour. At this point there is some fluctuation in the body rates, presumably due to the influence of the gravity gradient torque, but the controller corrects these disturbances and the body rates remain

Structural Parameters		
Length	d	75 m
Magnetorquer dip. to mass ratio	κ_τ	100 A m^2/kg
Magnetorquer mass fraction	λ_f	50%
Total Mass	M	200 kg
Bending stiffness	EI	10^3 N m^2
Structural units		20×20
Total number of torquers for each direction		380
Total number of particles		800
Orbital altitude	R	800 km
Detumbling		
Initial ang. velocity	$\boldsymbol{\omega}_0$	(0.01,0.07,0)
Bdot controller gain	k_{Bdot}	1×10^{12}
Simulation runtime	t_{end}	2.5 hours
Slew Manoeuvres		
Proportional Gains	$\mathcal{P}_q$	(10,50,1)
Derivative Gains	$\mathcal{P}_\omega$	(1600,8000,800)
Simulation runtime	t_{end}	4.2 hours
Simulation timestep	dt	0.1 s
Integration method	Runge-kutta 4th order	
Magnetic Field	World Magnetic Model (2020)	

Table 3.3: Parameters used for orbital simulations.

close to zero. Figure 3.36 shows the control profile during the simulation, which indicates the number of magnetorquers activated at a given time and their polarity. During the first hour of detumbling the controller is saturated, with nearly all magnetorquers activated. Later, once the majority of angular momentum has been removed, fewer magnetorquers are activated, although there is another point of saturation at approximately 2 hours. This is due to the coincidence of a point of maximum gravity gradient torque with minimum control effectiveness, which occurs when the field is oriented within the plane of the structure. The surface is seen to experience large deformations while detumbling, with the surface standard deviation reaching a maximum value of 0.5 m. As the surface deviation is oscillating regularly it is likely some normal modes have been excited, which could be caused by the actuator torques changing periodically while the structure rotates, or by the difference in magnitude of the gravitational forces acting upon the lumped masses of the structure. The surface deformation is shown in Figs. 3.37 and 3.38, which shows the local surface angle and shape of the structure at the point of maximum surface SD. The edges of the surface make an angle of 4° to the average plane, and the structure is visibly twisted in Fig. 3.38. The allowable deformation would depend on the specific structure and a limit on this is not considered here, but again it is noted that the deformation is smooth with no points of high curvature that may cause buckling.

3.3.3 Slew Manoeuvres with Quaternion Error Feedback Control

In addition to angular momentum dumping, magnetorquers can also be used directly for manoeuvring, although the geometric constraint of being unable to generate a torque in the external field direction leads to an underactuated control problem for general re-orientations.

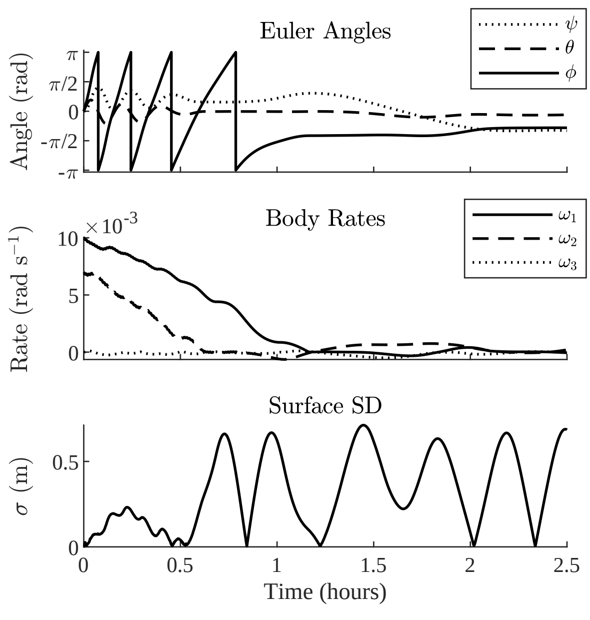

Figure 3.35: Detumbling of a structure with distributed torques.

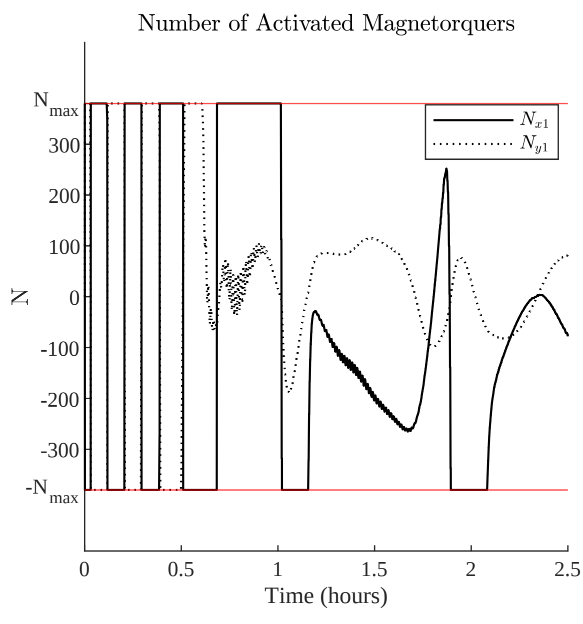

Figure 3.36: Control signal during detumbling.

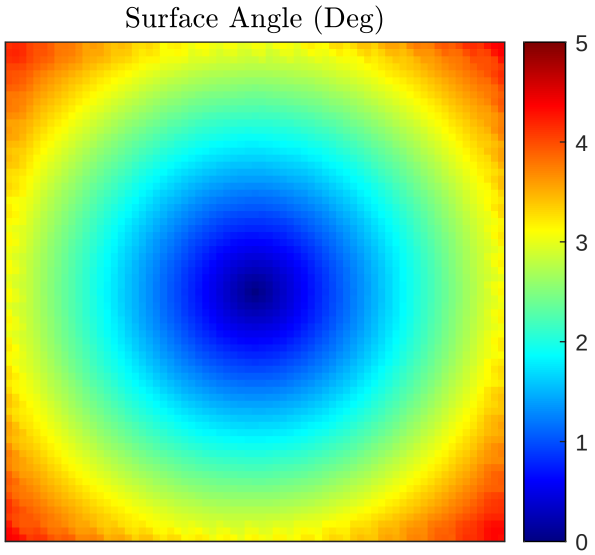

Figure 3.37: Local surface angle at point of maximum surface SD during detumbling.

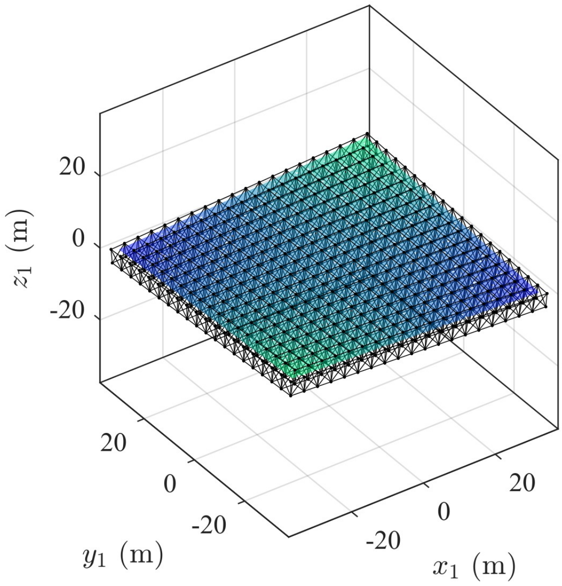

Figure 3.38: Structural deformation at point of maximum surface SD.

Despite these disadvantages, some limited attitude control is still possible, depending on the orbit selected, and here we investigate the capabilities of the distributed magnetorquer array for performing slew manoeuvres. The aim of these simulations is to demonstrate which manoeuvres can be achieved when the proposed array geometry is placed in a polar orbit, and how effective the distributed array is at enacting these manoeuvres.

A quaternion error feedback controller is again used to generate a reference torque for performing these manoeuvres. This controller is primarily used for rigid-body rotations, and it is applied to the flexible structure by considering the best-fitting rotation for the set of nodal positions. As in Eq. 3.27, a reference torque is found by evaluating:

$$\boldsymbol{T}_{ref} = -P_q \boldsymbol{q}_{\text{err}} - P_\omega \boldsymbol{\omega} \tag{3.38}$$

The controller is modified to take into account the gravity gradient torque. Equation 3.33 is for the torque on a rigid body, where the inertia matrix is found by integrating over the body's volume. For the spring-mass structure this is therefore an estimation, but is assumed accurate so long as the original shape is sufficiently maintained. The inertia tensor is taken to be the initial mass-moments-of-inertia of the particle distribution around the principal axes, which is found by summation over the point masses. The diagonal components of **I** are given by:

$$\begin{aligned}
\mathrm{I}_1 &= \sum_i m_p(y_{1i}^2 + z_{1i}^2) \\
\mathrm{I}_2 &= \sum_i m_p(x_{1i}^2 + z_{1i}^2) \\
\mathrm{I}_3 &= \sum_i m_p(x_{1i}^2 + y_{1i}^2)
\end{aligned} \tag{3.39}$$

where x_{1i} is the x_1 component of the i^{th} particle in the body frame, and likewise for y_{1i} and z_{1i}. For the 200 kg structure these components are $\mathrm{I}_1 = \mathrm{I}_2 = 1893$ kg m^2 and $\mathrm{I}_3 = 2867$ kg m^2. The reference torque in Eq. 4.2 is modified to give:

$$\boldsymbol{T}_{ref} = -P_q \boldsymbol{q}_{\text{err}} - P_\omega \boldsymbol{\omega} - 3\frac{\mu}{r^5}\boldsymbol{r}_b \times \mathbf{I}\boldsymbol{r}_b \tag{3.40}$$

assuring the controller will now compensate for the estimated gravity gradient torque. When selecting the control gains, it was found that replacing the proportional and derivative gains P_q and P_ω with diagonal matrices $\mathcal{P}_q$ and $\mathcal{P}_\omega$ resulted in better performance. This can be understood intuitively as applying a different gain to each axis of rotation. It was found that disturbances in the angle of rotation around the z and y axis were more likely to lead to tumbling of the structure, so a larger gain is selected for the corresponding entry the gain matrices. This results in the controller prioritising the correction of any disturbances in these directions and thus reduces the risk of the structure beginning to tumble. The feedback gains are selected as $(10, 50, 1)$ N m and $(1600, 8000, 800)$ N m s rad^{-1}, for the diagonal entries of $\mathcal{P}_q$ and $\mathcal{P}_\omega$ respectively.

The attempted manoeuvres are illustrated in Fig. 3.39. The structure is again placed in a polar orbit. As the structure orbits, the magnetic field direction is primarily in the yz-plane, and rotates around the x-axis. There is always a slight x-component to the field because it's not an ideal dipole field. Additionally, because magnetic north and true north are not aligned, this variation in this component changes over multiple orbits due to the Earth's rotation, which is taken into account when calculating the field components from the WMM. The selected manoeuvres are chosen to demonstrate rotation around all three inertial axes, (I,III and IV), and to demonstrate the ability of the system to either work against the gravity gradient torque (I) or to move between gravity-gradient stable configurations (II). Simulation parameters are summarised in Table 3.3.

Results of the simulations are shown in Figs. 3.40 -3.43b, where all manoeuvres are performed successfully within approximately 1.5 hours, with the exception of Manoeuvre IV. In the case of Manoeuvre IV the desired attitude is not achieved and the structure begins to tumble. This is because when attempting to rotate around the inertial y-axis, the direction of the gravity gradient torque is not in a direction that can be counteracted by the magnetic torques produced by the system. Therefore, this is a limitation imposed on the use of magnetic control in general rather than the control strategy presented here. Figure 3.40c shows the torques experienced by the structure during Manoeuvre I, with the gravity gradient and control torques shown in red and blue respectively, and dashing used to indicate the body axis components of each. The torques are primarily around the body x_1 axis, as the desired axis of rotation, and the results show that the controller successfully counteracts this component of the gravity gradient torque over the simulation runtime of four hours. There are points at which the controller is unable to produce the required torque, due to the relative orientation of the external field and the structure, which are shown in this figure as points where T_{ac} falls to zero briefly. Notably this occurs at 0.5 hours for a significant period, when the structure is still performing the manoeuvre. The result of this period of control ineffectiveness is the structure overshooting the desired angle of $\pi/2$ rad, as shown in Fig. 3.40a. This overshooting is not underdamping caused by the gain selection, rather it is due to the coincidence of a point of large gravity gradient torque with a point of minimum control effectiveness. Therefore this scenario may be typical of the control strategy and may need to be taken into account when planning manoeuvres. Manoeuvre II was performed to investigate the controller performance when moving between gravity gradient stabilised configurations, as opposed to working against the gravity gradient torque. As illustrated in Fig. 3.41b, the control effort is greatly reduced

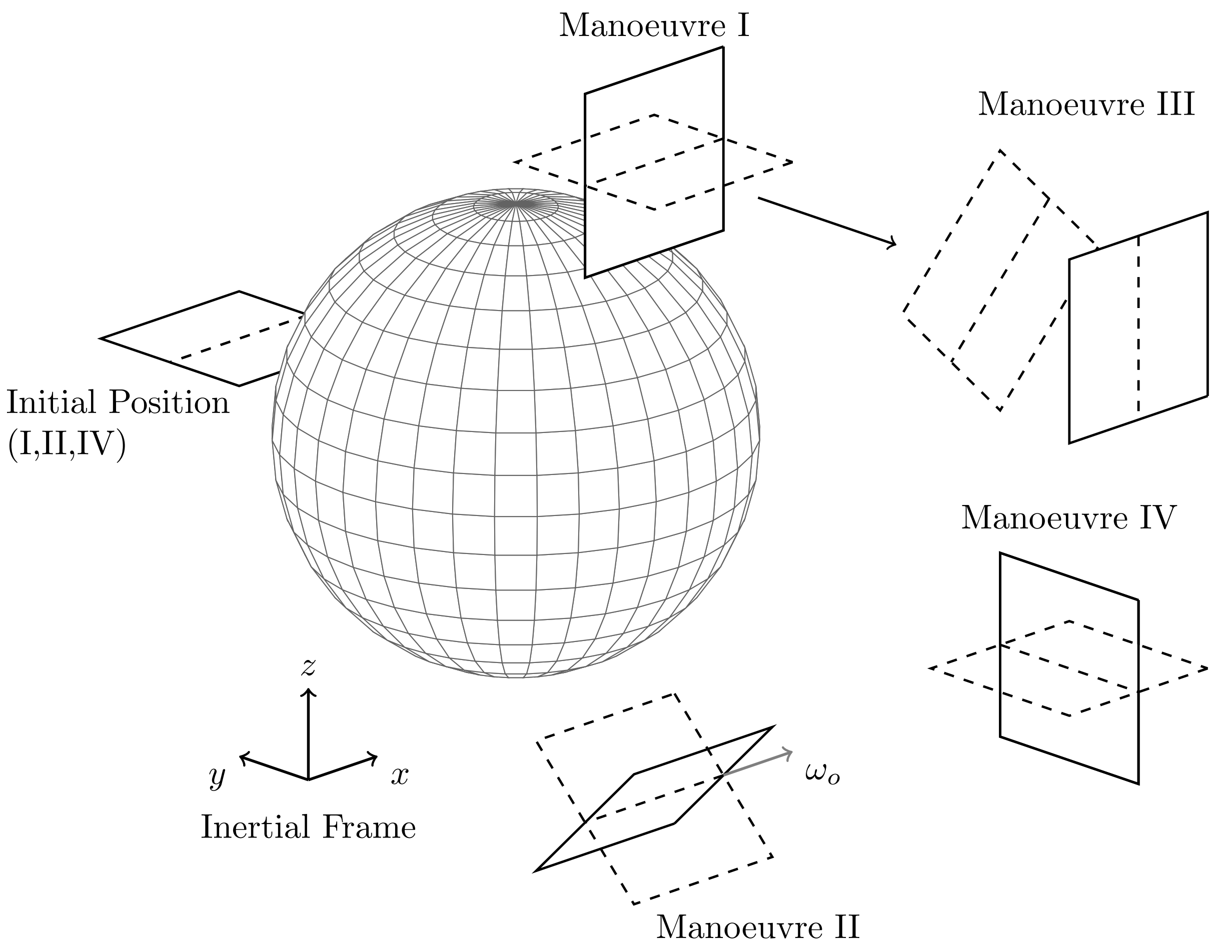

Figure 3.39: Illustration of Manoeuvres I-IV.

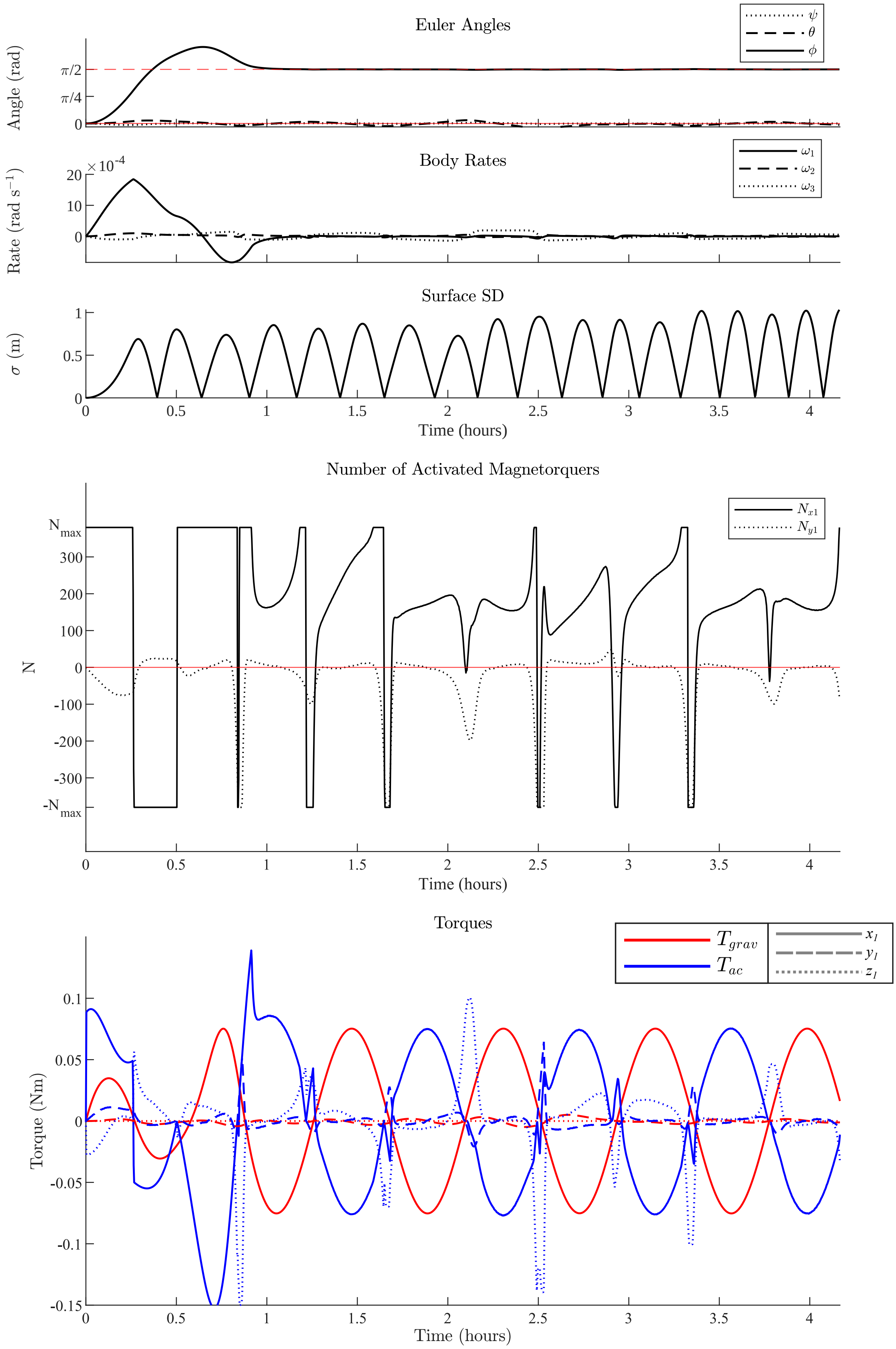

Figure 3.40: Results of simulation for Manoeuvre I.

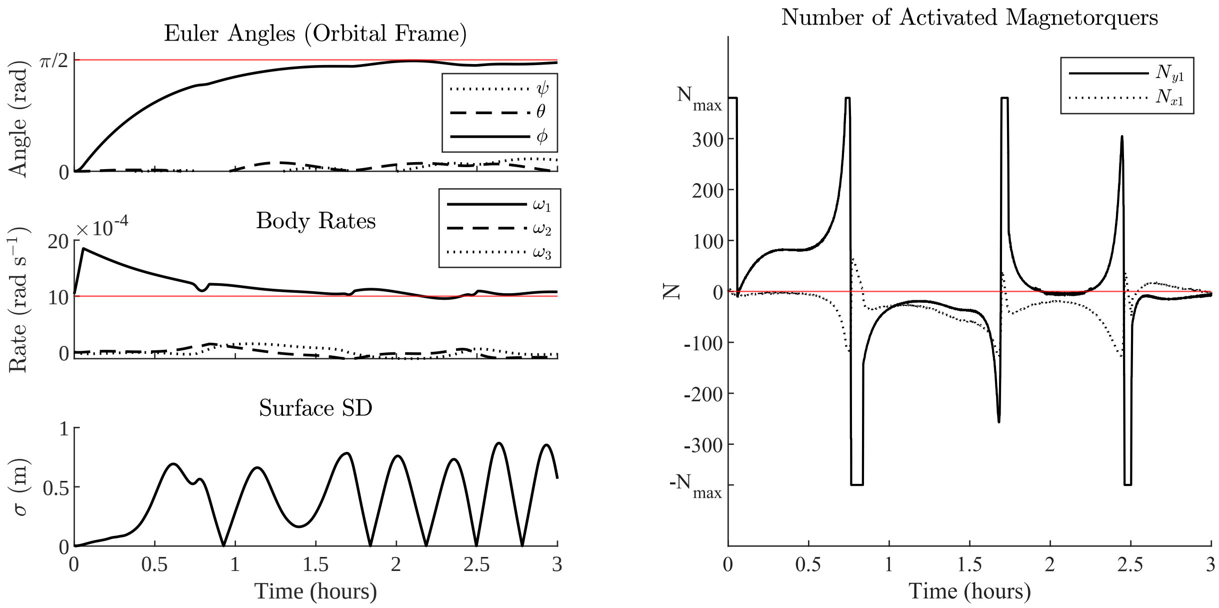

(a) **(b)**

Figure 3.41: Results of simulation for Manoeuvre II.

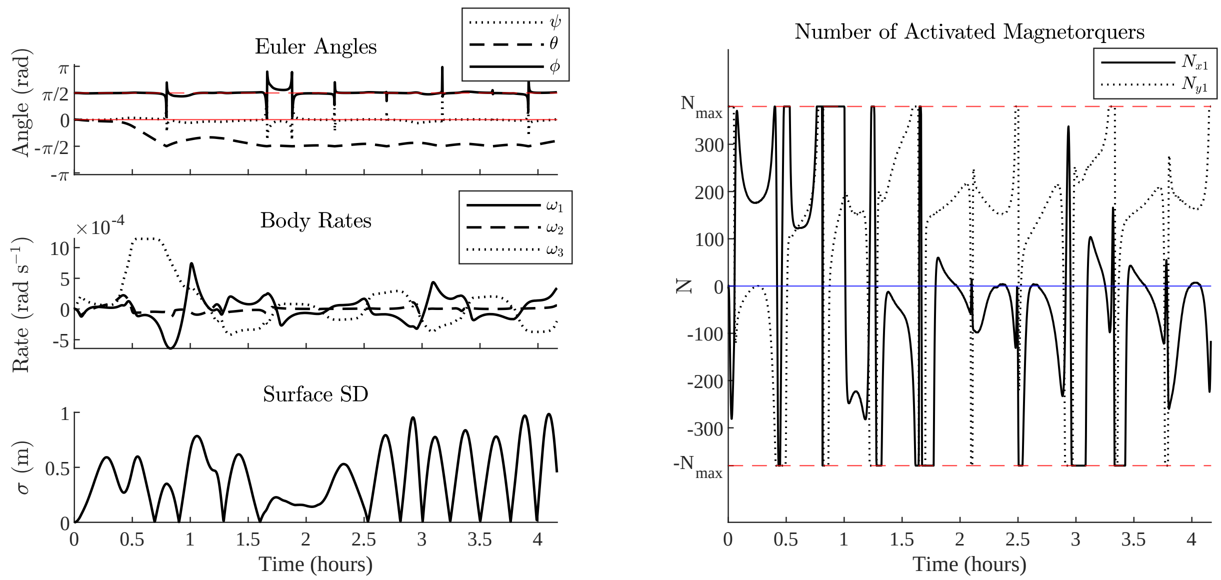

(a) **(b)**

Figure 3.42: Results of simulation for Manoeuvre III.

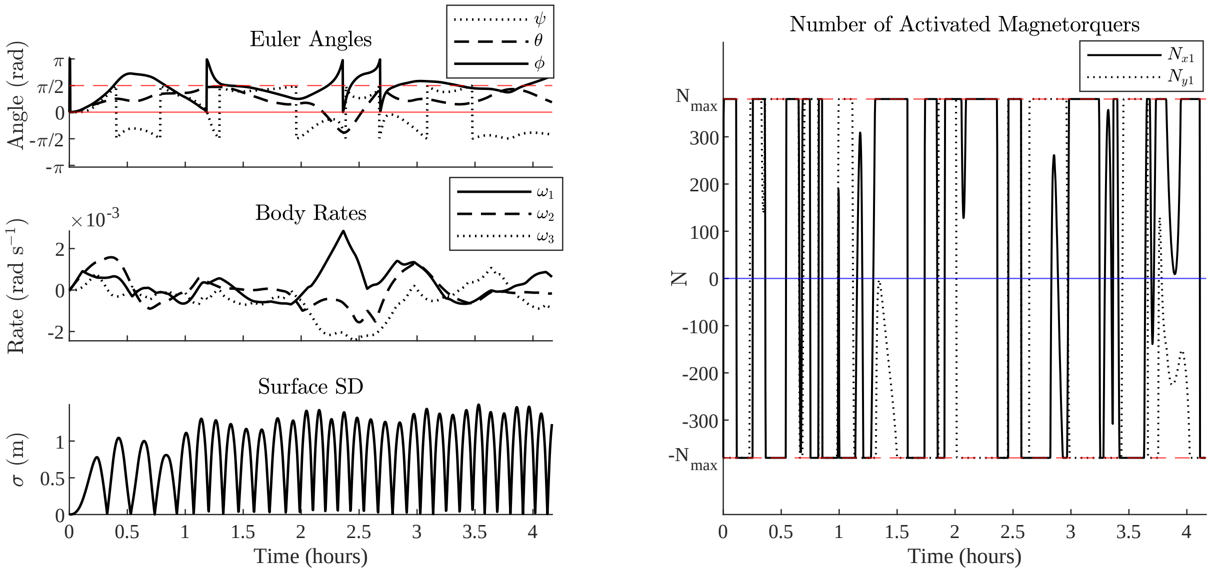

(a) **(b)**

Figure 3.43: Results of simulation for Manoeuvre IV.

when compared to the results of Manoeuvre I. This shows that the use of gravity gradient stabilised configurations as "resting points" in between attitude manoeuvres could be an efficient strategy, depending on the mission requirements and desired attitudes. Manoeuvre III begins with the structure facing the inertial y-direction because with the initial orientation used for the other manoeuvres, as shown in Fig. 3.39, the magnetic torques are unable to cause rotation around the inertial z-axis. This is because the field direction is near to the positive or negative z direction for the majority of the time. However, manoeuvres I and III could be combined, in the sequence I, III and then the reverse of I, to achieve a rotation equivalent to purely rotating around the inertial z-axis. A final note is that the surface SD is much higher in all cases here than in the previous results of Sec. 3.1.2, approaching 1 m for the successful manoeuvres. This is due to the gravity gradient torque acting on the structure, as it was found that performing manoeuvres in the absence of this torque did not produce such large surface deformations. Although the surface SD is much higher here, the deformation itself is smooth with no points of large local curvature, as would be the result of using centralised torquing.

3.4 Chapter Summary

In this chapter, a novel attitude control strategy for large space structures was proposed and analysed. First, the use of distributed torques for the attitude control of flexible structures was investigated, through the use of a 2D flexible beam model and then with a 3D spring mass model of a generic, flexible truss structures. In both cases it was found that distributed torquing led to significant reductions in structural deformation during slew manoeuvres, and thus the motivating assumption that it may be desirable to distribute the torquing actuators throughout a 3D-printed large space structure was verified numerically. Two configurations of a distributed magnetorquer array were then presented, the radial and orthogonal arrays. Each configuration was analysed through the use of rigid body simulations, and due to its reduced computational complexity the orthogonal array was selected as a more suitable strategy for further analysis. A length-scaling analysis was then performed, which found that the strategy could be suitable for lightweight structures at a length-scale of approximately 100 m. The spring-mass model was then used to perform orbital simulations of a flexible structure and demonstrate attitude control in the presence of gravity gradient torques and a time-varying magnetic field.

Chapter 4

Laboratory Demonstration of a Magnetorquer Array

Magnetorquer arrays were proposed as a form of distributed attitude control in the previous chapter, with a length-scaling analysis of the concept and numerical simulations presented. In this chapter, a laboratory-scale demonstration of the concept is presented, and used to investigate an implementation of the control algorithms developed on physical hardware. While Chapter 3 demonstrated attitude control of a LSS with the strategy through simulation, it was thought necessary to develop a hardware implementation of the control algorithms and array, in order to further investigate the strategy and demonstrate the feasibility of implementing the strategy physically. This led to the development of a Distributed Magnetorquer Demonstration Platform (DMDP), a 25×25 cm PCB onto which a 5×5 array of custom-built magnetorquers are mounted, the design and testing of which are the subject of this chapter.

Research questions for this chapter are as follows:

1. Can a laboratory-scale demonstration of a magnetorquer array be produced, capable of producing torques large enough to demonstrate attitude control on a spherical air-bearing?

2. Can the torque scaling, torque distribution, and attitude control algorithms presented in Chapter 3 be implemented on physical hardware and run in real-time?

3. Are any modifications to the control loop demonstrated through simulation required, to account for the use of real hardware?

The chapter is organised as follows. In Sec. 4.1, the electrical design of the DMDP is described, including details of the build and testing of the magnetorquer rods, magnetorquer driver circuitry, control circuit, and balancing platform. Section 4.2 then describes the proposed control algorithm, as used in Chapter 3 for a simulated magnetorquer array and adapted here to account for the particularities of the hardware implementation. Section 4.3 then describes the setup of attitude control experiments, performed by placing the DMDP atop a spherical air-bearing within the magnetic field of a Helmholtz cage. Results of experiments are presented and discussed, in which slew manoeuvres and detumbling in 1-axis are demonstrated using the distributed array control and torque distribution algorithm, demonstrating the effectiveness of the proposed strategy. Finally a chapter summary is given in Sec. 4.4.

4.1 DMDP Design and Fabrication

In this section, information regarding the design and construction of the DMDP are presented, including details regarding the magnetorquer coil winding and characterisation, and the design of a 3D-printed balancing platform, used to adjust the position of the system's centre-of-mass when mounted on a spherical air bearing.

An annotated figure of the fully assembled DMDP system is shown in Fig. 4.1. The DMDP consists of a 250×250 mm printed circuit board, onto which 48, 35-mm-long, ferrite-core magnetorquers are mounted. Two magnetorquers are mounted in orthogonal directions on the front and back side of the PCB, at each point of a 5×5 grid (omitting the central point, where the controller, sensors and batteries are located). A top down view of the front and reverse side of the magnetorquer array is shown in Fig. 4.2 and 4.3 respectively. The PCB has two layers. Through hole components were used for ease of assembly, and to aid in finding of faults once soldered together. The PCB is mounted to a custom-built balancing platform, which consists of three 3D-printed adjustable hinges, which house M8 threaded steel rods onto which sets of balancing weights (lasercut acrylic discs) are secured by fasteners. The balancing platform allows the position of the centre-of-mass of the system to be adjusted, with the hinged supports giving coarse adjustments while fine tuning is achieved by moving the balancing weights along the threaded rods. With the exception of the PCB fabrication, all other construction and assembly of the DMDP took place using the facilities of the Integrated Space and Exploration Technology laboratory.

4.1.1 Magnetorquers

The 48 magnetorquers were designed and built specifically for the experiment. The torquers consist of a 5-mm-diameter, 35-mm-long cylindrical ferrite core, around which 1000 turns of 0.1 mm diameter enamelled copper wire is wound. The magnetorquers were wound using a mechanical coil winder, onto which a drill chuck was attached to hold the ferrite core in place. Once wound, the ferrite core was secured via a press fit into two 3D-printed mounting brackets, which allow the completed magnetorquer to be mounted to the PCB via four M2 screws, while the copper wire is soldered directly into a through-hole on the PCB. A key requirement of the proposed control strategy developed in Ref. [140] is that the torquers are individually addressable, and have 3 discrete states, on, with positive or negative polarity, and off. This was achieved here by driving each magnetorquer via a H-bridge circuit, depicted in Fig. 4.4. This circuit allows the state of the torquer to be specified by two input signals,

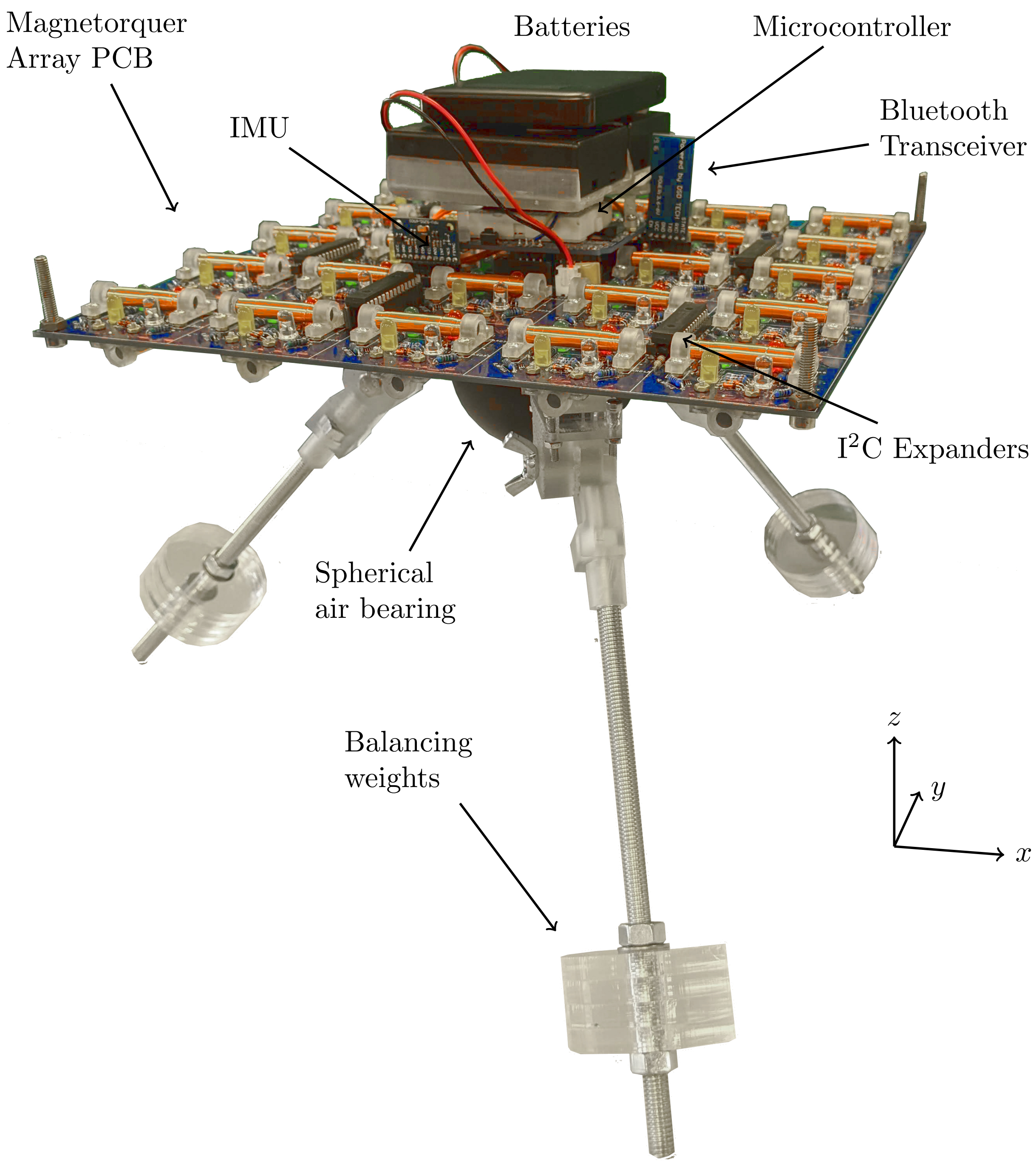

Figure 4.1: DMDP assembly, mounted on the air-bearing balancing platform and showing the main components of the system, and the body xyz frame orientation.

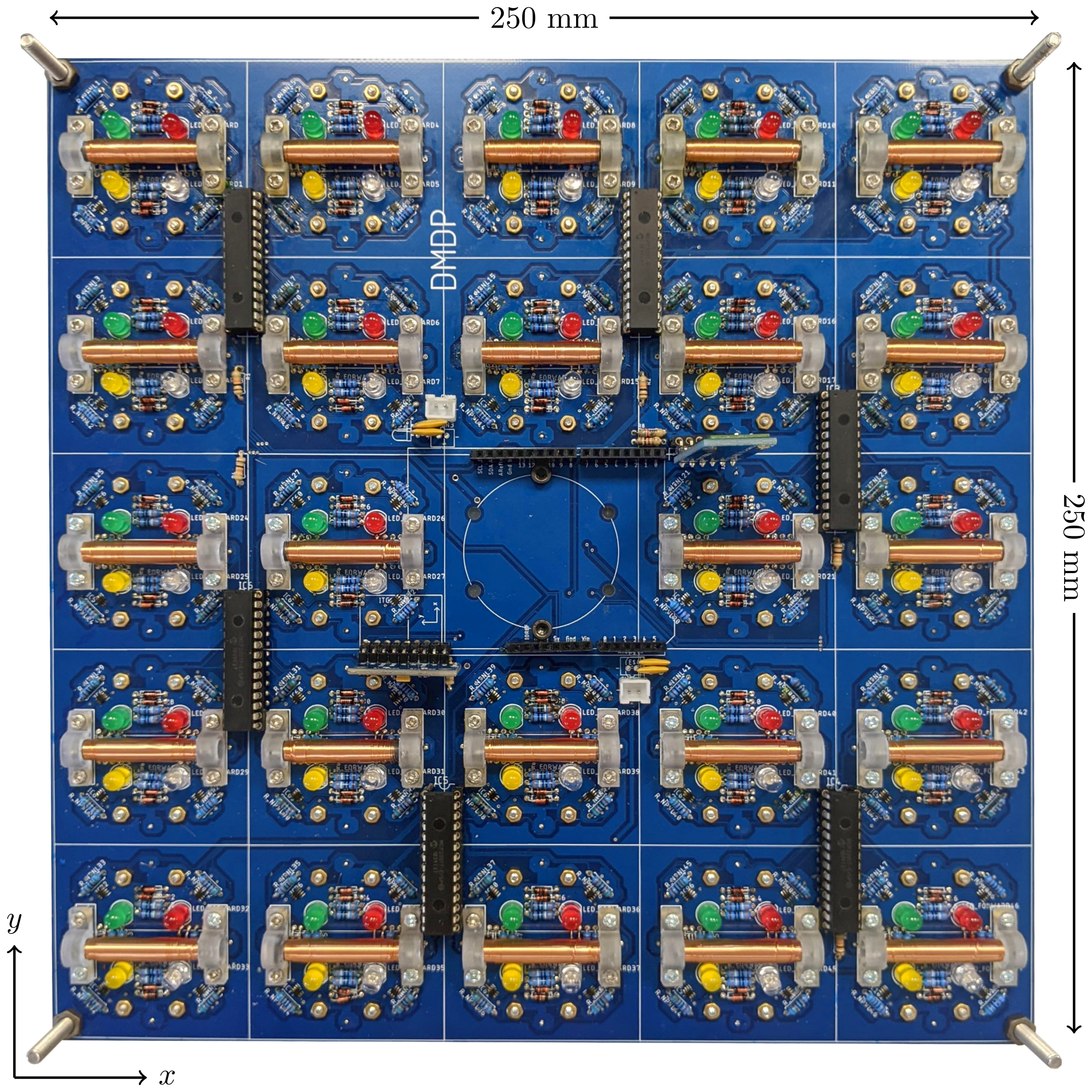

Figure 4.2: Front view of the DMDP PCB, showing the 5 × 5 array of orthogonal magnetorquers (x-direction torquers shown mounted on the front of the board).

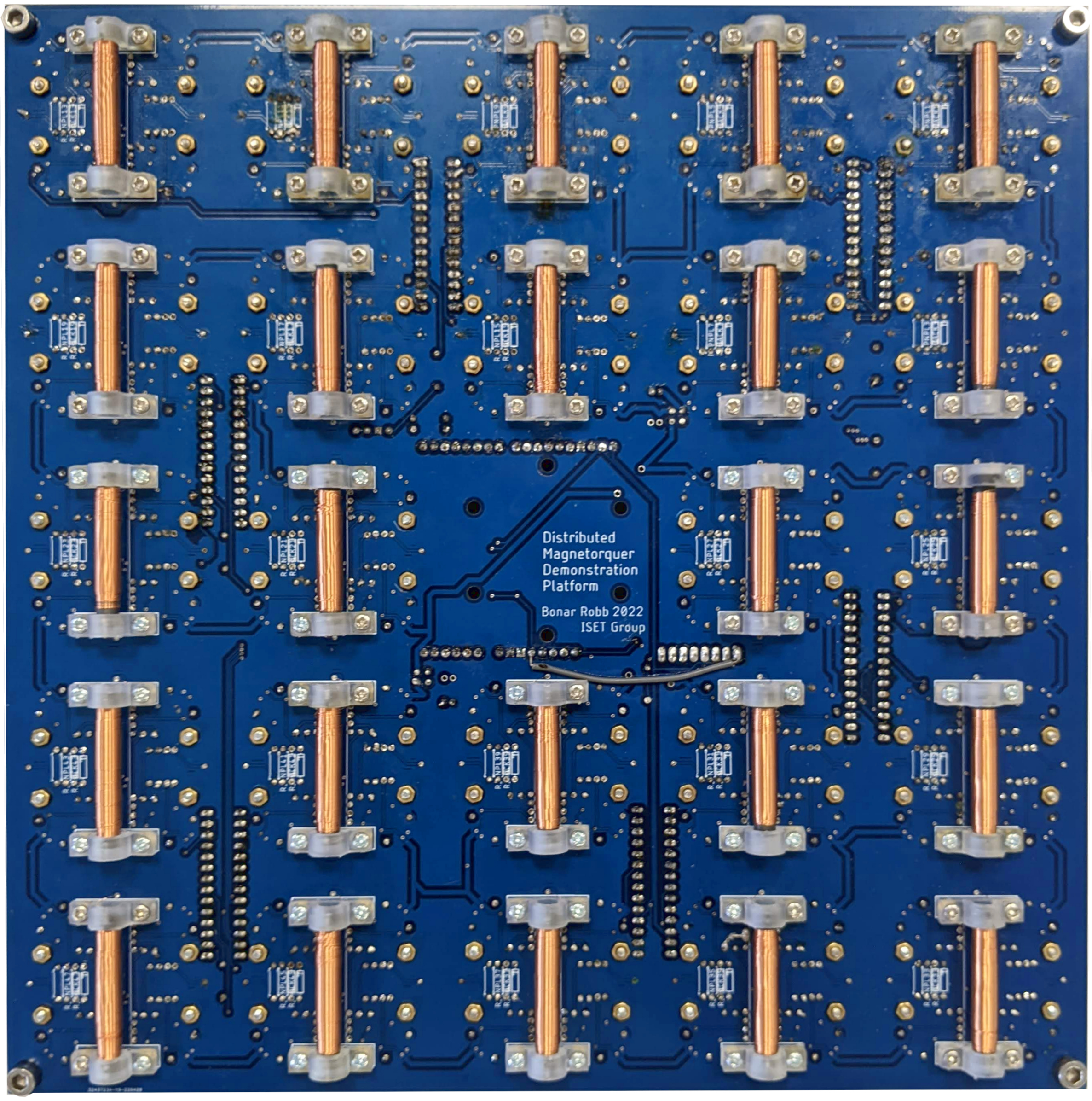

Figure 4.3: Reverse side of the DMDP PCB, showing the y-direction magnetorquers.

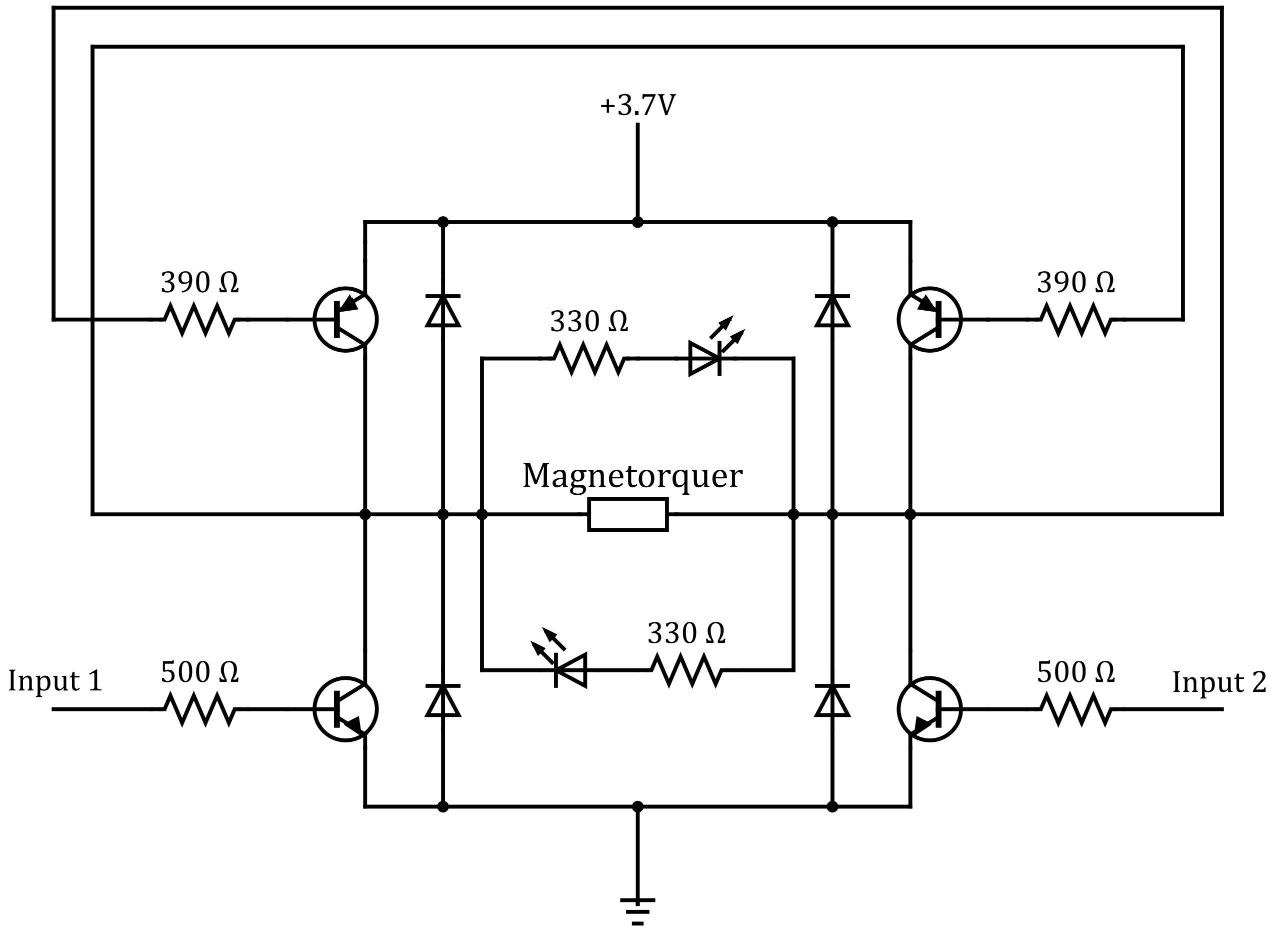

Figure 4.4: H-bridge driving circuit for each magnetorquer, allowing the polarity to be reversed via two input signals

through the use of opposing pairs of PNP and NPN transistors acting as digital switches. As illustrated in the Fig. 4.4, when both inputs are logic low, the two lower NPN transistors are closed, and current cannot flow from the magnetorquer power supply. Setting one input high opens the corresponding NPN transistor switch, which subsequently connects the base of the opposite PNP transistor to ground. This allows current to flow in one direction, energising the magnetorquer. Two LEDs are included as shown in the circuit diagram, to indicate the direction of the magnetorquer's polarity when energised and give a visual indication when the array is in operation. Further diodes are included to protect the switching transistors when the magnetorquer is switched off, at which point the collapsing field results in a back e.m.f which could potentially damage the components.

A prototype of two magnetorquers and their driving circuit was fabricated before the full array PCB, to test the H-bridge circuit performed as expected and to attempt to characterise the magnetic dipole moment of the energised magnetorquers. This prototype is shown in Fig. 4.5, showing the component placement and giving a detailed illustration of the magnetorquer construction. The prototype circuit shown here was designed to fit within a 50 mm square footprint, such that the prototype circuit could then be used on the final array by replicating the design at each point of the 5×5 grid.

An attempt was made to determine the magnetic dipole moment of the magnetorquers, by measuring the axial field strength at varying distances from the torquer. The dipole moment was calculated following the procedure outlined by Lee et. al in Ref. [170], who derive an expression for the magnetic dipole moment m, of a magnetorquer (a uniformly magnetised core of length L), given by:

$$m = \frac{4\pi}{\mu_0} \frac{1}{\left(\frac{\frac{R}{L}-\frac{1}{2}}{\left(R^2-RL+\frac{L^2}{4}\right)^{3/2}} \right) - \left(\frac{\frac{R}{L}+\frac{1}{2}}{\left(R^2+RL+\frac{L^2}{4}\right)^{3/2}} \right)} B_a \tag{4.1}$$

where R is the distance from the centre of the magnetorquer at which the axially directed field strength B_a is measured, and $\mu_0 = 1.256 \times 10^{-6}$ H/m is the permeability of free space. A magnetorquer was tested with 40 mA of current, and the magnetic field measured at 10mm intervals along the torquer axis using the magnetometer of an Invensense MPU9250 IMU unit. For each data point, 250 measurements were taken of the background field (i.e. with the magnetorquer supply switched off), which were averaged and then subtracted from 250 measurements with the supply turned on. Applying Eq. 4.1 to the data gave a final calculated value of 0.027 A m^2 for the magnetorquer at 40 mA (the nominal operational current when installed in the DMDP). Due to the small scale of the magnetorquers (requiring precise placement of the magnetometer to measure the axial field) and relatively weak generated field strength (compared to the background noise), the collected data suffered a high degree of variation. Though the calculated value is not likely to be highly accurate, an approximate value was sufficient for verifying that the torquers would be powerful enough to produce sufficient torques for rotating the DMDP within reasonable timescales, and overcoming the turbine torque of the spherical air

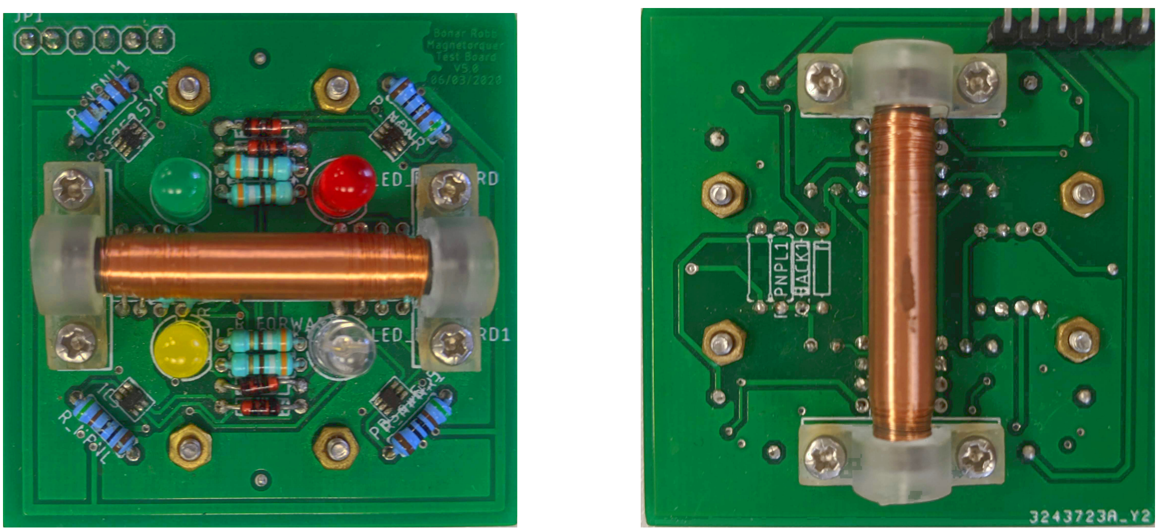

Figure 4.5: Prototype of magnetorquer driver circuit, with H-bridge circuit for front and back magnetorquers within 5cm square.

bearing. Furthermore, since a closed loop feedback scheme is employed, some degree of error in the assumed value of the magnetic dipole moment can be accounted for by the control gains of the algorithm (as discussed in Sec. 4.2).

4.1.2 Control System

As noted, each magnetorquer requires two digital inputs to specify the magnetorquer state (polarity), operating the H-bridge switches and energising the magnetorquer with the separate 3.6 V magnetorquer supply. For the 48 magnetorquers, a total of 96 inputs are required to control the full array. Magnetorquer switching commands are processed by an onboard microcontroller, with an Arduino Leonardo initially selected and later replaced with a Teensy LC board (due to the greater memory available). These boards were chosen for ease of programming, and to make use of standard, well-documented libraries for the other DMDP components. The microcontroller plugs into the magnetorquer array at the central node (as seen in Fig. 4.2), and so the controller can be easily replaced or exchanged for any with the Arduino form factor. The 96 digital outputs required to address each magnetorquer of the array is achieved through the use of six MCP23017 I^2C expansion devices (the 28 pin packages seen in Fig. 4.2), which each provide 16 digital inputs/outputs which are controlled by the microcontroller over the I^2C bus. The control system is completed by an InvenSense MPU-9250 9-axis inertial measurement unit (IMU), which combines an accelerometer, gyroscope and magnetometer on a single device, and a DSDTech HC-05 bluetooth transceiver board, which allows IMU data and switching commands to be communicated wirelessly between the DMDP and a desktop computer. Power for the magnetorquers is provided by six AA Ni-MH batteries, connected in two sets of three to provide a nominal supply of 3.6 V, and a capacity of 4200 mA h. As each torquer draws a current of approximately 40 mA, the power supply then provides over an hour of continuous operation of the full array. The controller and related devices are powered by a separate battery.

4.2 Control Algorithm and Implementation

A quaternion error feedback scheme is implemented to generate control torques for the DMDP and provide attitude control. This control law has been used widely for magnetic attitude control [113]. As noted, the motivation for developing the DMDP was to test the control strategy put forward in Chapter 3, which is repeated here for clarity of discussion. A block diagram of the control scheme is illustrated in Fig. 4.6. A measurement from the IMU is made, which provides the current values of the magnetic field, body rates and accelerometer readings. A quaternion $\overline{q}$ describing the current orientation relative to the inertial lab frame is found by applying a Madgwick orientation filter to the IMU readings [171]. This processing is performed on the onboard microcontroller, using an open source library written for processing data from the MPU9250 board [172], which also includes calibration routines which were used to determine the sensor offsets and biases. The quaternion product of $\overline{q}$ and the desired orientation $\overline{q}_{ref}$ is

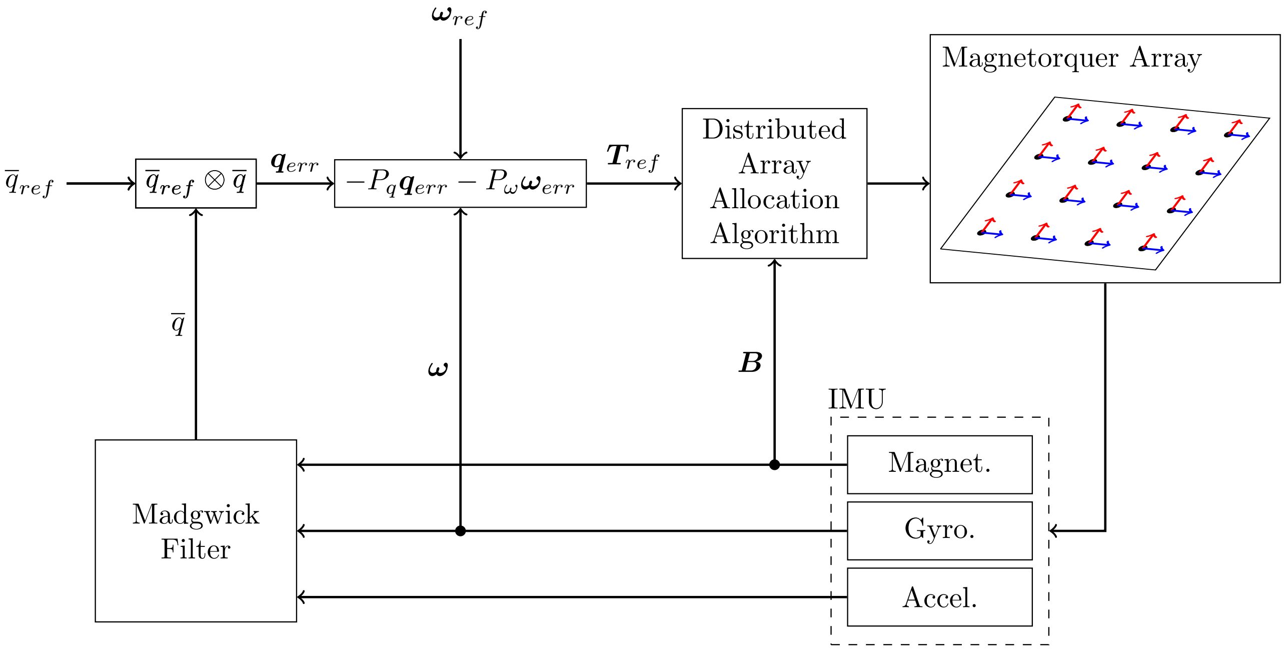

Figure 4.6: Block diagram of the DMDP control strategy

then calculated, which gives an error quaternion $\bar{q}_{err}$, describing the required rotation between the current and desired attitude. The vector part of this error quaternion is then input into the control law, along with the current and desired angular velocity vector to generate the reference torque $\boldsymbol{T}_{ref}$:

$$\boldsymbol{T}_{ref} = -P_q\boldsymbol{q}_{err} - P_\omega\boldsymbol{\omega}_{err} \tag{4.2}$$

where P_q and P_ω are the control gains. This reference torque is then input to the magnetorquer allocation algorithm described in Ref. [140], along with the current magnetic field reading $\boldsymbol{B}$. This algorithm finds the nearest possible torque to $\boldsymbol{T}_{ref}$ that can be achieved by the array for the current orientation, and outputs a command specifying which magnetorquers of the array are to be activated, and their polarity.

Following Ref. [140], the magnetic dipole moments of the magnetorquers, which are labelled $\boldsymbol{m}_x$ and $\boldsymbol{m}_y$, are coplanar with the structure's surface, and aligned with the body-frame x and y axes (as illustrated in Fig. 4.2). The torque produced by each dipole is found by taking the cross product with the external field $\boldsymbol{B}$, and are denoted by $\boldsymbol{\tau}_x$ and $\boldsymbol{\tau}_y$, though it is noted that $\boldsymbol{\tau}_x$ and $\boldsymbol{\tau}_y$ are not aligned with the x and y axes, instead lying in the plane normal to the magnetic field. Although $\boldsymbol{m}_x$ and $\boldsymbol{m}_y$ are perpendicular, for an arbitrary orientation of the plane with respect to the magnetic field, $\boldsymbol{\tau}_x$ and $\boldsymbol{\tau}_y$ will not be perpendicular in general. The total actuation torque, $\boldsymbol{T}$, must be constructed from some integer multiples of $\boldsymbol{\tau}_x$ and $\boldsymbol{\tau}_y$, since there can only be an integer number of activated dipoles. This requirement is written as:

$$\boldsymbol{T} = N_x\boldsymbol{\tau}_x + N_y\boldsymbol{\tau}_y \tag{4.3}$$

where N_x and N_y denote the number of x and y direction torquers to be activated respectively. N_x is found using the scalar product of the reference torque and $\boldsymbol{\tau}_x$, and rounding to the nearest integer, unless the value is greater than 24 (the maximum number of torquers in each direction). In that case, all the magnetorquers of that direction on the array are activated and the controller is saturated. Therefore:

$$N_x = \left\lfloor \frac{\boldsymbol{T}_{ref} \cdot \boldsymbol{\tau}_x}{|\boldsymbol{\tau}_x|^2} \right\rceil \tag{4.4}$$

Similarly, N_y is given by an equivalent expression, except that N_y is reduced by taking into account the contribution to the $\boldsymbol{\tau}_y$ direction already given by $N_x \boldsymbol{\tau}_x$, so that:

$$N_y = \left\lfloor \frac{\boldsymbol{T}_{ref} \cdot \boldsymbol{\tau}_y - N_x \boldsymbol{\tau}_1 \cdot \boldsymbol{\tau}_y}{|\boldsymbol{\tau}_y|^2} \right\rceil \tag{4.5}$$

From N_x and N_y, an activation pattern is then generated which specifies which torquers on the array are to be activated. The activation pattern is found by finding a centroidal voronoi tesselation for N_i points placed in the 5×5 grid of the array, which ensures that for any activation number, the activated torquers are as evenly distributed across the array as possible, as was shown to reduce structural deformations for flexible structures in Ref. [140]. Again it is noted that further details of this step of the torque allocation algorithm are available in Ref. [140], while the process has only been outlined here for clarity of discussion. The magnetorquer switching commands are sent to the DMDP, and the next IMU reading is taken to complete the closed loop feedback control strategy.

4.2.1 Hardware Implementation

The control strategy is implemented essentially as described on the DMDP hardware, although some modifications to the algorithm as presented in Ref [140] were required. The control torques and array allocation algorithm calculations are all performed on a laptop computer, which communicates with the DMDP via the bluetooth serial port. IMU data is read from the serial port using a MATLAB program, which then calculates the required switching command and returns this to the DMDP. The communication protocol for switching commands consists of a string constructed of consecutive sets of 3 integers ijk, for each activated magnetorquer. This is read by the DMDP controller and the corresponding output pins of the I^2C expanders set to logic high or low. The integers correspond to the expander address $i = 1, ..6$, the node $j = 1, ..., 4$ (each expander controls 4 array nodes or eight torquers total), and the torquer direction and polarity $k = 1, ..., 4$, corresponding to $+x, -x, +y, -y$ respectively. As the Madgwick filter used to estimate the DMDP attitude relies on the IMU's magnetometer reading, the magnetorquers must be switched off while an IMU reading is taken, otherwise the magnetic field generated by the magnetorquers interferes with the reading and large errors in the attitude estimation are returned. It was found that the magnetometer reading returned to the normal background field in a time of approximately 2 s after the magnetorquers were switched off. Therefore a cycle of 2 s off, 5 s on was implemented for the actuators. The IMU data is read at the end of the 2 s period, the control calculations are performed and then the specified magnetorquers are switched on for 5 s. These values were found through trial and error, and were found to provide a balance between stable attitude estimation and control effectiveness for the angular rates encountered.

4.3 Attitude Control Experiments

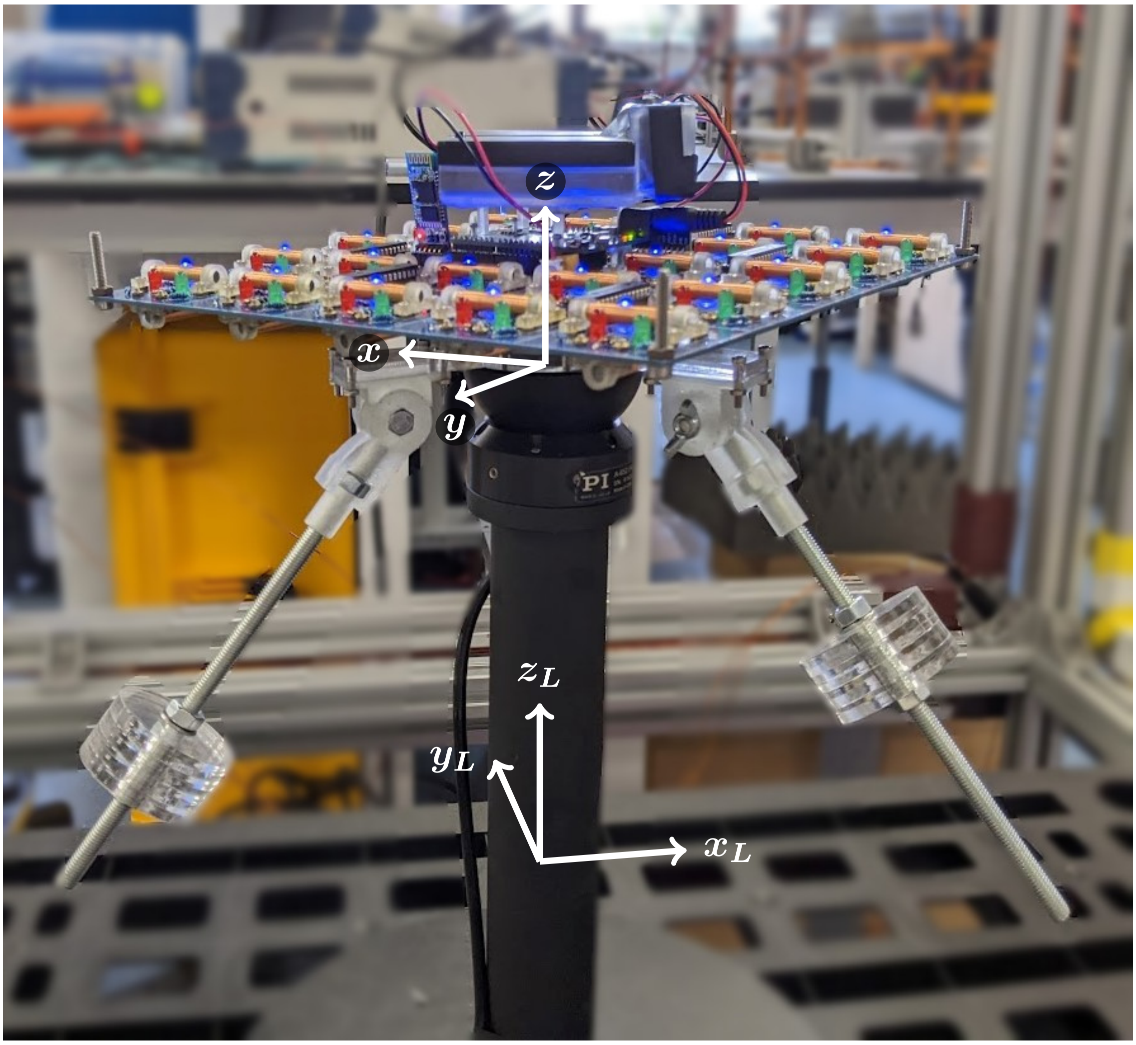

Figure 4.7: DMDP mounted on a spherical air-bearing within a Helmholtz cage for attitude control experiments, showing the inertial $x_Ly_Lz_L$ lab frame and xyz body frame.

In this section the results of attitude control experiments are presented, in which the DMDP was mounted upon a spherical air bearing, simulating free-fall, and a Helmholtz cage is used to generate an external magnetic field. The aim of these experiments is to verify the performance of the control algorithm described in Sec. 4.2, and demonstrate that the torquer allocation algorithm developed in Ref. [140] conforms with the results of numerical simulations and produces the torques expected by this previous analysis. Furthermore, the aim of this hardware implementation of the strategy is to determine what effect the modifications to the control loop such as the required duty cycling, inclusion of sensor noise and uncertainties, and other disturbances have on the performance of the strategy when compared with the more ideal scenarios considered in previous numerical simulations.

Table 4.1: DMDP and experiment data.

Side length		250 mm
Mass		
Array		0.7222 kg
Batteries		0.3476 kg
Platform		0.6390 kg
Bearing		0.2112 kg
Total		1.92 kg
Mom. of inertia (CAD estimate)		[0.026,0.026,0.034] kg m^2
Mag. dipole moment (approx.)	m	0.03 A m^2
Mag. Field (Lab frame)	$\boldsymbol{B}$	[2,100,45] μT
Max. Torque (est.)	$\boldsymbol{T}$	1.5×10^{-4} N m
Control gains	P_q	40
	P_ω	400
Duty cycle off time		2 s
Duty cycle on time		5 s

The DMDP and balancing platform were mounted on a PIglide HB Hemispherical Air Bearing, a 75 mm diameter hemisphere which sits upon a cushion of air in a curved pedestal, supplied by an air compressor at 60 PSI, shown in Fig. 4.7, which also shows the body xyz frame, and the inertial lab frame $x_L y_L z_L$. The air bearing allows the system to rotate freely around the lab z_L axis, and gives $\pm 45°$ of rotation around the other axes. The system was balanced by trial and error, by adjusting the vertical and relative position of the three sets of weights on the platforms legs. When the centre-of-mass of the system is below the centre of rotation (centre of the bearing hemisphere), the system oscillates as a pendulum, while when above it the system will tilt over due to the torque exerted by gravity. At this stage, attitude control was sought to be demonstrated around a single axis (the lab z_L-axis), and so the centre-of-mass was placed just below the centre of rotation, to ensure stability around the other axes. The lateral position of the centre-of-mass (it's location relative to the central axis) determines the equilibrium attitude of the system, and it was sought that this orientation would result in the DMDP z-axis and lab z_L axis being aligned. This was again adjusted by trial and error, by adjusting the position of the balancing weights until the desired equilibrium point was reached. The platform is placed in the centre of a Helmholtz cage, which consists of three pairs of copper coils wound around the faces of a square frame. One pair of coils was energised, and supplied with a current of 3 A. The resultant field was measured with a handheld magnetometer and found to be [2,100,45] μT (in the lab frame), giving a total field strength of 205 μT, approximately four times greater than the background field strength of 54.02 μT measured in the laboratory. As the largest component of the field is directed in the y_L direction, the DMDP is then capable of producing torques around the z_L axis for attitude control purposes, although there will be some component in the other axes which then act to excite or dampen the oscillation of the system around the equilibrium position. The physical properties of the DMDP and other data is summarised in Table 4.1.

Results of attitude control experiments are presented in Figs. 4.8, 4.9 and 4.10, which show the IMU measurements and number of active torquers during a 90° and 180° slew manoeuvre around the z-axis, and detumbling from an initial rate of 15 deg/s respectively. Though the system orientation is described by quaternions within the control algorithm, Euler angles are plotted here for clarity of discussion. The angles ψ, θ and ϕ correspond to a sequence of rotations corresponding to the z, y and x axis respectively, describing the orientation of the body xyz frame relative to the lab $x_Ly_Lz_L$ frame, as illustrated in Fig. 4.7. For the slew manoevures, the angle error is seen to smoothly rise to 0 in both cases, though there is some overshoot of approximately 5° during the 90° manoeuvre, and a slight steady state error of approximately 2° after the 180° manoeuvre. Not that the Euler angles and magnetic field are only measured once every 7 s, at the end of the 2 s period where the magnetorquers are switched off, while the body rates, taken directly from the gyroscope measurement, are taken as frequently as they

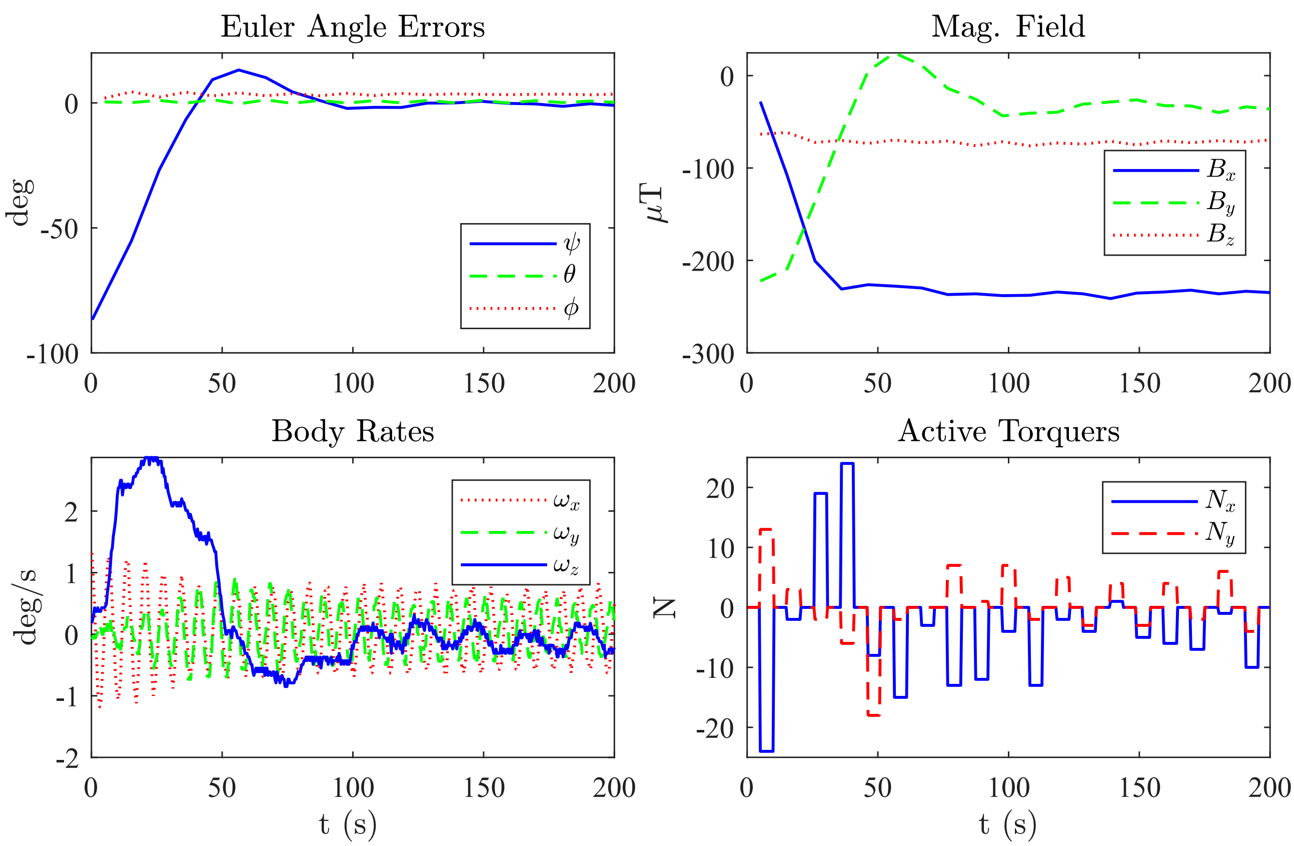

Figure 4.8: Results of experiment for a 90° slew manoeuvre around the z-axis.

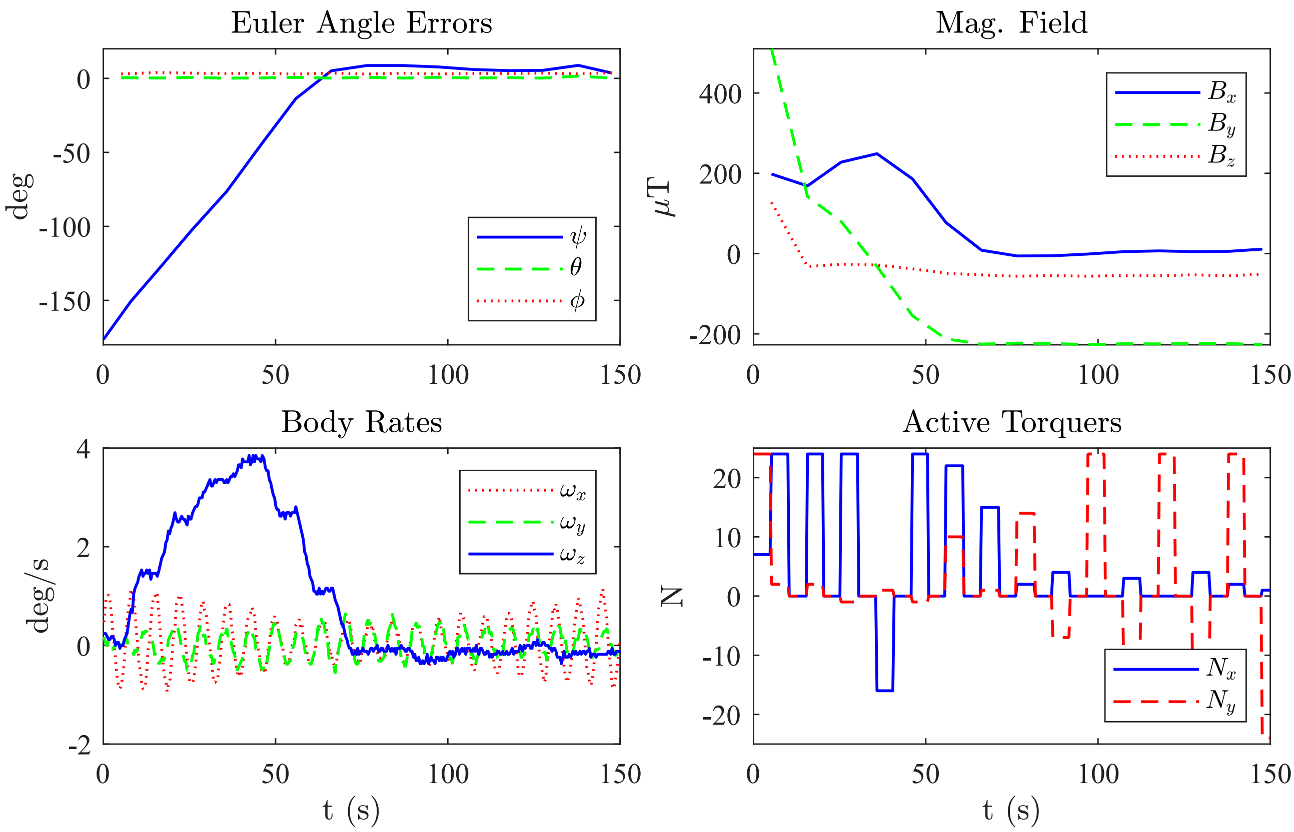

Figure 4.9: Results of experiment for a 180° slew manoeuvre around the z-axis.

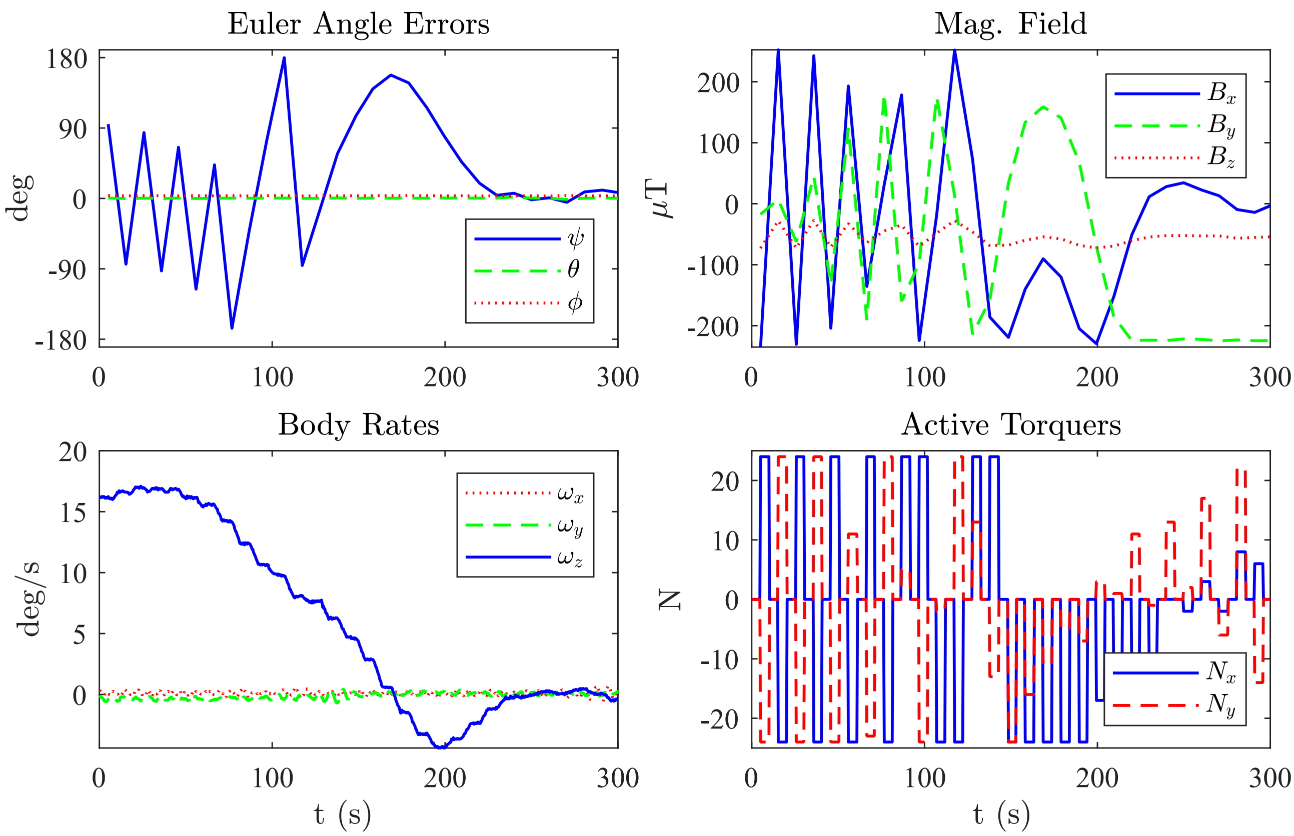

Figure 4.10: Results of experiment, detumbling from an initial rate of 15°/s around the z-axis to rest.

are available to be read by the MATLAB program. This data was available at a frequency of approximately 3 Hz. The torque activation plot shows that the array is performing as expected, with the initially large torque provided by activating all 24 torquers in the x-direction, before the polarity is reversed to brake the system and minor adjustments provided by a lower number of torquers for the remainder of the manoeuvre. This behaviour corresponds well with the results of simulations in Ref. [140], where manoeuvres were also performed by first activating the full array and minor adjustments later made by activating a fewer number of magnetorquers. Similarly, the torque distribution procedure is seen to correspond well with earlier simulation results, with the location of the activated torquers being evenly distributed across the array at all times. This was confirmed visually when the DMDP was in operation by observing the illuminated LEDs, which are used to indicate magnetorquer activation. While the manoeuvre is performed around the z-axis, oscillations due to the gravitational torque are clearly visible in the body rate plots, though these oscillations remain below 3° around either axis. While the controller is attempting to counteract these oscillations, we note again that the DMDP is oscillating around an equilibrium point and so it is not clear if the system is having an effect on these oscillations. The time taken to perform a 90° slew of approximately 1 minute corresponds with the expected time for an array of 0.03 A m^2 torquers, which is close to the result of Eq. 4.1 which it was noted was likely only an approximate value due to high uncertainties in the field measurement. When detumbling, the DMDP is found to come to rest from the initial rate of 15 deg/s in approximately 175 s, before moving to the target attitude. Note that for the initial 100 s of the detumbling phase the shape of the Euler angles plot and magnetic field are due to the sampling frequency being lower than the rotation rate. This is also why initially, the deceleration is quite low, as the system is rotating fast enough that the magnetic field direction in the body frame changes significantly during a single magnetorquer activation cucle. Therefore, this tumbling value of 15 deg/s is likely close to the maximum rate that the system can detumble, without some modification to the control algorithm or duty cycling of the torquers.

4.4 Chapter Summary

This chapter has described the design, build and testing of a distributed magnetorquer array for spacecraft attitude control. The DMDP was built to test the control algorithms developed in the earlier work of Chapter 3, and so the quaternion error feedback scheme used previously was implemented, where the torque produced by the array is scaled by changing the number of activated torquers at a given time, and using a torquer selection algorithm which results in the activated torquers being as evenly distributed across the array as possible for any number of activated torquers. First, the design and construction of the DMDP, its magnetorquers, and the 3D-printed balancing platform used to adjust the position of the centre-of-mass of the system were presented. The adaptation of the control algorithm of Chapter 3 for the DMDP hardware was then discussed, and then the results of experiments presented in which slew manoeuvres and detumbling around 1-axis are demonstrated.

Chapter 5

3D-Printed Conductive Structures

Another potential strategy for the magnetic attitude control of LSS is the use of large current loops, embedded within the spacecraft structure. As opposed to the magnetorquer rods considered in Chapter 3, which increase the magnetic field strength generated through the use of a core material with high magnetic permeability, large current loops (or "air-core" magnetorquers) can achieve a large magnetic dipole moment by virtue of enclosing large areas. This is a key difference between the two strategies, and results in a difference in the length-scaling of the concepts. As discussed in Chapter 3, estimates of the dipole moment to mass ratio for magnetorquer rods were given, but these were based on values of commercially available magnetorquer rods. As these are designed primarily for microsatellites, it is likely that the dipole moment (and thus torque) values given are limited by the thermal constraints of being housed within a microsatellite, or by the power available. For a large current loop in a LSS, it is likely that the thermal and power constraints will be much less limiting than for microsatellites, as the conducting wire can be placed at a greater distance from the other subsystems, and the spacecraft can intercept a large amount of solar radiation for power. A further significant difference between the two concepts is that, for the distributed magnetorquer arrays, the actuator torques were considered to be applied at single points. For a large current loop, the torque produced is a result of integrating the Lorentz forces acting on each section of the pathway, which will act in various different directions at different points of the structure. The structural deformation caused by a current loop must therefore be considered in the analysis, and the Lorentz forces acting on the pathway must be modelled, whereas for the distributed magnetorquer array, the torque can be directly calculated and applied to the structure as a point torque at the magnetorquer sites. The control-structure interaction is then a further key difference between this control strategy and the magnetorquer arrays of the previous chapter, with quite different analysis and modelling required to demonstrate the feasibility of the concept.

The research questions for this chapter are the following:

1. What is the maximum length-scale that a conductive structure could provide useful attitude control, considering thermal and power limitations?

2. How rigid would a structure need to be for current loops to provide attitude control without excessive deformation?

3. Can large embedded current loops demonstrate attitude control of a flexible structure in orbital simulations, where the external field direction is constantly changing and there are disturbing gravity gradient torques?

Section 5.1 first discusses the physical principles of current loops, considering how Lorentz forces lead to a torque which can be exploited for attitude control purposes. A variety of current loop geometries for planar spacecraft are presented, demonstrating that in theory it is possible to achieve three axes of effective dipole moment by combining different conducting pathway geometries. A preliminary feasibility analysis of the concept is performed in Sec. 5.2, where a representative calculation is first performed to estimate the torque generated by a conducting pathway, and rigid body-simulations are then used to estimate whether the strategy could provide attitude control, where pointing requirements are provided by a simplified orbital reflector mission concept. Length-scaling laws are then derived in Sec. 5.3, by defining a simplified thermal model and deriving an expression for what fraction of a spacecraft's mass would need to be taken up by a conducting pathway in order to counteract the maximum gravity gradient torque which that spacecraft may experience. In Sec. 5.4, the spring-mass model first introduced in Chapter 3 is then modified and used to model the Lorentz forces acting on a conductive pathway, with numerical simulations performed to investigate the ability of current loops to rotate planar spacecraft in the absence of disturbances and across a range of structural flexibility and truss densities. Section 5.5 then presents an attitude control simulation of a flexible, conductive structure, demonstrating that the strategy is capable of performing slew manoeuvres in LEO and in the presence of gravity gradient torques and a time-varying magnetic field direction. Section 5.6 then summarises the findings of the chapter.

5.1 Current Loop Geometries for Planar Spacecraft

As presented in Sec. 2.4 of the technical introduction, A rigid current loop in a uniform external magnetic field will experience a torque given by :

$$\boldsymbol{T} = I\boldsymbol{A}_e \times \boldsymbol{B} \tag{5.1}$$

Considering a planar, 3D-printed spacecraft with conducting pathways, there are a number of possibilities for the geometries that these current loops could take. The most straightforward geometry is to have one large current loop around the perimeter of the spacecraft (as in Ref. [116]). This current loop would enclose the maximum possible area on the spacecraft, and could only produce attitude control torques around some axis lying in the plane of the structure, due to the cross product in Eq. 5.1.

The most efficient geometry in terms of the mass required would be a large closed loop, since the maximum area enclosed for a given perimeter length is given by a circle. This geometry is illustrated in Fig. 5.1a), where the current loop is shown as a blue path on the perimeter of the top layer of the structure. Although less efficient in terms of the path length to enclosed area ratio, for a flexible structure it may be desirable to have multiple current loops spaced throughout the structure, illustrated in Fig. 5.1b). This geometry would distribute the control torques throughout the flexible structure, which has previously been shown to reduce structural deformations during slew manoeuvres, as was demonstrated in Chapter 3. Figure 5.1b) shows three current loops on both the top and bottom layer of the structure, though an arbitrary number of loops could be fabricated depending on the flexibility of the structure and thus the need to distribute control torques. A given current loop can only produce torques around one axis, defined by the cross product of the enclosed area surface normal vector and the magnetic field vector in Eq. 5.1. Magnetic attitude control systems generally employ three orthogonal magnetorquers, so that by varying the current in each torquer control torques can be produced around any axis lying in the plane normal to the field vector. Similarly, this could be achieved for a 3D-printed conductive structure by constructing current loops which enclose area in the

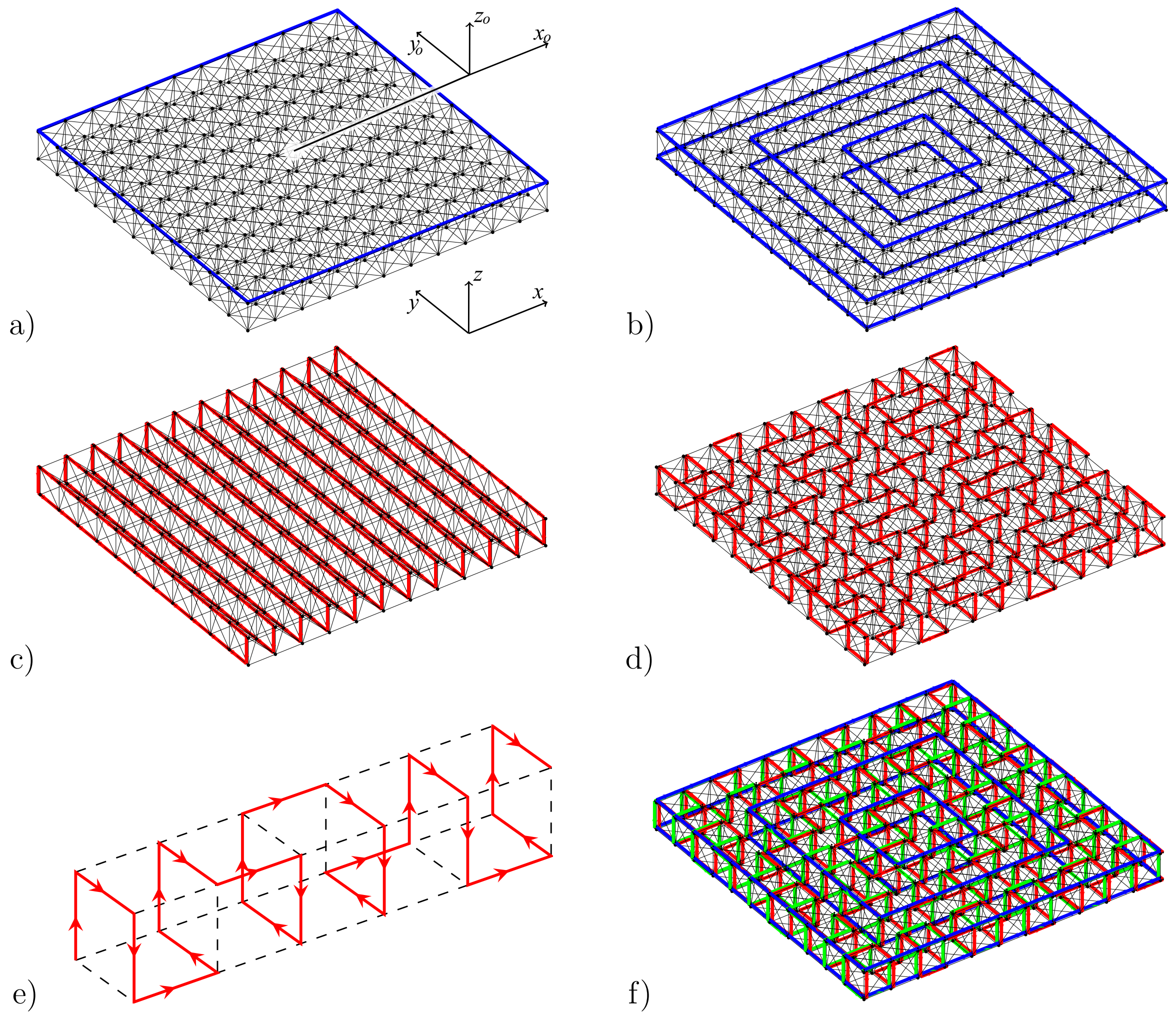

Figure 5.1: Current loop geometries for attitude control of a square, planar truss structure

yz or xz plane of Fig. 5.1. Although we are considering a planar structure, these current loops would require the structure to have some depth. One possible configuration is shown in Fig. 5.1c), which shows current loops lying in the yz plane on each layer of the structure. Another possible configuration is shown in Fig. 5.1d) and detailed in Fig. 5.1e). Figure 5.2 gives a more detailed illustration of the concept, highlighting how the single, rectangular coil section detailed in Fig. 5.1e) forms part of the continuous pathway. In this case, the conducting pathway is formed of a single continuous circuit, rather than separate loops, which winds back and forth across the structure, as shown for a single unit in Fig. 5.1e). Though this geometry may be less mass efficient than the multiple current loops of Fig. 5.1d), it may be desirable to have a single continuous pathway, and furthermore this geometry is included as it demonstrates a path geometry that could be implemented in long trusses as well as the planar lattice structure shown here. Figure 5.1f) shows how three orthogonal coil directions can be achieved by overlaying patterns b) and d), where the third direction is achieved by rotating the pattern shown in Fig. 5.1d) by 90°, shown in green on the figure. By varying the current in each loop, the strength and direction of the overall magnetic dipole moment of the system can be specified, allowing torques to be produced in any direction perpendicular to the magnetic field. Rather than overlaying the conductive pathways, it is possible to envision multiple conducting paths within

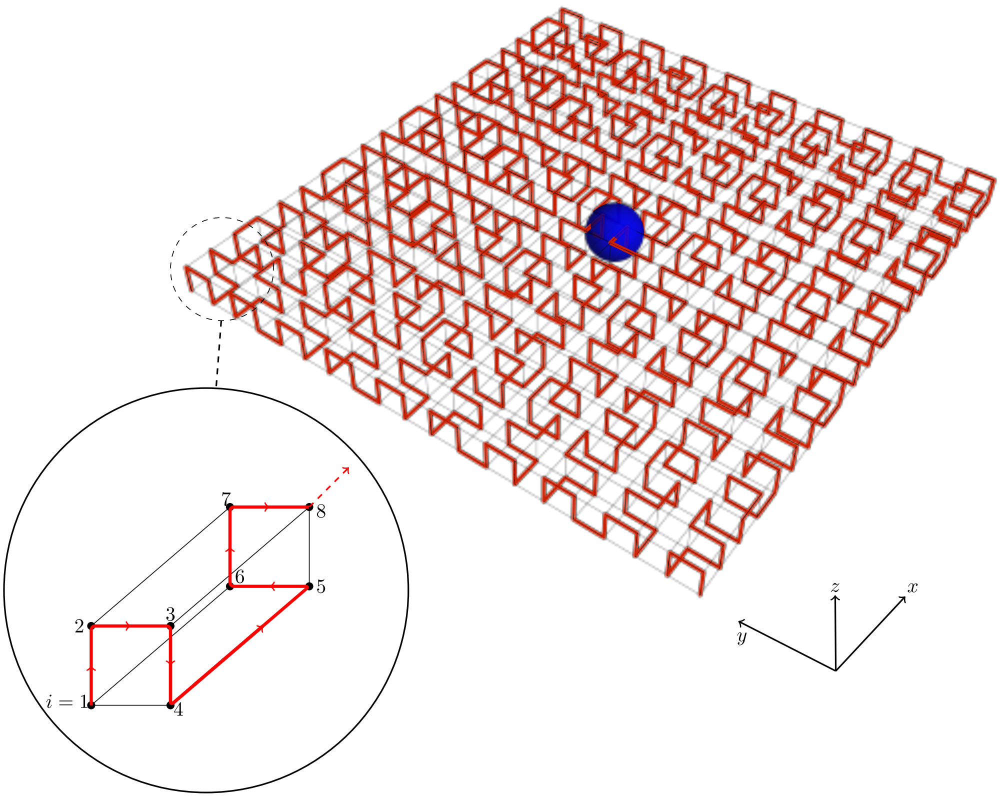

Figure 5.2: A cubic lattice support structure with an embedded conducting path shown in red. Interaction between the structure's current-carrying elements and the Earth's magnetic field generates torques which may then be used for attitude control. The blue sphere represents the spacecraft bus. The expanded image illustrates the first points in the path sequence on a segment of the structure.

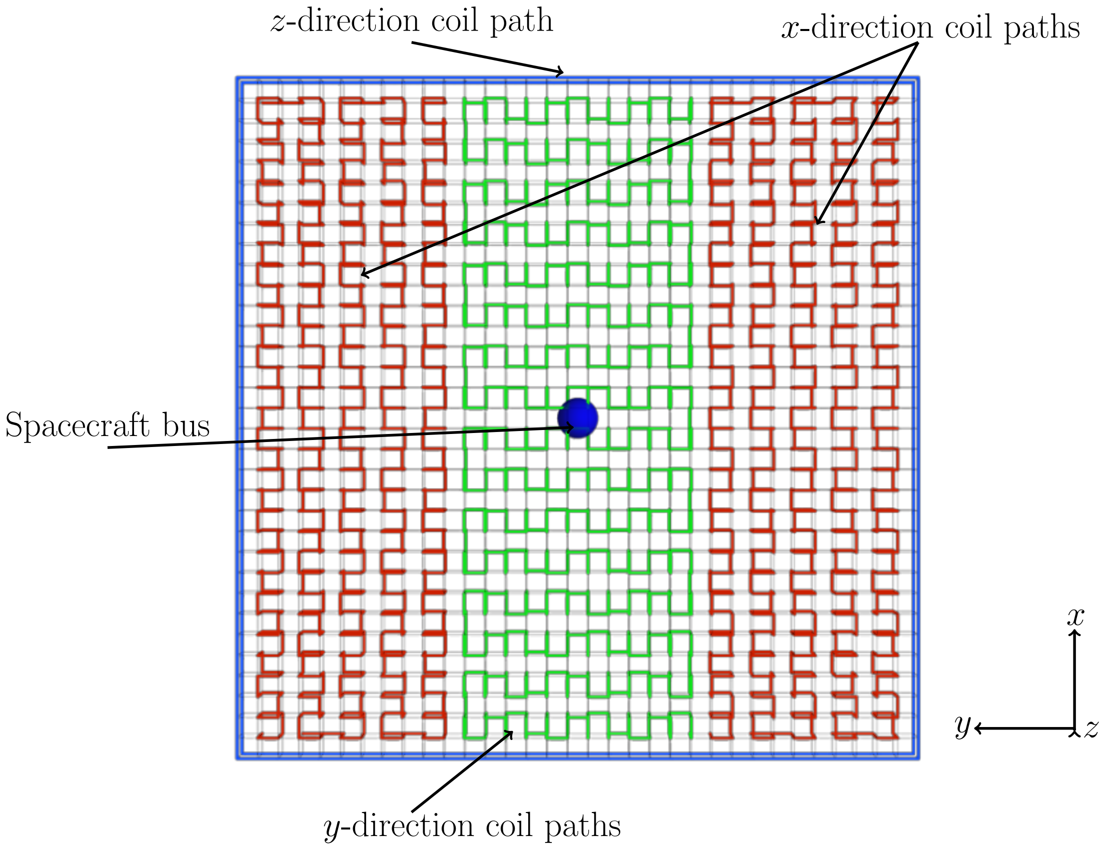

Figure 5.3: A conducting structure with 3 different conducting paths. An "effective" magnetic dipole moment is given in the x direction by the green path, the y direction by the red, and z direction by the blue path.

the structure. Figure 5.3 illustrates this concept, where the paths in are separated into different sections of the structure. This may be required if overlaying the pathways was not possible due to the specific construction of the structure, i.e. if the structural elements themselves were conductive and so pathways could not be overlaid without short circuiting each current loop. In this case, a further possible configuration allowing 3-axes of controllable dipole moment would be to have switching nodes at each node of the structure, allowing the conductive pathway geometry to be programmed as required, switching between the geometries of Fig. 5.1a-d, or sectioned pathways as in Fig. 5.3 to produce the desired magnetic dipole moment.

5.2 Rigid-Body Conductive Structures

In this section, a preliminary analysis is performed of the attitude control concept by considering the torque generated by a rigid conductive structure. The structure is considered to be a rigid body here so that the current geometry does not change shape as the structure deforms, which would alter the enclosed area and thus torque generated by the current loop. First, a method for calculating the torque produced by geometry D of Fig. 5.1 by direct summation of the contributing Lorentz forces is presented. Then, some first estimates of the physical properties of a conducting structure are made and used to determine the magnitude of torque that could be achieved with strategy. Preliminary attitude control simulations are then performed for this example spacecraft, demonstrating detumbling and attitude control for a simplified orbital reflector mission scenario, again considering the spacecraft to be a rigid body. Later analysis then considers the potential physical properties of a conductive structure spacecraft in more detail, and simulates the current loop/structure interaction for a flexible structure. The aim of the preliminary analysis in this section is firstly to further demonstrate the principle of operation of the concept, through explicitly calculating the torque generated by a current loop, and then to give a preliminary assessment of the feasibility of the concept with regards to potential mission requirements and physical parameters such as the structure's areal mass density and length-scale.

5.2.1 Torque Calculation for a Rigid Conductive Structure

Figure 5.2 shows an illustration of the proposed spacecraft, where a conducting path is shown in red, and winds back and forth across the structure. The spacecraft bus is represented by the blue sphere at the centre-of-mass, and the reflective film is not shown for clarity. The coil path is taken to consist of 3/4 of a turn in the xz-plane, followed by a step in the y-direction which repeats back and forth across the structure, as shown in the expanded view of Fig. 5.2. The following analysis refers to a list of nodes which sequentially describe this path. The force on an individual path segment between points with indices i and $i+1$, in the presence of an external magnetic field $\boldsymbol{B}$, is given by the Lorentz force law:

$$\boldsymbol{f}_i = I\ \boldsymbol{L}_i \times \boldsymbol{B} \tag{5.2}$$

where $\boldsymbol{L}_i$ is a vector with magnitude equal to the segment length and aligned from i to $i+1$, and I is the current. The expanded view in Fig. 5.2 shows the first points in the path sequence, from which it is evident that this vector is given by the difference in position of points i and $i+1$. Position vectors are taken from the centre-of-mass of the spacecraft, such that:

$$\boldsymbol{L}_i = \boldsymbol{r}_{i+1} - \boldsymbol{r}_i \tag{5.3}$$

To calculate the torque contributed by this line segment, it is assumed that the entirety of the force acts upon the midpoint of the line segment rather than being distributed evenly across the path element. This assumption is made since the segment length is small compared to the overall spacecraft side length. In this case, the torque contributed by path segment i is given by:

$$\boldsymbol{\tau}_i = \frac{1}{2}(\boldsymbol{r}_i + \boldsymbol{r}_{i+1}) \times (I\ \boldsymbol{L}_i \times \boldsymbol{B}) \tag{5.4}$$

The total torque generated by the conducting path is then found by summation over the n individual segments:

$$\boldsymbol{T} = \sum_{i=1}^{n-1} \frac{1}{2} I \ (\boldsymbol{r}_i + \boldsymbol{r}_{i+1}) \times [(\boldsymbol{r}_{i+1} - \boldsymbol{r}_i) \times \boldsymbol{B}] \tag{5.5}$$

where the sequence $\{\boldsymbol{L}_1, ..., \boldsymbol{L}_n\}$ is defined by the geometry of the structure and the connections between the conducting pathways.

For a square structure such as that shown in Fig. 5.2, with physical data given in Table 5.1, the maximum achievable torque would be 1.12 N m. The magnetic field strength in Table 5.1 is taken to be 30 μT as this is a typical value for LEO [169], and the areal mass density, σ, assumes an ultra-lightweight structure, composed of a 3D-printed polymer or composite material, overlaid with a thin film. This areal density may in fact be a conservative estimate, as solar sails with areal densities on the order of 10 g m^{-2} have been proposed [51]. However, a higher value was used here as it is expected that the mass of conductor required to carry a current of 10 A would increase the areal mass density significantly. Further work would be required to assess the feasibility of fabricating a functional spacecraft of this density and scale in orbit, however these values are used to provide an order of magnitude estimate of the potential torques achievable.

Side length	d	100 m
Path segment length	L	1 m
Field Strength (LEO)	B	30 μT
Current	I	10 A
Areal Mass Density	σ	100 g m^{-2}

Table 5.1: Example spacecraft configuration.

A further refinement of the concept could entail placing addressable switches at each node of the square lattice. These switches could then be commanded to change the current-path direction as required, depending on the direction of the desired control torque. This would then allow the maximum conducting path length to be used for torque generation in all directions, with a lower mass than having multiple conducting paths as the same conducting elements are used for each coil direction.

5.2.2 Detumbling Simulation of a Conductive Structure In-Orbit

The utility of the conducting structure as an attitude control system is now assessed by simulating a square structure in-orbit, with control torques generated by the representative model defined in Table 5.1. The structure is taken to be a rigid-body, and so the system dynamics are again described by the Newton-Euler equations:

$$\mathbf{I}\dot{\boldsymbol{\omega}} + \boldsymbol{\omega} \times (\mathbf{I}\boldsymbol{\omega}) = \boldsymbol{T} \tag{5.6}$$

where $\boldsymbol{T}$ is the external torque acting upon the spacecraft, $\mathbf{I}$ is the inertia tensor and $\boldsymbol{\omega}$ the angular rates expressed in the principal-axes frame. The dynamics are implemented along with the quaternion kinematic equations:

$$\dot{q} = \frac{1}{2}q[0, \boldsymbol{\omega}] \tag{5.7}$$

where q is the quaternion describing the current attitude, and $[0, \boldsymbol{\omega}]$ is a quaternion with scalar component 0, and vector part $\boldsymbol{\omega}$, the angular velocity components in the principal axes frame [145]. The equations of motion are implemented in the *MATLAB* programming environment, and solved numerically with the *ode45* integrator. Again, the physical data is taken from Table 5.1, and the inertia tensor taken to be that of a rigid, flat square plate, given by:

$$\mathbf{I} = \begin{pmatrix} \frac{1}{12}md^2 & 0 & 0 \\ 0 & \frac{1}{12}md^2 & 0 \\ 0 & 0 & \frac{1}{6}md^2 \end{pmatrix} \tag{5.8}$$

where $m = \sigma d^2$ is the total mass of the structure, d the sidelength and σ the areal mass density. The components of the tensor then have values $I_1 = I_2 = 8.3 \times 10^5$ kg m^2 and $I_3 = 16.7 \times 10^5$ kg m^2. In order to assess the ability of the conducting structure to detumble itself, the well-known *Bdot* control law [168] is implemented, which provides an expression for the desired control torque, $\boldsymbol{T}_{Bdot}$, in terms of the body rates, $\boldsymbol{\omega}$, of the spacecraft and the magnetic field, $\boldsymbol{B}$, such that:

$$\boldsymbol{T}_{Bdot} = k(\boldsymbol{\omega} \times \boldsymbol{B}) \times \boldsymbol{B} \tag{5.9}$$

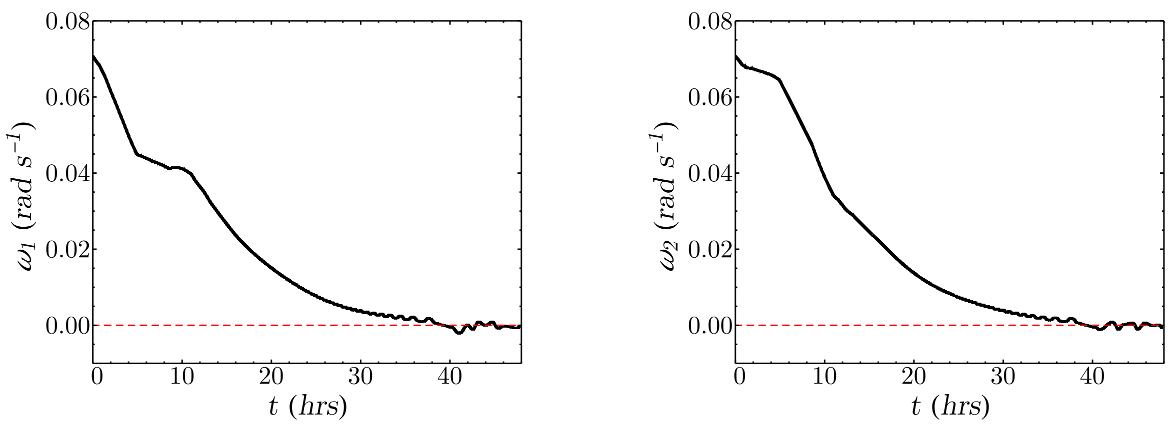

Figure 5.4: Body rates of the structure over the simulation time of two days. The structure is detumbled from an initial angular velocity vector of $\boldsymbol{\omega} = (0.707, 0.707, 0)$ rad s^{-1}, nearly to rest.

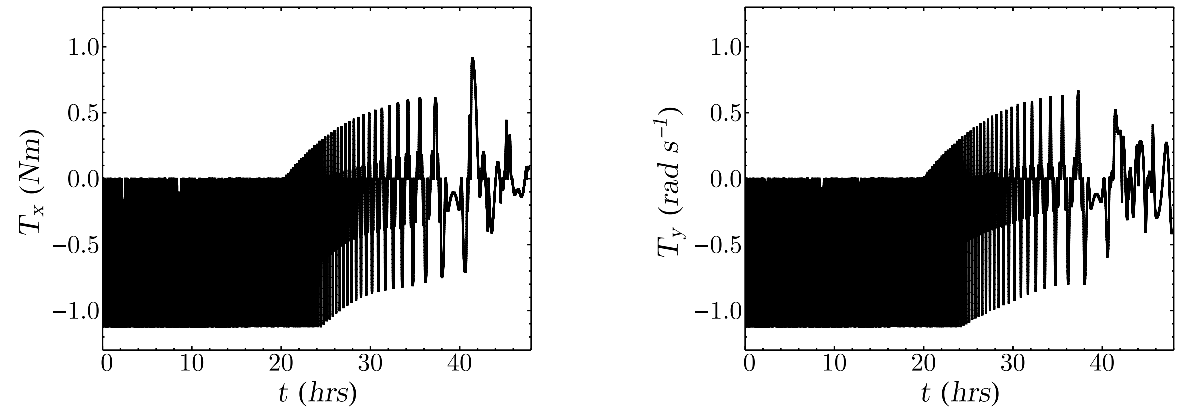

Figure 5.5: Torques produced by the conducting structure during simulation. Initially the controller is delivering the maximum torque of 1.12 N m until the end of the detumbling phase when finer control is required.

for some fixed gain k. This torque is used as the external torque $\boldsymbol{T}$ in Eq. 5.6, and no other disturbing torques are considered at present. The field direction is taken to be constant throughout the simulation for ease of illustration. The initial angular velocity of the structure is set to $\boldsymbol{\omega} = (0.707, 0.707, 0)$ rad s^{-1}, such that the magnitude of the initial angular velocity is 0.1 rad s^{-1}, a significant spin rate for a 100×100 m^2 structure. The simulation is performed over two days. The geometry of the structure is taken to be two overlaid conducting paths, with orthogonal coil directions, i.e. the path shown in Fig. 1 overlaid with a duplicate path rotated by 90°. The maximum torque generated by each path is 1.12 N m, as calculated using Eq. 5.5. A further assumption is that the current in the paths can be varied between zero and a maximum of 10 A, and that the direction of the current can be reversed, allowing the torque magnitude to be varied and the direction to be reversed.

Results of the simulation are shown in Fig. 5.4, demonstrating that the conducting structure is able to detumble itself in just under two days. The torques are shown in Fig. 5.5, where it can be seen that initially the controller is delivering the maximum torque of 1.12 N m when required, until the end of the simulation when the angular rates are reduced sufficiently that finer control is required. It is important to note that the initial angular velocity in the field direction, in this case the z-axis, is zero, as magnetic control is not capable of producing torques in the magnetic field direction and so any angular momentum in this direction would remain after detumbling.

5.2.3 Attitude Requirements for Simplified Reflector System

An investigation is now made of whether the attitude control system could, at least partially, provide the torques required to continuously illuminate a fixed point on the Earth's surface. For this analysis, a simplified model is used to provide an illustration of the operational concept, and to provide a representative example of the angular rates and accelerations required. The purpose of this analysis is to demonstrate that the magnitude of the torque produced by a conducting structure in polar orbit within a dipole magnetic field could be sufficient to control the reflector, and to demonstrate operation by simulating the system over multiple orbits.

Figure 5.6 shows the geometry of an orbiting solar reflector in a circular, polar orbit. The figure shows the orbital plane, to which we ascribe the inertial coordinate system xyz. This coordinate system is Earth centered and rotates with the orbital plane, such that the y direction always points towards the Sun. The following simplifications are made: 1) the orbit is Sun-synchronous, 2) the tilt of the Earth's axis relative to the ecliptic is ignored, and is taken to be around the z-axis, and 3) the Earth's magnetic field is a dipole field, also centered on the z-axis. The target ground-point which is to be illuminated by the reflector is located at $\boldsymbol{R}$, which changes over time as the Earth rotates. This is assumed to be a large equatorial terrestrial solar power farm. The reflector position is given by vector $\boldsymbol{r}$, and so $\boldsymbol{r}_{rad} = \boldsymbol{r} - \boldsymbol{R}$ is the relative position of the target ground-point and reflector, and the direction in which sunlight is to be

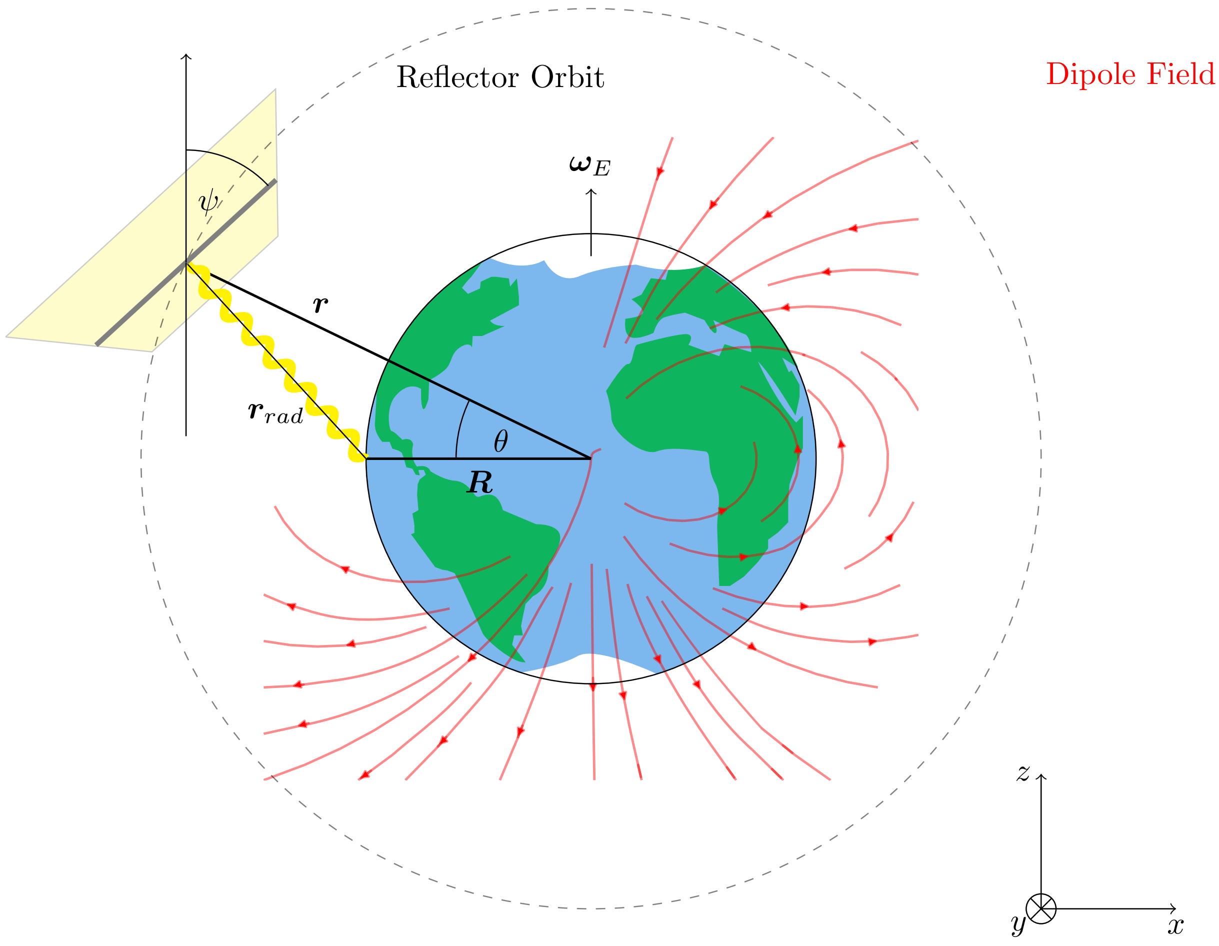

Figure 5.6: Geometry of a reflector on a circular, polar orbit, illuminating a point on the Earth's equator. The Earth-Sun vector is in the y direction, so the Sun's radiation is directed into the page. The dipole magnetic field, shown in red, is hidden in the top left of the figure for clarity and is not shown to scale.

reflected. Within this simplified model, the position vectors are given by:

$$\boldsymbol{r} = \begin{pmatrix} r\cos\theta \\ 0 \\ r\sin\theta \end{pmatrix} \tag{5.10}$$

$$\boldsymbol{R} = \begin{pmatrix} R_e\cos\omega_e t \\ R_e\sin\omega_e t \\ 0 \end{pmatrix} \tag{5.11}$$

where θ is the true anomaly of the reflector, which changes at a constant rate, as shown in Fig. 5.6, and R_e, ω_e are the radius and angular velocity of the Earth, respectively. The magnetic field components in the orbital plane are those of a dipole field, with polar components given by:

$$\begin{aligned} B_r &= -2B_0\left(\frac{R_e}{r}\right)^3 \sin\theta \\ B_\theta &= -B_0\left(\frac{R_e}{r}\right)^3 \cos\theta \end{aligned} \tag{5.12}$$

where $B_0 = 3.12\times10^{-5}$ T is the mean value of the magnetic field at the magnetic equator on the Earth's surface [173]. The angle ψ lies between the z-axis and the line of intersection between the reflector surface and the orbital plane. This line of intersection is shown in grey in Fig. 5.6. For sunlight incoming along the y-direction to be reflected along $\boldsymbol{r}_{rad}$ to the target ground-point, this line of intersection must be perpendicular to $\boldsymbol{r}_{rad}$, which defines the angle ψ. An expression for ψ is now sought, as this angle needs to be maintained by applying control torques with the conducting structure. As the ground point rotates with the Earth and moves out of the orbital plane, the reflector would also need to roll around the reflector axis shown in grey in Figs. 5.6 and 5.7 to give the correct angle of reflection. This component of the reflector attitude dynamics is ignored in this analysis because this angle changes at a much slower rate than the angle ψ. Changes in this angle depend on the target ground-point velocity, while changes in ψ depend mainly upon the reflector orbital velocity which is much greater. Another reason this component of the attitude dynamics is ignored is because it would require control torques with a component in the z-direction. A torque in this direction could not always be achieved due to the fact that torques can only be produced in the plane normal to the field direction, which is an inherent constraint of magnetic attitude control. If the conducting support structure is found capable of maintaining the pitch angle ψ, it could then be supplemented by reaction wheels or another attitude control system to achieve the required angle of reflection. The constraints made on the system for this model allow us to consider only the 2D geometry of the xz plane to find this expression. Figure 5.7 shows the geometry in the orbital plane, where R_x is the projection of the ground-point position onto the plane. An equation for ψ can then be found as:

$$\psi = \frac{\pi}{2} - \varepsilon = \frac{\pi}{2} - \tan^{-1}\left(\frac{r\cos\theta - R_e\cos\omega_e t}{r\sin\theta}\right) \tag{5.13}$$

As the time dependence of θ is known, it is then possible to find an expression for the required angular velocity of the solar reflector by taking the time derivative of Eq. 5.13, resulting in:

$$\dot{\psi} = \frac{-rR_e\omega_e\sin(\omega_e t)\sin\theta + r\dot{\theta}(r - R_e\cos(\omega_e t)\cos\theta)}{r^2 + R_e\cos(\omega_e t)(R_e\cos(\omega_e t) - 2r\cos\theta)} \tag{5.14}$$

An exact expression for the angular acceleration can also be found by taking the time derivative again, omitted here for conciseness.

Equation 5.13 provides a steering law for the pitch around the Sun-reflector axis which must be maintained. Additionally, the reflector must be angled correctly towards the Sun to provide the required angle of reflection towards the target. In Fig. 5.6, the reflector, represented by the yellow plane, would be angled at 45° to the page since the target is positioned in the xz plane. This ensures that $\boldsymbol{r}_{rad}$ would be perpendicular to the sun-line direction, providing an angle of reflection of 45°.

A simulation is now performed of a reflector in orbit, with torques generated by the conducting paths which attempt to maintain the reflector attitude such that the angle ψ, given by

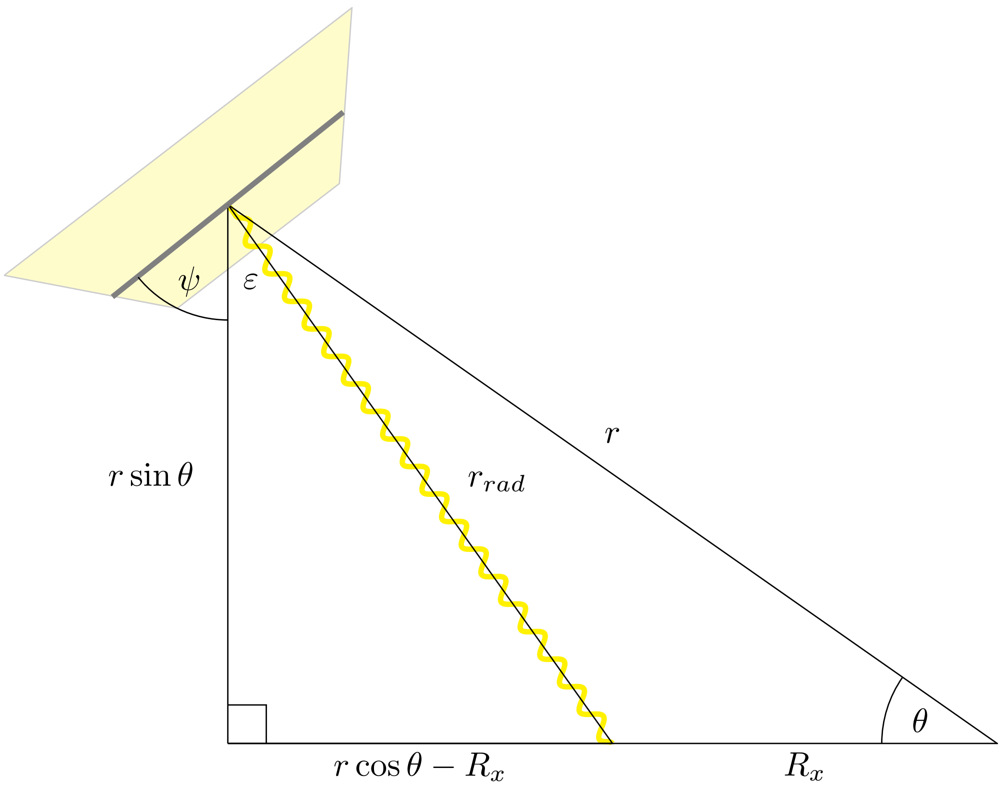

Figure 5.7: Geometry of the reflector-target vector $\boldsymbol{r}_{rad}$, illustrating how the angle ψ can be determined

Eq. 5.13, is continually maintained. The physical data given in Table. 5.1 is again assumed. Rather than the *Bdot* controller used previously to detumble the structure, tracking behaviour is now sought by using a quaternion error feedback controller to generate control torques, with the desired orientation specified by Eq. 5.14. The control law is given by:

$$\boldsymbol{T}_{ref} = -P_q \boldsymbol{q}_{\text{err}} - P_\omega \boldsymbol{\omega} \tag{5.15}$$

where P_q and P_ω are the controller gains, $\boldsymbol{\omega}$ the angular rates, and

$$\boldsymbol{q}_{err} = \boldsymbol{q}_{ref} \boldsymbol{q}_t^* \tag{5.16}$$

is the error quaternion, given by quaternion multiplication between the current attitude, $\boldsymbol{q}_t$, and the desired, $\boldsymbol{q}_{ref}$. This generates a reference torque, and the nearest achievable torque which can be generated by the conducting structure is used to propagate the Newton-Euler equations. The nearest achievable torque is found by assuming that again the structure consists of two overlaid paths, described in Sec. 5.2.3, with the addition of a third path consisting of coils lying in the plane of the structure, shown in blue in Fig. 5.3, also capable of producing 1.12 N m. With this geometric configuration, analogous to having three perpendicular magnetorquers, a torque can be generated in any direction in the plane normal to the magnetic field direction. To find the actuator torque, the reference torque is projected onto the plane normal to the magnetic field and is then taken to be the torque generated by the array, up to the maximum achievable torque calculated by Eq. 5.5. A key difference to the previous detumbling simulation is that the magnetic field direction is no longer constant, instead it's components are given by Eq. 5.12. Due to the constrained geometry of the system, these torques will always lie on the y-axis, and so deliver an angular acceleration around the Sun-reflector direction. The orbital altitude is taken to be 800 km, resulting in an orbital period of 100.7 minutes. The simulation is performed for 10 orbital periods, and so 10 passes of the ground-point are made, and the initial position of the ground-point is chosen such that halfway through the simulation it is located directly underneath the reflector. The attitude control system attempts to point towards the target ground-point even when it is not visible from the reflector, as this ensures the reflector will have the correct orientation when the ground-point next becomes visible. Results of the simulation are shown in Fig. 5.8. The attitude control system is able to maintain the required pitch angle, ψ, until approximately $t = 5.5$ hrs. This is because at this point, the required torque exceeds the torque achievable by the structure, and so the angular acceleration of the reflector lags behind that required by Eq. 5.13. The results show that larger torques are required at approximately the halfway point of the simulation. This is because, at this time the ground-point has rotated with the Earth into the orbital plane, and so is directly underneath the reflector. Since the distance between the reflector and target is then much lower, the reflector must rotate faster to maintain illumination. However, other than the three passes nearest this point, the system is capable of producing the required torques.

As discussed previously, the areal mass density value of 100 g m^{-2} used in this analysis is an order of magnitude higher than that which may be assumed for solar sails, and was a conservative value chosen by assuming that the conducting mass required to fabricate such a structure would increase the density substantially. If it were possible to fabricate a structure with an areal density of 10 g m^{-2}, this would decrease the moments of inertia by a factor of 10. Such a structure was simulated and results are shown in Fig. 5.9. Due to the lower mass, the maximum torque achievable by the conducting structure is now sufficient to provide the required attitude control, as the values of ψ and $\dot{\psi}$ are now seen to match the reference values for the duration of the simulation. When the reflector passes directly over the ground-point, at t = 8.3 hrs, the torque can still not match the reference reference torque, however this is seen to have minimal effect on the error in ψ, as the reference torque is not achieved for only a small period of time. While it remains to be seen whether a conducting structure capable of conducting 10 A of current could be realised, even the results for a structure with an areal density of 100 g m^{-2} demonstrate that at the required pitch angle could be achieved by this system for the majority of the reflector's operation. The reflector could then be supplemented

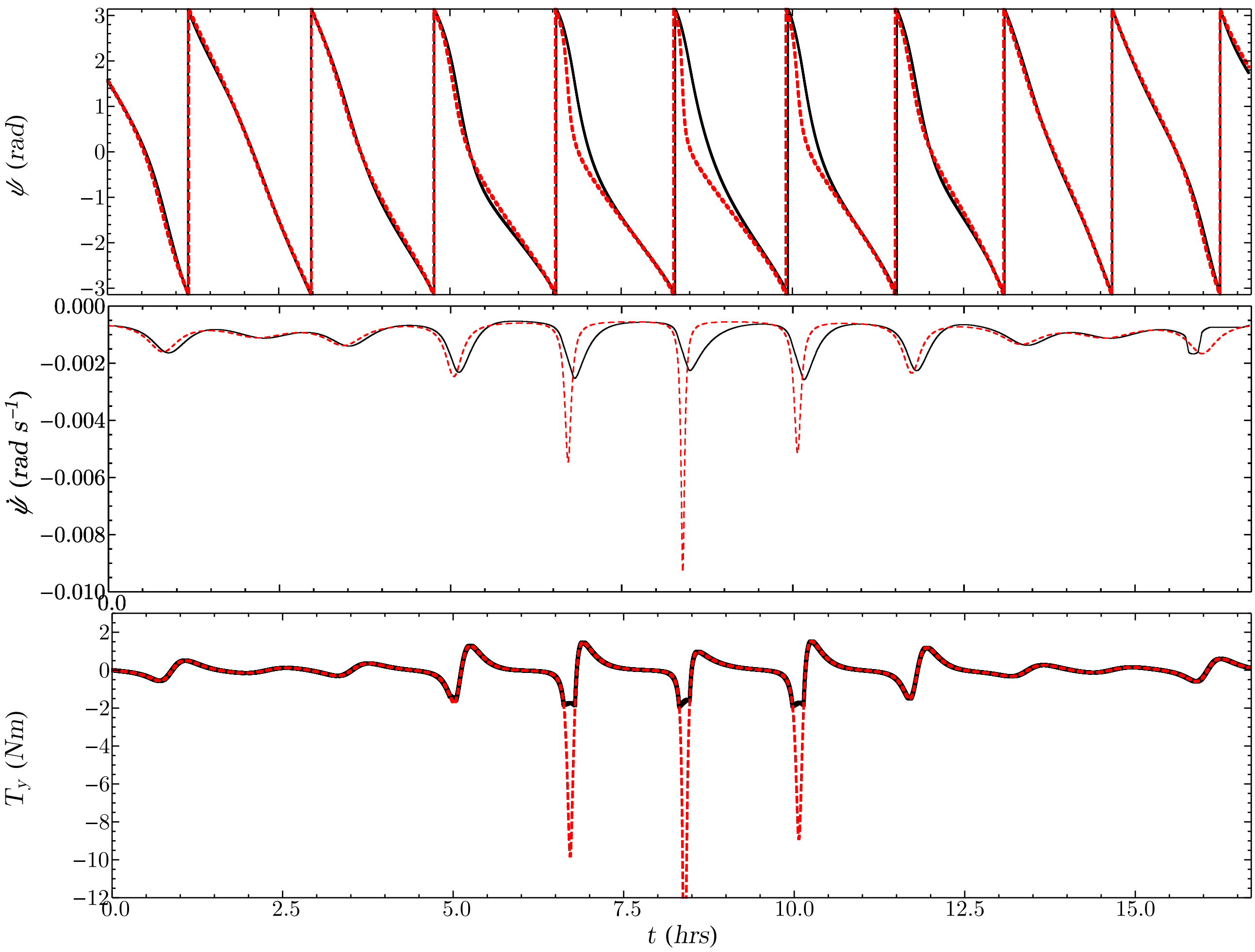

Figure 5.8: Results of simulation for a 100×100 m orbiting solar reflector, showing the conducting structure is only capable of maintaining the required pitch angle ψ for part of the simulation. Actual values are shown in black with reference values shown in red.

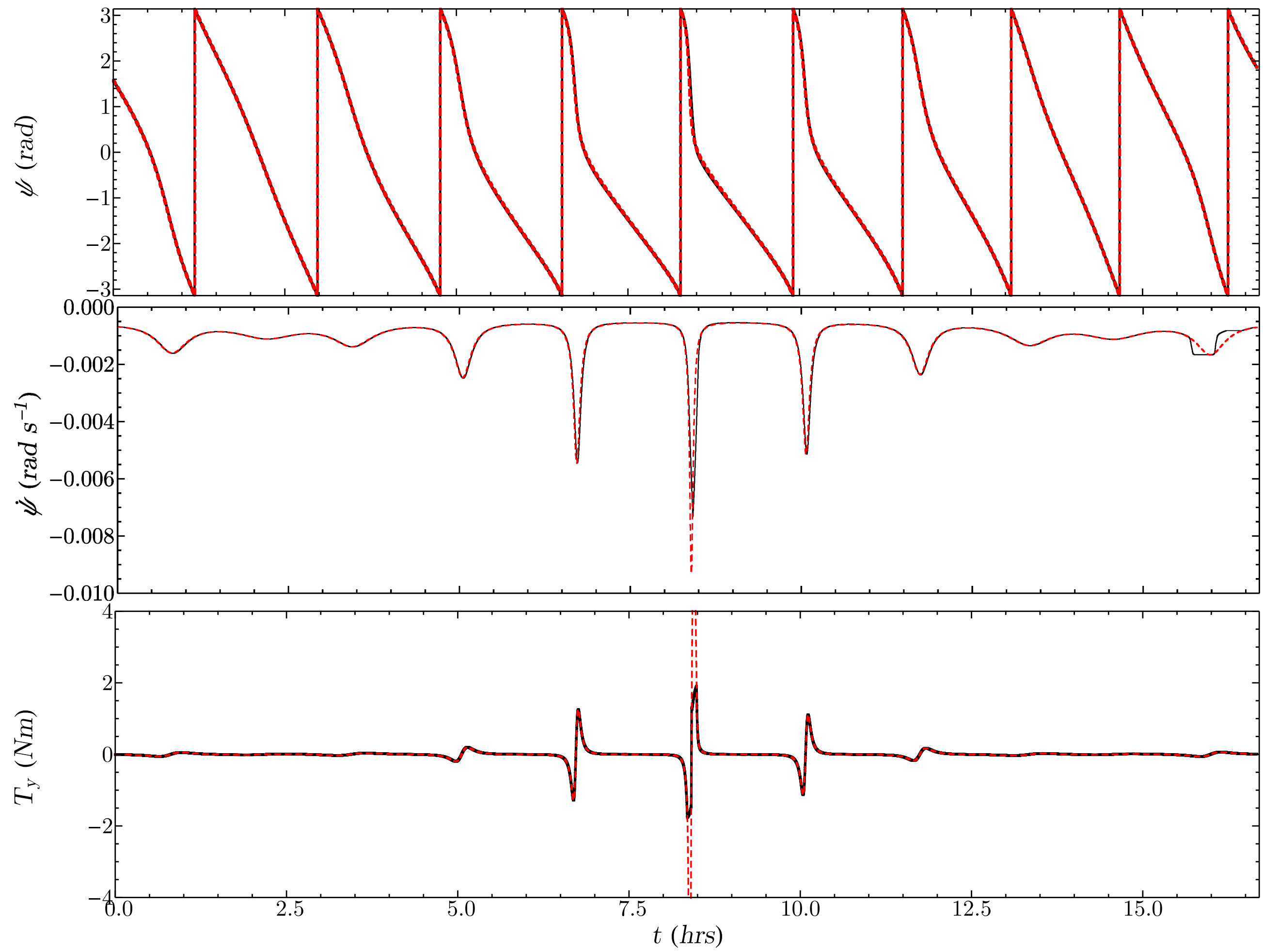

Figure 5.9: Results of simulation for a 100×100 m orbiting solar reflector with areal density of 10 g m^{-2}, showing that a maximum torque of 2 N m is now sufficient to maintain the required pitch angle ψ. Actual values are shown in black with reference values shown in red.

by another attitude control system for the time period when the reflector passes directly over the target, and for fine-pointing.

5.3 Length Scaling of Large Current Loops

In this section, analysis is undertaken to determine how the effectiveness of the proposed attitude control strategy changes with the length-scale of the spacecraft structure. For this analysis it is assumed that the spacecraft is a homogeneous, square planar structure which has been 3D-printed on-orbit. A further assumption is that during manufacturing, conductive pathways have been embedded in the structure which form closed current loops. It is also assumed that the conductive pathway itself is a solid, cylindrical wire, and that the spacecraft is orbiting the Earth, where the Earth's magnetic field is approximated as a dipole field.

The torque generated by the conducting structure is proportional to the current flowing through the conducting pathway. The maximum current depends upon the power available, but will also be limited by the temperature rise in the conductor allowed by the materials of the supporting structure and heat flow between the conductor and support structure. For the analysis of this section, a simplified thermal model of the conductive structure is considered to estimate the extent to which a maximum wire temperature will limit the achievable torque.

Figure 5.10 illustrates a single unit cube of a conducting structure, consisting of 3D-printed booms or trusses onto which a conducting wire is anchored by thermally insulated nodes attached to the main structure. With a current applied, the power loss due to resistive heating in the wire is given by:

$$P_j = I^2 R \tag{5.17}$$

for current I and resistance R. The resistance is assumed to vary linearly with temperature over the operational temperature ranges, and is given by [174]:

$$R = R_r \left[1 + \alpha(\Gamma - \Gamma_r)\right] \tag{5.18}$$

where R_r is the resistance at reference temperature Γ_r, α is the temperature coefficient and Γ the current temperature of the conductor. R_r is inversely proportional to the cross sectional area of the wire, which is assumed to be circular:

$$R_r = \frac{4\rho_r l}{\pi d^2} \tag{5.19}$$

where ρ_r is the resistivity of the conducting material at the reference temperature, l is the total length of the conductor and d the wire diameter.

Heat leaves the wire through thermal radiation only, as it is assumed that the anchor points are thermally insulating so any heat flow into the support structure is negligible. It is also assumed that a thin film membrane shields the wire from any incoming radiation, as the membrane side of the spacecraft would be directed towards the Sun during operation if the spacecraft were acting as a reflector or solar sail. The effect of heat being reflected by the back of the membrane and reabsorbed by the wire is also not considered, nor is the potential temperature rise of the membrane itself. It is assumed that the wire is a grey body with emissivity ϵ, so that the power dissipated through thermal radiation is given by the Stefan-Boltzmann law:

$$P_r = \epsilon\sigma A_s \Gamma^4 = \epsilon\sigma\pi d l \Gamma^4 \tag{5.20}$$

where $\sigma = 5.670373 \times 10^{-8}$ W m^{-2}K^{-4} is the Stefan-Boltzmann constant, and A_s the surface area of the wire. Of note is that both the resistive heating and thermal radiation are proportional to the length of the conducting wire, and so the heat flow can be considered per unit length of the conductive path, with units of Watts per meter.

The wire will rise to the temperature at which the resistive heating and thermal radiation are in equilibrium. For a given diameter of wire, there will be a maximum allowable temperature in the conductor depending on the specific construction of the spacecraft. This temperature then determines the maximum current that can be applied to the wire and thus the maximum achievable torque. If the wire were perfectly insulated from the supporting structure, this temperature could be very high, approaching the melting point of the conductor. In practice, it may be desirable to restrict the maximum temperature of the conductor to be below the melting point of the support structure, in case of accidental contact or because there will be radiative heat transfer from the wire to the structure. This restriction would also allow the anchor points to be constructed from the same material as the support structure in a continuous 3D print. Potential materials for 3D-printing the support structure are thermoplastics which could be printed through fused deposition modelling (FDM). We consider polycarbonate as a candidate material for such structures [175], which has a glass transition temperature of around 147°, and a melting point of 155°C.

Equating P_j and P_r allows an expression for d to be found, in terms of I and Γ_e for a given wire material, such that:

$$\epsilon\sigma\pi d\Gamma_e^4 = \frac{4\rho_r}{\pi d^2}\left[1+\alpha(\Gamma_e-\Gamma_r)\right] \tag{5.21}$$

Therefore, Eq. 5.21 gives an expression for the wire diameter required to carry a specified current while maintaining thermal equilibrium at the desired temperature. The torque produced is proportional to the current in the conductive path, and to the magnetic field strength which will vary with orbital altitude and position. To proceed we approximate the Earth's magnetic field as a dipole field and consider an equatorial orbit, such that the field strength is given by

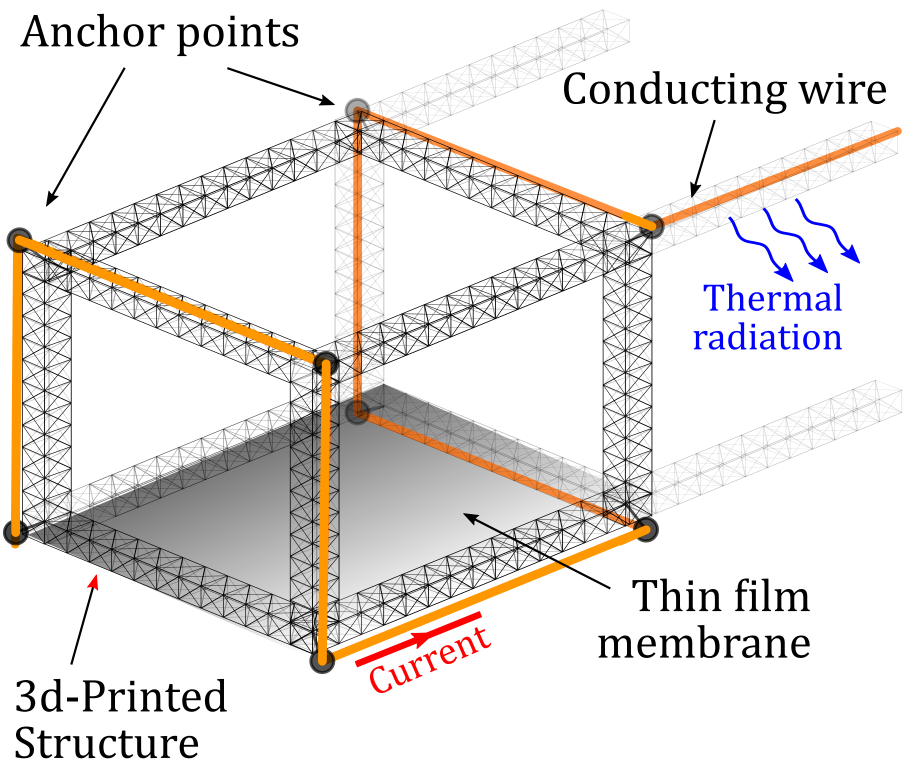

Figure 5.10: A unit cube of an implementation of the concept, consisting of a conducting wire anchored to lightweight 3D-printed structural members.

[173]:

$$B = B_0 \left(\frac{R_E}{R_o} \right)^3 \tag{5.22}$$

where $B_0 = 3.12 \times 10^{-5}$ T is the typical field strength on the Earth's surface at the equator, $R_E = 6370$ km is the mean radius of the Earth, and R_o is the orbital altitude. The attitude control torque requirements for structures with different length scales will vary greatly, due to the scaling of the mass moment of inertia and the scaling of various disturbance torques that will need to be counteracted by the attitude control system. Furthermore, these factors will all vary with altitude as well. We assume that the torque produced by a current loop may be considered "useful" if, for a given length-scale, the torque produced by the current loop has a magnitude at least as great as the maximum gravity gradient torque that the spacecraft will experience, following the discussion in Ch. 3. The maximum gravity gradient torque for a square, planar structure occurs when the face of the structure is oriented at 45° to nadir, and is given by:

$$T_g^{\max} = \frac{D^2 M \mu}{8 R_o^3} \tag{5.23}$$

where D is the side-length of the square spacecraft, M the total mass, and $\mu = 3.986 \times 10^{14}$ m^3 s^{-2} the standard gravitational parameter of Earth. Equation 5.23 is found by evaluating the standard gravity gradient torque equation (e.g. [146]) for a square structure with which has an inertia tensor with principal components given by $i_1 = i_2 = \frac{1}{12} M D^2$, $i_3 = 2i_1$, i.e. a square plate with uniform mass density. The subscripts 1, 2 and 3 refer to the x_o, y_o, z_o body frame axes respectively, which is fixed to the structure as shown in Fig. 5.1, along with the inertial xyz frame.

The torque produced by a current loop depends on the enclosed area, while the mass of that current loops depends on its length. Expressions for both the enclosed area and path length as a function of structural side-length are now found. For geometry A of Fig. 5.1, the enclosed area is given by $A_e = D^2$ for side-length D, and the path length is given by $l = 4D$. For geometries B and C, a general expression is found for N equally spaced loops, while for geometry D the expression is given for N "layers" of coils arranged lengthways across the structure. Additionally, for geometries C and D, the enclosed area of the coils depends on the depth of the structure, w, which is taken to be D/N. Of note is that the following analysis is only accurate for sufficiently large N that $w << D$, as it was assumed in Eq. 5.23 that the structure's inertia tensor is that of a thin square plate. The expressions for A_e and l for the coil geometries considered are summarised in Table 5.2. For the geometries which contain multiple current loops the number of coils/layers is denoted N, and it is assumed the loops are equally spaced. For the last two geometries, it is further assumed that the depth of the structure is given by D/N, i.e. that the structure can be considered to be composed of square unit cells.

The maximum torque produced by the current loop is $T_{\mathrm{L}}^{\max} = I A_e B$, from Eq. 2.23. Equating this with the maximum gravity gradient torque (Eq. 5.23), which is taken as the reference requirement for useful attitude control, and substituting the dipole field magnitude from Eq. 5.22 allows an expression for the current required of a current loop to counteract the gravity gradient torque:

$$IA_eB_0R_E^3 = \frac{D^2M\mu}{8} \tag{5.24}$$

The conductor mass fraction $\lambda_f = M_c/M$ is defined as the conductor mass divided by the total mass, and expresses the total mass in terms of the areal mass density σ_A, giving:

$$M = \frac{M_c}{\lambda_f} = \frac{\frac{1}{4}\pi d^2 l}{\lambda_f} = \sigma_A D^2 \tag{5.25}$$

Equations 5.21, 5.24 and 5.25 are then used to find an expression for λ_f with d and I eliminated:

Table 5.2: Current Loop Geometries

Loop Geometry	Enclosed Area, A_e	Path Length, l
A) 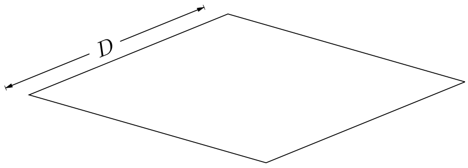	$A_e = D^2$	$l = 4D$
B) 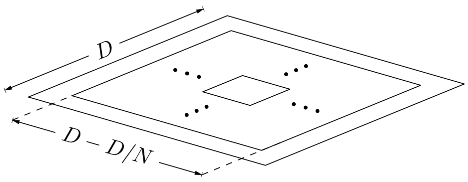	$A_e = \sum_{i=1}^{N}\left(\frac{i}{N}D\right)^2 = \frac{D^2(N+1)(2N+1)}{6N}$	$l = \sum_{i=1}^{N} 4\frac{i}{N}D = 2D(N+1)$
C) 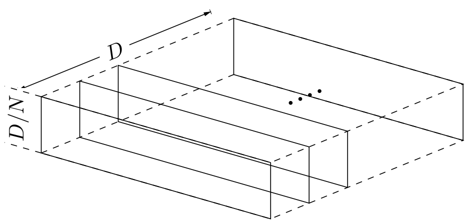	$A_e = \sum_{i=1}^{N+1}\frac{D^2}{N} = \frac{D^2(N+1)}{N}$	$l = \sum_{i=1}^{N+1}\frac{2D}{N} + 2D = \frac{2D}{N}(N+1)^2$
D) 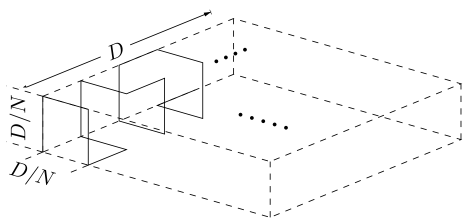	$A_e = N\sum_{i=1}^{N+1}\frac{3}{4}\left(\frac{D}{N}\right)^2 = \frac{3D^2(N+1)}{4N}$	$l = 4ND$

$$\lambda_f = \left(\frac{\mu^4 \rho_c^3 \rho_r^2 (1+\alpha(\Gamma_e - \Gamma_r))^2}{16384 \cdot \pi \Gamma_e^8 \epsilon^2 \sigma_B^2 B_0^4 R_E^{12}} \right)^{\frac{1}{3}} \cdot \frac{D^{\frac{10}{3}} l}{A_e^{\frac{4}{3}}} \sigma_A^{\frac{1}{3}} \\ = C_1 G(N) D^{\frac{5}{3}} \sigma_A^{\frac{1}{3}} \tag{5.26}$$

where the constant C_1 is the bracketed term in Eq. 5.26 (including the exponent), and $G(N) = (D^{\frac{5}{3}} l)/A_e^{\frac{4}{3}}$ is a factor determined by the coil geometry, where it is noted that the D term is eliminated for the geometries considered here in Table 5.2 leaving some function of the coil number N. This is the case for any geometry where the enclosed area A_e scales with D^2 while path length scales with D, which is true in general if both dimensions of the enclosed area scale with D.

Equation 5.26 holds for geometries B, C and D in Table 5.2, so long as the number of

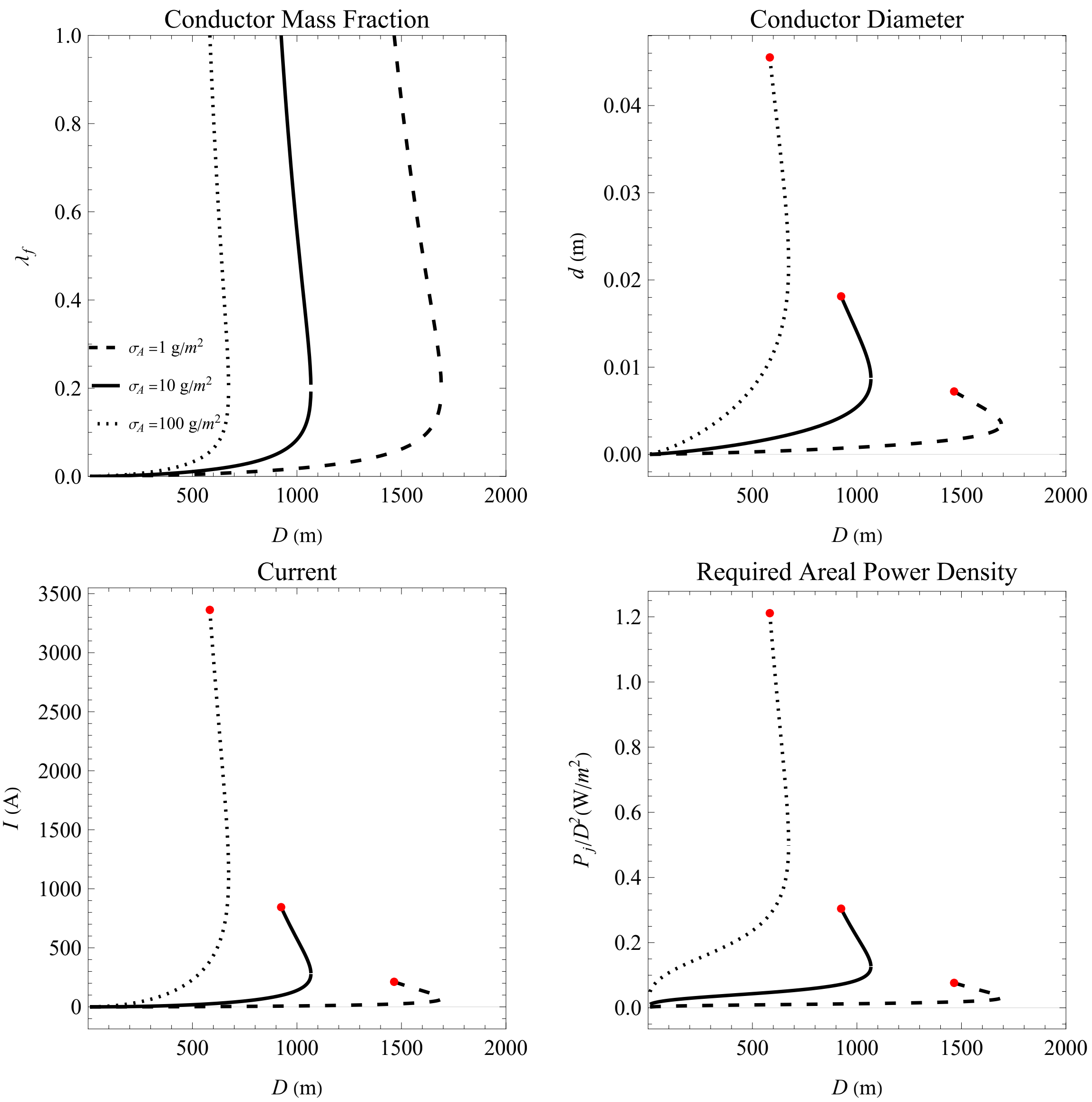

Figure 5.11: Scaling for coil geometry A

coils/layers in the structure N is sufficiently large that the mass density of the structure can be assumed to be approximately uniform, as was assumed in Eq. 5.23. For geometry A, this assumption does not hold and the derivation must be modified to account for the uneven mass distribution of the single, outer current loop. The final expression for λ_f in this case is omitted here for brevity, but is derived by calculating the maximum gravity gradient torque for a body with inertia tensor components $i_1 = i_2 = (\frac{1}{12}(M - M_c) + \frac{4}{3}M_c)D^2$, and $i_3 = 2i_1$.

In summary, an expression for λ_f has been derived, which gives the fraction of the total mass that must be comprised by the conducting pathway in order to produce a torque as great as the maximum gravity gradient torque a planar spacecraft may experience, while maintaining

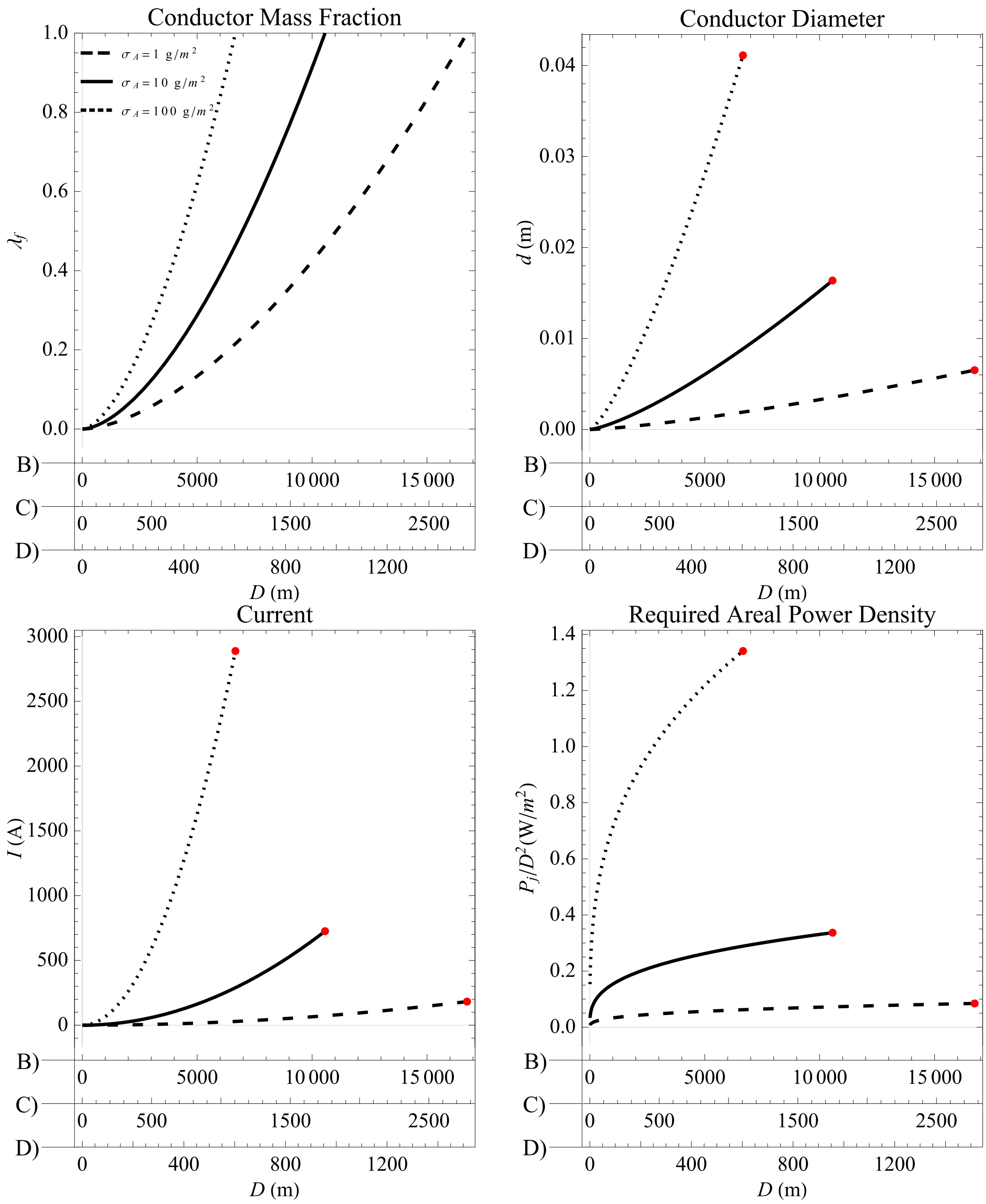

Figure 5.12: Scaling for coil geometries B, C & D ($N = 27$)

a specified equilibrium temperature in the conducting path.

Plots of λ_f, d, I and P_j/D^2 are shown in Fig. 5.11 for geometry A, and Fig. 5.12 for geometries B-D. It is assumed the conductor is a copper wire, and that the spacecraft is fabricated from some polycarbonate printed structure, so that the wire temperature should not exceed the glass temperature of 147°C. Other physical data is summarised in Table 5.3. For geometries B-D the equations have the same form with different horizontal axis scaling since the $G(N)$ factor is unique to each geometry. For geometry A it is noted that there are two branches for the solutions due to the uneven mass distribution. This is because at some length scales the gravity gradient torque can be counteracted either by a lightweight current loop with a more massive structure, or by a more massive current loop capable of carrying a greater current. This more massive current loop is capable of carrying a greater current, thus producing a greater torque and offsetting the increase in inertia and thus greater gravity gradient torque. For the other coil geometries, the conductor mass is uniformly distributed and therefore this branching of the solutions does not appear. Figure 5.11 shows that for a single, outer current loop, length scales on the order of 100 m to 1000 m could be feasible to meet the given criteria, for areal mass densities on the order of near to far term solar sails. The plot of the required areal power density is included, as it was assumed in the derivation that the available power would not be a limiting factor for this attitude control strategy. This assumption is likely valid, as the required areal power density is relatively insignificant when compared to the solar insolation of 1368 W/m^2 the spacecraft will intercept on-orbit, and PV panels covering a small fraction of the spacecraft surface will be capable of powering the system. Note that the red points on the plots represent the length scale at which λ_f=1, and therefore solutions beyond (or below for that branch of the solution in the case of geometry A) are unphysical.

For geometry B, the length-scaling is found to be much more favourable than the outer loop geometry, with length scales on the order of 10 km meeting the criteria of the thermal and torque equilibrium equations. Both geometries C and D are seen to have much more adverse scaling than geometry B. As discussed previously, this is due to the fact that the area enclosed by these current loops relies on the structure having some depth, which will by definition be the smallest dimension of the planar structures considered here. For both cases, length scales on the order of 100 m would be feasible, and the power requirements are also well within what could be considered reasonable for such structures. Figures 5.11 and 5.12 both show the scaling functions for $N = 27$, i.e. for a structure with a depth dimension that is 3.7% its length. This value was chosen here as this is the value used in later simulations, where larger values would result in excessive computation times. For geometries B-D, the factor $G(N)$ influences the length-scaling however and must be considered. The change in the maximum length scale - i.e. the length scale at which $\lambda_f = 1$ (the top line of the λ_f plots in figs/Condstruc 5.11 and 5.12) with N is shown in 5.13. For geometry B, increasing N increases the number of current loops (which lie in the plane of the structure), and it is seen to increase the maximum possible length scale at which the torque from the current loops can equal the gravity gradient torque (i.e. the plot shows that having multiple, thinner current loops is more thermally efficient than fewer loops). Although the plot suggests that N could be increased indefinitely to achieve greater torques, there will be a practical limit on how thin a useable conductive wire can be which we do not consider here. For both geometries C and D, the maximum length scale decreases with N, as these geometries rely on the structure's depth which also decreases with increasing N, and so a greater number of current loops enclosing an ever-decreasing area is seen to be less mass-efficient in this case.

In the length-scaling analysis, radiative heating due to the wire being illuminated by the Sun was not included in the thermal model, both for simplicity and as it was assumed the reflective membrane would be directed towards the Sun and thus shade the conductive wire. Given solar irradiance in LEO of 1360 W/m^2, assuming that 70% of this is absorbed by the wire, ($\epsilon = 0.7$), which has an illuminated area of $l \times d$, the (worst-case) radiative heating power is $P_S = 952 \times ld$. The power dissipated through thermal radiation (Eq. 5.20), for a wire temperature of $\Gamma_e = 420$ K, is given by $P_r = 3880.2 \times ld$, or approximately $4P_S$. This addition to the thermal energy balance would require an increased wire diameter to maintain the required temperature, but as a 25% increase it is not the dominant contribution and does not significantly alter the length-scaling analysis here. In practice, this increase in wire diameter may be built in as a safety factor anyway, or another solution could be to reduce the current or implement pulse width modulation (PWM) when the current loop is illuminated. This would reduce the control effectiveness during illumination, but maintain the lower mass requirement of non-illuminated operation. A trade-off between these strategies could be performed, depending on the specific pointing requirements of the application considered and whether the wire will be shaded by the membrane during operation.

Results of analysis for all geometries show that the use of conductive pathways embedded

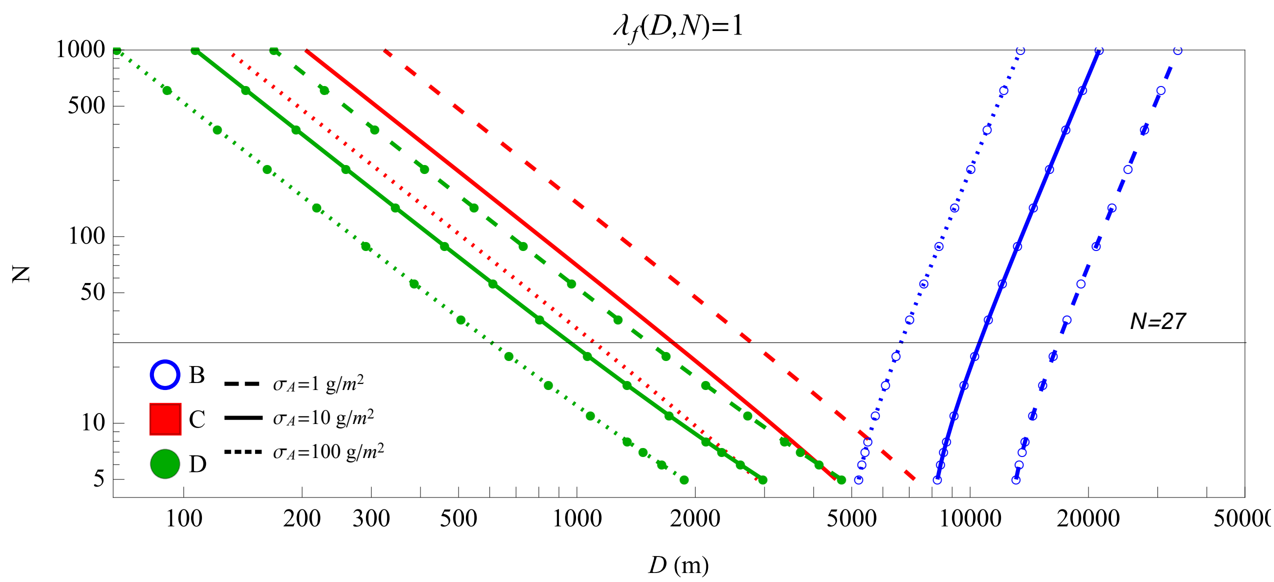

Figure 5.13: Number of coils N against maximum length scale (D at which λ_f=1) for uniform mass density coil geometries.

in a large, planar structure could feasibly be used for attitude control purposes at length-scales on the order of kilometres, though in practice this length scale is more likely to be reduced to the order of 100 m. This is due to the fact that large values of λ_f would not be physically realisable, as this would constitute the structure being comprised solely of the thin copper wire and leave no mass for the actual supporting structure. Furthermore, the analysis was performed for each coil geometry individually, while in practice it would most likely be required to have three, orthogonal current loop geometries overlaid with one another, such that three-axis magnetic control could be implemented. In other words, although analysis of geometry B has suggested length-scales on the order of 10 km may be feasible, the length-scale of the worst-performing geometry will be the limiting factor if three-axis control is desired. Although other actuation strategies have not been analysed here, it may be possible that geometry B could be employed for a kilometre scale structure, providing torque around one axis only, and then be supplemented by another form of attitude control such as an array of CMGs or the use of solar radiation pressure to enact torques around other axes.

5.4 Simulations of Flexible Structures with Embedded Current Loops

Although it has been demonstrated that current loops can provide sufficiently large torques for attitude control purposes, a further consideration is whether they are capable of reorienting a highly flexible structure successfully. The structural response is particularly of interest for current loops because the torque produced by the current loop is the result of integrating the Lorentz forces on the current carrying wire around the loop. For a rigid current loop this produces a pure torque as described by Eq. 2.23, but for a flexible loop these forces act to deform the structure (effectively modifying the enclosed area). Additionally, this behaviour is highly nonlinear in that the direction of the forces acting on the current loop depends on the changing shape of the current loop/structure at a given point in time. The dynamics of flexible structures with embedded current loops are investigated in this section by performing numerical simulations of a 250×250 m square truss structure, for a range of structural flexibilities and N, for each of the coil geometries presented in the previous section. The aim of these simulations is to determine how rigid a structure of this length-scale would need to be for this attitude control strategy to be considered feasible, and furthermore to gain some general insight into the nature of the structural deformations and dynamics observed in the structure when the current loops are energised.

5.4.1 Model Description

The structure is again modelled as a spring-mass system (also commonly known as a lumped-parameter or multi-particle model [147]), following Chapter 3. This gives a computationally efficient model of a general, flexible LSS. In this chapter, the equations are recast in matrix form, as opposed to in Chapter 3 where the particle forces were determined iteratively. This reduces the computation time of the model and also allows a modification to the damping term detailed here. In matrix form, the equations are:

$$\mathrm{M}\ddot{\boldsymbol{r}} = \boldsymbol{F}^{\mathrm{mag}} - \mathrm{K}(\boldsymbol{r} - R_\theta \boldsymbol{r}_0) - \gamma \dot{\boldsymbol{r}} \tag{5.27}$$

where M is the diagonal mass matrix, $\boldsymbol{F}^{\mathrm{mag}}$ the Lorentz forces, K the stiffness matrix, $\boldsymbol{r}$ the particle positions, $\boldsymbol{r}_0$ the equilibrium/initial particle positions (and R_θ the rotation matrix found by least-squares fitting a rotation between $\boldsymbol{r}_0$ and $\boldsymbol{r}$) and γ the damping matrix. As in Chapter 3, the system is comprised of point masses connected by linear springs, and so the stiffness matrix is assembled in the usual way (e.g. [176]). In terms of the adjacency matrix A defining the structural connectivity (defined in Chapter 3), the stiffness matrix can be constructed from 3×3 submatrices according to:

$$\mathrm{K}_{ij}^{3\times 3} = \begin{cases} \sum_{i'=1}^{i-1} \mathrm{A}_{i'j} + \sum_{j'=j}^{N_p} \mathrm{A}_{ij'} \mathcal{K}^{ij'} & \text{if } i = j \\ -\mathrm{A}_{ij} \mathcal{K}^{ij} & \text{otherwise} \end{cases} \tag{5.28}$$

where N_p is the number of particles, and $\mathcal{K}^{ij}$ the first 3×3 submatrix of the global stiffness matrix of a 3D linear spring [176], given by:

$$\mathcal{K}^{ij} = k_{i,j} \begin{bmatrix} c_x^2 & c_x c_y & c_x c_z \\ c_x c_y & c_y^2 & c_y c_z \\ c_x c_z & c_y c_z & c_z^2 \end{bmatrix} \tag{5.29}$$

where $c_x = (x_j - x_i)/L_{i,j}$ is the cosine of the angle between the local and global x axes (with equivalent expressions for y and z), and k_{ij} is the spring constant of the spring connecting particles i and j. This is determined by first selecting the desired the overall beam-like bending stiffness EI of the structure, relating this to an equivalent beam element elastic modulus E and cross section A_c following Chapter 3 ($EI = 2EA_cR_c^2$), and setting $k_{i,j} = EA_c/L_{i,j}$, for $L_{i,j} = \sqrt{(x_j - x_i)^2 + (y_j - y_i)^2 + (z_j - z_i)^2}$ which is the natural length of the spring.

In Chapter 3 viscous damping with a uniform damping coefficient for each spring element was used, with a value chosen that provided numerical stability without significantly affecting the response (i.e. near zero damping for all vibration modes). In this section, Caughey or modal damping is instead used to provide increased numerical stability and to give damping behaviour more closely representing that of an LSS in general, though of course the damping behaviour can vary greatly depending on the specific design and construction. The Caughey damping matrix is defined as[177]:

$$\gamma = \mathrm{M}\left(\sum_{n=1}^{N_\phi} 2\xi_n\omega_n\phi_n\phi_n^T\right)\mathrm{M} \tag{5.30}$$

where M is the (diagonal) mass matrix, ξ_n the damping ratio, N_ϕ the total number of vibration modes, ω_n the modal frequency and ϕ_n the mode shape for the nth mode of the undamped system in all cases. The mode shapes and natural frequencies of the undamped system are found in the usual manner by solving the eigenvalue problem $|\mathrm{K} - \omega^2\mathrm{M}| = 0$ (e.g. [178]). The damping ratios for each mode are then specified. For the first 100 modes, the damping ratio was set to 1% of critical damping. For all modes with mode number $n > 100$ the damping ratio is either equal to the Rayleigh (proportional) damping value, $\xi_n = 2\xi_{100}\omega_n/\omega_{100}$ or 10, whichever is greater, where $\xi_{100} = 0.01$ is the damping ratio of the 100th mode. These values are chosen in an attempt to represent a general LSS, which will most likely have very light damping of the low-frequency modes (under 10% without active vibration control [179]) while the high-frequency, more localised vibration modes would have higher damping. The damping ratio was given an upper limit of $\xi = 10$ as it was found that higher values led to numerical instability for the structural cases considered here.

The Lorentz forces acting on particle i of the spring-mass model due to the current carrying wires is determined by:

$$\boldsymbol{F}_i^{\mathrm{mag}} = \sum_{j\in C_L} \frac{1}{2} I_L \boldsymbol{r}_{ij} \times \boldsymbol{B} - \sum_{j\in C_L^-} \frac{1}{2} I_L \boldsymbol{r}_{ij} \times \boldsymbol{B} \tag{5.31}$$

where $C_L = \{j|\mathrm{A}_{ij}^L = 1\}$ and $C_L^- = \{j|\mathrm{A}_{ji}^L = 1\}$ are the sets of particle indices where a current carrying element of loop L is connecting particles i and j, with current flowing from i to j or from j to i respectively. The current loops are defined by the directional adjacency matrix A^L, in which $\mathrm{A}_{ij}^L = 1$ if a current carrying element connects particles i and j with current flowing in that direction. The adjacency matrices define the direction of "positive" current, and the same matrix then gives the correct forces for current flowing in the opposite direction if the loop current I_L takes a negative value. The "positive" current direction is defined for the current loop geometries here such that the magnetic dipole moment of the current loop points in the positive xyz direction for the geometries shown in Fig. 5.1 (i.e. the current loops all follow the right hand rule, winding anti-clockwise around their respective axis). Each current loop geometry has a unique adjacency matrix, which is computed prior to the simulation being performed. The overall magnetic force vector $\boldsymbol{F}^{\mathrm{mag}}$ is then found by summation over all current loops (if multiple loops are defined/present) and assembling the particle force vectors into a single vector for use in Eq. 5.27. Note that only forces due to interaction with the external geomagnetic field are considered, and not any interaction with the magnetic field generated by the current loops themselves. This assumption is made because it was found that the magnetic field strength generated by the current loop, measured at some other perpendicular point of the loop, would be much lower than the geomagnetic field strength and thus would not be a significant contribution to the particle forces. The magnetic field generated by a straight, current carrying wire is given by:

$$B_w = \frac{\mu_0 I}{2\pi r} \tag{5.32}$$

where $\mu_0 = 4\pi \times 10^{-7}$ H/m is the magnetic permeability of free space, and r the distance from the wire. For the cases considered in the following simulations, the current is on the order of 10 A, and the structural unit spacing (and thus closest spacing between parallel wire elements) is on the order of 10 m, resulting in the self-interaction field being on the order of 10^{-7} T, two orders of magnitude lower than the geomagnetic field in LEO. The self-forces due to the current loop's own magnetic field are therefore assumed to be negligible for the cases considered here. For a tightly packed structure (< 1 m unit spacing) with loop currents > 100 A, the field generated by the current loop could be comparable to the geomagnetic field and act to compress/expand the units of the structure, and would need to be considered in the analysis.

5.4.2 Simulation Results

Using the spring-mass model, simulations have been performed for each of the current loop geometries (A-D) shown in Table 5.2. As noted, the aim of these simulations is to determine how rigid the structure must be to withstand the forces acting on the current loop and be gently rotated, when that current loop is capable of producing a torque at least as large as the maximum gravity gradient torque the structure would experience. Simulations are performed for each of the four loop geometries, and for three values of both the equivalent bending stiffness EI and the number of structural units N. Varying N changes both the number of current loops for geometries B-D, and the structural depth. There are therefore nine simulations performed for each of the four geometries, resulting in 36 simulations total. Each simulation is performed

Structural Simulation Parameters		
Length	D	250 m
Areal mass density	σ_A	100 g/m^2
Damping ratio	ξ_n	0.01 ($n < 99$)
Beam-like bending stiffness	EI	10^3, 10^4, 10^5 N m^2
Integration timestep (for EI)	dt	0.1, 0.05 , 0.01 s
Integration method		4th order Runge-Kutta
Magnetic field strength	B	27.7 μT (800 km)
Current Loop Physical Data		
Density of copper wire	P	8960 kg/m^3
Reference temperature	Γ_r	293 K
Equilibrium Temperature	Γ_e	420 K
Reference resistivity at Γ_r	ρ_r	1.68×10−8 Ω m
Grey-body emissivity	ϵ	0.7
Temperature coefficent	α	0.00404 K^{-1}
Stefan-Boltzmann constant	σ_B	5.67×10^{-8} Wm^{-2}K^{-4}
Magnetic field (sea-level)	B_0	3.12×10^{-5} T
Std. gravitational parameter	μ	3.986×10^{14} m^3 s^{-2}
Mean radius of Earth	r_e	6370 km

Loop geometry:	A	B	C	D
N	Current, I (Amps)			
12	42.60	15.28	35.64	47.53
19	42.60	10.02	36.68	48.91
27	42.60	7.457	37.24	49.65

Attitude Control Simulation Parameters		
Length	D	250 m
Unit number	N	19
Bending stiffness	EI	10^4 N m^2
Loop Geometries	-	$[C, C, B]$
Max. currents	$\boldsymbol{I}^{max}$	$[36.68, 36.68, 5.644]$
Max. dip. moment	m^{max}	2.413×10^6 A m^2
Control Gains	k_p	600
	k_ω	4×10^5
Orbital altitude	R_o	800 km
Integration timestep	dt	0.05 s
Simulation runtime		10000 s
Mag. Field Model		WMM (2022) [169]
(Other data same as structural simulations.)		

Table 5.3: Simulation parameters

in free-space with a fixed external magnetic field direction with no other disturbing forces considered. This choice is made so that the deformation of the structure under application of the Lorentz forces can be directly observed and compared for each case without other factors affecting the structural dynamics. In all cases the structure is initially at rest, and the magnetic dipole moment is perpendicular to the magnetic field. The loop has a constant current, and then Eq. 5.27 is numerically integrated for 4000 s. Under these conditions, a rigid current loop would undergo simple harmonic motion, completing a rotation of 180 deg and then reversing direction. The simulation parameters are summarised in Table. 5.3, where the loop currents are calculated following the derivations in Sec. 5.1. A length scale of 250 m is selected as this results in a λ_f value of <10% in all cases (following Fig. 5.11 and 5.12), which is considered to be an upper limit on a reasonable mass allowance for the attitude control system of a gossamer structure of this size. Following Chapter 3, 10^3 N m ^{2} is taken as a reference beam like bending stiffness for a solar sail-type gossamer spacecraft, and then two orders of magnitude greater are considered, to cover a wide range of structural flexibilities. The areal mass density is selected as 100 g/m ^{2} by considering that near term solar sails can have an areal mass density on the order of 10 g/m ^{2}, and thus an order of magnitude greater than this is thought to be a reasonable value to cover the range of flexibilities we consider here, as discussed in Sec. 5.2.3. The magnetic field strength is considered a typical value for an orbital altitude of 800 km, determined by Eq. 5.22. The values of N were chosen to cover a range of values, with an upper limit of 27 selected due to exceedingly long computation times for values greater than this.

Results of the simulations are shown in Tables 5.4 to 5.7. The figures show the structure at the point of maximum strain energy (shown in the $x_oy_oz_o$ body frame), and a plot of strain against time throughout the simulation. The $x_oy_oz_o$ body frame is initially aligned with the xyz inertial frame as shown in Fig. 5.1. The structure itself is drawn in black while the current loops are coloured blue and green for the z and y direction dipole moment loops respectively. In all cases, it was found that a bending stiffness of $EI = 10^3$ N m^2 was too flexible for the current loop to rotate successfully, and the structure would collapse (as in the first column of Table 5.4). In particular, for geometries C and D, the orientation of the magnetic field and resultant Lorentz forces ended up stretching the structure in the z direction, to a distance of over 500 m. Although the structure essentially folds up in these simulations, it is important to note that this model does not exactly represent a membrane, in that the springs here are linear, behaving the same under tension and compression. This represents a general, homogeneous flexible truss structure rather than a gossamer spacecraft specifically. For a gossamer spacecraft of this flexibility, it is likely that the tensioning of the membrane would be a significant contribution to the structural response. Although it was thought that an electromagnetic current loop could in fact be used to tension the membrane of such a spacecraft, our results suggest that this would not be possible in practice. This is because, although some of the forces on the current loop would act to tension the membrane in one direction, there are always force pairs that will act to collapse/fold the structure in a direction perpendicular to these forces. In the simulation

N	EI (Nm^2) 10^3	10^4	10^5
12	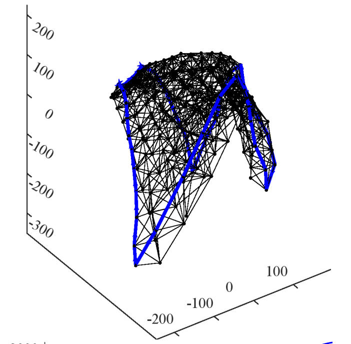	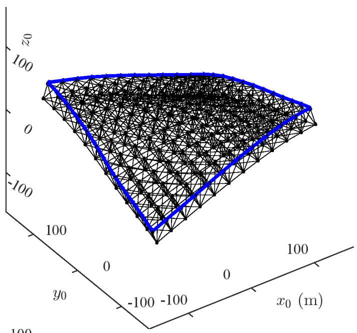	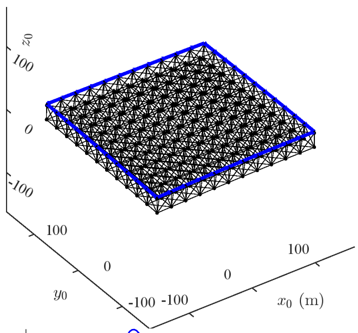
U (J)	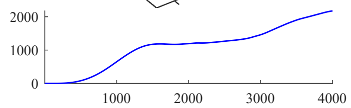	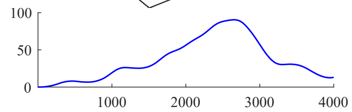	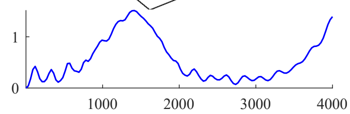
19	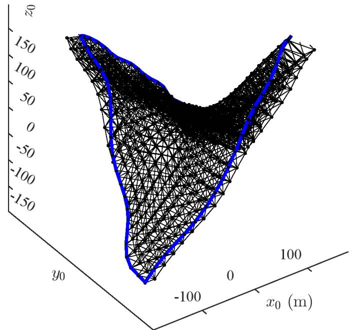	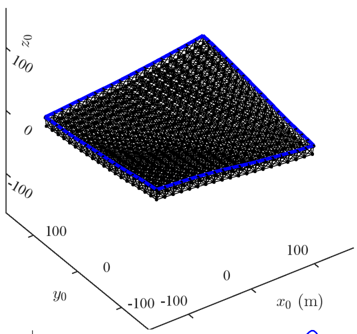	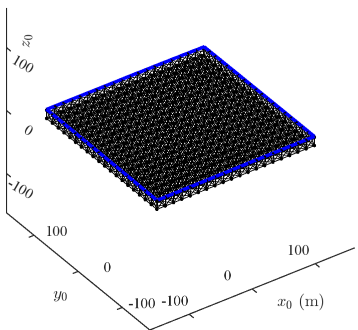
U (J)	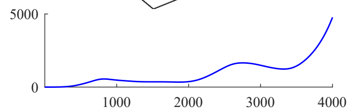	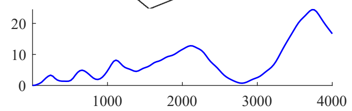	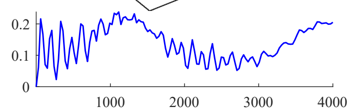
27	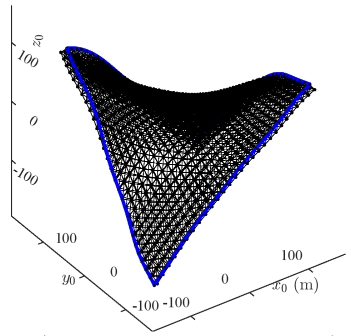	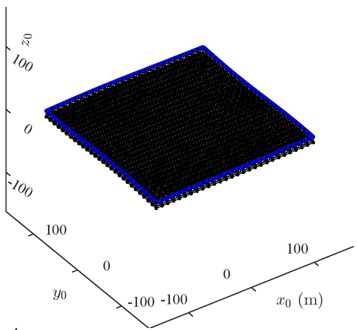	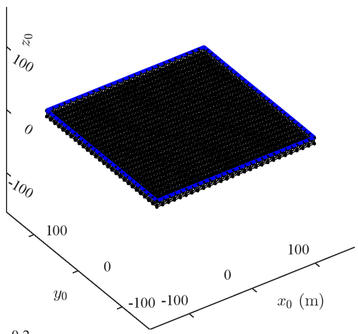
U (J)	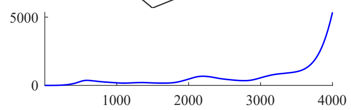	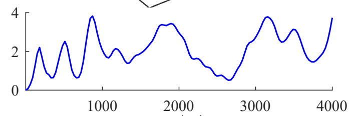	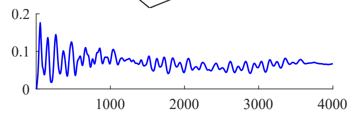
	t (s)	t (s)	t (s)

Table 5.4: Results of simulation for Geometry A

N	EI (Nm^2) 10^3	10^4	10^5
12	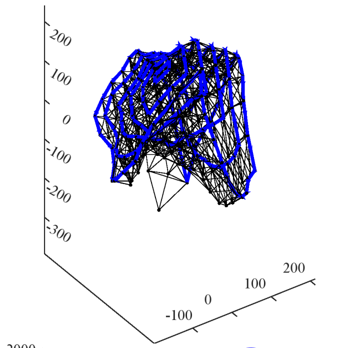	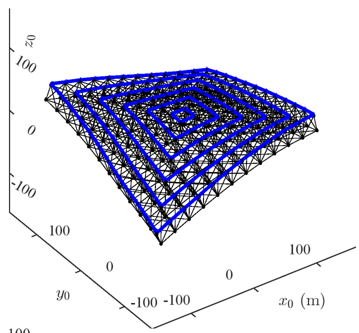	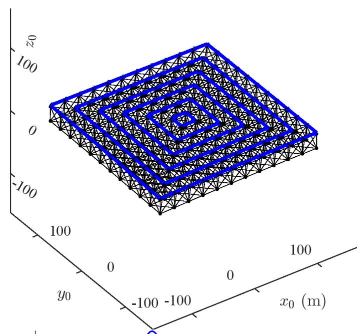
U (J)	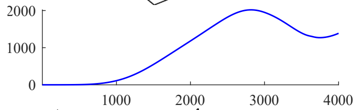	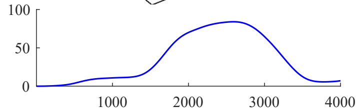	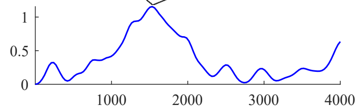
19	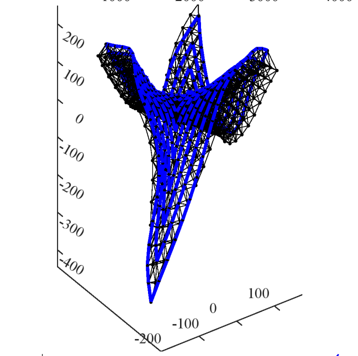	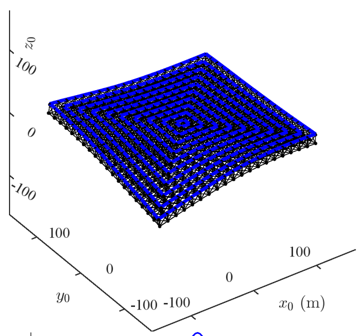	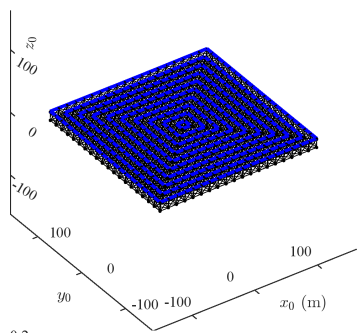
U (J)	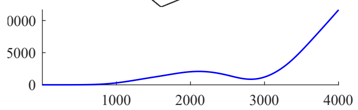	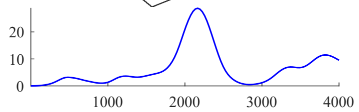	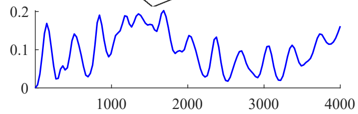
27	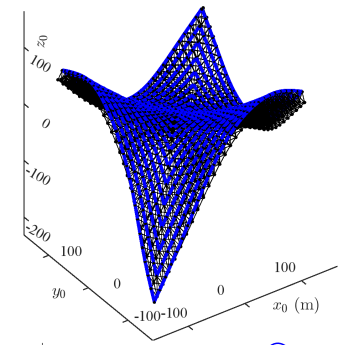	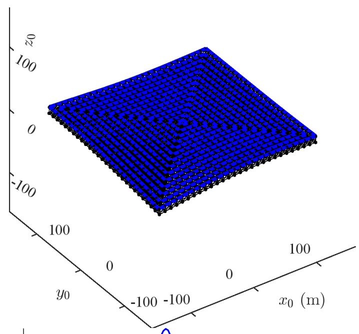	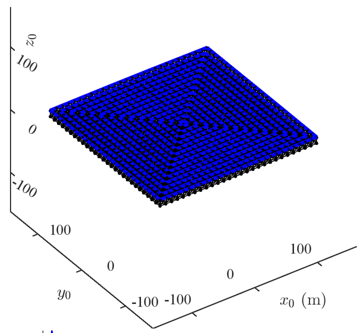
U (J)	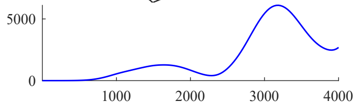	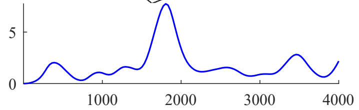	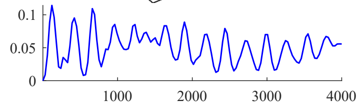
	t (s)	t (s)	t (s)

Table 5.5: Results of simulation for Geometries B

N	EI (Nm^2) 10^3	10^4	10^5
12	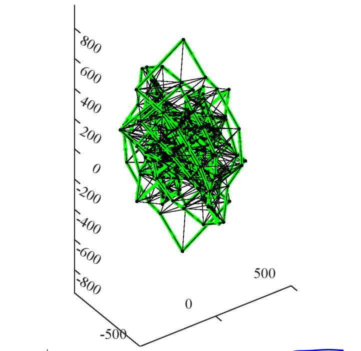	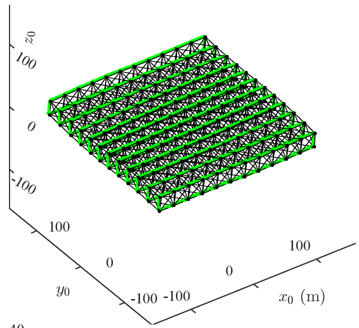	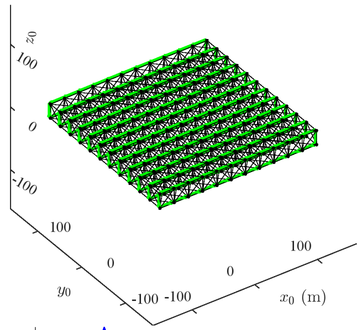
U (J)	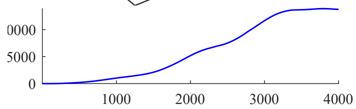	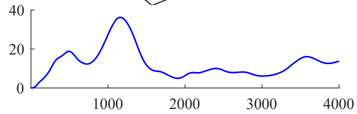	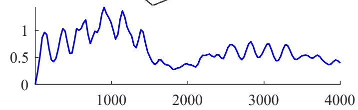
19	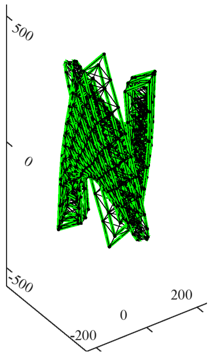	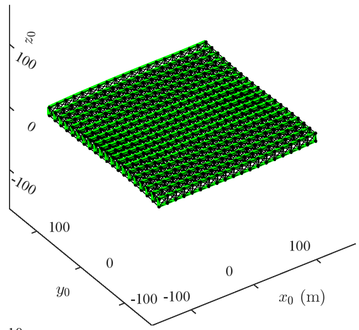	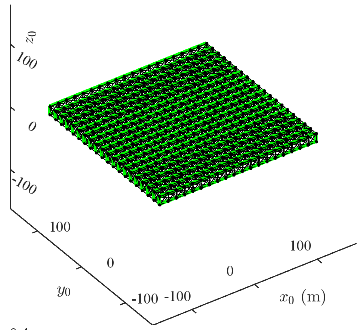
U (J)	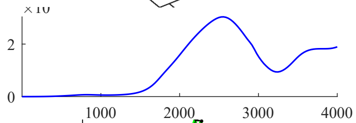	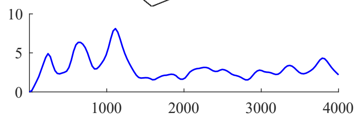	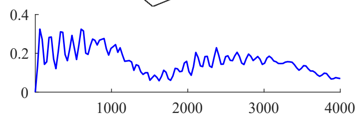
27	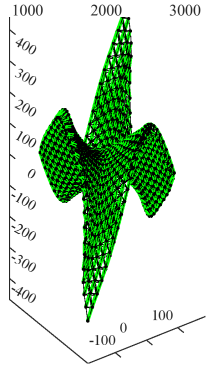	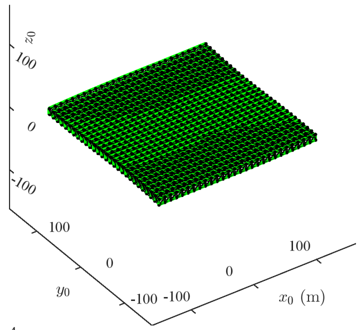	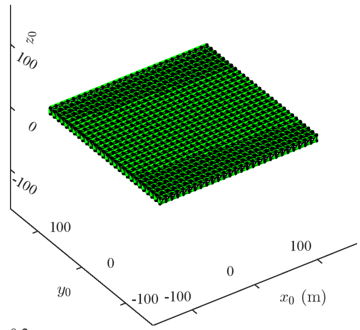
U (J)	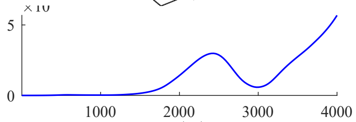	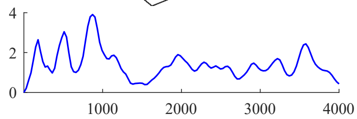	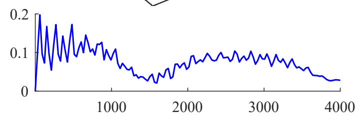
	t (s)	t (s)	t (s)

Table 5.6: Results of simulation for Geometry C

N	EI (Nm^2)		
	10^3	10^4	10^5
12	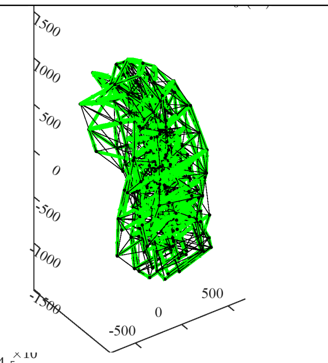	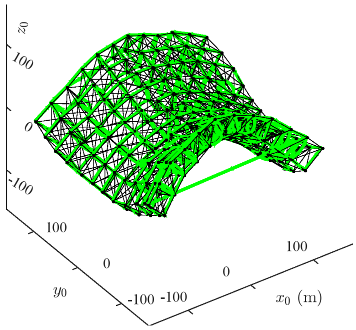	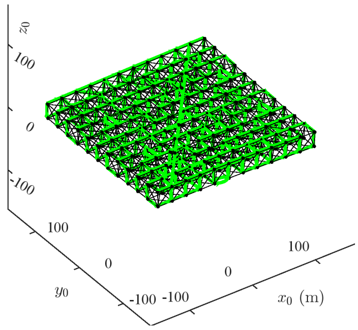
U (J)	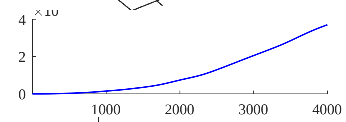	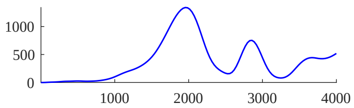	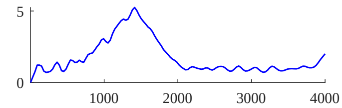
19	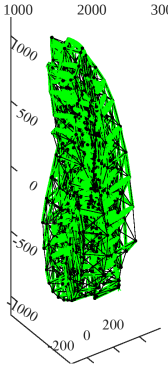	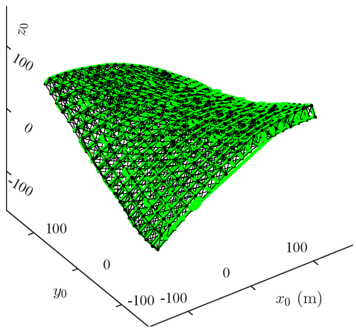	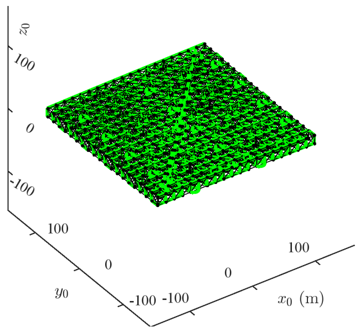
U (J)	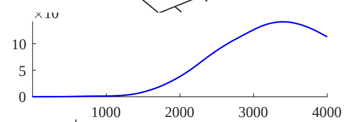	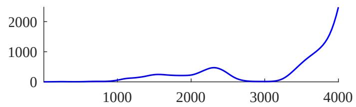	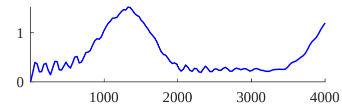
27	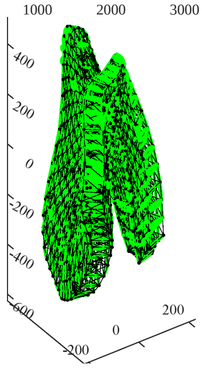	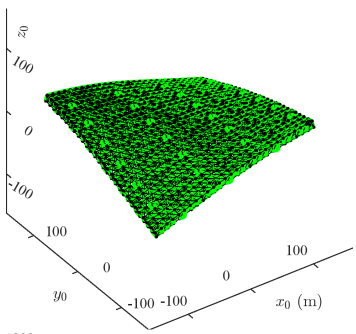	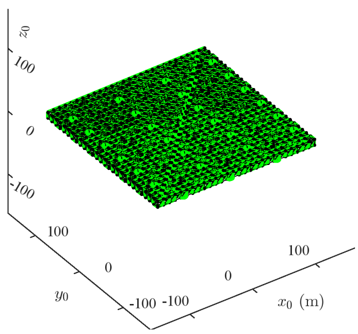
U (J)	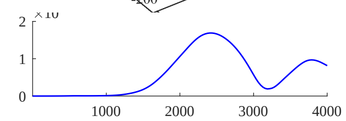	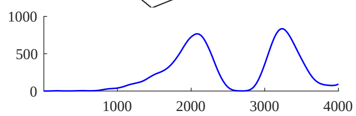	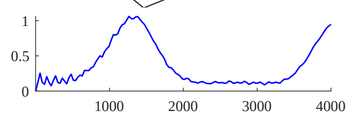
	t (s)	t (s)	t (s)

Table 5.7: Results of simulation for Geometry D

results this was observed most clearly for geometries C and D, as the structure was stretched in the z direction, and simultaneously compressed in the x direction. However, we note that this result is due to the interaction of the current loop with the external, geomagnetic field. For much higher currents, requiring superconducting loops, it has been demonstrated [119–121] that tensioning could be achieved via the self-forces in the wire. For $EI = 10^5$ N m^2, it was found that the structure behaves essentially as a rigid body in all cases, and thus for structures of this rigidity large current loops would be an effective means of attitude control, and standard rigid-body control laws may be used.

The chosen current loop geometries all resulted in quite different structural responses. This is because although the torque in all cases is the same, the forces which result in that torque have different magnitudes and are applied at different points. Comparing the z direction loops (A and B), the structural deformation and maximum value of the total strain are quite similar in each case, though there is some difference in the strain profiles for $N = 19$ and 27. For geometry B, there is a large peak in U at approximately 2000 s, whereas for geometry A there are larger oscillations in U over the entire simulation. At 2000 s the magnetic dipole moment is aligned with the field direction, and this is the point of minimum torque, but maximum "stretching" of the structure (as discussed in the previous paragraph). This suggests that although there is a slight benefit to having multiple planar current loops in that the structure can be more smoothly rotated, the tensioning of the current loop(s) at certain orientations results in similar deformations for both cases. Comparison of geometries C and D shows that for achieving a magnetic dipole moment in this direction, geometry C performs much better than the coil type geometry, with the strain energy two to three orders of magnitudes lower for the cases here. This is because for geometry D, there are many more opposing force pairs present which act to deform the structure instead of producing the desired torque, and these force pairs are always located in the same unit of the structure, whereas for C these forces act at opposite ends of the structure (the vertical loop elements at the edge of the structure). Considering the variation of N for cases B and C, there is a clear benefit to having a greater number of current loops in that the total strain is greatly reduced and the rotation is more similar to that of a rigid body.

Overall the results show that current loops are capable of smoothly rotating flexible structures, though for a given areal mass density there will be a minimum level of structural rigidity required to prevent excessive stretching of the structure. For a 100 g/m^2 structure results suggest a beamlike bending stiffness of approximately 10^4 N m ^{2} is sufficient. Although the current loops failed to rotate more flexible structures in this case, it is important to note that more flexible structures may have a lower mass than that considered here, and thus the torque applied in these simulations may be greater than would be required for their attitude control, though our analysis is restricted to 100 g/m^2 here. In all cases, having a greater number of current loops which distribute the Lorentz forces more evenly across the structure was found to result in lower structural deformation.

5.5 Attitude Control Simulation of a Conductive Structure

Having found that embedded current loops are capable of rotating a flexible spacecraft, this section now demonstrates the attitude control of a large space structure using current loops, in the presence of gravity gradient torques and a representative magnetic field model. A 250 m square planar structure is again considered, with multiple embedded current loops allowing three axes of controllable magnetic dipole moment. Current loop geometries B and C are considered, such that the structure is composed of a square lattice containing loop geometry B and two perpendicular cases of geometry C overlapping in the same structure. The spacecraft is placed in an 800 km altitude, circular polar orbit. An areal mass density of 100 g/m^2 and beam-like bending stiffness of $EI = 10^4$ N m ^{2} is selected, in keeping with the previous section where it was determined such a structure may be successfully rotated by embedded current loops with relatively little structural deformation. Gravitational forces are now added to Eq. 5.27, which are calculated for each point-mass particle of the model (using $\boldsymbol{F}_i^{grav} = (\mu m_i/|\boldsymbol{R}_i|^2)\hat{\boldsymbol{R}}_i$, where $\boldsymbol{R}_i$ is the position vector of particle i in an Earth centred inertial frame). As the gravitational force on each particle is calculated individually using that particle's position, variations across the structure naturally lead to gravity-gradient torques in the simulation. The structure is placed onto the desired orbit by giving every particle an initial velocity in the z-direction equal to the orbital velocity $v_o = \sqrt{\mu/R_o}$. The magnetic field is now calculated at each timestep of the simulation by determining the position of the structure's centre of mass in an Earth-centred inertial frame and finding the value of the World Magnetic Model (WMM) at that position [169]. It is assumed that there is no variation of the field across the structure to avoid evaluating the WMM multiple times and save computation time. In all other respects the simulation and model are the same as the previous section.

A proportional-derivative (PD) type quaternion error feedback control law is again implemented, which is commonly used for magnetic attitude control [113], and was previously considered in Chapter 3. The controller generates reference control torques according to:

$$\boldsymbol{T}_{ref} = -k_p \boldsymbol{q}_{err} - k_\omega \boldsymbol{\omega} \tag{5.33}$$

where $\boldsymbol{q}_{err}$ is the vector part of a quaternion representing the rotation between the current attitude and the desired attitude, $\boldsymbol{\omega}$ is the body rate vector, and k_p and k_ω are the control gains. Once a reference torque is found, the magnetic dipole moment necessary to generate this torque is then given by:

$$\boldsymbol{m}_d = \frac{\boldsymbol{B} \times \boldsymbol{T}_{ref}}{|\boldsymbol{B}|} \tag{5.34}$$

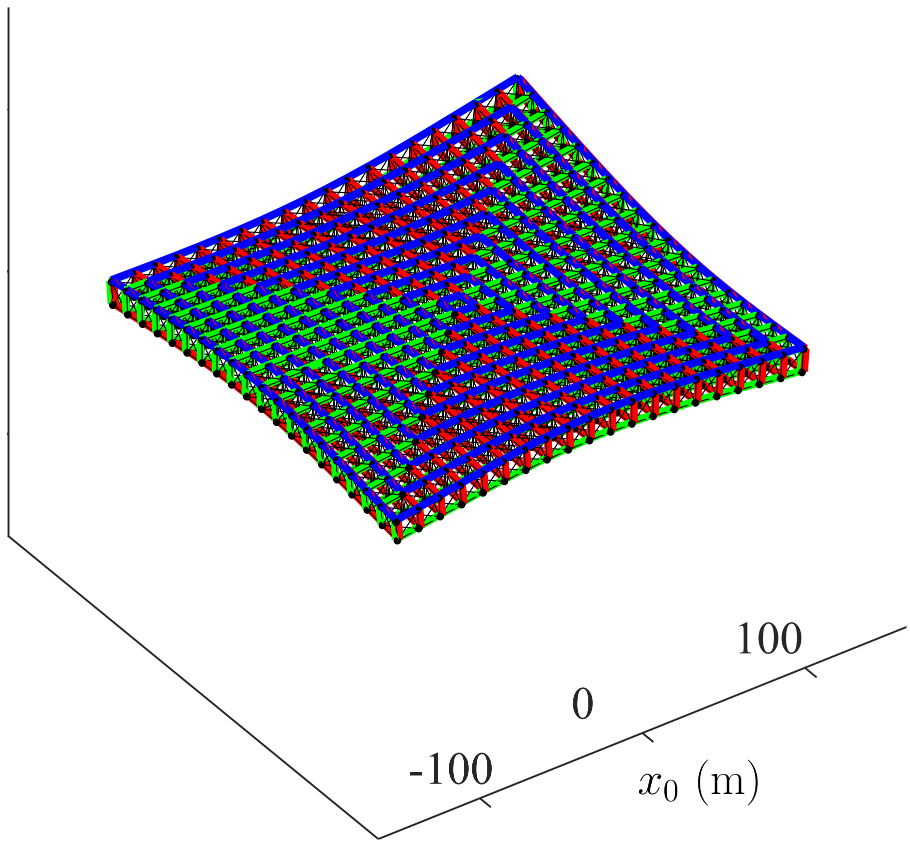

Figure 5.14: Structural displacement at point of maximum strain energy ($t = 9339$ s)

from which the loop currents are determined, according to:

$$\begin{aligned} \boldsymbol{I} &= \left(\frac{\boldsymbol{m}_d}{m^{max}}\right) \circ \boldsymbol{I}^{max} \\ I_L &= \text{sign}(I_L) I_L^{max} \qquad \text{if } I_L > I_L^{max} \end{aligned} \tag{5.35}$$

where $\boldsymbol{I}^{max}$ is the vector of maximum allowable currents in the loops calculated from Eq. 5.24, and m^{max} is the magnitude of the magnetic dipole moment of each loop at maximum current (which is the same value for all loops), and $\circ$ denotes elementwise multiplication of the vectors. The current vector $\boldsymbol{I}$ has components I_L, with $L = x, y, z$ corresponding to current in the xyz direction dipole loops respectively. The second line of Eq. 5.35 ensures that the current in each loop does not exceed the maximum allowable value. The control gains are selected following a trial-and-error approach, using a rigid-body simulation (which is faster to evaluate compared to the spring-mass model) with an equivalent inertia tensor to the spring-mass model. The structure is initially lying in the xy plane, and the desired rotation is a 90° slew manoeuvre around the y-axis. Simulation data and model parameters are summarised in Table. 5.3, using the same data as the length-scaling analysis of Sec. 5.3.

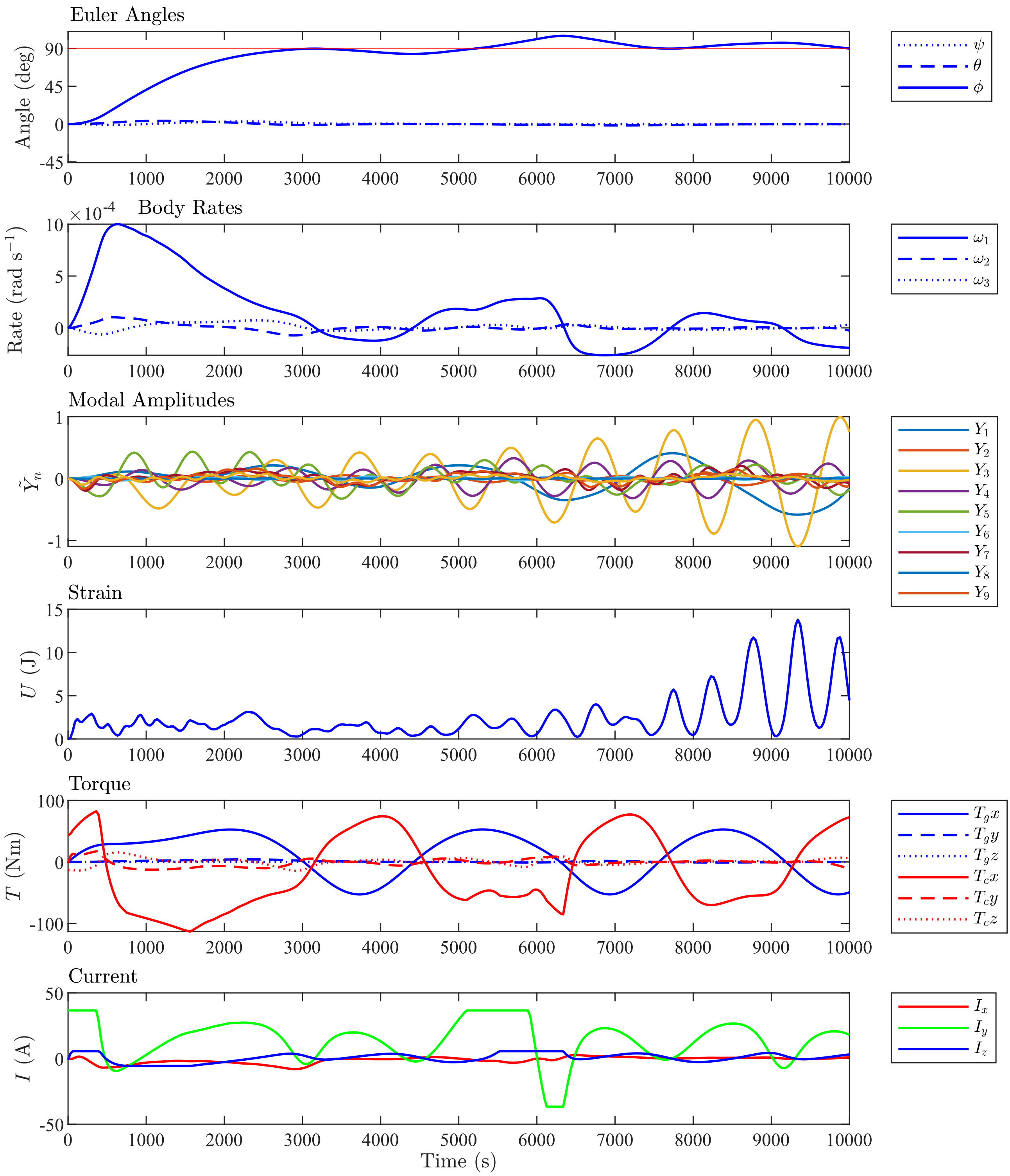

Figure 5.15: Attitude control simulation results

5.5.1 Results of Simulation

Simulation results are shown in Fig. 5.15. The simulation was performed for 10000 s, which is approximately 1.5 orbits. The structure is seen to smoothly rotate, reaching the target attitude in 3000 s. As the structure orbits, it is then periodically disturbed by the gravity gradient torque, which results in attitude errors of up to 18° (at 6500 s), which are then corrected by the controller. The torque profile shows that the actuation torque (blue) is mostly able to negate the gravity gradient torque (red), although at 5000 s there is a point where the controller is saturated, which leads to the large attitude error a short time later. The plots of strain energy and modal amplitudes (found by expressing the structure displacements as a superposition of the mode shapes in the standard way [176]) shows that the structural deformation is fairly small while the structure rotates, though there is some growing vibration of primarily the first and third mode shape towards the end of the simulation. Figure 5.14 shows a plot of the structure at 9339 s, the point of maximum strain energy in the system, showing that the structure is visibly deformed, though it is unlikely a displacement of this amplitude would cause failure due to buckling. While there are some growing vibrations towards the end of the simulation, these are to be expected due to the time-varying actuator and gravity forces. With some form of active or passive vibration control a damping ratio of closer to 10% of critical damping is expected to be a reasonable value for structures of this type [179], which would likely be sufficient to suppress these excitations on a longer timescale. We also note that although there is some control saturation, this could be avoided by increasing the wire mass. The current loops here were sized to produce a maximum torque equal to the maximum possible gravity gradient, but this maximum can only be achieved when the loop is oriented perpendicular to the magnetic field. Therefore, it is likely necessary that in practice the current loops should be sized to produce a maximum torque slightly greater than the maximum gravity gradient torque to avoid the control saturation which occurred in this simulation.

5.6 Chapter Summary

This chapter has investigated the attitude control of large space structures through the use of embedded current loops. First, the operating principle of the concept was discussed, and a variety of current loops geometries presented. A preliminary feasibility study was performed, considering the rigid-body dynamics of conductive structures, estimated values for spacecraft mass and loop current, and a simplified orbital reflector mission scenario for representative pointing requirements. This preliminary analysis was followed by more detailed consideration of the structures required mass and power. Results of a length-scaling analysis and a simple thermal model show that embedded current loops should be considered as a viable form of attitude control for large space structures, particularly for lightweight, planar structures which are most likely to be realised by on-orbit manufacturing techniques in the coming years. Simulations were then performed of a flexible structure with embedded current loops, investigating the behaviour of different path geometries for structures across a range of structural flexibilities and areal mass densities. Finally, an attitude control simulation was performed of a flexible structure with embedded conductive pathways, in the presence of gravity gradient torques and a time-varying magnetic field.

Chapter 6

Attitude and Shape Control of OrigamiSats

OrigamiSats are a new design paradigm in solar sailing, in which origami based designs are used to create reconfigurable, multifunctional membrane spacecraft. This chapter proposes and investigates a strategy for the attitude and shape control of OrigamiSats, in which the force due to SRP is used to enact folding and shape control of the origami spacecraft structure. This work was performed as part of a collaborative research project with the University of Liverpool, Oxford Space Systems, and JAXA, results of which have been published in Refs. [139] and [144] included in the list of publications in the thesis introduction. Research at the University of Liverpool investigated OrigamiSat manufacturing, considering the possibility of 3D-printing a rigid frame directly onto thin reflective films to produce the facets and foldable edges of the spacecraft. Various candidate materials and other considerations relating to the 3D-printing process were investigated, and a prototype of an OrigamiSat was produced in which shape memory polymer material was used to enact folding of the structure when heat was applied to the hinges. Complimentary to these practical experiments, the original work presented in this thesis chapter is concerned with numerical analysis and mathematical modelling of OrigamiSats, and an investigation into the potential of using SRP to enact OrigamiSat reconfiguration by controlling the reflectivity of each facet, through the use of Reflectivity Control Devices (RCDs). The research questions for this chapter are as follows:

1. Can the force due to SRP be used to reconfigure an OrigamiSat through the use of variable reflectivity?

2. At what length-scales or areal mass densities could the control strategy be considered feasible?

3. Can shape reconfiguration with variable reflectivity be controlled through the use of a closed-loop feedback control law, and can this be further extended to include attitude control?

These questions are investigated first by considering analytical solutions for the folding times of a simplified model, and then through the use of numerical simulations which model the dynamics of multibody OrigamiSat systems under the effect of SRP. As the research was not focussed on a specific OrigamiSat design/folding pattern, a further goal was to develop a simulation framework in which the origami design could be easily modified, in order to consider a variety of folding patterns.

The control strategy investigated in this chapter is quite a different form of actuation to the magnetic control strategies considered in previous chapters. However, there are a number of characteristics of the control problem and of the type of spacecraft being considered which all of the strategies proposed in this thesis have in common. Firstly, the control of an OrigamiSat with variable reflectivity is another form of distributed actuation, in that the actuators (RCD devices) are placed evenly across the spacecraft structure, distributing the control forces. Secondly, the control problem is underactuated, due to the constrained direction of the force due to SRP, a problem which was also encountered during the investigation of magnetic control. OrigamiSats, as a type of solar sail, will also have a similar areal mass density and length scale (i.e. ultra-light membrane spacecraft) as the structures considered in the previous chapters. Finally, it is noted that OrigamiSats are also a potential type of spacecraft for which on-orbit manufacturing could be an enabling technology. As noted, collaborators at the University of Liverpool have investigated the 3D-printing of OrigamiSat structures directly onto thin-films [139], a manufacturing process which could potentially be performed in-orbit to produce OrigamiSats at a greater length scale and lower mass than would otherwise be possible. While the content of this chapter is concerned with OrigamiSat control and dynamics, it is noted that the analysis is performed in the context of a spacecraft architecture which may be produced using on-orbit 3D-printing. This is therefore a further commonality between OrigamiSats and the other spacecraft architectures considered thus far, in accordance with the stated aims of the thesis.

In this chapter, mathematical models of OrigamiSats are developed and used to demonstrate that folding can be triggered by changing the local optical properties of the membrane. First, in Sec. 6.1 a simplified, planar model of a single facet folding is used to derive some approximate scaling laws. In Sec. 6.2, a 2D model of linked rigid facets is used to demonstrate the principle of SRP triggered shape reconfiguration. Section 6.3 then describes a 3D multibody dynamics formulation, which is used to derive the equations of motion for arbitrary OrigamiSat fold patterns. A ray-tracing module is described, which has been included in the model to consider the effects of inter-facet reflections or shadowing. Simulations are performed of different OrigamiSat designs, investigating the system dynamics and an initial attempt is made at implementing shape control of a constrained OrigamiSat. Section 6.4 then discusses a potential control strategy in which a closed-loop feedback controller is developed which combines both shape and attitude control for a Miura-fold OrigamiSat. Results of simulation for some example manoeuvres are presented and discussed, demonstrating the proposed strategy.

A summary of the chapter is then given in Sec. 6.5.

6.1 Folding Time of a Rigid Reflective OrigamiSat Facet

Here, the feasibility of using SRP to actuate the folding of high area-to-mass ratio, rigid facets is demonstrated using a simplified planar model of a rigid panel with a fixed edge constraint. This rigid panel represents a single facet of an OrigamiSat. The bending resistance from the hinge material of an OrigamiSat is estimated by assuming that the panel can be treated as a centre-loaded cantilever beam [180], and scaling laws for the hinge resistance torque and SRP force are developed.

Figure 6.1 illustrates a rigid, reflective, square facet with a fixed support at one edge and exposed to incoming radiation. The facet has sidelength l, and the unit vectors $\boldsymbol{n}$ an $\boldsymbol{t}$ define the surface normal and transverse vectors respectively. The transverse direction is defined to be the vector perpendicular to $\boldsymbol{n}$ and lying within the plane spanned by $\boldsymbol{n}$ and $\boldsymbol{u}_i$, which is the direction of the incident radiation. Considering only specular reflection and absorption of the

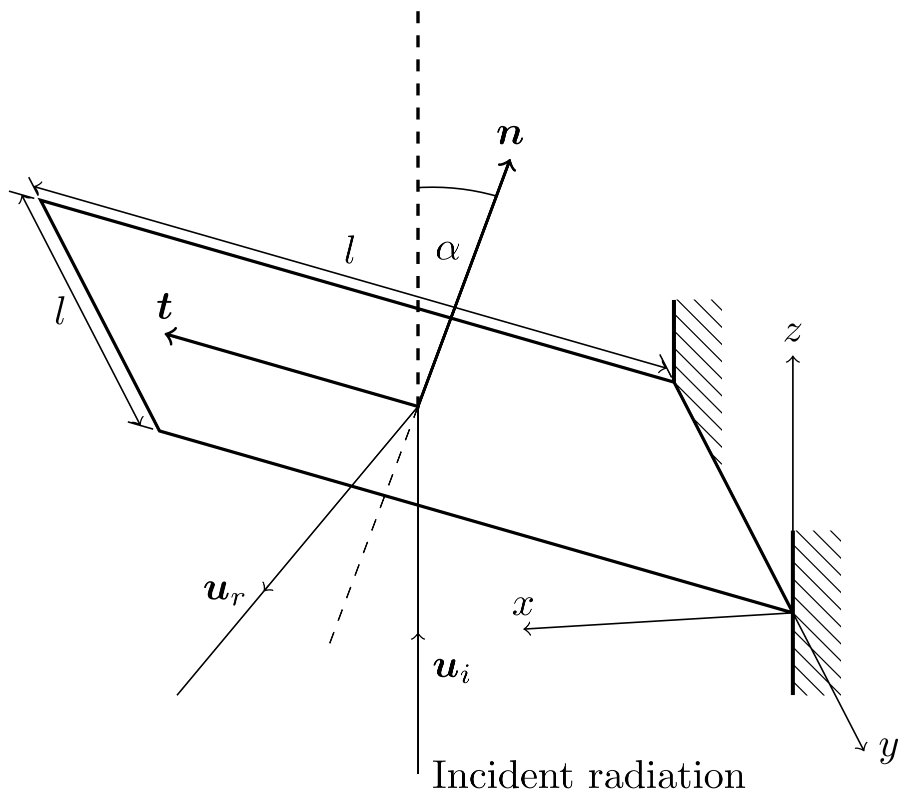

Figure 6.1: Reflective origami facet with fixed edge constraint.

incident radiation, for a Lambertian surface the force acting on the facet is given by:

$$\boldsymbol{F}_{\text{SRP}} = PA(1+\rho)\cos^2\alpha\boldsymbol{n} + PA(1-\rho)\cos\alpha\sin\alpha\boldsymbol{t} \tag{6.1}$$

where ρ, the reflectivity, is the fraction of the incident radiation that is reflected, $P = 4.563 \times 10^{-6}$ N m^{-2} is the SRP constant 1 AU from the Sun, and $A = l^2$ is the facet area [4].

The surface is further assumed to be perfectly reflective, in which case $\rho = 1$ and Eq. 6.1 reduces to $\boldsymbol{F}_{\text{SRP}} = 2PA\cos^2\alpha\boldsymbol{n}$. An expression is now derived for the time required for the facet to complete a fold through $\pi/2$ radians. If the facet has no bending resistance, and so is free to rotate around the fixed edge, the angular acceleration of the facet around the y-axis is given by:

$$\ddot{\alpha} = \frac{\tau}{I_y} = \frac{3P\cos^2\alpha}{\sigma l} \tag{6.2}$$

where $\tau = Pl^3\cos^2\alpha$ is the magnitude of the torque produced by the SRP force ($\boldsymbol{F}_{\text{SRP}}$), acting through the centre of the facet, and $I_y = \frac{1}{3}\sigma l^4$ is the mass moment of inertia of the facet around the y-axis, expressed in terms of the areal mass density σ. Equation 6.2 is then linearised in the range $\alpha = [0, \pi/2]$ by making the approximation $\cos^2\alpha \approx (1 - \frac{2}{\pi}\alpha)$. This approximation replaces $\cos^2\alpha$ with a linear function that varies from 1 to 0 in the range $\alpha = [0, \pi/2]$, as shown in Fig. 6.2, i.e. it is assumed that the force due to SRP is proportional to the angle of incidence. This approximation is sufficient for the purposes of the analysis here, where the aim is to find order of magnitude estimates for the time taken to fold an OrigamiSat facet. Of note is that an equivalent problem to that studied here is solved without this linearisation in Ref. [181], where the authors determine the oscillation period of a triangular solar sail. Though the approach taken in Ref. [181] does not require the linear approximation of $\cos^2$ adopted here, the resultant expression does include an integral expression which must be determined numerically in general. While the approximation adopted here may result in a less accurate expression, as noted it is considered sufficient for the discussion here and furthermore results in more straightforward expressions for $\alpha(t)$, which provide clarity of discussion. Following the aforementioned linearisation, an approximate solution for $\alpha(t)$ can be derived when setting $\dot{\alpha}(0) = \alpha(0) = 0$:

$$\alpha(t) = \frac{\pi}{2}\left[1 - \cos\left(\sqrt{\frac{6P}{\pi\sigma l}}t\right)\right] \tag{6.3}$$

The time taken for the facet to complete a rotation of $\pi/2$ rad is found by rearranging Eq. 6.3 for t and integrating between $\alpha = 0$ and $\pi/2$, which gives:

$$t_{\pi/2} = \frac{\pi}{2}\sqrt{\frac{\pi\sigma l}{6P}} \tag{6.4}$$

Equation 6.4 is illustrated in Fig. 6.3, for areal mass densities ranging from 10 g/m^2, that of near term solar sails, to two orders of magnitude higher. A range of areal mass densities are

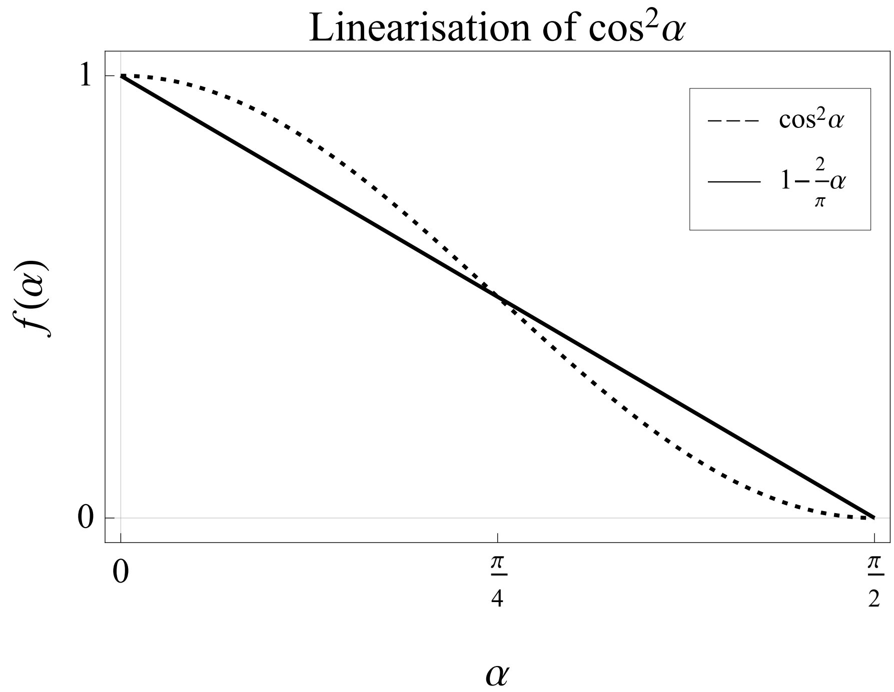

Figure 6.2: Dependence of folding time on length scale and areal mass density.

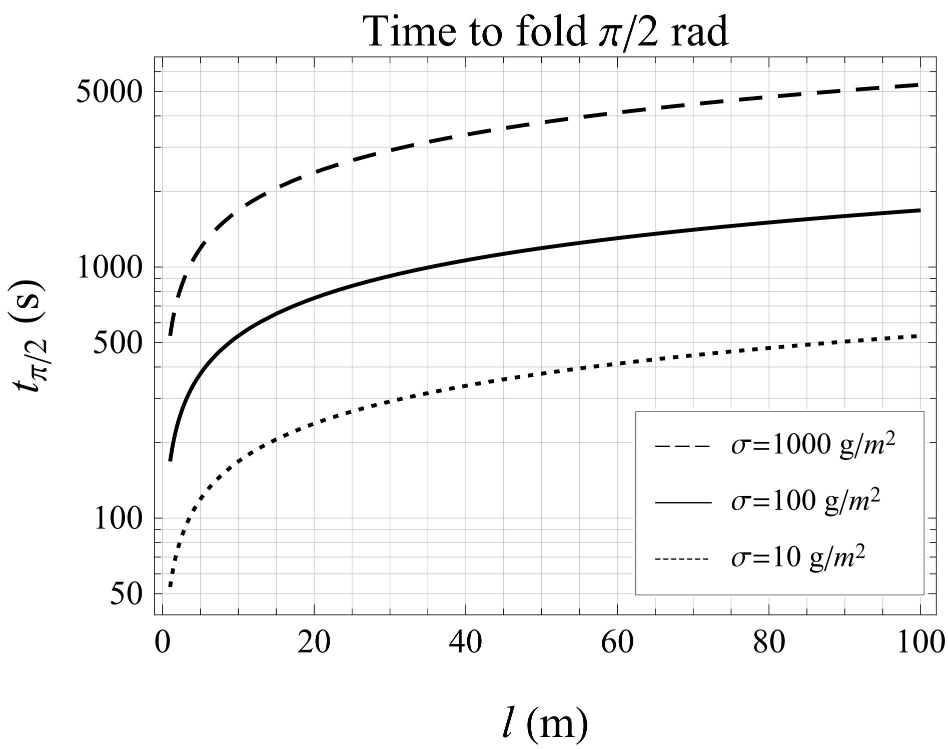

Figure 6.3: Dependence of folding time on length scale and areal mass density.

considered to take into account the fact that the areal mass density of OrigamiSats will likely be greater than that of a single (conventional) solar sail of equivalent total area. This is thought likely for two reasons, the first being that this analysis assumes a rigid facet, and the structural mass required to guarantee sufficient rigidity may increase the overall areal mass density. The second reason is that each OrigamiSat will require its own subsystems (communications, power etc), which will also contribute to an increase in mass (compared to a single, larger solar sail with a single bus). While near term solar sails are expected to have an areal mass-density on the order of 10 g/m^2, a more probable estimate for an OrigamiSat swarm is thought to be on the order of 100 g/m^2. This estimate is made by considering the typical areal mass density of Cubesat solar sail designs [182], and by supposing that a single OrigamiSat is likely to resemble a Cubesat in terms of the sail length scale and mass of the central spacecraft bus. As shown in Fig. 6.3, for areal mass densities of this order of magnitude the time required to fold the facet remains on minute time-scales for length-scales up to 100 m. This suggests that rapid, active shape re-configuration of OrigamiSats could be feasible using SRP.

6.1.0.1 Bending Resistance

In the previous section, a formulation was adopted where the rigid facet was free to rotate around the fixed edge in Fig. 6.1. Now, a more realistic model is introduced where the resistance to the facet's rotation due to the hinge material is taken into account. The hinge is only required to constrain the OrigamiSat edges together, allowing relative rotation, and so one solution would be to use the sail material itself as a flexure hinge. The hinge stress due to the inertial forces of the rotating facets would need to be considered in the sail design process, but at this stage it is assumed that the hinge can be thin enough that a flexure hinge of sail material would be the solution offering the lowest bending resistance. In other words, it is assumed that the resistance of the hinge can be modelled as a linear torsion spring, where the resistance to rotation comes from the bending stiffness of the hinge material, rather than the resistance coming from the friction in a hinge or bearing. The rotational bending stiffness is defined [180] by:

$$k = \frac{EI_{yA}}{l} = \frac{Ed^3w}{12L} \tag{6.5}$$

where E is the Young's modulus, I_{yA} the second moment of area of the hinge cross-section, and w, d and l the width, thickness and length of the hinge respectively, as illustrated in Fig. 6.4. It is assumed that the hinge material is thin enough that the curvature can be ignored, i.e. that the deflection discontinuously increases from 0 to ϕ at the hinge root, where ϕ is the hinge angle. This assumption was also made by [183] when modelling creases in a 7.5μm solar sail film and found to be accurate through non-linear finite element analysis, and through comparison with experiment. With this assumption, the bending resistance of the square facet illustrated in Fig. 6.1a is given by:

$$k = \frac{Ed^3}{12} \tag{6.6}$$

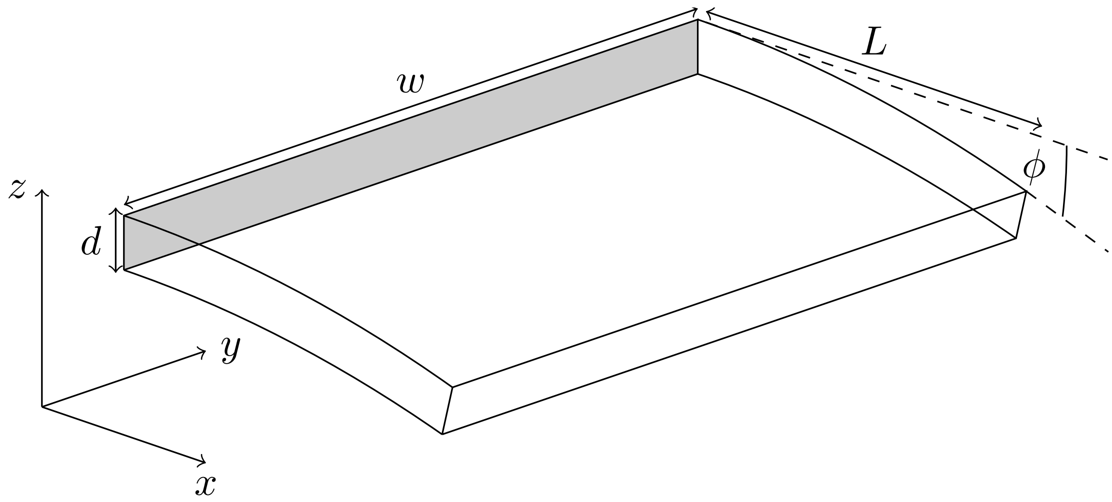

Figure 6.4: Flexure hinge geometry

which is found by taking Eq. 6.5 and setting $w = L = l$. The bending resistance does not depend on l because although the length of the fold root, and thus second moment of area increases proportional to l, the lever arm of the applied force also increases at the same rate. An expression is now derived for the time taken for a square facet subjected to SRP and with bending resistance to fold $\pi/2$ radians. With bending resistance, Eq. 6.2 becomes:

$$\ddot{\alpha} = \frac{Pl^3 \cos^2 \alpha - k\alpha}{\frac{1}{3}\sigma l^4} \tag{6.7}$$

Again approximating $\cos^2 \alpha \approx (1 - \frac{2}{\pi}\alpha)$, a solution for $\alpha(t)$ is:

$$\alpha(t) = \pi P l^3 \left(1 - \cos\left[\sqrt{\frac{6Pl^3 + \frac{1}{4}E\pi d^3}{\pi\sigma l^4}}t\right]\right) \tag{6.8}$$

and the time taken to reach a fold angle of $\pi/2$ rad is now given by:

$$t_{\pi/2} = \sqrt{\frac{\pi l^4 \sigma}{6l^3 P + \frac{1}{4}E\pi d^3}} \cos^{-1}\left[-\frac{\pi E d^3}{24 l^3 P}\right] \tag{6.9}$$

Equation 6.9 only has a solution if:

$$l > d\left(\frac{\pi E}{24P}\right)^{\frac{1}{3}} \tag{6.10}$$

If the inequality in Eq. 6.10 is not satisfied, physically this means that the facet does not complete a rotation of $\pi/2$ radians, as the bending stiffness is too large compared to the SRP torque. If l is equal to the right hand side of the inequality then the facet just reaches $\pi/2$ radians, but will oscillate between $\alpha = 0$ and $\pi/2$. For larger l, the facet will exceed this angle.

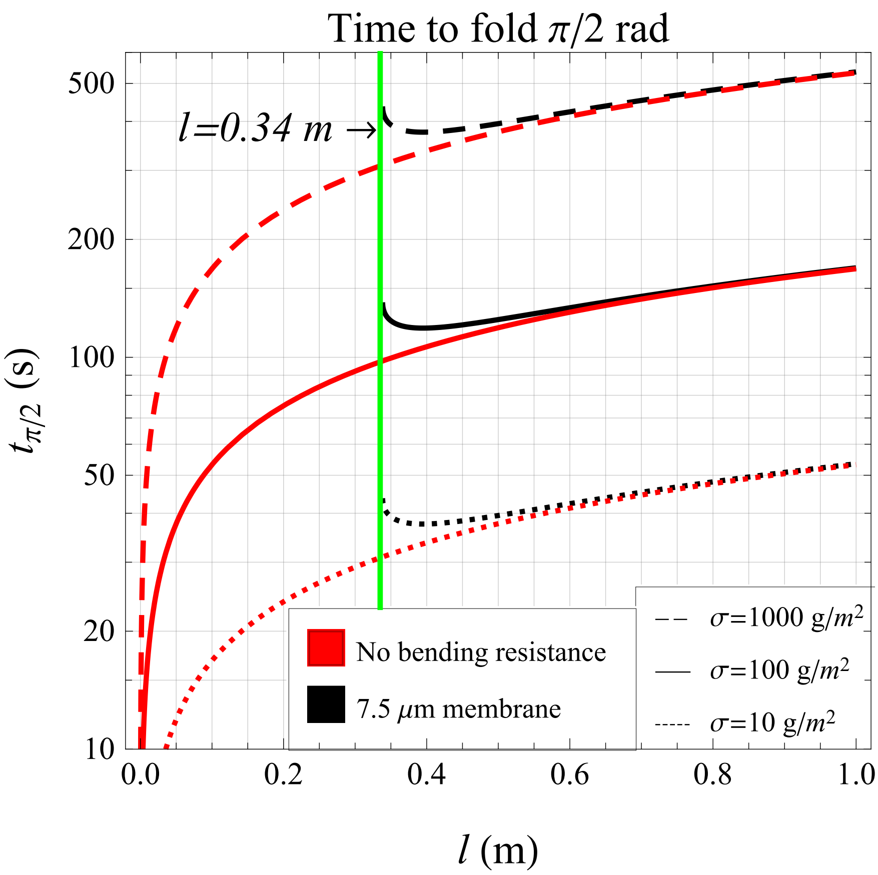

Figure 6.5: Change in facet folding time with length-scale, considering the bending stiffness of a 7.5 μm thick flexure hinge.

Equation 6.10 then gives the minimum facet length scale required to fold a facet using SRP for a given flexure hinge thickness. Using parameters of the IKAROS base membrane as an example [183], $d = 7.5$ μm and $E = 3.2$ GPa, Eq. 6.9 is shown in Fig. 6.5, along with the zero bending resistance case. For $l < 0.34$ m, there is no solution, while for $l > 0.34$ m the curve rapidly approaches the no bending resistance case, and the hinge resistance can effectively be ignored.

This analysis shows that, for a simplified, rigid facet model, it should be possible to rapidly fold an OrigamiSat using SRP. When the effect of the hinge bending resistance was considered, assuming the hinge is a thin flexure hinge of comparable thickness to the sail membrane itself, there is a minimum length scale required for the facet to be able to overcome the bending resistance and fold, but for length scales greater than this the bending resistance can essentially be ignored.

6.2 Planar Model of Linked, Reflective Facets

Having considered a simplified, single facet model in the previous section, the analysis is now extended to investigate the multibody dynamics of an OrigamiSat with multiple facets. To this end, a planar model of linked rigid bars has been developed, and is presented here. The aim of this work is to first verify results relating to folding-times obtained via the simplified single facet model of the previous section, and to assess the feasibility of using SRP to trigger the OrigamiSat folding when there are multiple rigid facets rotating relative to one another, and when the entire system is in free-space with no fixed supports.

6.2.0.1 Model Description

Here, the equations of motion for a multibody system consisting of N linked, rigid bars are presented. The generalised coordinates of the system are the x and y coordinates of each bar's centre-of-mass, and the angle θ each bar makes to the x-axis. These coordinates are contained in the state vector $q = [x_1, y_1, \theta_1, ..., x_N, y_N, \theta_N]$. The system dynamics are found using a Lagrange multipliers formulation, as described by, for example, Ref. [184]. The constraints are satisfied by first solving:

$$\mathbf{J}\mathbf{M}^{-1}\mathbf{J}^T\boldsymbol{\lambda} = -\dot{\mathbf{J}}\dot{\boldsymbol{q}} - \mathbf{J}\mathbf{M}^{-1}\boldsymbol{Q}_a \tag{6.11}$$

for a vector of Lagrange multipliers $\boldsymbol{\lambda}$, and then finding the constraint forces with:

$$\boldsymbol{Q}_c = \mathbf{J}^T\boldsymbol{\lambda} \tag{6.12}$$

where $\mathbf{J}$ is the Jacobian, defined by $\mathbf{J} = \partial\boldsymbol{C}/\partial\boldsymbol{q}$ for the constraint equation vector $\boldsymbol{C}$. $\boldsymbol{Q}_a$ is the vector of applied forces. $\mathbf{M}$ is the mass matrix, which is diagonal with elements $[m_1, m_1, I_1, ...m_N, m_N, I_N]$, where m_i, $I_i = \frac{1}{12}m_iL_i^2$ are the mass and mass moment of iner-

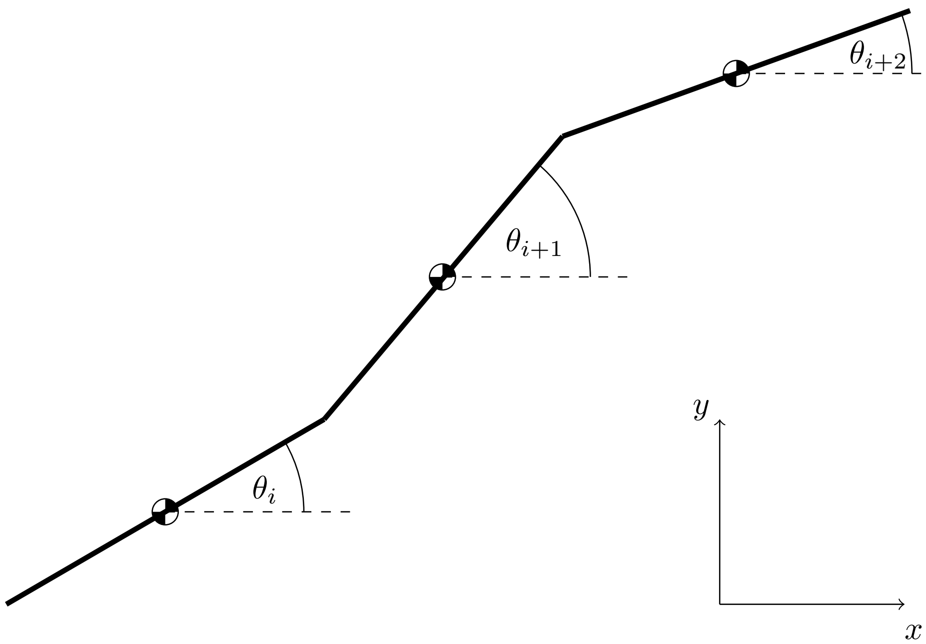

Figure 6.6: Planar multibody system of rigid bars linked by revolute joints.

tia of the ith bar, respectively, for bar length L_i. The constraint equations are given by first finding the position vector of the end of each bar, and enforcing that the ends of connected bars are coincident, such that:

$$\boldsymbol{C} = \begin{pmatrix} x_1 + \frac{1}{2}L_1\cos\theta_1 - x_2 + \frac{1}{2}L_2\cos\theta_2 \\ y_1 + \frac{1}{2}L_1\sin\theta_1 - y_2 + \frac{1}{2}L_2\sin\theta_2 \\ \vdots \\ x_{N-1} + \frac{1}{2}L_{N-1}\cos\theta_{N-1} - x_N + \frac{1}{2}L_N\cos\theta_N \\ y_{N-1} + \frac{1}{2}L_{N-1}\sin\theta_{N-1} - x_N + \frac{1}{2}L_N\sin\theta_N \end{pmatrix} = 0 \tag{6.13}$$

The equations of motion are then given by:

$$\ddot{\boldsymbol{q}} = \mathbf{M}(\boldsymbol{Q}_a + \boldsymbol{Q}_c) \tag{6.14}$$

which may be numerically integrated to evaluate the time-evolution of the system. The applied force vector $\boldsymbol{Q}_a$ is the force due to SRP on each bar, and is found by evaluating Eq. 6.1 for each bar, for a given radiation incidence direction and the reflectivity ρ_i of each facet, and again assuming square facets such that $A_i = L_i^2$. The bending stiffness of the edges is not considered at this stage, since the previous analysis found this force to be negligible compared to the force due to SRP for large enough facets.

6.2.0.2 Results of Simulation

The planar multibody model is now used to investigate the dynamics of linked rigid, reflective facets in free space, subject to SRP. Simulations are performed using custom code developed in MATLAB, in which the equations of motion are implemented and numerically integrated. Numerical integration is performed with a Runge-Kutta 4$^{\text{th}}$ order integration scheme, and a simulation timestep of 1 s. The bar elements are given a length of 1 m, and the mass is calculated assuming an areal mass density of 10 g/m^2. The incident radiation is directed along the positive y-axis. In the first simulation, two linked bars with perfect reflectivity $\rho = 1$ are considered. If initially, $\theta_1 = \theta_2 = 0$ rad, there is no relative rotation of the bars, as the SRP force is normal to both surfaces and thus in the same direction, so it is experienced by the system as rigid body motion. A small initial relative angle is introduced, by setting $\theta_1 = -0.01$ rad and $\theta_2 = 0.01$ rad. This means that the SRP acts to fold the facets together as there is a small difference in the direction of the force on each facet. The system is shown plotted at three points in Fig. 6.7. Through simulation, it was found that the two facets fold together in a time of 412 s. This is greater than the time suggested by Fig. 6.3 for facets of this size. This is because there is no fixed support at the edge and each facet is free to accelerate in the y-direction when the force is applied. However, once the rotation begins it rapidly accelerates, as a greater portion of the SRP torque acts in opposing directions on the two facets, and the majority of the fold is completed within approximately 50 s which is more in line with the

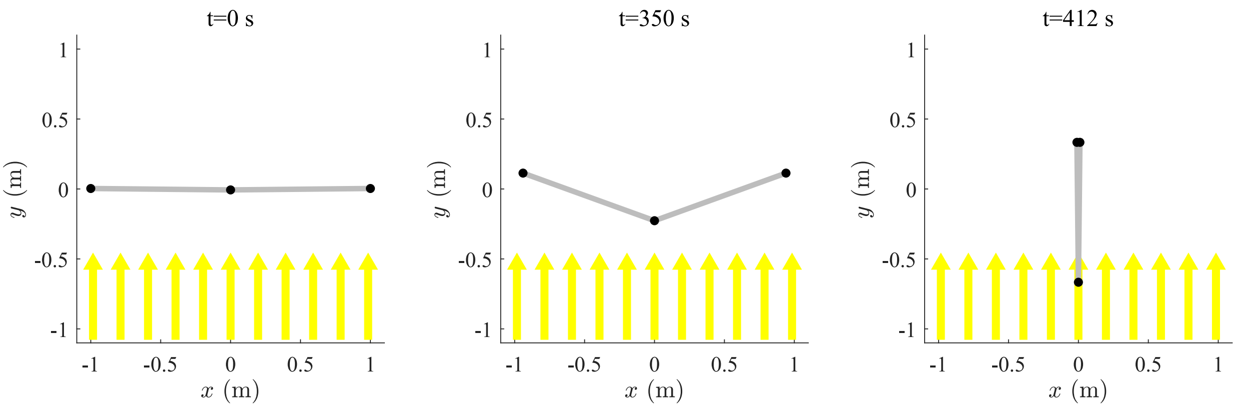

Figure 6.7: Planar dynamics of two perfectly reflective, linked, rigid panels subject to SRP

expected folding times given in Fig. 6.3.

By controlling the surface reflectivity of each facet, through the use of RCDs for example, folding can be induced without the need for an initial relative angular displacement, as was required in the previous simulation. This is because, as a consequence of Eq. 6.1, a facet of equal area with higher reflectivity will experience a greater force, and thus accelerate relative to a less reflective facet, resulting in a rotation around the joint between them.

A simulation was performed of a three facet system, with reflectivities given by $[1, 0, 1]$ for facets one to three respectively, and all initial angles zero. These reflectivities represent an idealised case, though in practice the difference in reflectivity that could be achieved with RCDs will most likely be much smaller. Due to the difference in surface reflectivity between the facets, a fold is induced. Three facets are used here such that the symmetry prevents the

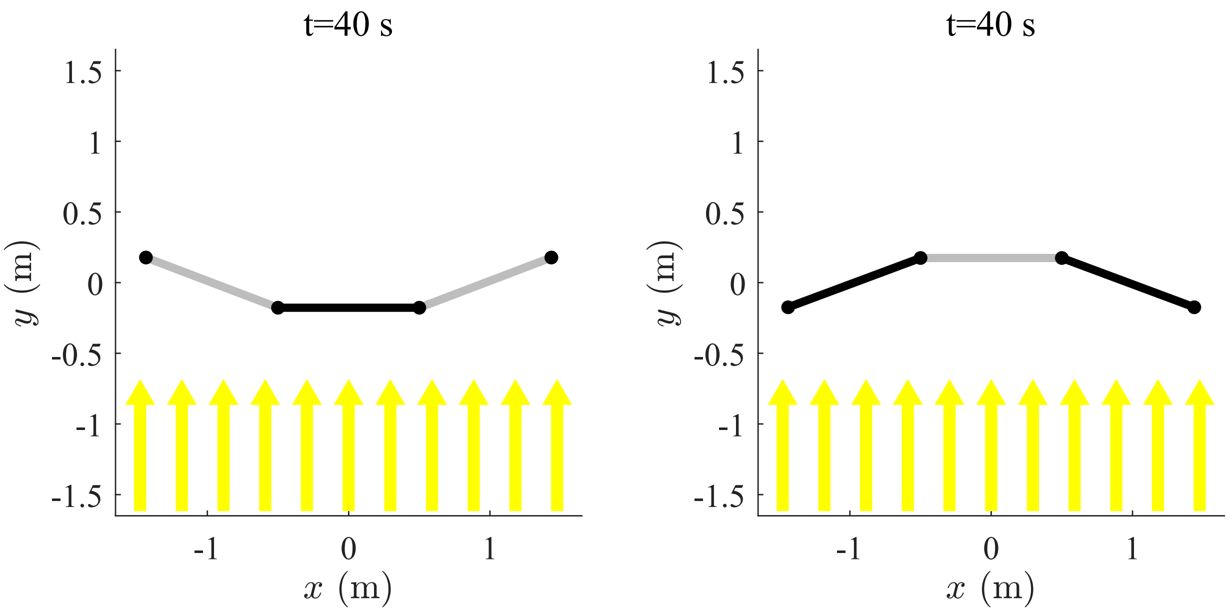

Figure 6.8: Three panel system, plotted in the centre-of-mass frame at $t = 40s$ for alternating reflectivty patterns.

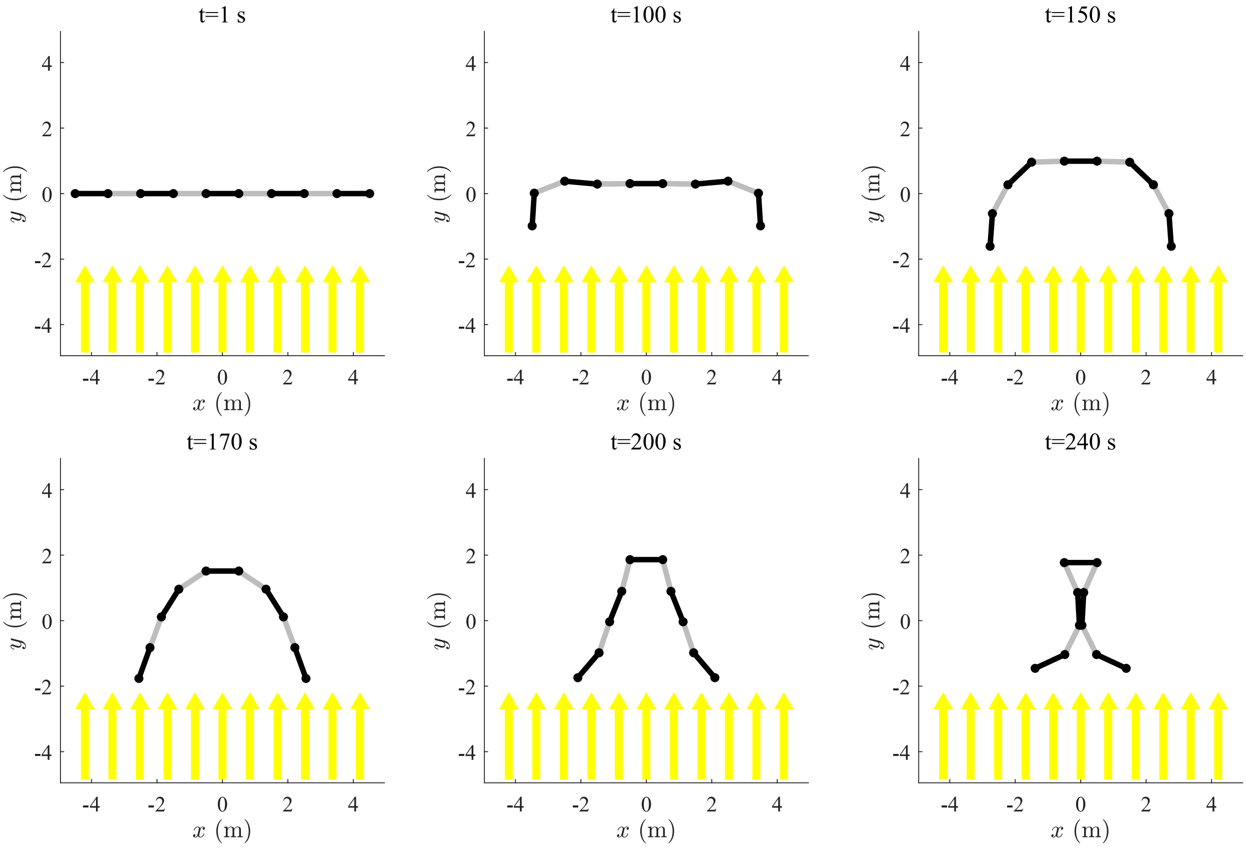

Figure 6.9: Results of simulations of a planar multibody system, consisting of linked rigid bars and subjected to SRP. Black represents a perfectly absorbing facet, while gray is perfectly reflecting.

overall system rotating, and so only the outer facets fold in while the centre facet remains flat. The facets are found to complete a fold of $\pi/2$ radians in 100 s. This is twice the value expected in from the fixed edge analysis in Fig. 6.3 for $l = 1$ m, because unlike the fixed edge case the centre facet here is also accelerating in the positive y-direction. Since the force on the perfectly absorbing centre facet is exactly half that on the outer facets (initially), in the centre-of-mass frame the angular acceleration is half that which would be found for the fixed edge case. The system is shown in Fig. 6.8 at $t = 40$ s, showing the outer facets have begun to fold inwards, away from the incident radiation. In Fig. 6.8, grey facets are perfectly reflective while black facets are perfectly absorbing.

By inverting the surface reflectivity, the fold direction can be reversed, as shown in Fig. 6.8. The facets again fold inwards in the exact same time as the previous case but this time in the opposite direction. Note that in the previous simulations, the facets are free to pass through each other, and do not shadow other facets from the incoming radiation. This causes the facet's rotation to slow as they approach an angle of π rad, as the SRP passes through the centre facet and acts to decelerate them. The effects of self reflection and shadowing are considered in later modelling.

A planar model of linked rigid facets has been used to demonstrate that SRP can be used to fold rigid reflective facets in free space, although the time taken to fold the facets may be higher than was suggested by the previous analysis. This is due to the rotation axis of the fold also undergoing transverse acceleration, whereas the previous analysis was for a facet with a fixed edge. Considering the relative motion of the facet edges, it was found that folding times were a minimum of a factor of two times greater than for the fixed edge case. It was also found that controlling the local surface reflectivity of the facets could be used to induce folding of facets, both towards and away from the incident radiation. However, symmetric configurations were used here to avoid rotation of the overall system relative to the radiation direction.

For more complicated geometries, the planar model is not a suitable model of an OrigamiSat, because it only represents a chain of facets each connected to their adjacent facets, whereas a 3D origami fold pattern would have multiple facets mutually connected. In the planar model, each new facet added to the system introduces a new degree of freedom, as that facet is free to rotate. For 3D origami patterns the number of degrees of freedom are reduced, since multiple facets are interconnected and so restrict the overall motion. A system with a greater number of facets has been simulated with results of simulation shown in Fig. 6.9, which shows the system at selected time steps. The outer facets are seen to rotate inwards first, and then the inner facets consecutively fold inwards while the centre facet remains flat, due to the symmetry of the system. This simulation is included to demonstrate that a linked facet system, modelled by the planar model here, behaves like a long flexible chain for large numbers of facets. Although the parabolic shape achieved in Fig. 6.9 could conceivably be used as a reflector or receiver, this would be formed of a long chain of facets and so may have limited utility. This concept is similar to the work of Ref. [100], which shows that SRP can be used to produce a parabola by modulating the reflectivity across a slack membrane, though this strategy required a rigid supporting hoop to achieve the desired shape. It is unclear whether the shape of a facet chain without this type of supporting rigid structure could be effectively controlled solely through the use of SRM, though this was not investigated further here.

6.3 3D Multibody Dynamics Model of Rigid Origami

Having examined the planar dynamics of linked rigid facets, a model is now presented for simulating the spatial dynamics of 3D rigid origami patterns, subjected to SRP. The aim of this section is to use this model to demonstrate that 3D origami patterns can be folded using SRP, when the reduced degrees of freedom of 3D fold patterns and the limited direction of the applied force due to SRP are taken into account. A general expression for the multibody dynamics of rigid origami patterns is presented, and a ray-tracing module for the calculation of SRP force that has been developed for this work is included and verified. The model is then used to demonstrate through simulation that SRM can be used to reconfigure a Miura fold [128] OrigamiSat, and then to demonstrate the active shape control of a pyramidal OrigamiSat design.

6.3.0.1 Model Description

In this section, the procedure for generating the equations of motion of a multibody system consisting of linked, flat, rigid facets is presented. The formulation allows the multibody equations of motion to be generated for different origami designs, which are specified as collection of polygons. The dynamics of the multibody system are described using the well-known "augmented formulation", described by Ref. [185]:

$$\begin{bmatrix} \mathbf{M} & \mathbf{J}^T \\ \mathbf{J} & 0 \end{bmatrix} \begin{bmatrix} \ddot{\boldsymbol{q}} \\ \boldsymbol{\lambda} \end{bmatrix} = \begin{bmatrix} \boldsymbol{Q}_a + \boldsymbol{Q}_v \\ \boldsymbol{Q}_c \end{bmatrix} \tag{6.15}$$

where $\mathbf{M}$ is the system mass matrix, $\boldsymbol{q}$ the state vector of body coordinates and $\mathbf{J} = \partial \boldsymbol{C}/\partial \boldsymbol{q}$ is again the constraint Jacobian, for the vector of system constraint equations $\boldsymbol{C}$. $\boldsymbol{\lambda}$ is a vector of Lagrange multipliers, used to solve for the constraint forces $\boldsymbol{Q}_c$, while $\boldsymbol{Q}_a$ and $\boldsymbol{Q}_v$ are the applied and inertial force vectors respectively.

The OrigamiSat is modelled as a system of flat, rigid facets, constrained by spherical joints at overlapping vertices of the facets. The state vector $\boldsymbol{q}$ contains the Cartesian coordinates of each facet's centre-of-mass, $\boldsymbol{r}_i$, and the three $ZY'X''$ Euler angles, ψ, θ, ϕ describe its orientation relative to the inertial xyz frame. Figure 6.10 shows the reference frames, Euler angles and sequence of rotations for the i^{th} facet. The state vector $\boldsymbol{q}$ is then ordered such that $\boldsymbol{q} = [x_1, y_1, z_1, \psi_1, \theta_1, \phi_1, ..., x_N, y_N, z_N, \psi_N, \theta_N, \phi_N]^T$, where N is the total number of facets. The mass matrix $\mathbf{M}$ is composed diagonally by $[m_1\mathbf{I}_{3\times3}, \mathcal{I}_1, ..., m_N\mathbf{I}_{3\times3}, \mathcal{I}_N]$ where $\mathbf{I}_{3\times3}$ is the three by three identity matrix, and m_i and $\mathcal{I}_i$ are the mass and inertia tensor (in the body frame) of the ith facet respectively.

The origami fold pattern is defined as a set of N polygons, which are themselves a set of n_i vertex coordinates, such that the vector of all vertex positions is $\boldsymbol{V} = [\boldsymbol{v}_{11}, ..., \boldsymbol{v}_{1n_1}, ..., \boldsymbol{v}_{N1}, ..., \boldsymbol{v}_{Nn_N}]^T$. An example fold pattern is shown in Fig. 6.11 for a nine (a) and four (b) facet structure, showing the fold lines, numbered polygons and vertices, and a graph illustrating the vertex connectivity.

The constraint equations are found by first generating an adjacency matrix $\mathbf{A}$, which is a square $N_v \times N_v$ matrix, where N_v is the total number of vertices, given by $N_v = \sum_{i=1}^{N} n_i$. The adjacency matrix elements are equal to one if the vertices overlap, and zero otherwise, i.e. $\mathbf{A}_{ij} = 1$ if $\boldsymbol{V}_i = \boldsymbol{V}_j, 0$ otherwise. The constraint equations are given by:

$$\mathbf{A}_C \boldsymbol{V} = \boldsymbol{C} = 0 \tag{6.16}$$

where $\mathbf{A}_C$ is the constraint adjacency matrix, defined by:

$$\mathbf{A}_{C,ij} = \begin{cases} \sum_{j'=j}^{N_V} \mathbf{A}_{ij'} & \text{if } \mathbf{A}_{ij'} = 0 \; \forall \; j' < j \text{ and } \mathbf{A}_{ij} = 1 \\ -1 & \text{if } \mathbf{A}_{ij'} \neq 0 \; \forall \; j' < j \text{ and } \mathbf{A}_{ij} = 1 \\ 0 & \text{otherwise} \end{cases} \tag{6.17}$$

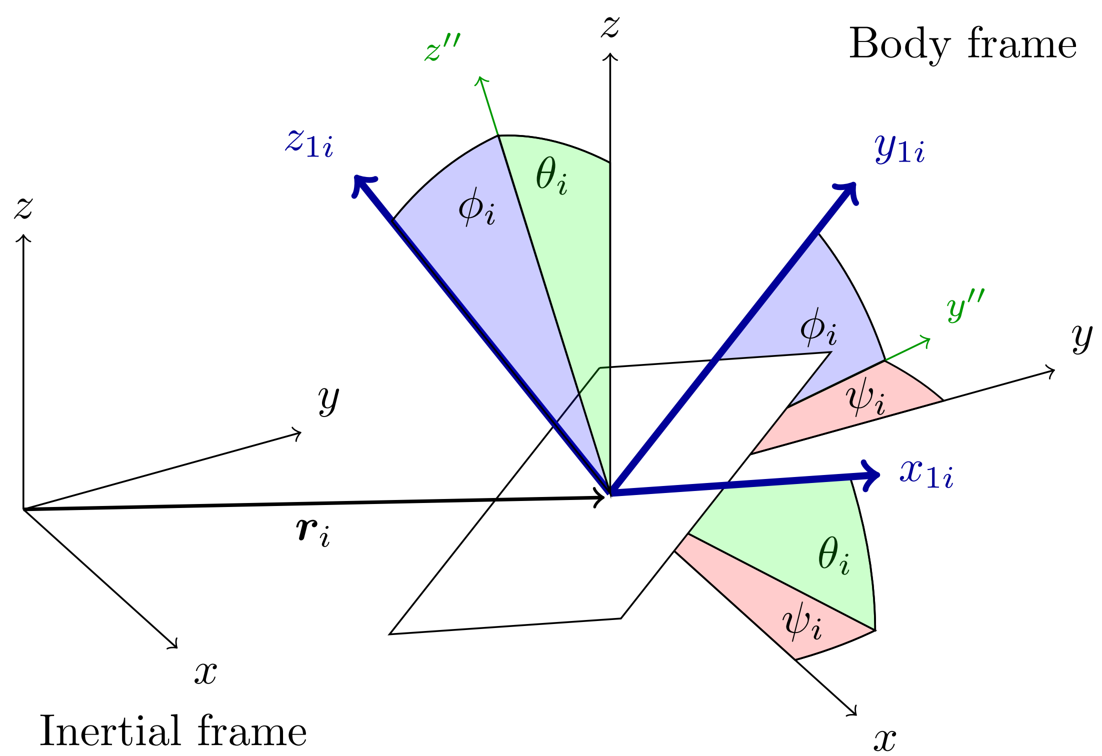

Figure 6.10: Sequence of rotations between the inertial frame xyz and the ith facet body frame $x_{1i}y_{1i}z_{1i}$.

with all zero rows removed, resulting in an $N_v \times N_c$ matrix, where N_c is the number of constraints. For example, if vertices i, j and k are coincident, Eq. 6.16 leads to the constraint equation $2\boldsymbol{v}_i - \boldsymbol{v}_j - \boldsymbol{v}_k = 0$ appearing in the constraint vector $\boldsymbol{C}$. This procedure allows the multibody dynamics to be formulated for arbitrary fold patterns, where the pattern is defined as a collection of polygons. For an initial state vector $\boldsymbol{q}$ and applied force vector $\boldsymbol{Q}_a$, the differential algebraic system of equations in Eq. 6.15 is solved for the Lagrange multipliers $\boldsymbol{\lambda}$, and the accelerations $\ddot{\boldsymbol{q}}$, which are then numerically integrated to simulate the system dynamics. Although the notation of this section is somewhat cumbersome this approach has proved convenient for implementing within a mathematical programming environment, as the functions required to generate the required expressions are included in standard libraries and the origami design can be simply input as a list of points. A flow chart of the software implementation of the model is given in Fig. 6.12, showing the separation between model generation (Mathematica) and the numerical integration and panel force calculations (MATLAB). The controller included in Figure 6.12 will be presented in Sec. 6.4.

6.3.0.2 Ray-Tracing for SRP Calculation

To take into account the effects of self-shadowing and reflection of light between facets, ray-tracing is used to calculate the path of the incident and reflected radiation, and to then evaluate the resultant force due to SRP on each facet. Ray-tracing is commonly used in computer graphics for accurate rendering of 3D models [186]. In spaceflight engineering, ray-tracing is used for precise orbit determination when the SRP force needs to be known within a tolerance such that the variation in the optical properties of the spacecraft's surface lead to unacceptable errors when estimating the orbital position [187]. For an origami spacecraft, it is possible that in a certain configuration the entire incident radiation on a perfectly reflective facet could be reflected onto another facet, effectively doubling the force due to SRP on that second facet and greatly affecting the system dynamics. Ray-tracing gives a computationally efficient method of calculating these inter-facet reflections and shadowing. A description of the module is given in this section.

The ray-tracing procedure begins by defining an $N_R \times N_R$ grid of points, evenly distributed within a square region that has a surface normal aligned with the incident radiation direction, and directed at the centre-of-mass of the multibody system. The square region has a spatial dimension D_R large enough to completely contain the projected area of the OrigamiSat within

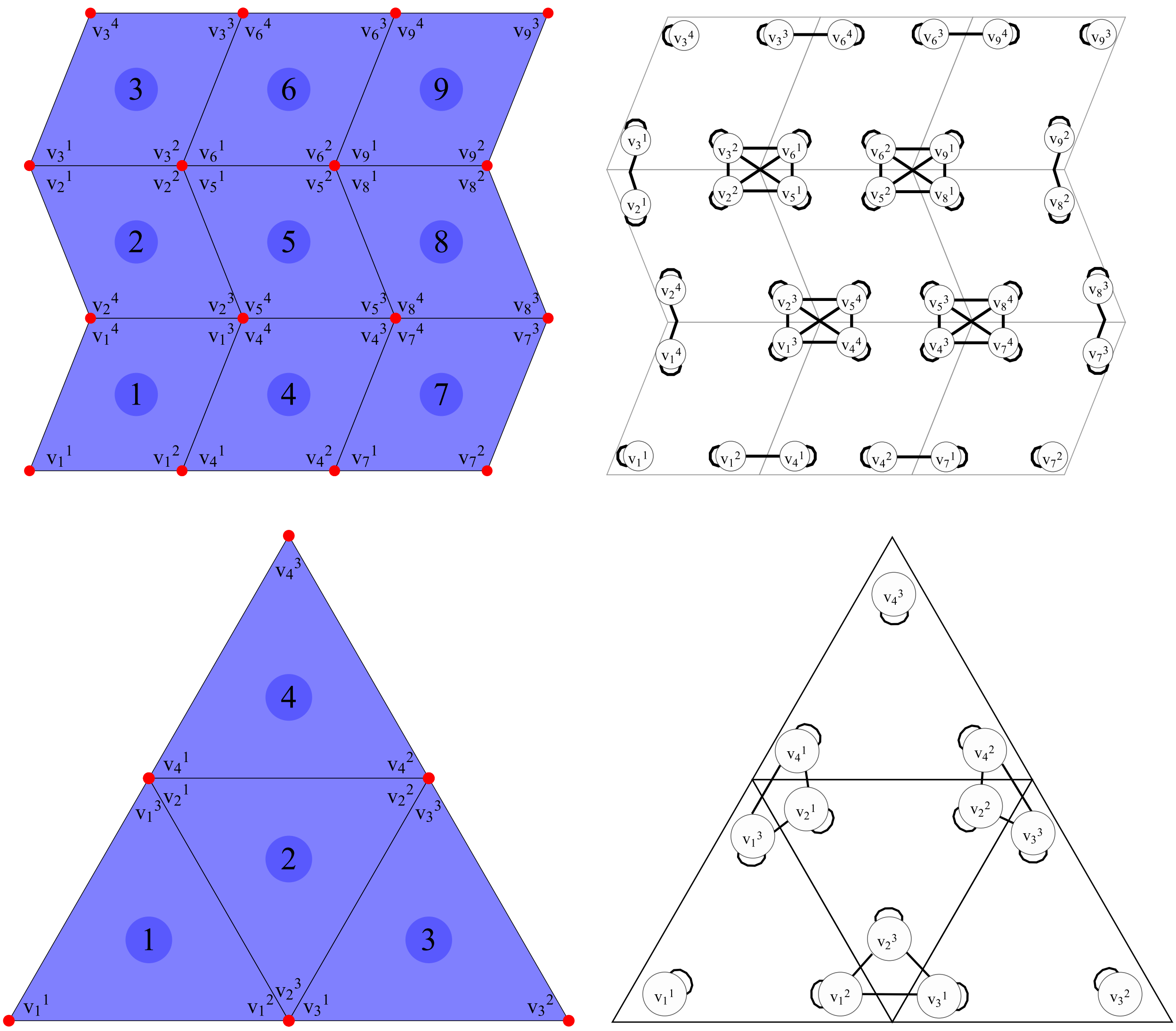

Figure 6.11: Polygon and vertex numbering scheme, and a graph showing the vertex connectivity for a Miura fold pattern (a) and a pyramidal sail pattern (b)

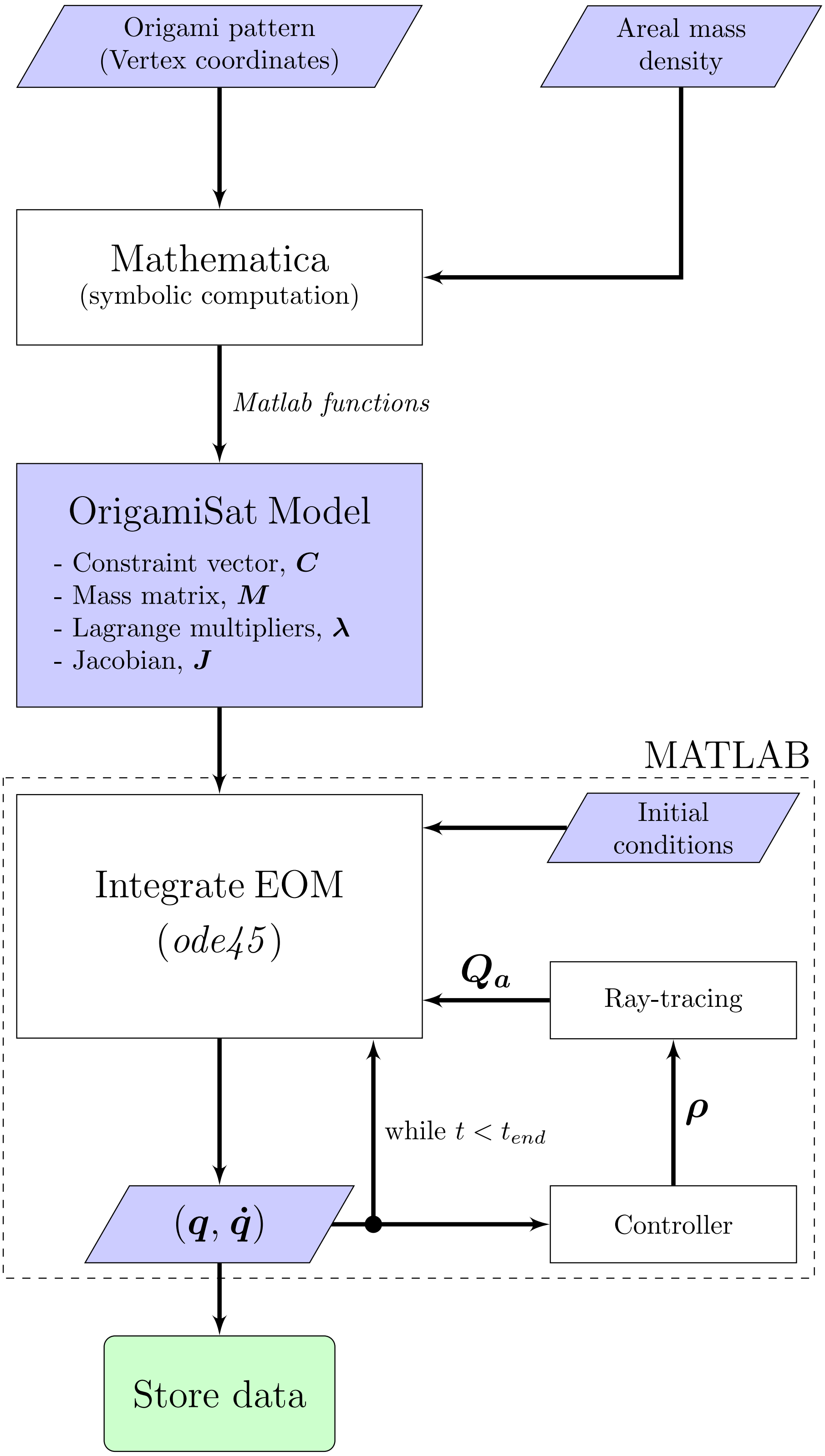

Figure 6.12: Flow chart of the software implementation of the OrigamiSat multibody dynamics equation generation and numerical simulation.

the $D_R \times D_R$ square. Rays are then cast from these points and the resultant force is found by determining whether each ray intercepts a sail facet. These collision calculations are performed using a MATLAB wrapper [188] for the OPCODE collision detection library [189], which makes use of bounding volume hierarchies. If a ray intercepts a sail facet, the ray is then specularly reflected from the facet's surface, and the collision detection repeated to determine whether the ray intercepts a further facet. This process is repeated until no further reflections are found. Throughout the ray-tracing calculation, the location of rays which intercept each facet are stored, and the resultant force and torque on each facet is found by summation of the contribution of every intercepted ray, according to Eq. 6.18, which gives the total force on facet i due to SRP:

$$\boldsymbol{F}_i^{SRP} = P \sum_j \text{sign}(\boldsymbol{u}_j \cdot \boldsymbol{n}) \left(\frac{D_R}{N_R}\right)^2 \left[\prod_c \rho_c^j\right] \left((1+\rho_i)\cos\alpha\boldsymbol{n} + (1-\rho_i)\sin\alpha\boldsymbol{t}\right) \tag{6.18}$$

Equation 6.18 is derived by evaluating Eq. 6.1 for every incident ray on facet i. The facet area A in Eq. 6.1 is replaced with $D_R^2/N_R^2 \prod_c \rho_c^p/\cos\alpha$, where α is the angle between the incident ray and the facet normal, which ensures that the total intensity of light from all rays sums to the total flux through a $D_R \times D_R$ square. The term $\prod_c \rho_c^j$ is the product of the reflectivity of all facets previously intercepted by ray j, which takes into account the reduced intensity of a reflected ray due to imperfect surface reflectivity. The torque is also found by summation over each ray's contribution, and this may be nonzero now as the centre-of-pressure may not coincide with the centre-of-mass for a partially illuminated facet. The torque is given by:

$$\boldsymbol{\tau}_i^{SRP} = \sum_j \boldsymbol{r}_{ij} \times \boldsymbol{f}_j^{SRP} \tag{6.19}$$

where $\boldsymbol{r}_{ij}$ is the position vector of the incidence point of ray j from the centre-of-mass of facet i, and $\boldsymbol{f}_j^{SRP}$ is the expression within the summation of Eq. 6.18. The ray-tracing procedure is illustrated in Fig. 6.13, showing the ray paths for a three facet system. The light blue facets are perfectly reflecting, while the dark blue facet is perfectly absorbing. Figure 6.13 shows the incident rays being reflected from the outer facets then absorbed by the centre facet, thus increasing the force on the centre facet in this configuration.

The ray-tracing module was verified by comparing the force applied to a simple structure consisting of three square facets, as illustrated in Fig. 6.13. Simulations were performed with the facets facing the incident radiation, and facet reflectivities given by [1,0,1], i.e. a 3D implementation of the planar model shown in Fig. 6.8. The simulation was performed until the two outer facets folded to the vertical position, and the total impulse experienced by all facets throughout the simulation was calculated by summation of the contribution of each incident ray on each timestep. During the simulation, the difference between the force calculated using the ray-tracing module, and the exact value given by evaluation of Eq. 6.1 is calculated on each time step. The summation of this force difference over the entire simulation then gives the ray-tracing error impulse, ϵ_R. This is divided by the total impulse for a simulation in which the exact SRP force of Eq. 6.1 is used, ϵ_A, to give a relative value for the overall force error when using ray-tracing. This process was repeated with different resolutions used in the ray-tracer, with results shown in Fig. 6.14. The results show that the difference between the ray-tracing and exact SRP impulse is less than 0.1% of the total exact impulse when more than 10^4 rays are used in the simulation. Figure 6.14 also shows the computation time for a single timestep of the simulation against the number of rays used, which increases linearly from a value of 0.01 s for a number of rays greater than 10^4. Overall, ray-tracing using the opcode library for collision detection is found to be an accurate and computationally fast method for calculating the SRP force on origami spacecraft.

6.3.1 Simulations of Self-Reconfiguring OrigamiSats

The multibody dynamics formulation presented in the previous section is now used to demonstrate through simulation that SRP and local SRM can be used to control the shape reconfiguration of rigid origami structures. In addition to demonstrating the basic principle of SRP triggered shape reconfiguration, these simulations are used to illustrate the limitations of the strategy and to highlight some considerations for the future development of control algorithms for the active shape control of OrigamiSats.

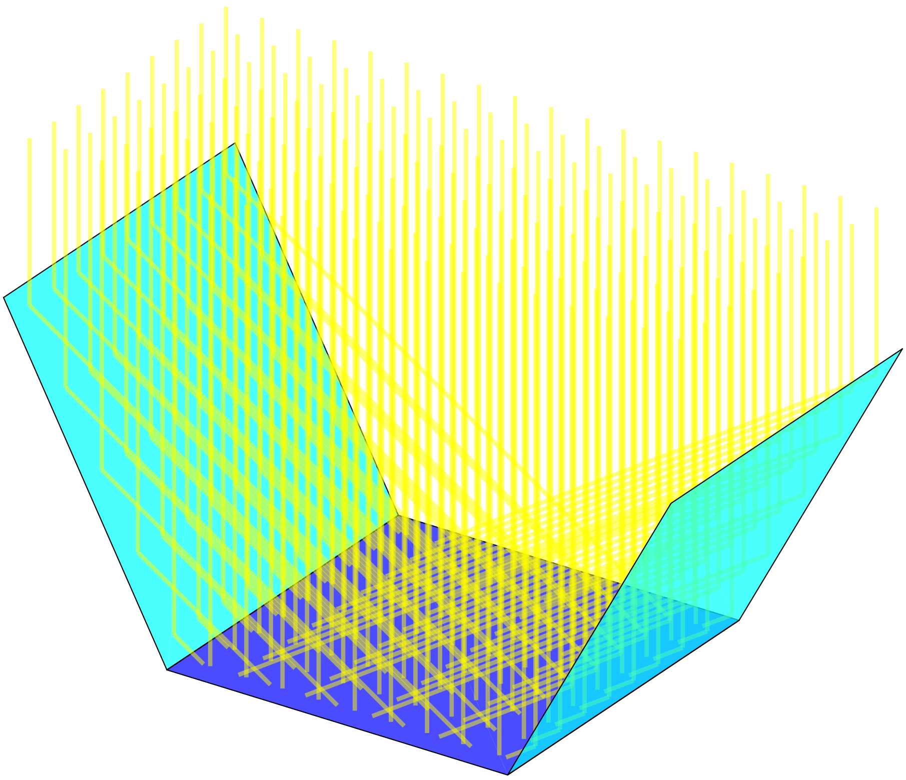

Figure 6.13: Illustration of ray-tracing for an example three-facet OrigamiSat

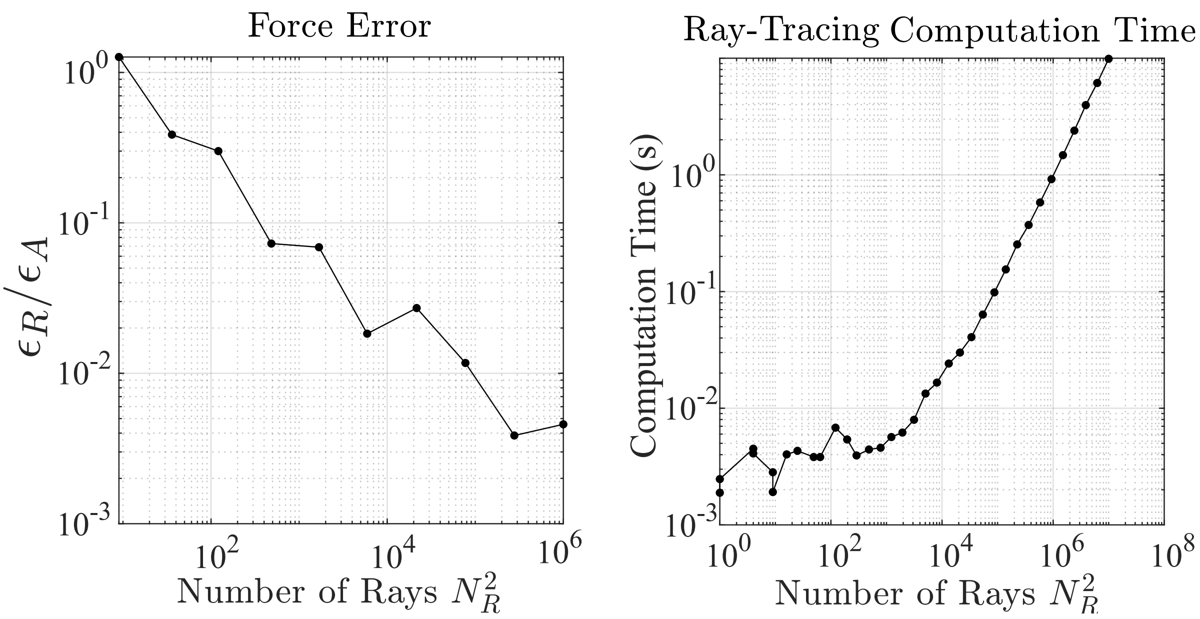

Figure 6.14: Force error and computation time of the ray-tracing module against the number of rays.

6.3.1.1 Miura Fold Pattern

The first simulation is of a Miura fold pattern, consisting of a 4×4 grid of rhombic unit cells. The Miura fold is well known to have only one degree of freedom in folding, making it particularly useful for deploying planar structures as the unfolding requires minimal actuation. The OrigamiSat is 1×1 m, with an areal mass density of 10 g/m^2, again considering the areal mass density of near-term solar sails. Reference to Fig. 6.3 suggests that at this length scale, the time to complete a fold should be on the order of minutes. Additionally, Fig. 6.3 shows that at this length scale the effect of bending resistance for a thin film hinge is insignificant and as such is not considered in the following simulations. The simulation timestep was chosen to be 0.1 s, and the system given in Eq. 6.15 solved numerically in MATLAB using the *ode*45 solver, where the applied forces $\boldsymbol{Q}_a$ are calculated using the ray-tracing module and the evaluation of Eq. 6.18 and 6.19. For simplicity, the structure is assumed to be at rest in free space with no other external forces acting upon it. The structure is initially flat and lying in the xy plane, and incident radiation is directed in the $-z$ direction. To ensure the structure folds correctly, the correct pattern of valley/mountain folds for the Miura pattern must be initiated. This is achieved by applying a torque of $\pm 1 \times 10^{-8}$ N m to alternating facets, integrating the equations of motion for one timestep, and then setting the facet velocities and forces to zero before beginning the simulation. This results in a slight angular displacement of the facets which achieves the desired mountain/valley folds and allows the main simulation to proceed. Note that in reality, the correct pattern of mountain and valley folds would be preserved by either the plastic deformation of the creases in the hinge material, or by a physical mechanism. This "fold initiation" is only a concern for the simulation here because the exactly-flat condition can lead to numerical instability. First, the outer columns of facets are set to be perfectly reflective with

$\rho = 1$, while the middle two columns are perfectly absorbing with $\rho = 0$. Reflective/absorbing facets are illustrated in all figures as light/dark blue respectively.

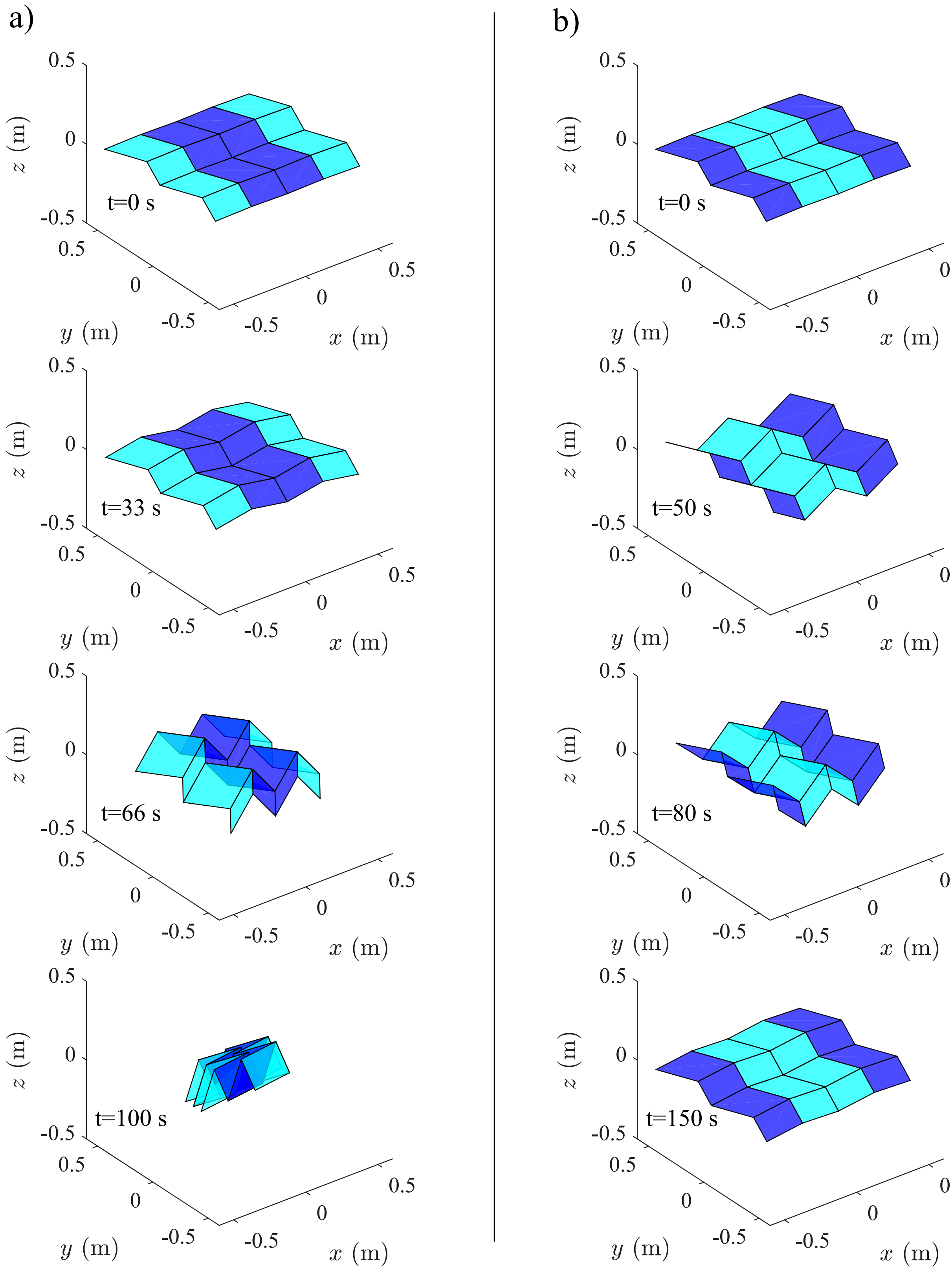

Figure 6.15: a) Reconfiguration of a Miura fold pattern using SRP. Light blue facets are perfectly reflective and dark blue are perfectly absorbing. b) Reversing the folding direction by reversing the reflectivity pattern. After 80 s, inter-facet reflections cause the sail to reopen.

The simulation was run for a duration of 100 s and results are shown in Fig. 6.15a, which shows the OrigamiSat drawn in the centre-of-mass frame at selected timesteps. The OrigamiSat is seen to completely fold inwards in this time, due to the relatively larger force acting on the outer, reflecting facets. This force acts in the correct direction to effectively fold the single-degree-of-freedom Miura fold pattern. As in the planar simulations, it was thought that by reversing the reflectivity pattern that the folding action could also be reversed. The simulation was repeated, this time with the inner facets perfectly reflective, with results shown in Fig. 6.15b. The folding direction is indeed found to have reversed here. However, after t=80 s, the folding ceases and the sail instead begins to open and return to the flat configuration. This is due to the inter-facet reflections, as incident radiation is reflected from the central facets and is then absorbed by the outer facets. This increases the force acting on the outer facets enough to reopen the sail. It was found that the sail could still be folded completely if the reflectivity of the central facets is set to zero after a time of approximately 30 s, as the remaining momentum of the facets is enough to complete the fold and there are then no inter-facet reflections to prevent the motion.

6.3.1.2 PD Shape Control of a Pyramidal OrigamiSat

If the reflectivity of each facet can be individually controlled using RCDs, it would be possible to actively control the shape reconfiguration of an OrigamiSat. This is demonstrated here through simulation of a pyramidal sail design, in which the facet reflectivities can be individually controlled continuously in the interval $\rho = [0, 1]$, again assuming some ideal form of RCD. In attempting to perform this simulation, it was found that the OrigamiSat's overall attitude was unstable and it would begin to rotate relative to the incident radiation direction. For simplicity, this instability was removed by constraining the x, y coordinates of the centre facet's vertices, such that this facet always faced the incoming radiation. This constraint was imposed here to simplify the dynamics for this demonstration of shape control, but in practice control algorithms will be required which combine shape and attitude control requirements.

A triangular design is selected, consisting of four triangular facets. The facet and vertex numbering and connectivity, used to generate the equations of motion, are shown in Fig. 6.11. The areal mass density is again selected as 10 g/m^2, and the sidelength of each triangular facet is set to 1 m, again assuming that this scale will give folding times on the order of minutes and that the hinge bending resistance can be ignored. Shape control is achieved through the use of a proportional derivative (PD) controller, where the variables being controlled are the hinge angles of the outer facets, contained in the vector $\mathbf{\Phi} = [\phi_1, \phi_3, \phi_4]$. The hinge angles are defined as $\phi = 0$ for a facet lying in the xy plane, and positive when the facet folds downwards in the $-z$ direction. A PD control law is implemented to determine the required reflectivity values of the outer facets (labelled 1,3 and 4), given by:

$$\boldsymbol{\rho}_{1,3,4} = -k_p \mathbf{\Phi}_e - k_d \mathbf{\Phi}'_e \tag{6.20}$$

where the values are constrained to the range [0,1]. k_p and k_d are the proportional and derivative control gains respectively, and $\mathbf{\Phi}_e = \mathbf{\Phi} - \mathbf{\Phi}_{ref}$ is the vector of angle errors, given by the difference between the current facet angles and the target angles. The derivative term $\mathbf{\Phi}'_e$ is estimated using a backwards difference formula, using the values at the previous timestep of the simulation. The reflectivity of the centre facet, $\boldsymbol{\rho}_2$ is found by summation of the outer facet reflectivities and subtraction from one, $\boldsymbol{\rho}_2 = 1 - \sum_{i=1,3,4} \boldsymbol{\rho}_i$. This gives the required difference in reflectivity for the facets to fold in either direction, as illustrated in Fig. 6.8 for the planar case.

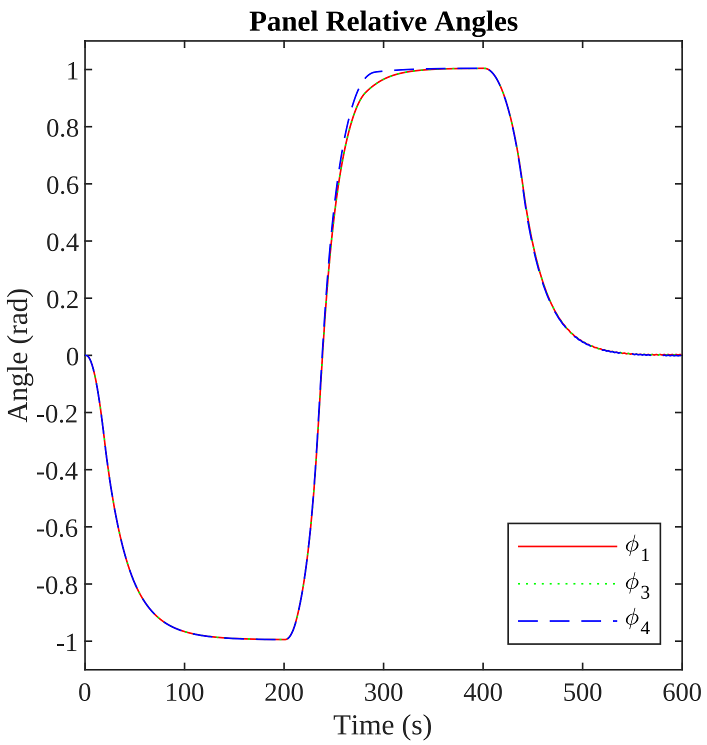

Figure 6.16: Relative angle of outer facets during PD control simulation moving between the three target configurations.

The simulation is run for a duration of 600 s, with the target angles set to -1 rad for the first 200 s, 1 rad for the next 200 s, and 0 for the final 200 s. The controller was tuned manually , resulting in control gains of $k_p = 50$ and $k_d = 1200$. The control gains were selected by trial and error, by first finding a proportional gain that gave a reasonable rise time, and then finding a derivative gain that eliminated any overshoot. Results of the simulation are shown in Fig. 6.16, showing a plot of the angles of the outer facets, and in Fig. 6.17, which shows the system plotted at 5 s intervals for the first 300 s of the simulation, showing the transition between the first two target configurations. Figure 6.17 shows the sail configuration plotted sequentially for the duration of the simulation, in order from left to right and top to bottom. The controller successfully reconfigures the OrigamiSat between the two target shapes, before returning to the flat position. As seen in Fig. 6.16, there is a slight discrepancy between the angle of facet 4 and the other outer facets, which is thought to be due to a rounding error in the numerical

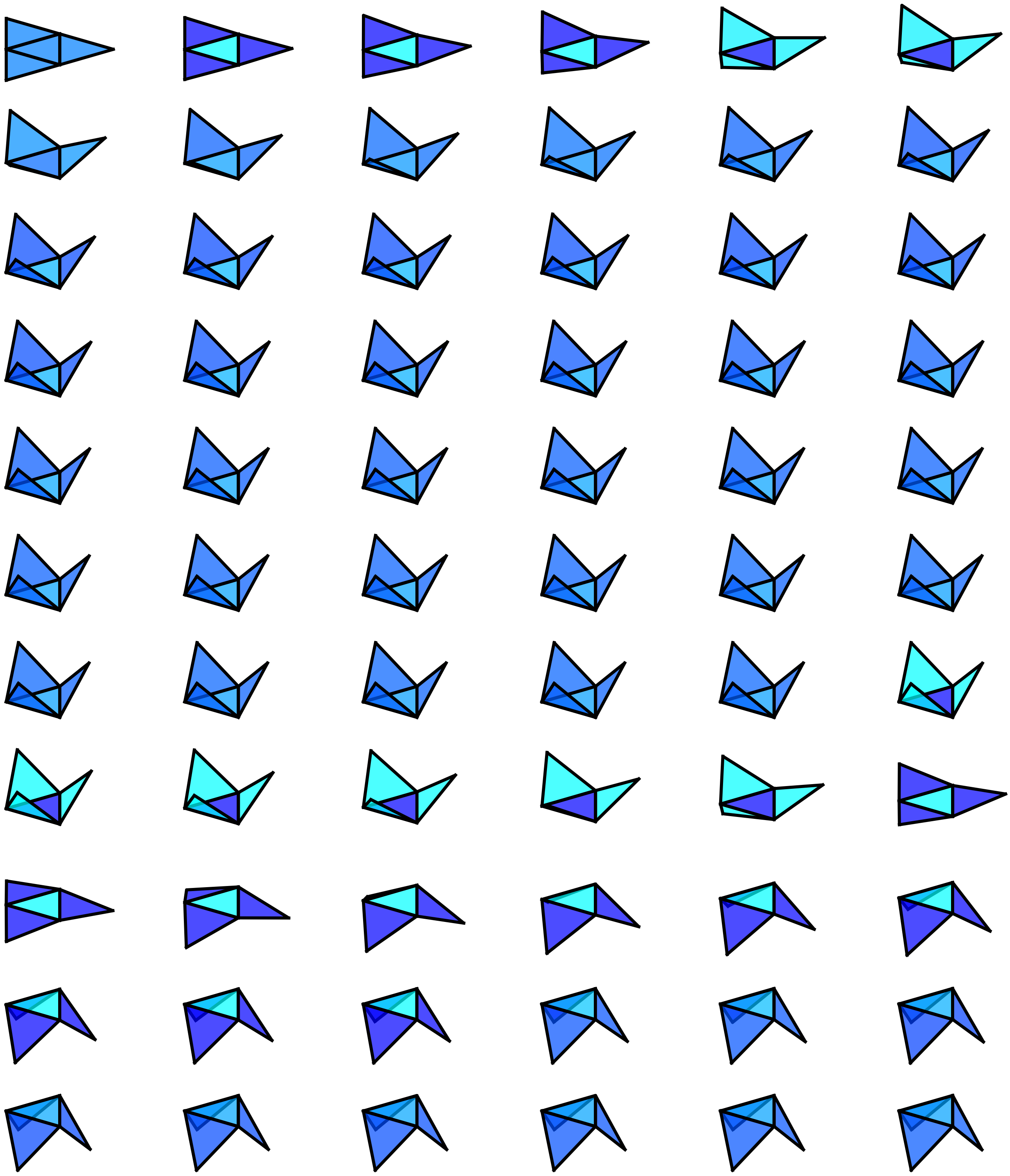

Figure 6.17: Pyramid OrigamiSat plotted at 5 s intervals for the first 300 s of PD control simulation, plotted sequentially from left to right along the rows, showing the transition between the first two target configurations. The reflectivity of each facet represented by shade of blue interpolated for values between 0 and 1.

simulation. As the shape is triangular, the vertex coordinates cannot all be integers. This slight difference in the facet coordinates is then carried through the simulation and the effect amplified by the feedback controller, since each facet is controlled individually.

Overall, the simulation has demonstrated that PD control of shape reconfiguration through the use of local SRM is possible, but some limitations have been encountered. Firstly, it is again noted that the orientation of the central facet was constrained to remain facing the direction of the incident SRP. This constraint was imposed because it was found that otherwise the spacecraft began to tumble. This highlights the need for either an integrated attitude/shape control algorithm, or for a separate attitude control system to maintain attitude stability while shape reconfiguration is performed. A further note is that some knowledge of the shape reconfiguration was assumed a priori when implementing the PD control equation. Specifically, it was assumed that reflectivity patterns of $\boldsymbol{\rho} = [1, 0, 1, 1]$ and $\boldsymbol{\rho} = [0, 1, 0, 0]$ would result in folding in the positive and negative directions respectively. While this was an obvious assumption for this sail design, for more complex origami structures with coupled degrees-of-freedom in folding, the relationship between facet reflectivity patterns and folding behaviour may be difficult to predict. For more complicated origami designs, this relationship could potentially be deduced through simulation by creating a lookup table of possible reflectivity patterns and observing the resulting dynamics, or it may be possible to find analytic expressions for the resulting motion of specific reflectivity patterns. A further level of complexity is introduced here by the fact that the system will have different folding behaviour for a given reflectivity pattern depending on the direction of incoming radiation, i.e. the coupling of the attitude/reconfiguration dynamics further complicates the development of potential control strategies. For this reason it is assumed that an additional attitude control system may be desired for spacecraft of this type, which is capable of maintaining a fixed orientation relative to the Sun vector while the reflective facets are used to enact shape reconfiguration.

A further challenge encountered is that the extent of the shape reconfiguration that can be achieved with this strategy is limited. There is an obvious limit in that, if the outer facets fold over past the vertical position, they then occlude the centre facet and SRP can not be used to return to a flat position. In practice, it was found through simulation that the achievable angle was less than $\pi/2$ rad, with the controller struggling to not overshoot and lose control effectiveness for target angles greater than approximately 1 rad, hence the target value selected for the simulations here. This limit means that for some OrigamiSats, reversible shape reconfiguration would require further actuation in addition to the RCDs. For example, SMPs or SMAs could be used in the hinges of such a spaceraft to actuate the deployment, while SRM could then be used for shape reconfiguration within the achievable angles during normal operation. Of note however is that this limitation depends on the origami folding pattern, as for the Miura pattern of the previous simulation reversible folding was achieved through the use of SRP alone. The need for additional hinge actuation will depend upon the folding degrees-of-freedom of the origami design, and also on whether inter-facet shadowing or reflections break the symmetry of the folding process, as was observed for the Miura fold.

6.4 Integrated Shape and Attitude Control for OrigamiSats

In this section a control logic is proposed for integrating the attitude and shape control of an OrigamiSat through the use of variable reflectivity facets. In principle the reflectivity of the OrigamiSat facets could be controlled through the use of RCDs, a proven technology for solar sails with their use for attitude control demonstrated on the IKAROS mission [5], as noted previously. In the previous section, shape control through variable reflectivity was demonstrated for a pyramidal OrigamiSat, with a PD control law implemented. As noted however, the attitude dynamics were decoupled from the shape control strategy in this simulation by constraining the central panel of the sail to always remain sun-pointing. Now, a control law is sought which integrates attitude control with shape reconfiguration for an unconstrained OrigamiSat in free space. A Miura-fold pattern is again selected as a test case for the control design. This origami pattern represents a simplified case (in terms of the Origami kinematics), as the system has only one degree of freedom in folding (in addition to the three degrees of freedom in rotation). The Miura-fold is also a well known design, and has tesselation properties so the system could potentially be scaled to a greater number of panels. The shape and attitude of the Miura-fold OrigamiSat are still coupled however, and so even as a simplified case the system is still challenging from a control perspective. Furthermore, since there is only one folding degree-of-freedom, it was thought it would be easier to gain a qualitative understanding of the nature of the attitude/shape coupling of the system. This can provide some deeper insight into the controller performance which could in the future be applied to more complex OrigamiSat designs.

In the thesis introduction (Sec. 1.3.3), it was noted that the control of multibody systems/spacecraft is well studied, with some examples given of different approaches taken for a variety of spacecraft architectures. A key difference between these previously studied systems and the control strategy proposed in this chapter is that the RCD-controlled OrigamiSat system is underactuated and non-conservative, as SRP introduces angular momentum to the system. Therefore some previously proposed strategies for multibody spacecraft control are not suitable for this problem. Due to the complexity of the system dynamics and underactuation, it is unlikely that a straightforward solution for the general OrigamiSat SRP control problem (i.e. a strategy which may be applied to any Origami folding pattern) is achievable, though it is possible that some general results and guidance for controller design can be gained by studying specific scenarios. Therefore, the aim of this section is to present an investigation into OrigamiSat SRP controllability through the use of numerical simulations of a Miura-fold OrigamiSat.

As noted, the system dynamics are coupled and the system is underactuated, as changing the panel reflectivity has a limited effect on the change in direction or magnitude of the force due to SRP. Nevertheless, it was found in Sec. 6.3.1 that the multibody dynamics of the system can be exploited to enact folding of the OrigamiSat, and that often the reflectivity pattern required to perform the desired "folds" could be intuited by considering opposing reflectivities for panels on either side of the required fold line. In the case of the Miura fold pattern for example, it was found that folding/unfolding of the pattern could be enacted by two opposite reflectivity patterns. While it is likely not always possible to simply guess the required reflectivity patterns, or even likely that their always exists a reflectivity pattern to perform the desired fold, for the relatively simple Miura pattern this approach is again adopted to simplify the integration of shape and attitude control. A further complication and added nonlinearity to the dynamics is the effects of interpanel shadowing or reflection, where the panel forces can change discontinuously as the OrigamiSat changes shape and different panels become illuminated. As this effect depends on both the (time-varying) OrigamiSat geometry and attitude, it is non-trivial to determine when or if interpanel reflections become a dominant contribution to the panel forces, and indeed these effects require the use of ray-tracing to accurately calculate the force due to SRP on the spacecraft. Again however, for simple fold patterns it is likely possible to intuitively deduce or predetermine which configurations result in interpanel reflections and build this knowledge into the control design on a case-by-case basis. For the Miura fold for example, it was found in Sec. 6.3.1 that the configuration shown in Fig. 6.18 resulted in interpanel reflections which reversed the folding effect of the shown reflectivity pattern (light blue implies $\rho = 1$, dark blue $\rho = 0$), causing the sail to reopen due to the increase force on the outer panels. As noted previously, RCDs are a proven technology for attitude control of solar sails. By varying the reflectivity of these devices mounted on a sailcraft, the force due to SRP is modified on the device and thus useful torques can be produced for attitude control purposes. In the case of OrigamiSats, it is assumed that the reflectivity of each panel can be controlled individually, and varied between perfectly absorbing ($\rho = 0$) and perfectly reflecting ($\rho = 1$), which represents an ideal scenario. In practice, many RCD devices have two discrete states, which are switched when a voltage is applied to the material. In practice some variation between these two reflectivities could be achieved by having a large number of (discrete) RCD devices on each panel, and switching a specified portion of them at a time. Previously, attitude control through the use of an array of variable reflectivity panels has been demonstrated through simulation by Borggräfe et. al [101], though in this case the authors assumed discrete reflectivity states (0 or 1 for each cell), and determined the required reflectivity pattern by considering all possible reflectivity patterns and creating a lookup table of the generated torques, then comparing these with the desired reference torque output by the controller. While this strategy could also be employed for OrigamiSats, a limitation is that the number of possible patterns increases exponentially with the number of panels, and furthermore imposing discrete states on the panels would complicate the shape/attitude control integration by not allowing the separate control signals to be superimposed, as described in the following section.

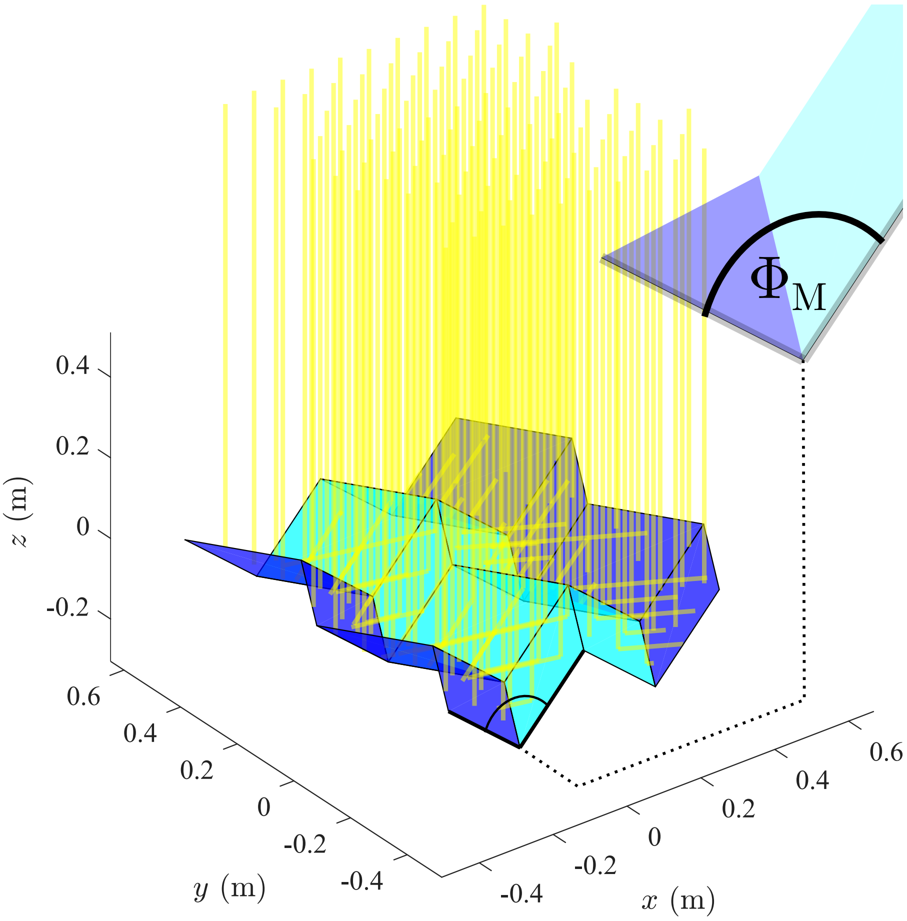

Figure 6.18: Interpanel reflections reverse the folding effect of some reflectivity patterns for a Miura OrigamiSat. Reference "Fold angle", Φ_M, highlighted.

6.4.1 Controller design

In this section, a closed-loop feedback controller for the shape and attitude of a Miura type OrigamiSat is presented and analysed through numerical simulation. Shape reconfiguration is controlled through a classical PID control law, with the output signal used to produce a reflectivity pattern of panel reflectivity values for the OrigamiSat. Simultaneously, a quaternion error feedback controller is used to generate a reference desired torque for attitude control, and a further reflectivity pattern generated, calculated to produce a torque as near to the reference as possible with the RCD panels. These two (shape and attitude) reflectivity patterns are then superimposed, scaled, and applied to the OrigamiSat. While the control scheme is relatively straightforward (in terms of the individual classical control laws used), some further modifications are made to improve control performance and build in some knowledge of the system dynamics and nonlinearities associated with the multibody dynamics and interpanel reflections.

A block diagram of the controller is shown in Fig. 6.19, showing the separate attitude/shape control loops and their integration. For attitude control, first a quaternion representation is found from the OrigamiSat panel coordinates by fitting a rotation between the initial panel centre of masses and the current positions (using singular value decomposition, as in Sec. 3.1.2 for the spring-mass model). This quaternion is then input to the quaternion error feedback controller, along with the desired reference orientation and current body rates, found through backwards difference interpolation of the current rotation and and that of the previous timestep. This produces a reference torque given by:

$$\boldsymbol{T}_{ref} = -P_q \boldsymbol{q}_u^{err} - P_\omega \boldsymbol{\omega} = \begin{pmatrix} T_x \\ T_y \\ T_z \end{pmatrix} \tag{6.21}$$

This is then used to produce a reflectivity pattern by superimposing three reflectivity patterns which are known to produce a torque in each of the body frame axes. The method here is similar to that proposed by Borgräffe et. al [101] for an RCD array, though as noted the panel reflectivities are considered in this section to be continuously variable between 0 and 1, and thus the desired torque can be composed of a combination of the three basis patterns shown in Fig. 6.19. A further key difference is that the planar spacecraft considered by Borgräffe et. al was only capabe of producing torques around the body x, y axes, but the Miura pattern OrigamiSat is capable of producing a torque in the z direction, as long as the sail is not perfectly flat. The "attitude reflectivity vector", where each element gives the desired reflectivity of the corresponding OrigamiSat panel, is given by:

$$\boldsymbol{\rho}_a = T_x \boldsymbol{\rho}_x + T_y \boldsymbol{\rho}_y + T_z \boldsymbol{\rho}_z \tag{6.22}$$

where $\boldsymbol{\rho}_x$, $\boldsymbol{\rho}_y$, $\boldsymbol{\rho}_z$ are the vectors corresponding to the patterns illustrated in Fig. 6.19 for the three torque axes if the corresponding torque component is positive, and the opposite patterns if it is negative. Shape control is provided by a PID controller. First the fold angle Φ_M is calculated from the OrigamiSat panel coordinates (the fold angle is highlighted in Fig. 6.18) and then fed into the PID controller, along with the desired fold angle, interpolated fold angle rate (again estimated with a backwards difference formula), and previous measurements to calculate the error integral. The controller output u_S, which physically represents the desired generalised folding force associated with the folding angle $\Phi_m$is given by:

$$u_S = k_p \Phi_E + k_i \int_0^\tau \Phi_E(\tau) d\tau + k_d \dot{\Phi}_E \tag{6.23}$$

where Φ_E is the error between Φ_M and the desired fold angle, and k_p, k_i, k_d the PID control gains. This is then converted to a reflectivity pattern, where again known patterns are used which correspond to folding and unfolding of the OrigamiSat (as demonstrated for the Miura sail in Sec. 6.3.1). The shape control pattern is thus:

$$\boldsymbol{\rho}_s = u_S \boldsymbol{\rho}_f \tag{6.24}$$

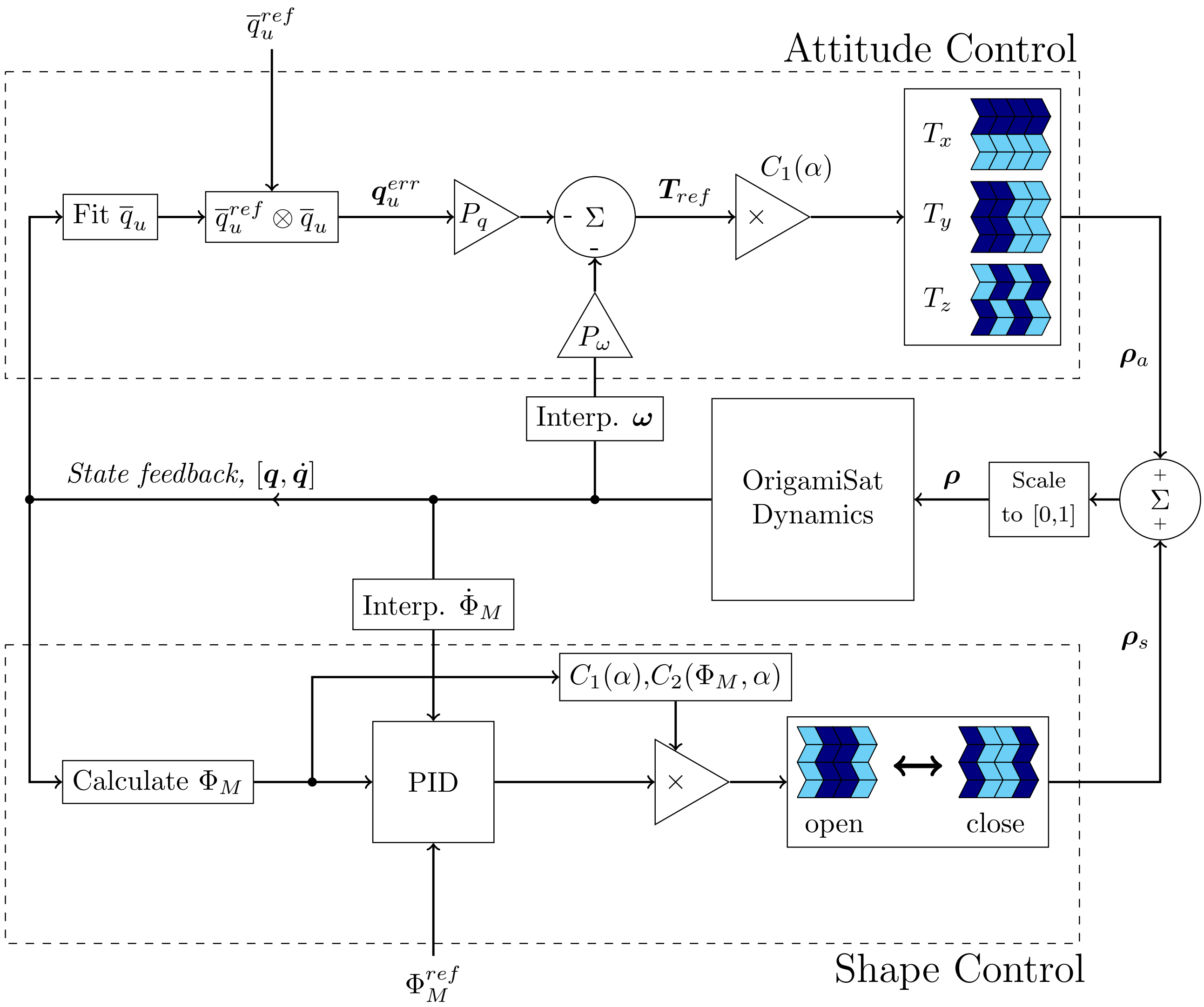

Figure 6.19: Block diagram of the closed-loop feedback controller

where $\boldsymbol{\rho}_f$ is the "open" pattern depicted in Fig. 6.19 for u_S positive, and "closed" for negative. This results in two separate control outputs, $\boldsymbol{\rho}_a$ and $\boldsymbol{\rho}_s$, which are vectors of positive values corresponding to the panel reflectivities (though at this point the raw values may exceed 1).

6.4.1.1 Gain-Scheduling

The control outputs u_s and $\boldsymbol{T}^{ref}$, from Eqs. 6.21 and 6.23 respectively, are further modified by some gain scheduling functions. Gain scheduling modifies the control gains in different operation regions, as determined by some preset values based on measured scheduling parameters, and is therefore a simple method of dealing with the nonlinear dynamics of the system if there are certain known or determined features. The required scheduling functions were deduced by performing simulations of different manoeuvres and addressing obvious points of failure for the controller. Two scheduling parameters are used, the first being Φ_M, the fold angle, and the second the sail pitch angle, α, which is the angle between the incident radiation, and the sail normal (body z-axis). Two scheduling functions, C_1 and C_2 are implemented, such that the overall panel reflectivity vector is given by:

$$\boldsymbol{\rho} = C_1(\alpha)\left[C_2(\Phi_M,\alpha)u_s\boldsymbol{\rho_f} + T_x\boldsymbol{\rho_x} + T_y\boldsymbol{\rho_y} + T_z\boldsymbol{\rho_z}\right] \tag{6.25}$$

The first of the gain-scheduling functions is given by:

$$C_1 = \begin{cases} 1 & \text{if } \alpha < 90^\circ \\ -1 & \text{otherwise} \end{cases}$$

which ensures the reflectivity pattern is reversed for angles of incidence greater than 90°. This is required as the effect of the reflectivity patterns is reversed depending on which side of the sail is illuminated (where it is assumed that both sides of the panels are fitted with RCD devices). The second scheduling function modifies the shape/folding output only, and is given by:

$$C_2 = \begin{cases} (\Phi_M - 170)^2 + 1 & \text{if } \Phi_M > 170^\circ \\ 1 & \text{if } 170^\circ > \Phi_M > 114^\circ \\ 0 & \text{if } \Phi_M < 114^\circ \text{ and } \alpha > 90^\circ \end{cases}$$

Due to the interpanel reflections depicted in Fig. 6.18, the reflectivity pattern used to close the sail loses effectiveness when the fold angle is below 114° (determined through simulation). Therefore, further attempts to close the sail beyond this angle are counterproductive, and it is better to rely on any remaining folding momentum to achieve smaller fold angles. This is only required for $\alpha < 90^\circ$, where folding is achieved by setting the inner panels to $\rho = 1$ (and so the Miura pattern is folding towards the incident radiation). For folding in the opposite direction, i.e. where the outer panels have $\rho = 1$, interpanel reflections are not a concern and folding can be enacted in the full range of Φ_M. Above $\Phi_M = 170^\circ$, C_2 is set to the given quadratic, to rapidly increase the shape-control gain when the sail approaches the perfectly flat condition. This factor was included as the sail is restricted to not exceed a fold angle of 180°, where the Miura pattern becomes perfectly flat and folds can be induced around incorrect fold lines. In practice, it would likely be possible to design a Miura fold pattern which could reverse folding directions around 180°, as mechanical hinges or creased folding lines could ensure the correct folds are made at this point. In the simulation however it was found that the perfectly flat condition often led to computational instability, and therefore incorporating reversible folding would require some modification to the constraint equations. C_2 instead ensures that for angles above 170°, the shape control gain is increased significantly and the controller thus favours shape control over attitude in this region - since the desired attitude control pattern may act to further unfold the OrigamiSat at this point.

As noted, the predefined reflectivity patterns $\boldsymbol{\rho}_{f,x,y,z}$ which appear in Eq. 6.25 are one of two vectors/patterns depending on the sign of the control signal with which they are multiplied. For positive values of $C_1C_2u_s$, $\boldsymbol{\rho}_f$ is the "open" pattern shown in Fig. 4.6, and for negative values the opposite. The components of $\boldsymbol{T}^{ref}$ have the equivalent effect, in that the three corresponding patterns in the top of Fig. 4.6 are reversed for negative values. Equation 6.25 then gives a vector of positive values corresponding to the desired reflectivity of each panel, and as a final step the values are scaled to lie between $[0, 1]$, by dividing all values are by the value of the largest element (if the maximum is greater than 1). This scaling then automatically balances the attitude/shape control requirements at a given moment, where the weighting for each is determined by the magnitude of the control signals output by each block of the controller.

6.4.1.2 Controller Tuning

The shape PID-control gains are tuned following the well-known Zeigler-Nichols method (e.g Ref. [190]), where first the integral and derivative gains are set to zero, and the proportional gain is increased until steady oscillations are seen in the response. The gains are then set in relation to this following the standard Ziegler-Nichols equations [190]. The control response for a desired fold of 20° is shown in 6.20. The fold angle is seen to smoothly fall to the set point, though there is not the expected overshoot and settling that would be expected following Zeigler-Nichols tuning. This is likely due to the nonlinearity of the folding process, in that the "unfolding" reflectivity pattern results in a greater acceleration of the folding angle than the "folding" pattern. Despite this, the selected gains were found to perform well enough, and in fact it may be desirable to have no overshoot in the response as it is known that beyond some fold angles the controller loses effectiveness due to the interpanel reflections illustrated in Fig. 6.18. The attitude control gains are selected by adjusting P_q and P_w to produce an output that is comparable to the shape control output for similar error values, so that there is nominally an equal weighting given to the two control signals, and the available reflectivity control is evenly split between both requirements. The system response for a 20° slew manoeuvre around the body x-axis is shown in Fig. 6.21, again showing the response is smooth and with no overshoot. While performing the manoeuvre, the shape becomes disturbed due to the coupling

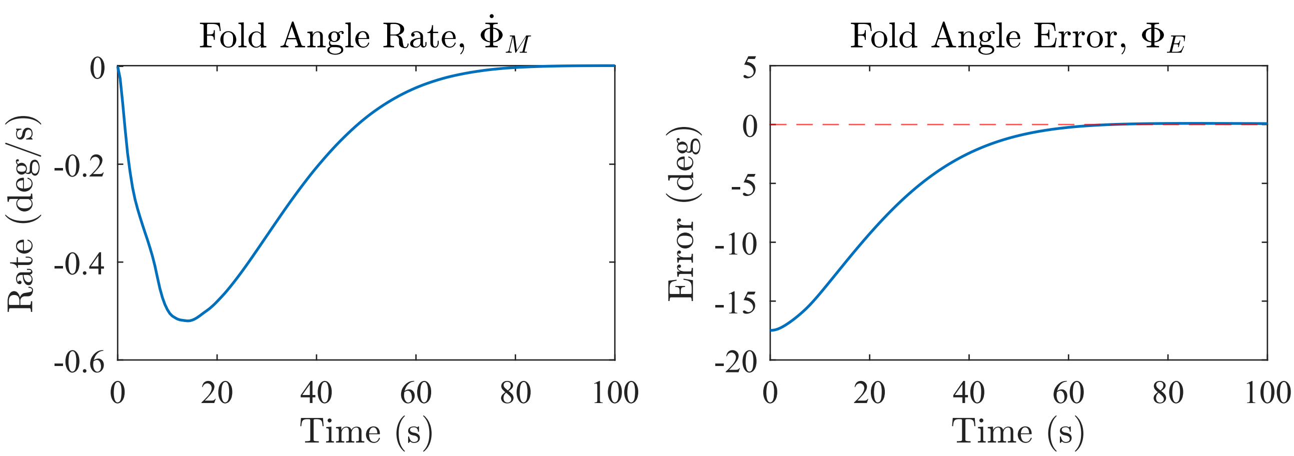

Figure 6.20: PID tuning of shape control law for Miura fold OrigamiSat.

of the multibody system. The fold angle disturbance and recovery is shown in Fig. 6.21, showing that there is a relatively large disturbance of approximately 5° in the fold angle, but this is then corrected by the shape-controller over the remainder of the simulation. The control gains, spacecraft data and simulation parameters are summarised in Table. 6.1.

6.4.2 Demonstration of Integrated Shape and Attitude Control

The control law is now demonstrated through simulations of two example manoeuvres. The two manoeuvres are illustrated in Fig. 6.22. The first is comprised of a rotation of 180° around the body x-axis, while simultaneously folding the sail to a fold angle of 140°. The second manoeuvre is a 90° rotation around the z-axis, again while folding to an angle of 140°. This second manoeuvre demonstrates how the sail can generate a torque in the z-direction with the given pattern, but only when the sail is not perfectly flat so that some panel surfaces are at an angle to the xy frame. Figure 6.22 shows the sail plotted at 200 s intervals during the simulation. The panel reflectivities are also shown, ranging from light to dark blue, corresponding to perfectly reflective and absorbing respectively. Plots of the sail angles, rates and control signals are shown in Figs 6.23 and 6.24. In both cases the desired attitude is approached smoothly, while the shape configuration is less smooth with larger disturbances during the manoeuvre. Plots

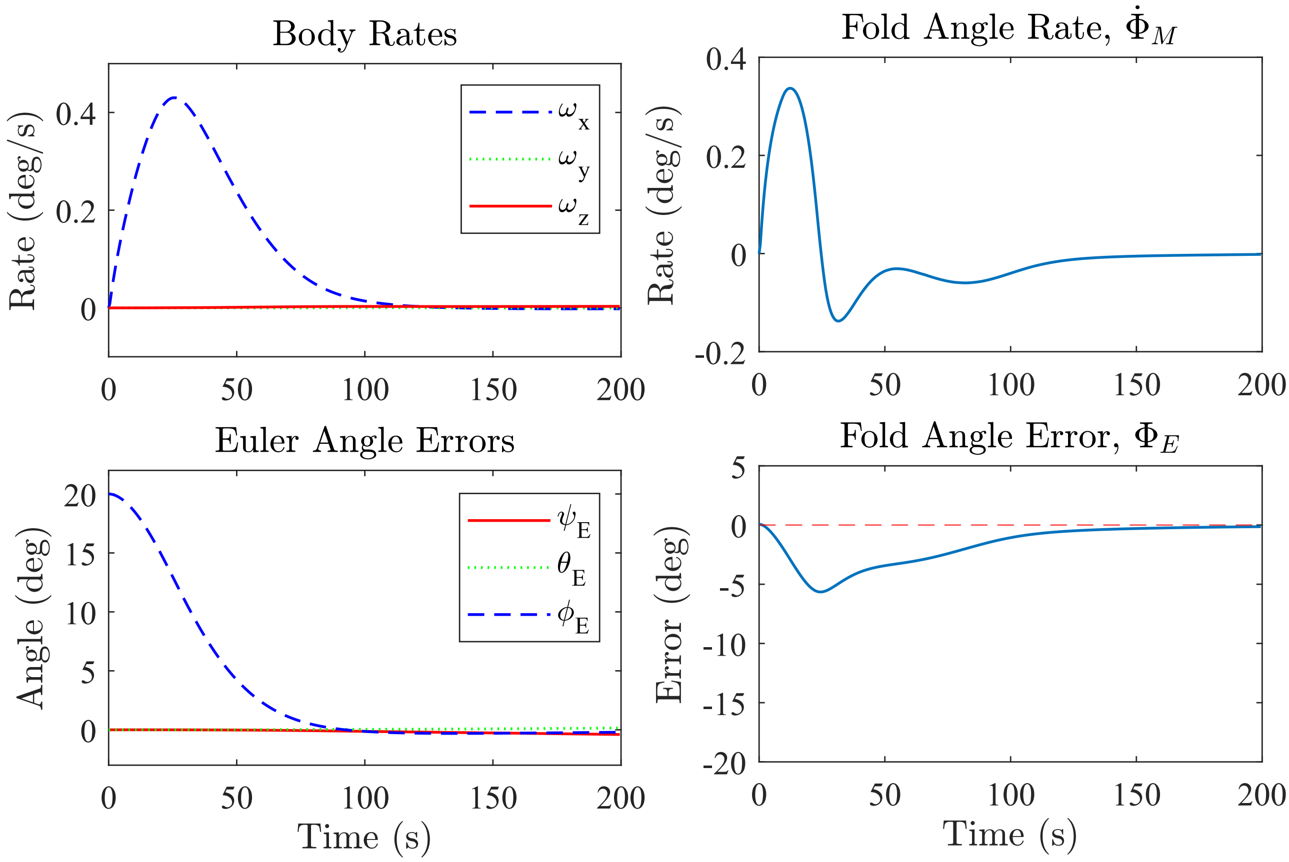

Figure 6.21: Attitude and shape response during 20° slew manoeuvre after attitude control tuning.

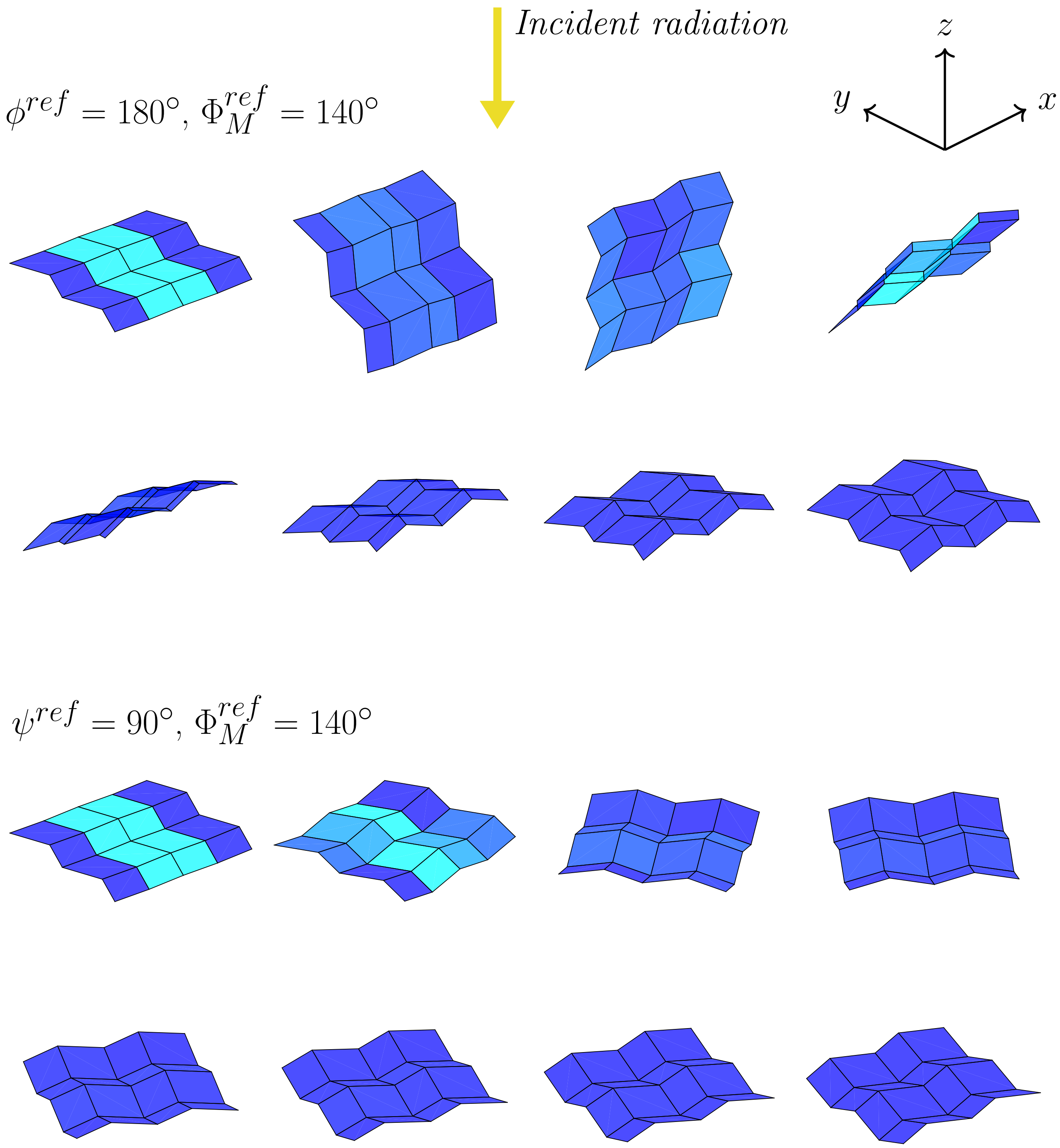

Figure 6.22: Miura OrigamiSat plotted at 200 s intervals for the two example manoeuvres. Light and dark blue represent perfectly reflecting/absorbing panels respectively.

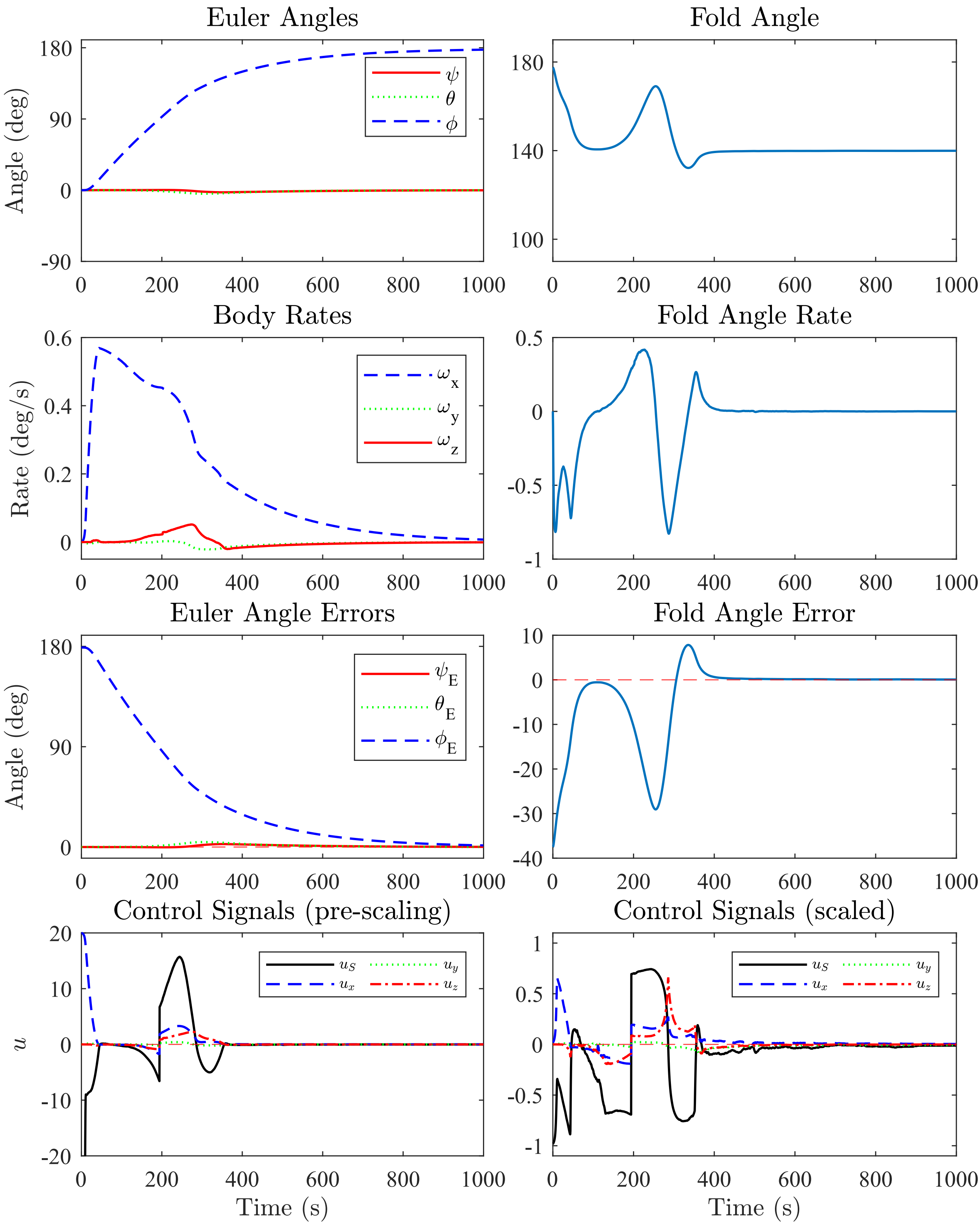

Figure 6.23: Results of simulation for a 180° manoeuvre around the body x-axis and simultaneous shape reconfiguration

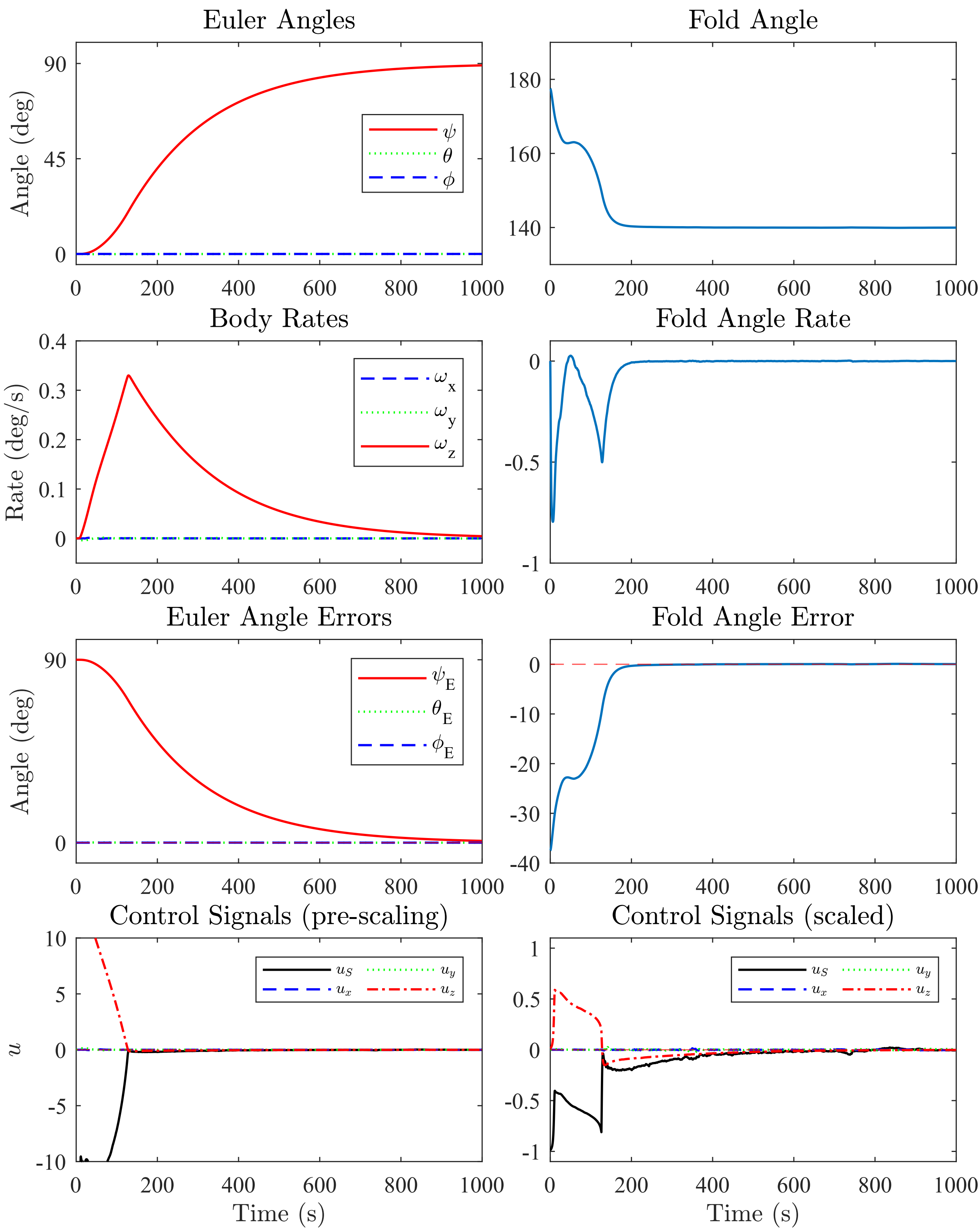

Figure 6.24: Results of simulation for a 90° manoeuvre around the z-axis and simultaneous shape reconfiguration

Side length		1 m
Areal Mass Density		10 g/m^2
Simulation timestep	$\mathrm{d}t$	0.1 s
Simulation time		1000 s
Number of rays	N_R	500^2
Control gains	P_q	15
	P_ω	1000
	k_p	0.48
	k_i	0.0069
	k_d	8.4

Table 6.1: Simulation data.

of the control signals are given for both before and after the scaling process, demonstrating the relative values of the shape and attitude control outputs and how these are balanced at different points of the simulation. Initially the fold angle is greater than 170°, and so shape-control is favoured (due to the quadratic C_2 function described previously). Once the angle falls below 170°, both the shape and attitude signal are approximately equal in magnitude, and so the two objectives share the scaled control values evenly. For the first manoeuvre, as shown in Fig. 6.23, there is a period after 200 s where the shape control signal dominates the scaled values. This is the point where the sail approaches a rotation of 90°, and so is nearly side-on to the incident radiation. The force due to SRP is therefore much lower in this configuration, and the system loses control effectiveness, hence the large errors in fold angle at this point.

6.5 Chapter Summary

In this chapter, the attitude and shape control of OrigamiSats through the use of surface reflectivity modulation was investigated. First, a length-scaling analysis was performed by considering a simplified, single-facet model. It was found that for lightweight OrigamiSats, folding times could be expected on the order of minutes for length-scales up to the order of 100 m, even when the bending resistance of a flexure hinge was considered in the analysis. A 2D multibody dynamics OrigamiSat model consisting of linked, rigid bars was then presented and used to investigate the principle of SRP induced OrigamiSat folding. It was found that varying the reflectivity of adjacent facets could in principle be used to control the folding process in 2D. A 3D multibody dynamics formulation was then used to further investigate the concept. An automatic procedure for generating the equations of motion for any OrigamiSat folding pattern was presented, and the need for and development of a ray-tracing module discussed. This model was then used to demonstrate shape reconfiguration of a Miura-fold OrigamiSat, and PD control was demonstrated for a pyramidal OrigamiSat design. As it was found that the folding of the OrigamiSat caused large disturbances to the attitude, it was then investigated whether attitude control could be integrated with the shape control process, again solely through the use of surface reflectivity modulation. A control strategy was developed for a Miura-fold OrigamiSat, consisting of two separate closed loop feedback control laws, the outputs of which are superimposed and used to provide attitude and shape control simultaneously. Finally, numerical simulations were used to demonstrate this control strategy, with two example manoeuvres presented in which a Miura fold OrigamiSat performs a simultaneous attitude manoeuvre and shape reconfiguration.

Chapter 7

Conclusions and Future Work

This thesis has considered the dynamics and control of large space structures, proposing and investigating a number of strategies for the attitude control of such spacecraft through the use of distributed actuation. In particular, the proposed strategies have been designed and analysed as potential forms of attitude control for a specific class of large space structure: ultra lightweight, flexible spacecraft, likely to be 3D-printed on-orbit in the coming years.

A motivating factor, common to all the proposed attitude control strategies, has been the relative ease with which an implementation of the concept could integrated with the 3D-printing of a structure itself. The magnetorquer arrays discussed in Chapters 3 an 4 could be fabricated by embedding magnetorquer rods within structural elements at regular intervals during the 3D-printing of the structure. The conductive structures of Chapter 5 take this idea a step further, in that in this case the structure itself provides the actuation. For the OrigamiSats of Chapter 6, actuation is provided by solar radiation pressure through the use of reflectivity control devices, relatively simple electronic components which can be embedded within a flexible membrane onto which the OrigamiSat structure is then printed. A further commonality of the proposed concepts is the fact that the actuation in all cases is distributed across the structure. As demonstrated in Chapter 3, distributed actuation was found to greatly reduce structural deformation during slew manoeuvres for structures in the range of flexibility and mass considered here. Additionally, distribution of the attitude control system gives greater robustness compared to having a single central bus and set of large actuators. Such a (distributed) spacecraft could be designed such that failure or damage to one area of the structure does not affect the performance of the rest of the attitude control system, or the structure could be designed in a scalable, modular fashion with attitude control available for each of the smaller component structures which make up the whole. In this sense, the control strategies proposed in this thesis take advantage of the new opportunities in spacecraft design afforded by on-orbit manufacturing, leveraging the 3D-printing process to fabricate a distributed attitude control system and the potential benefits thereof.

In this chapter, a summary of the findings and conclusions are given for the technical chapters of the thesis, followed by some suggestions for future work and a discussion of questions raised by the research presented here.

7.1 Chapter 3

This chapter proposed and analysed the use of distributed magnetorquer arrays for the attitude control of large structures. Simulation has demonstrated that distributed torques are in principle more effective at rotating a large, flexible structure than centralised torques, even when the increase in inertia of the distributed actuators is taken into account. This was demonstrated for 100 m structures with different parameters which cover a range of structural stiffnesses representative of large space structures of this scale. Of three cases considered, distributed torques are found to be more effective at inducing rotation than an equivalent torque applied to the centre-of-mass only. In addition to being able to achieve rotations, distributed torques result in lower deformation of the structure's surface, which may be desirable for many applications of large space structures.

Given that distributed torquing was found to be a desirable control strategy, magnetorquers in particular were then considered as a potential actuator. A configuration of magnetorquers was proposed for the control of a large planar structure, and a torque distribution algorithm developed which allows the overall control torque to be scaled by activating patterns of magnetorquers in the array. It was found that a large, 75 m flexible structure may be controlled by an array of magnetorquers through the application of this torque distribution algorithm, and rigid-body control laws. Both detumbling and slew manoeuvres were demonstrated through simulation, using the magnetorquer array in the presence of gravity gradient torques and a changing magnetic field. The application of these rigid-body control laws is only possible due to the torque being distributed across the structure sufficiently to approximate a rigid body, as was demonstrated previously. Slew manoeuvres were selected to demonstrate the range of possible rotations that can be enacted by the system, and it was found that rotations around the inertial x and z axes are possible for a square structure placed in polar orbit, but that due to the relative directions of the external field and gravity gradient, rotations around the inertial y-axis are not possible.

Despite the limitations of magnetic attitude control, an array of magnetorquers is attractive as they could be easily integrated into the on-orbit fabrication of a large space structure. For large space structures fabricated on-orbit, the system proposed here could provide a basic level of attitude control and stability, where the majority of the control effort is generated by the distributed magnetorquers. This could then be augmented by further actuation to suit specific mission requirements such as shape control and pointing accuracy.

7.2 Chapter 4

This chapter described the design, build and testing of a distributed magnetorquer array for spacecraft attitude control. The DMDP was built to test the control algorithms developed in Chapter 3, where a quaternion error feedback scheme was implemented in which the torque produced by the array is scaled by changing the number of activated torquers at a given time. A torquer selection algorithm is used which results in the activated torquers being as evenly distributed across the array as possible for any number of activated torquers. This approach has been demonstrated to succesfully perform single-axis slew manoeuvres and detumbling, through experiments performed on a spherical air bearing and using the magnetic field generated by a Helmholtz cage. The torque scaling and distribution algorithms investigated previously through simulation are thus considered to be verified for single axis rotation by this practical implementation, despite the required inclusion of magnetorquer duty cycling, sensor noise, and the resultant sampling rates and other limitations of the hardware used.

7.3 Chapter 5

This chapter proposed the use of large current loops as a further potential magnetic control strategy to the distributed arrays of the previous chapter. Results of a length-scaling analysis and a simple thermal model show that embedded current loops should be considered as a viable form of attitude control for large space structures, particularly for lightweight, planar structures which are most likely to be realised by on-orbit manufacturing techniques in the coming years. The analysis suggests that current loops lying in the plane of the structure are capable of producing torques at least as large as the maximum gravity gradient torque for structures on the order of 1000 m in length, when a modest portion ($<$10%) of the total structural mass is afforded to the conductive material. To achieve 3-axis magnetic attitude control, some structural depth is required, and the length-scaling is found to be more adverse, though it seems feasible that this could be achieved for structures of lengths on the order of 100 m, again assuming $<$10% of the mass for the conductive loops and that the structures depth is at least 3% of the length.

Considering structural flexibility, results of simulation have shown that a 250 m square structure, with areal mass density of 100 g/m^2, would require a beam-like bending stiffness of at least 10^4 N m^2 in order to not completely collapse under the effect of the Lorentz forces acting on the current loop. However, it is noted that a more flexible structure of lower mass would require lower torques to control, and it is possible current loops could still be viable in this case. Although it is possible that membrane tensioning via current loops could be possible, the results do suggest that any tensioning effect using current loops occurs simultaneously with a perpendicular compression of the structure, and so it appears unlikely that conductive loops interacting with the geomagnetic field could be used for this purpose. Simulations have shown that all the current loop geometries considered here are capable of rotating a flexible structure, though the structural deformation observed varies. In particular it was found that for current loops which enclose area in the depth dimension of a planar structure, having multiple large current loops is much preferred to having the coil type conducting pathway which was originally proposed in this chapter.

Finally, an attitude control simulation has demonstrated that the strategy is capable of performing a slew manoeuvre and maintaining a set attitude, in the presence of gravity gradient torques and a representative magnetic field model. Overall, it has been demonstrated that embedded current loops or conductive structures appear to be a promising form of attitude control strategy for large, lightweight space structures. The strategy is particularly appealing for the type of structure that may be 3D printed on-orbit, due to the simplicity of the design and relative ease with which production of the large current loops could be integrated with the 3D printing process.

7.4 Chapter 6

In this chapter, the use of combined thermo-optical properties for triggering shape reconfiguration of an OrigamiSat was investigated. It was shown that for a reflective flat square facet with a fixed edge, the time to complete a fold of $\pi/2$ rad under the influence of SRP is on the order of minutes for areal mass densities on the order of 10 g/m^2 and length-scales on the order of metres. Furthermore, it was shown that for a hinge constructed of the same thin film material as a conventional solar sail, the bending resistance of this hinge can be neglected above a critical length scale, due to the advantageous scaling of the force as a result of the SRP compared to the hinge resistance. Results of planar simulations show that folding can be induced, and the direction of folding reversed by controlling the surface reflectivity of linked, rigid facets. However, long chains of connected facets may be difficult to control in this manner, due to the large number of rotational degrees of freedom in the system.

A method for generating the multibody equations of motion for 3D rigid origami systems was then developed, and used to demonstrate the use of SRM to enact shape reconfiguration of 3D origami structures in free space. Simulations have shown that shape control with this strategy is possible in principle, but the degree of control that can be achieved depends upon a number of factors: the kinematics of the origami pattern design and in particular the degrees of freedom in folding of the design; the effect of inter-facet reflections and shadowing; and the ability to decouple the attitude dynamics from the shape reconfiguration, either through a dedicated attitude control system or the development of an integrated shape and attitude control algorithm. Active shape control was demonstrated for a simple triangular OrigamiSat design with a PD control law, though the results here suggest that in practice additional actuation will be required to achieve deployment and shape control within the full range of possible motion for many origami designs.

An integrated shape and attitude closed feedback control law was then developed and demonstrated for a Miura-fold pattern OrigamiSat. The proposed control law was seen to perform well, with 3-axis attitude control achievable, and shape reconfiguration possible between $\Phi_M = 180°$ and $114°$ when folding towards the incident sunlight, and in the full range when folding away from the Sun. While an ideal model has been assumed, in which panel reflectivities are controllable between 0 and 1, the principle of variable reflectivity as a form of attitude and shape control has been demonstrated. In particular, the proposed strategy of combining the shape and attitude control patterns from the separate closed loop controllers has proven to be a simple and effective method, where judicious selection of the control gains is found to lead to the controller performing a natural trade-off between these competing objectives.

The proposed strategy could likely be applied to other OrigamiSat designs, though the predefined reflectivity patterns would need to be known in advance for each degree of freedom of the origami pattern. Indeed, for many origami patterns it is likely that the patterns required to enact a fold around a certain edge will change depending on the sail attitude, and thus could not be predefined in the same way as was possible here for the Miura sail. In this case it may be possible to employ some form of model predictive control, whereby at each timestep the set or a subset of the possible reflectivity patterns are tested through simulation, to determine which degrees of freedom are acted upon by different combinations, and the pattern best matching an optimal trajectory to the desired configuration are selected. While such a strategy could be promising the computational power required to test every possible combination of panel reflectivities would be large, and would not scale well for an increased number of panels.

7.5 Future Work

Analysis of the attitude control strategies in this thesis has largely consisted of mathematical modelling and numerical simulation, though in the case of the distributed magnetorquer array of Chapter 3 a laboratory scale demonstration of the concept was developed and presented in Chapter 4. Future work in this area would require further experimentation with the laboratory scale demonstration, to further test the characteristics of the control system and extend the work of Chapter 4 to consider 3-axis control. As noted, this work would require much more precise balancing of the DMDP system on the spherical air-bearing, such that the residual gravitational torque can be overcome by the relatively small magnetic torques generated by the array. The full set of (3-axis) manoeuvres demonstrated in Chapter 3 through numerical simulation could then be attempted at the laboratory scale, to fully verify these results. Another important topic of research required to further develop the concept would be to determine the minimum areal mass density that could be achieved with the proposed strategy of 3D-printing the structure on-orbit, and what structural bending stiffness this would provide. In Chapter 3, a wide range of areal mass density and bending stiffness were considered, and so future work could narrow this range by considering more detailed structural modelling and/or characterisation of structures or structural units 3D-printed at the laboratory scale.

Similarly, the most pressing research topic following the results of Chapter 5 regards the feasibility of developing a practical implementation of the concept, and how best a conductive structure could be achieved in practice. It was suggested that copper wire could be embedded within or affixed to structural elements as they are 3D-printed on-orbit, and so future work could entail the development of a system capable of such a process. Again this would allow printed elements and structural units to be characterised at the laboratory-scale, giving better estimates of the minimum achievable areal mass density for such a structure and the resultant flexibility. These printed models could also be characterised to investigate the validity of the thermal model presented in Sec. 5.3, as the thermal balance of the conducting wire was a key factor in the length-scaling analysis here. More future work regarding conductive structures would be more detailed modelling which includes the self-interaction of the conducting elements. Calculation in Sec. 5.3 suggested that these forces would be negligible so long as the spacing of the structural units was sufficiently large. It may still be worth consideration of more densely packed structures, in which self-interaction forces become more important, to examine if the concept could still be applied in these cases. This research would be required if it was found, through structural analysis or physical experiments, that more densely packed truss structures were required to provide sufficient structural rigidity.

The analysis and results of simulation of OrigamiSats, presented in Chapter 6, also open a number of potential avenues of research. Regarding integrated attitude and shape control, future work would be to apply the strategy developed in Sec. 6.4 for the Miura-fold OrigamiSat to further, more complex Origami designs. Another topic of future research would be to extend the control system design to include further actuation, for example the use of shape-memory materials in the hinges (as was investigated from a manufacturing perspective in Ref. [139]), or the ability to lock/unlock the Origami edges on command using mechanical devices. Given the promising results of Chapter 6 in achieving shape reconfiguration with variable reflectivity as the sole form of actuation, it is thought likely that some limited further actuation could allow much more complex Origami designs to be reconfigured with ease, and allow a greater variety of potential applications. As with the other strategies considered in the thesis, development of a practical implementation of the OrigamiSat concept is another obvious area of future research. As noted, the feasibility study which the work of Chapter 6 was conducted under took some first steps in this direction. The work of colleagues at the University of Liverpool (not included in this thesis) investigated potential materials for 3D-printing an origami structure directly onto a thin film, and incorporating shape-memory polymers in the printed hinges. Future work could include the development of larger prototype OrigamiSats and efforts to determine the required structural mass, or the development of a prototype which includes RCDs mounted on the OrigamiSat panels. Such a prototype could then be used to demonstrate shape reconfiguration, for example by suspending the OrigamiSat in a vacuum chamber and using a solar simulator to illuminate the panels. This experiment could be used to verify the multibody dynamics simulations presented in Chapter 6. It may prove challenging to develop an experimental rig which can suspend the prototype OrigamiSat and simulate free-fall however, in which case an in-orbit demonstration may be the only way to fully demonstrate the concept.

7.6 Final Remarks

Through numerical analysis and experimental work, this thesis has investigated the feasibility of a variety of distributed attitude control strategies for future LSS. In the analysis of each chapter, attempts were made to determine the boundaries of the LSS design space at which each of the proposed strategies could prove feasible, in terms of length-scale, structural flexibility and areal mass density. The future work proposed in this chapter can then be seen as potential ways of increasing the level of confidence in these design space boundaries, a process which will require both further numerical analysis but in particular further practical demonstrations and experimental work.

As discussed in the introduction, LSS may be constructed to serve a number of purposes, both in Earth-orbit and beyond. Though there are many potential applications, the analysis of the thesis has remained largely application-agnostic, instead considering the general range of physical properties (areal mass density, stuctural flexibility, length-scale), that this next generation of LSS will likely possess. It is therefore hoped that the results of the thesis are general enough to be of use in the future development of LSS covering a wide range of potential applications and properties. A guiding principle in the work of this thesis was to consider forms of actuation which have not received considerable attention previously in the study of LSS, and to explore their potential. Therefore, even if future research finds control strategies which are more suitable for adaptation to on-orbit manufactured structures, or more efficient by some measures, it is hoped that this thesis can at least offer some contribution to future efforts in the form of a wider range of choices for their attitude control systems and add to the body of knowledge regarding the modelling, simulation and analysis this class of spacecraft.

In each of the technical chapters, it was posited that the principal advantage that the proposed strategies may have is the ease with which they may be deployed within a 3D-printed structure during the fabrication process, due to the relative simplicity of the required components. As such the primary development which would first be required for any of the strategies to be fully realised is that of an operational on-orbit manufacturing platform itself. As presented in the thesis introduction, there has been considerable interest in on-orbit manufacturing, from the early NASA studies to the more recent research and development of various companies and researchers. Given this level of interest and the potential benefits of the strategy, it seems increasingly likely that the coming years will see the first large-scale demonstration of an on-orbit manufactured structure, in which case it is hoped the assumptions, analysis and conclusions of this thesis may be fully tested in practice for this new generation of truly large space structures.

Bibliography

[1] R. Gibson. The next step - Space stations. *Futures*, 16(6):610–626, 1984. doi:10.1016/0016-3287(84)90123-X.

[2] D. S. F. Portree. Mir Hardware Heritage NASA RP 1357. Technical Report March, 1995.

[3] G. H. Kitmacher. Reference Guide to the International Space Station Assembly Complete Edition, NASA NP-2010-09-682-HQ. Technical report, 2010.

[4] C. R. McInnes. *Solar Sailing: Technology, Dynamics, and Mission Applications.* Springer-Praxis, 1st edition, 1999. doi:10.2514/2.4604.

[5] Y. Tsuda, O. Mori, R. Funase, H. Sawada, T. Yamamoto, T. Saiki, T. Endo, and J. Kawaguchi. Flight status of IKAROS deep space solar sail demonstrator. *Acta Astronautica*, 69(9-10):833–840, 2011. doi:10.1016/j.actaastro.2011.06.005.

[6] J. Heiligers and C. R. McInnes. Agile solar sailing in three-body problem: Motion between artificial equilibrium points. *Proceedings of the International Astronautical Congress, IAC*, pages 5439–5451, 2013.

[7] M. A. Greenhouse. The James Webb Space Telescope: Mission overview and status. *2019 IEEE Aerospace Conference*, pages 1–13, 2019. doi:10.1109/AERO.2019.8742209.

[8] R. E. Freeland and G. Bilyeu. In-Step Inflatable Antenna Experiment. *Acta Astronautica*, 30:29–40, 1993.

[9] Y. Hong. The "Tiangong" Chinese Space Station project. *Frontiers of Engineering Management*, 5(2):278–283, 2018.

[10] M. W. Thomson. The AstroMesh deployable reflector. *IEEE Antennas and Propagation Society International Symposium*, 3(September 1999):1516–1519, 1999. doi:10.1109/APS.1999.838231.

[11] J. E. Hylan, G. Bronke, J. Generie, W. Hayden, C. Collins, A. Jones, G. West, J. Crooke, J. Corsetti, T. Groff, B. Matonak, and N. Zimmerman. The Large UV/Optical/lnfrared Surveyor (LUVOIR): Decadal Mission Concept Study Update. In *2019 IEEE Aerospace Conference*, pages 1–15, 2019.

[12] V. M. Melnikov and V. A. Koshelev. *Large Space Structures Formed by Centrifugal Forces.* Earth Space Institute Book Series, 1st edition, 1998.

[13] G. W. Hughes, M. Macdonald, C. R. McInnes, A. Atzei, and P. Falkner. Analysis of a Solar Sail Mercury Sample Return Mission. *International Astronautical Federation - 55th International Astronautical Congress 2004*, 9:6106–6116, 2004. doi:10.2514/6.iac-04-q.2.b.08.

[14] J. E. Canady and J. L. Allen. Illumination From Space With Orbiting Solar-Reflector Spacecraft, NASA TP 2065. Technical report, 1982.

[15] F. C. Schwenk. Overview of Systems Definition Activities for Satellite Power Systems. In *Final Proceedings of the Solar Power Satellite Program Review, 1980.*, number April, pages 21–35. U.S. Department of Energy, 1980.

[16] J. G. Bodle. Development of a Beam Builder for Automatic Fabrication of Large Composite Space Structures. *NASA. Johnson Space Center The 13th Aerospace Mech. Symp.*, pages 293–304, 1979.

[17] E. Adams and C. Irvine. MSFC Evaluation of the Space Fabrication Demonstration System (Beam Builder). *NASA TM-82440*, 1981.

[18] W. K. Belvin. Advances in Structures for Large Space Systems. In *AIAA Space 2004 Conference and Exposition*, volume 1, pages 739–748, 2004. doi:10.2514/6.2004-5898.

[19] C. H. M. Jenkins. *Recent Advances in Gossamer Spacecraft.* AIAA, Progress in Astronautics and Aeronautics Volume 212, 1 edition, 2006. doi:https://doi.org/10.2514/4.866814.

[20] J. Catchpole. *The International Space Station Building for the Future.* Springer Praxis, 2008.

[21] J. Crusan, J. Bleacher, J. Caram, D. Craig, K. Goodliff, N. Herrmann, E. Mahoney, and M. Smith. NASA's Gateway: An Update on Progress and Plans for Extending Human Presence to Cislunar Space. *IEEE Aerospace Conference Proceedings*, 2019-March, 2019. doi:10.1109/AERO.2019.8741561.

[22] A Step Closer to the Axiom Commercial Space Station. *Thales Alenia (accessed 21/04/2022)*, 2021. `https://www.thalesgroup.com/en/worldwide/space/news/step-closer-axiom-commercial-space-station`.

[23] Blue Origin and Sierra Space Developing Commercial Space Station, 2021. `https://www.blueorigin.com/news/orbital-reef-commercial-space-station`.

[24] E. Messerschmid and R. Bertrand. *Space Stations Systems and Utilization.* Springer-Verlag, 1999. doi:10.4324/9780429307263-1.

[25] M. J. Balas. Trends in Large Space Structure Control Theory: Fondest Hopes, Wildest Dreams. *IEEE Transactions on Automatic Control*, 27(3):522–535, 1982. doi:10.1109/TAC.1982.1102953.

[26] J. J. Watson, T. J. Collins, and H. G. Bush. A history of astronaut construction of large space structures at NASA Langley Research Center. *IEEE Aerospace Conference Proceedings*, 7(figure 3):3569–3586, 2002. doi:10.1109/AERO.2002.1035334.

[27] M. M. Mikulas and J. M. Hedgepeth. Structural Concepts for very Large (400-Meter-Diameter) Solar Concentrators. Technical report, NASA CR N90-10153.

[28] R. B. Erb. Power from Space - The Tough Questions. *Acta Astronautica*, 38(4-8):539–550, 1996.

[29] J. C. Mankins. A Technical Overview of the "Suntower" Solar Power Satellite Concept. *Acta Astronautica*, 50(6):369–377, 2002. doi:10.1016/S0094-5765(01)00167-9.

[30] J. C. Mankins. *Space Solar Power, The First International Assessment of Space Solar Power: Opportunities, Issues and Potential Pathways Forward.* International Academy of Astronautics, 2011.

[31] J. C. Mankins. A fresh look at space solar power: New architectures, concepts and technologies. *Acta Astronautica*, 41(4-10):347–359, 1997. doi:10.1016/S0094-5765(98)00075-7.

[32] L. Boccia and O. Breinbjerg. Antenna Basics. *Space Antenna Handbook*, pages 1–35, 2012. doi:10.1002/9781119945147.ch1.

[33] N. English. *Space Telescopes, Capturing the Rays of the Electromagnetic Spectrum.* Springer, 2017.

[34] J. A. Angelo. *Spacecraft for Astronomy.* Facts On File, 2007.

[35] C. F. Lillie, R. S. Polidan, and D. R. Dailey. Key enabling technologies for the next generation of space telescopes. *Space Telescopes and Instrumentation 2010: Optical, Infrared, and Millimeter Wave*, 7731(May):773102, 2010. doi:10.1117/12.857826.

[36] L. D. Feinberg, J. Budinoff, H. MacEwen, G. Matthews, and M. Postman. Modular assembled space telescope. *Optical Engineering*, 52(9):091802, 2013. doi:10.1117/1.oe.52.9.091802.

[37] M. Chandra, S. Kumar, S. Chattopadhyaya, S. Chatterjee, and P. Kumar. A review on developments of deployable membrane-based reflector antennas. *Advances in Space Research*, 68(9):3749–3764, 2021. doi:10.1016/j.asr.2021.06.051.

[38] C. A. Rogers, W. L. Stutzman, T. G. Campbell, and J. M. Hedgepeth. Technology Assessment and Development of Large Deployable Antennas. *Journal of Aerospace Engineering*, 6(1):34–54, 1993.

[39] R. E. Freeland, G. D. Bilyeu, G. R. Veal, M. D. Steiner, and D. E. Carson. Large Inflatable Deployable Antenna Flight Experiment Results. *Acta Astronautica*, 41(4 10): 267–277, 1998.

[40] M. W. Thomson. Astromesh Deployable Reflectors for KU- and KA- Band Commercial Satellites. *20th AIAA International Communication Satellite Systems Conference and Exhibit*, 12-15 May(5), 2002.

[41] K. Nakamura, Y. Tsutsumi, K. Uchimaru, A. Tsujihata, and A. Meguro. Large Deployable Reflector on ETS-VIII. *17th AIAA International Communications Satellite Systems Conference and Exhibit*, pages 1–10, 1998.

[42] D. C. Alhorn, J. P. Casas, E. F. Agasid, C. L. Adams, G. Laue, C. Kitts, and S. O'Brien. NanoSail-D: The Small Satellite That Could! *25th Annual AIAA/USU Conference on Small Satellites*, pages 1–15, 2011.

[43] R. Ridenoure, R. Munakata, and A. Diaz. LightSail Program Status: One Down, One to Go. *29th AIAA/USU Conference on Small Satellites*, (626):1–50, 2015.

[44] D. A. Spencer, B. Betts, J. M. Bellardo, A. Diaz, B. Plante, and J. R. Mansell. The LightSail 2 solar sailing technology demonstration. *Advances in Space Research*, 67(9): 2878–2889, 2021. doi:10.1016/j.asr.2020.06.029.

[45] T. R. Lockett, J. Castillo-Rogez, L. Johnson, J. Matus, J. Lightholder, A. Marinan, and A. Few. Near-Earth Asteroid Scout Flight Mission. *IEEE Aerospace and Electronic Systems Magazine*, 35(3):20–29, 2020. doi:10.1109/MAES.2019.2958729.

[46] M. Cannella, S. Enger, A. Puls, and J. Rodriguez. Design and Overview of the Solar Cruiser Mission. *35th Annual Small Satellite Conference*, pages 1–7.

[47] P. Seefeldt, P. Spietz, T. Sproewitz, J. T. Grundmann, M. Hillebrandt, C. Hobbie, M. Ruffer, M. Straubel, N. Tóth, and M. Zander. Gossamer-1: Mission concept and technology for a controlled deployment of gossamer spacecraft. *Advances in Space Research*, 59(1): 434–456, 2017. doi:10.1016/j.asr.2016.09.022.

[48] P. Spietz, T. Spröwitz, P. Seefeldt, J. T. Grundmann, R. Jahnke, T. Mikschl, E. Mikulz, S. Montenegro, S. Reershemius, T. Renger, M. Ruffer, K. Sasaki, M. Sznajder, N. Tóth, M. Ceriotti, B. Dachwald, M. Macdonald, C. R. McInnes, W. Seboldt, D. Quantius, W. Bauer, C. Wiedemann, C. D. Grimm, D. Herčík, T. M. Ho, C. Lange, and N. Schmitz. Paths not taken – The GOSSAMER roadmap's other options. *Advances in Space Research*, 67(9):2912–2956, 2021. doi:10.1016/j.asr.2021.01.044.

[49] M. MacDonald and C. R. McInnes. Solar sail science mission applications and advancement. *Advances in Space Research*, 48:1702–1716, 2011. doi:10.1016/j.asr.2011.03.018.

[50] K. W. Billman, W. P. Gillbreath, and S. W. Bowen. Introductory Assessment of Orbiting Reflectors for Terrestrial Power Generation. Technical report, NASA TM X-73230, 1977.

[51] N. Lior. Mirrors in the sky : Status , sustainability , and some supporting materials experiments. *Renewable and Sustainable Energy Reviews*, 18:401–415, 2013.

[52] L. M. Fraas, G. A. Landis, A. Palisoc, and P. Jaffe. Space Mirror Development for Solar Electric Power And the International Space Station. *2016 IEEE 43rd Photovoltaic Specialists Conference (PVSC)*, pages 2558–2561, 2016. doi:10.1109/PVSC.2016.7750109.

[53] O. Çelik, A. Viale, T. Oderinwale, L. Sulbhewar, and C. R. McInnes. Enhancing terrestrial solar power using orbiting solar reflectors. *Acta Astronautica*, 195(February):276–286, 2022. doi:10.1016/j.actaastro.2022.03.015.

[54] T. Oderinwale and C. R. McInnes. Enhancing solar energy generation and usage : Orbiting solar reflectors as alternative to energy storage. *Applied Energy*, 317(December 2021): 119154, 2022. doi:10.1016/j.apenergy.2022.119154.

[55] O. Çelik and C. R. McInnes. An analytical model for solar energy reflected from space with selected applications. *Advances in Space Research*, 2021. doi:10.1016/j.asr.2021.10.033.

[56] C. R. McInnes. Space-based geoengineering: Challenges and requirements. *Proceedings of the Institution of Mechanical Engineers, Part C: Journal of Mechanical Engineering Science*, 224(3):571–580, 2009. doi:10.1243/09544062JMES1439.

[57] R. Bewick, J. P. Sanchez, and C. R. McInnes. The feasibility of using an L 1 positioned dust cloud as a method of space-based geoengineering. *Advances in Space Research*, 49 (7):1212–1228, 2012. doi:10.1016/j.asr.2012.01.010.

[58] C. R. McInnes. Planetary Macro-Engineering Using Orbiting Solar Reflectors. In *Macro-Engineering: A Challenge for the Future*, pages 215–250. Springer Netherlands, Dordrecht, 2006. doi:10.1007/1-4020-4604-9_11.

[59] NASA. Technology for Large Space Systems A Special Bibliography with Indexes. *NASA SP-7046(03)*, 1980.

[60] W. K. Muench. Automatic fabrication of large space structures-the next step. *Journal of Spacecraft and Rockets*, 17(3):286–288, 1980. doi:10.2514/3.57739.

[61] On-orbit Servicing, Assembly, and Manufacturing (OSAM) State of Play 2021. *OSAM National Initiative*, 2021.

[62] D. King. SPACE SERVICING: PAST, PRESENT AND FUTURE. *Proceeding of the 6th International Symposium on Artificial Intelligence and Robotics & Automation in Space: i-SAIRAS 2001*, (6):1–8, 2001.

[63] T. Prater, N. Werkheiser, F. Ledbetter, D. Timucin, K. Wheeler, and M. Snyder. 3D Printing in Zero G Technology Demonstration Mission: complete experimental results and summary of related material modeling efforts. *International Journal of Advanced Manufacturing Technology*, 101(1-4):391–417, 2019. doi:10.1007/s00170-018-2827-7.

[64] M. J. Werkheiser, J. Dunn, M. P. Snyder, J. Edmunson, K. Cooper, and M. M. Johnston. 3D Printing In Zero-G ISS Technology Demonstration. *AIAA SPACE 2014 Conference and Exposition*, 25(6):1521–1528, 2014. doi:10.2514/6.2014-4470.

[65] J. Clinton, Raymond, T. Prater, K. Morgan, and F. Ledbetter. NASA Additive Manufacturing Initiatives for Deep Space Human Exploration. *69th International Astronautical Congress (IAC);MSFC-E-DAA-TN61658;IAC-18C29*, (October):1–5, 2018.

[66] T. Prater, J. Edmunsson, M. Fiske, F. Ledbetter, C. Hill, M. Meyyappan, C. Roberts, L. Huebner, P. Hall, and N. Werkheiser. NASA's In-Space Manufacturing Project: Update on Manufacturing Technologies and Materials to Enable More Sustainable and Safer Exploration. *Proceedings of the International Astronautical Congress, IAC*, (October): 21–25, 2019.

[67] M. McRobb, B. Robb, S. Ridley, and C. R. McInnes. Emerging Space Technologies: Macro-scale On-orbit Manufacturing. *Journal of the British Interplanetary Society*, 72 (12), 2019.

[68] R. L. Spicer, W. Wautlet, T. Cote, and D. Roberts. Development of a 3D Printer Capable of Operation in a Vacuum. (January):1–17, 2020. doi:10.2514/6.2020-1120.

[69] D. Jonckers, O. Tauscher, A. R. Thakur, and L. Maywald. Additive Manufacturing of Large Structures Using Free-Flying Satellites. *Frontiers in Space Technologies*, 3(April): 1–12, 2022. doi:10.3389/frspt.2022.879542.

[70] R. P. Hoyt. SpiderFab: An Architecture for Self-Fabricating Space Systems. *AIAA SPACE 2013 Conference and Exposition*, pages 1–17, 2013. doi:10.2514/6.2013-5509.

[71] A. R. Hoyt, J. Cushing, J. Slostad, N. C. P. S, D. Suite, G. Nnxarg, and R. Hoyt. SpiderFab ™ : Process for On- - Orbit Construction of Kilometer- - Scale Apertures Report Date : NASA Innovative Advanced Concepts (NIAC) NASA Goddard Space Flight Center 8800 Greenbelt Road. *NASA NNX13AR26G – FINAL REPORT*, 2016.

[72] B. Levedahl, R. P. Hoyt, T. Silagy, J. Gorges, N. Britton, and J. Slostad. Trusselator™ Technology for In-Situ Fabrication of Solar Array Support Structures. *2018 AIAA Spacecraft Structures Conference*, (January), 2018. doi:10.2514/6.2018-2203.

[73] R. P. Hoyt, J. T. Slosad, T. J. Moser, J. I. Cushing, G. J. Jimmerson, R. L. Muhlbauer, A. J. Conley, S. R. Alvarado, and R. Dyer. In-space manufacturing of constructable™ long-baseline sensors using the trusselator™ technology. *AIAA Space and Astronautics Forum and Exposition, SPACE 2016*, (September):1–9, 2016. doi:10.2514/6.2016-5244.

[74] R. P. Hoyt, J. Cushing, J. Slostad, and G. Jimmerson. TRUSSELATOR: On-Orbit Fabrication of High-Performance Composite Truss Structures. In *AIAA SPACE 2014 Conference and Exposition*, number August, pages 1–10, 2014. doi:10.2514/6.2014-4337.

[75] S. C. Patané, J. J. Schomer, and M. P. Snyder. Design reference missions for archinaut: A roadmap for in-space manufacturing and assembly. *2018 AIAA SPACE and Astronautics Forum and Exposition*, (September):1–7, 2018. doi:10.2514/6.2018-5188.

[76] S. C. Patané, E. R. Joyce, M. P. Snyder, and P. Shestople. Archinaut: In-space manufacturing and assembly for next-generation space habitats. *AIAA SPACE and Astronautics Forum and Exposition, SPACE 2017*, (203999), 2017. doi:10.2514/6.2017-5227.

[77] A. H. de Ruiter. Gravity-Gradient Stabilization. In *Spacecraft Dynamics and Control: An Introduction*, chapter 16, pages 267–277. John Wiley & Sons, 2013.

[78] C. Arduini and P. Baiocco. Active Magnetic Damping Attitude Control for Gravity Gradient Stabilized Spacecraft. *Journal of Guidance, Control and Dynamics*, 20(1):117–122, 1997.

[79] R. Wiśniewski and M. Blanke. Fully magnetic attitude control for spacecraft subject to gravity gradient. *Automatica*, 35(7):1201–1214, 1999. doi:10.1016/S0005-1098(99)00021-7.

[80] J. M. Hedgepeth. Critical Requirements for the Design of Large Space Structures. Technical report, NASA Contractor Report 3484.

[81] G. B. Sincarsin and P. C. Hughes. Gravitational orbit-attitude coupling for very large spacecraft. *Celestial Mechanics*, 31(2):143–161, 1983. doi:10.1007/BF01686816.

[82] Y. Liu and L. Chen. *Chaos in attitude dynamics of spacecraft*. Tsinghua University Press, Springer, 2013. doi:10.1007/978-3-642-30080-6.

[83] K. Ishimura and K. Higuchi. Coupling among Pitch Motion , Axial Vibration , and Orbital Motion of Large Space Structures. *Journal of Aerospace Engineering*, 21(April): 61–71, 2008. doi:10.1061/(ASCE)0893-1321(2008)21:2(61).

[84] Y. Liu, S. Wu, G. Radice, and Z. Wu. Gravity-Gradient Effects on Flexible Solar Power Satellites. *Journal of Guidance, Control, and Dynamics*, 41(3):777–782, 2018. doi:10.2514/1.G003104.

[85] J. Mu, S. Gong, and J. Li. Coupled Control of Reflectivity Modulated Solar Sail for GeoSail Formation Flying. *Journal of Guidance, Control, and Dynamics*, 38(4):740–751, 2015. doi:10.2514/1.G000117.

[86] R. B. Malla. Structural and Orbital conditions on Response of Large Space Structures. *Journal of Aerospace Engineering*, 6(2):115–132, 1993.

[87] K. Ishimura and K. Higuchi. Coupling between structural deformation and attitude motion of large planar space structures suspended by multi-tethers. *Acta Astronautica*, 60(8-9):691–710, 2007. doi:10.1016/j.actaastro.2006.10.002.

[88] A. Colagrossi and M. Lavagna. Preliminary results on the dynamics of large and flexible space structures in Halo orbits. *Acta Astronautica*, 134(December 2016):355–367, 2017. doi:10.1016/j.actaastro.2017.02.020.

[89] L. Bucci and M. Lavagna. Coupled Dynamics Of Large Space Structures In Lagrangian Points. *International Conference on Astrodynamics Tools and Techniques*, (October), 2016.

[90] D. C. Hyland, J. L. Junkins, and R. W. Longman. Active control technology for large space structures. *Journal of Guidance, Control, and Dynamics*, 16(5):801–821, 1993. doi:10.2514/3.21087.

[91] S. N. Atluri and A. K. Amos. *Large Space Structures: Dynamics and Control*. Boundary Element Methods, 1988. doi:10.1080/10618560310000073036.

[92] Q. Li, Z. Deng, K. Zhang, and H. Huang. Unified Modeling Method for Large Space Structures Using Absolute Nodal Coordinate. *AIAA Journal*, 56(10):4146–4157, 2018. doi:10.2514/1.J057117.

[93] C. H. M. Jenkins and W. W. Schurt. *Mechanics Of Membrane Structures*. AIAA, 2001. doi:10.2514/5.9781600866616.0049.0110.

[94] A. Suleman. Multibody dynamics and nonlinear control of flexible space structures. *JVC/Journal of Vibration and Control*, 10(11):1639–1661, 2004. doi:10.1177/1077546304042049.

[95] Y. Kobayashi, M. Ikeda, and Y. Fujisaki. Stability of Large Space Structures Preserved Under Failures of Local Controllers. *IEEE Transactions on Automatic Control*, 52(2): 318–322, 2007. doi:10.1109/TAC.2006.887897.

[96] B. Fu, G. Gede, and F. O. Eke. Controllability of a square solar sail with movable membrane tips. *Proceedings of the Institution of Mechanical Engineers, Part G: Journal of Aerospace Engineering*, 231(6):1065–1075, 2017. doi:10.1177/0954410016647533.

[97] M. Choi and C. J. Damaren. Structural Dynamics and Attitude Control of a Solar Sail Using Tip Vanes. *Journal of Spacecraft and Rockets*, 52(6):1665–1679, 2015. doi:10.2514/1.A33179.

[98] B. Wie. Solar Sail Attitude Control and Dynamics , Part 2. *Journal of Guidance Control and Dynamics*, 27(4):536–544, 2004.

[99] B. Wie. Solar Sail Attitude Control and Dynamics , Part 1. *Journal of Guidance Control and Dynamics*, 27(4):526–535, 2004.

[100] A. Borggräfe, J. Heiligers, M. Ceriotti, and C. R. McInnes. Shape control of slack space reflectors using modulated solar pressure. *Proceedings of the Royal Society A: Mathematical, Physical and Engineering Sciences*, 471(2179), 2015. doi:10.1098/rspa.2015.0119.

[101] A. Borggräfe, J. Heiligers, M. Ceriotti, and C. R. McInnes. Attitude control of large gossamer spacecraft using surface reflectivity modulation. In *International Astronautical Congress*, pages 1753–1759, 2014. doi:10.1016/j.buildenv.2006.10.027.

[102] D. Ma, J. Murray, and J. N. Munday. Controllable Propulsion by Light: Steering a Solar Sail via Tunable Radiation Pressure. *Advanced Optical Materials*, 5(4):1–6, 2017. doi:10.1002/adom.201600668.

[103] P. Hughes. Dynamics of gyro-elastic continua. In *24th Structures, Structural Dynamics and Materials Conference*, 1983. doi:10.2514/6.1983-826.

[104] S. A. Chee and C. J. Damaren. Optimal Gyricity Distribution for Space Structure Vibration Control. *Journal of Guidance, Control, and Dynamics*, 38(7):1218–1228, 2015. doi:10.2514/1.G000293.

[105] Q. Hu, Y. Jia, and S. Xu. Dynamics and vibration suppression of space structures with control moment gyroscopes. *Acta Astronautica*, 96(1):232–245, 2014. doi:10.6002/ect.2017.0308.

[106] C. J. Damaren and G. M. T. D'Eleuterio. Optimal Control of Large Space Structures Using Distributed Gyricity. *Journal of Guidance Control and Dynamics*, 12(5):723–731, 1989. doi:10.1108/13598540610652492.

[107] Y. Hu, Y. Geng, and J. D. Biggs. Simultaneous Spacecraft Attitude Control and Vibration Suppression via Control Allocation. *Journal of Guidance, Control, and Dynamics*, 44(10): 1853–1861, 2021. doi:10.2514/1.g005834.

[108] M. J. Balas. Direct Velocity Feedback Control of Large Space Structures. *Journal of Guidance, Control, and Dynamics*, 1979. doi:10.2514/3.55869.

[109] N. B. Cramer, S. S.-M. Swei, K. Cheung, D. Cellucci, B. Jenett, and M. Teodorescu. Lattice-based Discrete Structure Modeling and Control for Large Flexible Space Structure Applications. *58th AIAA/ASCE/AHS/ASC Structures, Structural Dynamics, and Materials Conference*, (January):1–11, 2017. doi:10.2514/6.2017-1981.

[110] P. Gasbarri, R. Monti, and M. Sabatini. Very large space structures: Non-linear control and robustness to structural uncertainties. *Acta Astronautica*, 93:252–265, 2014. doi:10.1016/j.actaastro.2013.07.022.

[111] M. Polites, J. Kalmanson, and D. Mangus. Solar sail attitude control using small reaction wheels and magnetic torquers. 222:53–62, 2007. doi:10.1243/09544100JAERO250.

[112] M. Y. Ovchinnikov and D. S. Roldugin. A survey on active magnetic attitude control algorithms for small satellites. *Progress in Aerospace Sciences*, (May):0–1, 2019. doi:10.1016/j.paerosci.2019.05.006.

[113] M. Lovera and A. Astolfi. Spacecraft attitude control using magnetic actuators. *Automatica*, 40(8):1405–1414, 2004. doi:10.1016/j.automatica.2004.02.022.

[114] Y. Yang. Controllability of spacecraft using only magnetic torques. *IEEE Transactions on Aerospace and Electronic Systems*, 52(2):954–961, 2016. doi:10.1109/TAES.2015.150520.

[115] A. Colagrossi and M. Lavagna. Fully magnetic attitude control subsystem for picosat platforms. *Advances in Space Research*, 62(12):3383–3397, 2018. doi:10.1016/j.asr.2017.10.022.

[116] W. M. J. Robbins. The Feasibility of an Orbiting 1500-Meter Radiotelescope. Technical Report NASA CR-792, 1967.

[117] Y. Yamada, T. Inamori, J. Hyun Park, Y. Satou, Y. Sugawara, and K. Yamaguchi. Attitude Control of Spin-type Space Membrane Structures using Electromagnetic Force in Earth Orbit. *Advances in Space Research*, 2022. doi:10.1016/j.asr.2022.02.050.

[118] T. Inamori, T. Kawai, Y. Sugawara, and Y. Sato. Attitude control system of a space membrane using electromagnetic torque. *The Proceedings of the Asian Conference on Multibody Dynamics*, 2016.8(0):09_1256733, 2016. doi:10.1299/jsmeacmd.2016.8.09_1256733.

[119] V. Y. Kezerashvili and R. Y. Kezerashvili. Solar sail with superconducting circular current-carrying wire. *Advances in Space Research*, 69(1):664–676, 2022. doi:10.1016/j.asr.2021.10.052.

[120] G. V. Gettliffe, N. K. Inamdar, R. Masterson, and D. W. Miller. High-Temperature Superconductors as Electromagnetic Deployment and Support Structures in Spacecraft. Technical Report July, Massachusetts Institute of Technology, 2001.

[121] G. V. Gettliffe. *Stability Analysis of Electromagnetically Supported Large Space Structures*. PhD thesis, Massachusetts Institute of Technology, 2016.

[122] S. Soldini, J. J. Masdemont, and G. Gómez. Dynamics of solar radiation pressure-assisted maneuvers between lissajous orbits. *Journal of Guidance, Control, and Dynamics*, 42(4): 769–793, 2019. doi:10.2514/1.G003725.

[123] M. Ceriotti, P. Harkness, and M. McRobb. Variable-Geometry Solar Sailing: The Possibilities of the Quasi-Rhombic Pyramid. *Advances in Solar Sailing*, (February):899–919, 2014. doi:10.1007/978-3-642-34907-2_54.

[124] Y. Takao. *Active Shape Control of Spinning Solar Sails for Orbital Maneuvers*. PhD thesis, The University of Tokyo, 2020.

[125] J. Wertz and W. J. Larson. *Space Mission Analysis and Design*. Springer Dordrecht, 3 edition, 1999. doi:10.5860/choice.29-5149.

[126] E. A. Peraza Hernandez, D. J. Hartl, and D. C. Lagoudas. *Active Origami, Modeling, Design and Applications*. Springer, 2019. doi:10.1007/978-3-319-91866-2.

[127] J. Morgan, S. P. Magleby, and L. L. Howell. An Approach to Designing Origami-Adapted Aerospace Mechanisms. *Journal of Mechanical Design*, 138(May):2–10, 2016. doi:10.1115/1.4032973.

[128] Y. Nishiyama. Miura Folding: Applying Origami to Space Exploration. *International Journal of Pure and Applied Mathematics*, 79(2):269–279, 2012.

[129] B. N. Mcpherson, J. L. Kauffman, and C. Florida. Dynamics and Estimation of Origami-Inspired Deployable Space Structures : A Review. (January):1–18, 2019. doi:10.2514/6.2019-0480.

[130] Y. Miyazaki and Y. Iwai. Dynamics Model of Solar Sail Membrane. *14th Workshop on Astrodynamics and Flight Mechanics*, 2004.

[131] J. Zhang and C. R. McInnes. Using instability to reconfigure smart structures in a spring-mass model. *Mechanical Systems and Signal Processing*, 91:81–92, 2017. doi:10.1016/j.ymssp.2016.11.029.

[132] F. Trovarelli, M. McRobb, Z. Hu, and C. R. McInnes. Attitude control of an underactuated planar multibody system using momentum preserving internal torques. In *AIAA Scitech 2020 Forum*, Orlando, FL, 2020. doi:10.2514/6.2020-1686.

[133] F. Trovarelli. *Strategies for Attitude Control of Reconfigurable Modular Spacecraft*. Msc(res) thesis, The University of Glasgow, 2022.

[134] S. Gong, H. Gong, and P. Shi. Shape-based approach to attitude motion planning of reconfigurable spacecraft. *Advances in Space Research*, 70(5):1285–1296, 2022. doi:10.1016/j.asr.2022.06.004.

[135] H. Gong and S. Gong. Design of foldable PCBSat enabling three-axis attitude control. *Acta Astronautica*, 192(September 2021):291–300, 2022. doi:10.1016/j.actaastro.2021.12.004.

[136] H. Ashrafiuon and R. S. Erwin. Sliding mode control of underactuated multibody systems and its application to shape change control. *International Journal of Control*, 81(12): 1849–1858, 2008. doi:10.1080/00207170801910409.

[137] H. Gong, S. Gong, and D. Liu. Attitude dynamics and control of solar sail with multibody structure. *Advances in Space Research*, 69(1):609–619, 2022. doi:10.1016/j.asr.2021.10.012.

[138] T. Sinn and M. Vasile. Multibody dynamics for biologically inspired smart space structure. In *AIAA Spacecraft Structures Conference*, National Harbor, Maryland, 2014. doi:10.2514/6.2014-1364.

[139] A. Russo, B. Robb, S. Soldini, P. Paoletti, C. R. McInnes, J. Reveles, A. K. Sugihara, S. Bonardi, and O. Mori. Mechanical Design of Self-reconfiguring 4D-printed OrigamiSat: a New Concept for Solar Sailing. *Frontiers in Space Technologies*, 3, 2022.

[140] B. Robb, M. McRobb, G. Bailet, J. Beeley, and C. R. McInnes. Distributed Magnetic Attitude Control for Large Space Structures. *Acta Astronautica*, 198(September):587–605, 2022.

[141] B. Robb, M. McRobb, G. Bailet, and C. R. McInnes. 3D-printed, electrically conductive structures for magnetic attitude control. *Acta Astronautica*, 200(July):448–461, 2022.

[142] B. Robb, M. Mcrobb, and C. R. McInnes. Magnetic Attitude Control of Gossamer Spacecraft using a 3D-printed , Electrically Conducting Support Structure. In *AIAA Scitech 2020 Forum*, 2020.

[143] B. Robb, G. Bailet, J. Beeley, and C. R. McInnes. Laboratory-Scale Demonstration of a Distributed Magnetorquer Array for the Attitude Control of Large Space Structures. *73rd International Astronautical Congress*, (IAC-22,C1,2,3,x69274), 2022.

[144] B. Robb, A. Russo, S. Soldini, P. Paoletti, J. Reveles, G. Bailet, and C. R. McInnes. Integrated Attitude and Shape Control for OrigamiSats with Variable Surface Reflectivity. *73rd International Astronautical Congress*, (IAC-22,C2,9,2,x69275), 2022.

[145] B. Wie. *Space Vehicle Dynamics and Control.* AIAA Education Series, 2 edition, 2008.

[146] M. J. Sidi. *Spacecraft dynamics and control: A practical engineering approach*. Cambridge University Press, Cambridge, 1997. doi:10.1017/CBO9780511815652.

[147] Y. Shirasawa, O. Mori, Y. Miyazaki, H. Sakamoto, M. Hasome, N. Okuizumi, H. Sawada, H. Furuya, S. Matsunaga, M. Natori, and J. Kawaguchi. Analysis of membrane dynamics using multi-particle model for solar sail demonstrator "IKAROS". *Collection of Technical Papers - AIAA/ASME/ASCE/AHS/ASC Structures, Structural Dynamics and Materials Conference*, (April):3–4, 2011. doi:10.2514/6.2011-1890.

[148] G. Prathap. *The Finite Element Method in Structural Mechanics*. Springer Science+Business Media, Dordrecht, 1993. doi:10.3138/9781442676695-006.

[149] M. L. Gambhir. Rigid-Body Assemblages. In *Stability Analysis and Design of Structures*, chapter 3, pages 107–110. Springer-Verlag Berlin Heidelberg, 2004.

[150] K. Guidanean and D. Lichodziejewski. An Inflatable Rigidizable Truss Structure Based on New Sub-Tg Polyurethane Composites. In *43rd AIAA/ASME/ASCE/AHS/ASC Structures, Structural Dynamics, and Materials Conference*, number April, pages 1–11, Denver, 2002.

[151] M. M. Mikulas, T. J. Collins, W. Doggett, J. Dorsey, and J. Watson. Truss performance and packaging metrics. *AIP Conference Proceedings*, 813:1000–1009, 2006. doi:10.1063/1.2169281.

[152] D. M. Murphy, M. E. McEachen, B. D. Macy, and J. L. Gaspar. Demonstration of a 20-m solar sail system. *Collection of Technical Papers - AIAA/ASME/ASCE/AHS/ASC Structures, Structural Dynamics and Materials Conference*, 6(April):4028–4044, 2005. doi:10.2514/6.2005-2126.

[153] L. Herbeck, M. Eiden, M. Leipold, C. Sickinger, and W. Unckenbold. Development and test of deployable ultra-lightweight CFRP-booms for a Solar Sail. *European Space Agency, (Special Publication) ESA SP*, 49(468):107–112, 2001.

[154] T. L. Tien. Space Frame Structures. In *Structural Engineering Handbook*. CRC Press LLC, 1999.

[155] K. S. Arun, T. S. Huang, and S. D. Blostein. Least-Squares Fitting of Two 3-D Point Sets. *IEEE Transactions on Pattern Analysis and Machine Intelligence*, PAMI-9(5):698–700, 1987.

[156] L. Herbeck, C. Sickinger, M. Eiden, and M. Leipold. Solar sail hardware developments. *European Conference on Spacecraft Structures, Materials and Mechanical Testing*, pages 1–10, 2002.

[157] Magnetorquer Rod Datasheet. *NewSpace Systems (accessed 23/10/2022).* `http://www.newspacesystems.com/wp-content/uploads/2018/10/NewSpace-Magnetorquer-Rod{_}7b.pdf`.

[158] H. Ouyang, J. E. Mottershead, M. P. Cartmell, and M. I. Friswell. Friction-induced parametric resonances in discs: Effect of a negative friction-velocity relationship. *Journal of Sound and Vibration*, 209(2):251–264, 1998. doi:10.1006/jsvi.1997.1261.

[159] J. J. Kim and B. N. Agrawal. Experiments on jerk-limited slew maneuvers of a flexible spacecraft. *Collection of Technical Papers - AIAA Guidance, Navigation, and Control Conference 2006*, 2(August):1030–1049, 2006. doi:10.2514/6.2006-6187.

[160] G. Fracchia, J. D. Biggs, and M. Ceriotti. Analytical low-jerk reorientation maneuvers for multi-body spacecraft structures. *Acta Astronautica*, 178(April 2020):1–14, 2021. doi:10.1016/j.actaastro.2020.08.020.

[161] N. Jovanovic, B. Riwanto, P. Niemela, M. R. Mughal, and J. Praks. Design of Magnetorquer-Based Attitude Control Subsystem for FORESAIL-1 Satellite. *IEEE Journal on Miniaturization for Air and Space Systems*, 2(4):220–235, 2021. doi:10.1109/jmass.2021.3093695.

[162] E. Silani and M. Lovera. Magnetic spacecraft attitude control: A survey and some new results. *Control Engineering Practice*, 13(3):357–371, 2005. doi:10.1016/j.conengprac.2003.12.017.

[163] J. C. Urschel. On The Characterization and Uniqueness of Centroidal Voronoi Tessellations. *SIAM Journal on Numerical Analysis*, 55(3):1525–1547, 2017. doi:10.1137/15m1049166.

[164] J. Burns. Centroidal Voronoi Tessletions. *(Lecture notes, accessed 23/10/2022).* `https://people.math.sc.edu/Burkardt/classes/urop{_}2016/burns.pdf`.

[165] S. P. Lloyd. Least squares quantization in {PCM}. Special issue on quantization. *IEEE Transactions on Information Theory*, 28(2):129–137, 1982.

[166] Q. Du, V. Faber, and M. Gunzburger. Centroidal Voronoi Tessellations: Applications and Algorithms. *SIAM Review*, 41(4):637–676, 2005. doi:10.1137/s0036144599352836.

[167] NASA. State of the Art of Small Spacecraft Technology. *State of the Art of Small Spacecraft Technology*, (December):1–202, 2018. `https://sst-soa.arc.nasa.gov/04-propulsion`.

[168] A. S. Stickler. A Magnetic Control System for Attitude Acquisition. Technical report, Ithaco, Inc., Rep. 90345, 1972.

[169] B. M. Chulliat, A., W. Brown, P. Alken, C. Beggan, M. Nair, G. Cox, A. Woods, S. Macmillan and M. Paniccia. The US / UK World Magnetic Model for 2020-2025. Technical report, 2020.

[170] J. Lee, A. Ng, and R. Jobanputra. On determining dipole moments of a magnetic torquer rod - Experiments and discussions. *Canadian Aeronautics and Space Journal*, 48(1): 61–67, 2002.

[171] S. O. Madgwick. An efficient orientation filter for inertial and inertial/magnetic sensor arrays. *Report, University of Bristol*, 2010. doi:10.1177/00220345830620061401.

[172] Github user Hideakitai. MPU9250 - Arduino Library. *Github Repository - (accessed 26/08/2022)*, 2022. `https://github.com/hideakitai/MPU9250`.

[173] M. Walt. *Introduction to Geomagnetically Trapped Radiation*. Cambridge University Press, nov 1994. doi:10.1017/CBO9780511524981.

[174] M. R. Ward. *Electrical Engineering Science*. McGraw-Hill technical education series. McGraw-Hill, 1971. `https://books.google.co.uk/books?id=MeQxAAAACAAJ`.

[175] I. D. Boyd, R. S. Buenconsejo, D. Piskorz, B. Lal, K. W. Crane, and E. De La Rosa Blanco. On-Orbit Manufacturing and Assembly of Spacecraft. Technical report, IDA Science and Technology Policy Institute, 2017.

[176] W. McGuire, R. H. Gallagher, and R. D. Ziemian. *Matrix Structural Analysis*. Faculty Books, 2 edition, 2000.

[177] J. L. Humar. *Dynamics of Structures*. CRC Press, 3 edition, 2012.

[178] R. W. Clough and J. Penzien. *Dynamics of structures*. Computers & Structures, Inc., 3 edition, 2002. doi:10.1139/l90-078.

[179] M. S. Lake, L. D. Peterson, and M. B. Levine. Rationale for Defining Structural Requirements for Large Space Telescopes. *Journal of Spacecraft and Rockets*, 39(5):674–681, 2002. doi:10.2514/2.3889.

[180] R. Malka, A. L. Desbiens, Y. Chen, and R. J. Wood. Principles of microscale flexure hinge design for enhanced endurance. *IEEE International Conference on Intelligent Robots and Systems*, (Iros):2879–2885, 2014. doi:10.1109/IROS.2014.6942958.

[181] M. Ceriotti, P. Harkness, and M. McRobb. Synchronized orbits and oscillations for free altitude control. *Journal of Guidance, Control, and Dynamics*, 37(6):2062–2066, 2014. doi:10.2514/1.G000253.

[182] M. MacDonald and C. R. McInnes. Solar sail science mission applications and advancement. *Advances in Space Research*, 48(11):1702–1716, 2011. doi:10.1016/j.asr.2011.03.018.

[183] N. Okuizumi and T. Yamamoto. Centrifugal Deployment of Membrane with Spiral Folding: Experiment and Simulation. *Journal of Space Engineering*, 2(1):41–50, 2009. doi:10.1299/spacee.2.41.

[184] D. Baraff. Linear-time dynamics using Lagrange multipliers. *Proceedings of the 23rd Annual Conference on Computer Graphics and Interactive Techniques, SIGGRAPH 1996*, pages 137–146, 1996. doi:10.1145/237170.237226.

[185] A. A. Shabana. *Computational Dynamics*. Wiley, 3rd edition, 2010.

[186] A. Glassner. *An Introduction to Ray Tracing*. Elsevier, 1 edition, 1989.

[187] F. Darugna, P. Steigenberger, O. Montenbruck, and S. Casotto. Ray-tracing solar radiation pressure modeling for QZS-1. *Advances in Space Research*, 62(4):935–943, 2018. doi:10.1016/j.asr.2018.05.036.

[188] V. Vijayan. Ray casting for deformable triangular 3D meshes. *(accessed 18/07/2022)*, 2022. `https://www.mathworks.com/matlabcentral/fileexchange/41504-ray-casting-for-deformable-triangular-3d-meshes`.

[189] P. Terdiman. OPCODE Optimized Collision Detection Library (Version 1.3). *(accessed 18/07/2022)*, 2003. `http://www.codercorner.com/Opcode.htm`.

[190] G. Ellis. *Control System Design Guide*. Elsevier Inc., 1st edition, 2012. doi:10.1016/C2010-0-65994-3.